
On Simulations of Cosmic Rays in the Large-Scale Structure of the Universe

Ludwig Maximilian Böss



München 2023

On Simulations of Cosmic Rays in the Large-Scale Structure of the Universe

Ludwig Maximilian Böss

Dissertation
an der Fakultät für Physik
der Ludwig–Maximilians–Universität
München

vorgelegt von
Ludwig Maximilian Böss
aus München

München, den 23.11.2023

Erstgutachter: Prof. Dr. Harald Lesch
Zweitgutachter: Prof. Dr. Klaus Dolag
Tag der mündlichen Prüfung: 25.01.2024

Zusammenfassung

Kosmische Strahlung, auch Cosmic Rays (CRs) genannt, in Form von relativistischen Protonen und Elektronen sind die Quelle nicht-thermischer Strahlung in einer Vielzahl astrophysikalischer Systeme. Diese Strahlung gibt Einblicke in die Stärke und Struktur von Magnetfeldern, kosmische Stoßwellen und nicht-thermischer Druckkomponenten im interstellaren oder intergalaktischen Medium.

In der großräumigen Struktur des Universums sind CR Elektronen die Quelle für Synchrotron Emission in Radio Halos, Radio Relikten und den Jets aktiver galaktischer Kerne.

CR Protonen andererseits sollten durch die Interaktion zwischen CR Protonen und den thermischen Protonen des Intra-Cluster Medium diffuse γ -Strahlung produzieren. Diese γ -Strahlung wurde jedoch bisher nicht beobachtet. Eine Abschätzung dieser γ -Strahlung wird benötigt um einen Einblick in die nicht-thermischen Druckkomponenten von Galaxienhaufen zu erhalten und um Observationsfenster für die Beobachtung von Dunkler Materie zu finden.

Simulationen des sogenannten Cosmic Web ermöglichen Einblicke in die Entstehung und Entwicklung der größten gravitativ gebundenen Strukturen des Universums. Sogar die modernsten Simulationen verfügen nicht über die benötigte Auflösung, um kosmische Strahlung aus ersten Prinzipien zu simulieren. Wir benötigen deshalb eine sorgsame Beschreibung für die Physik kosmischer Strahlung, die sich unter der Auflösungsgrenze dieser Simulationen befindet, um den Effekt der kosmischen Strahlung auf die Strukturbildung unseres Universums zu studieren.

In dieser Arbeit fassen wir die Entwicklung von CRESCENDO: *Cosmic Ray Evolution with Spectral Electrons and protons* zusammen. CRESCENDO ist ein numerisches Modell, welches die Spektren von CR Protonen und Elektronen als stückweise Potenzgesetze darstellt und deren zeitliche Entwicklung in Simulationen kosmischer Strukturbildung berechnet. Diese zeitliche Entwicklung berücksichtigt folgende Aspekte: Die Beschleunigung kosmischer Strahlung an Stoßwellen, hervorgerufen durch Kollisionen massiver Galaxienhaufen und Massenakkretion, oder Supernova Explosionen, Energieänderungen durch adiabatische Expansion oder Kompression des umliegenden Gases, Energieverluste durch Synchrotron-, inverse Compton Strahlung und Teilchenkollisionen, Energiezunahme durch turbulente Nachbeschleunigung, sowie Transport von CR Teilchen durch Advektion und Diffusion. Die zeitliche Entwicklung der Spektren erlaubt es uns Observablen wie Synchrotron Emission und die Emission von γ -Strahlung selbstkonsistent zu berechnen und mit realen Beobachtungen zu vergleichen.

Nach einer allgemeinen Einleitung in Teil I stellen wir in Teil II das Modell vor und vergleichen die Genauigkeit mit analytischen Lösungen. In den Kapiteln von Teil III zeigen wir die Anwendung auf die Simulation verschiedener kosmischer Strukturen mit zunehmender Komplexität.

Zuerst wenden wir CRESCENDO auf idealisierte Simulationen kollidierender Galaxienhaufen an. Das erlaubt es uns die Beschleunigung von kosmischer Strahlung an den resultierenden Stoßwellen und deren Auswirkung auf die Entwicklung von Radio Relikten zu untersuchen. Wir sind in der Lage grundlegende Beobachtungen zu reproduzieren, wie beispielsweise die Form des Synchrotron Spektrums oder die Verteilung der Synchrotron Spektren hinter den Stoßwellen.

Im darauffolgenden Kapitel untersuchen wir die Wechselwirkung zwischen kollidierenden Stoßwellen und deren Einfluss auf die Beschleunigung kosmischer Strahlung in einer ultrahoch aufgelösten zoom-in Simulation eines massiven Galaxienhaufens. Das erlaubt es uns eine Erklärung für die Entstehung einer neu entdeckten Klasse von Radio Relikten zu finden, der sogenannten "Wrong Way Radio Relics". Diese Relikte zeigen komplexe Morphologie, wobei das Relikt zum Zentrum des Galaxienhaufens hingebeugt ist, anstatt die typische Beugung weg vom Zentrum des Haufens aufzuweisen. Mit unserem Modell sind wir in der Lage zu zeigen, dass diese Relikte entstehen können, wenn eine sich nach Außen bewegende Stoßwelle von einer einfallenden Galaxiengruppe deformiert wird.

In den zwei darauffolgenden Kapiteln wenden wir unser Modell in einer Simulation eines kosmologischen Volumens an, um diffuse nicht-thermische Strahlung im Cosmic Web vorherzusagen.

Wir konzentrieren uns dabei zuerst auf die Synchrotron Strahlung relativistischer Elektronen indem wir CRESCENDO auf eine Version des SLOW Simulationssatzes und zoom-in Simulationen des Coma Galaxienhaufen anwenden. Wir finden konsistente Teilchenbeschleunigung an Akkretionsschocks um Galaxienhaufen und Filamente des Cosmic Web, welche signifikante Saat-Populationen von CR Elektronen produziert. Wir untersuchen die daraus resultierende diffuse Synchrotron Strahlung unter Berücksichtigung verschiedener Magnetfeldmodelle und finden diffuse Emission in allen Bereichen des Cosmic Web. Allerdings liegt diese Emission selbst mit den optimistischsten Parametern für Teilchenbeschleunigung und Magnetfeldstärke 1-2 Größenordnungen unter der Sensitivität moderner Radioteleskope.

Zuletzt analysieren wir die CR Protonen derselben Simulation, um Vorhersagen für diffuse γ -Strahlung in Galaxienhaufen und Filamenten des Cosmic Web zu treffen. Wir finden CR Protonenbeschleunigung und damit diffuse γ -Strahlung in allen Bereichen des Cosmic Web. Der beobachtbare Strahlungsfluss liegt 3-4 Größenordnungen unter der derzeitigen oberen Grenze welche mit dem Fermi-LAT Instrument detektiert werden kann. Wir diskutieren daraufhin die Auswirkungen unserer Parameter für Teilchenbeschleunigung und die Genauigkeit unserer Stoßwellendetektion auf diese Ergebnisse und finden, dass die Auswirkungen signifikant sein können. Deshalb sind zukünftige zoom-in Simulationen nötig, um diese Ergebnisse zu verifizieren.

Abstract

Cosmic rays (CRs) in the shape of relativistic protons and electrons are the source of non-thermal radiation in a plethora of astrophysical systems. Their emission provides insights into the strength and structure of magnetic fields, cosmic shock waves, and non-thermal pressure components in the interstellar or intergalactic medium.

In the large-scale structure of the Universe CR electrons are the likely source of synchrotron emission from Radio Halos, Radio Relics, and AGN jets.

CR protons on the other hand should be detectable via diffuse γ -rays from their interaction with the thermal background gas, however, this emission has not yet been found. Estimating the γ -ray emission from this process is required to study the non-thermal pressure support in clusters, as well as finding observational windows for potential detection of Dark Matter interaction.

Simulations of the Large-Scale Structure of the Universe, the so-called Cosmic Web, give insights into the origin and evolution of the largest gravitationally bound structures in the Universe. Even state-of-the-art simulations of cosmological structure formation lack the resolution to simulate the effect cosmic rays have on their environment from first principles. We therefore require a careful sub-grid description of cosmic ray physics that can be included in such simulations to model the effect cosmic rays may have on the evolution of cosmic structure.

In this work, we summarize the development of *CRESCENDO: Cosmic Ray Evolution with Spectral Electrons and protons*, a cosmic ray model that represents the spectra of cosmic ray protons and electrons as piece-wise power-laws and evolves these spectra in time on-the-fly within simulations of cosmological structure formation. This time evolution accounts for: The acceleration of CRs at shocks caused by collisions between massive galaxy clusters and mass accretion, or supernova explosions, energy changes due to adiabatic compression or expansion of the surrounding gas, energy losses due to synchrotron emission, inverse Compton scattering, and Coulomb collisions, energy gains due to turbulent re-acceleration, and transport of CRs through advection and diffusion. The time evolution of these spectra further allows us to obtain observables such as synchrotron- and γ -ray emission self-consistently, which can be compared to real observations.

After a general introduction in Part I, we introduce the model and provide tests of its performance against analytic solutions in Part II. In the chapters of Part III, we show its application to a number of simulations of cosmic structures with increasing complexity.

First, we apply CRESCENDO to simulations of idealized galaxy cluster mergers. This allows us to study CR acceleration at merger shocks and the formation of Radio Relics. We are able to reproduce key observables such as the synchrotron spectrum and the spectral steepening downstream of the relic.

In the subsequent chapter, we study the interaction of colliding shock waves and their impact on CR acceleration in an ultra-high resolution zoom-in simulation of a massive galaxy cluster. This allows us to provide an explanation for the formation of an only recently discovered class of radio relics, referred to as "Wrong Way Radio Relics". These relics show complex morphologies with the relic bent towards the cluster center, instead of the typical bend away from the cluster center. With our model, we are able to show that these radio relics can form if an in-falling group of galaxies collides with an outwards traveling shock wave and deforms the radio relic as it passes through the shock surface.

In the two following chapters, we extend our modeling to a constrained simulation of a cosmological volume to study diffuse non-thermal emission from the Cosmic Web.

We will first study diffuse synchrotron emission from cosmic web filaments by applying CRESCENDO to a realization of the SLOW simulation set and a number of zoom-in simulations of the Coma cluster. We find consistent CR acceleration at accretion shocks onto galaxy clusters and cosmic web filaments, which produce significant CR seed populations. We then investigate the diffuse emission those CR populations can produce under various magnetic field models and with the influence of turbulent re-acceleration of CRs. We find diffuse emission in all regimes, however, even with the most optimistic parameters for magnetic field strength and CR injection this emission still lies 1-2 orders of magnitude below the detection limit of current radio telescopes.

Finally, we analyze the same simulation as in the previous chapter but consider the CR proton population. This allows us to make predictions for diffuse γ -ray emission in galaxy clusters and cosmic web filaments. We find CR proton acceleration and with that diffuse γ -ray emission in all regions of the cosmic web. However, the obtained γ -ray flux lies 3-4 orders of magnitude below the current upper limits obtained with Fermi-LAT. We discuss the impact of CR injection parameters and the performance of our on-the-fly shock finder on these results and find that the impact can be substantial. Future higher-resolution zoom-in simulations will be required to verify these results.

Contents

Zusammenfassung	v
Abstract	vii
List of Acronyms	xii
I Introduction	1
1 The Large-Scale Structure of the Universe	3
1.1 Evolution of Cosmic Structure	3
1.2 Galaxy Clusters	9
1.3 Cosmic Web Filaments	12
1.4 Cosmic Voids	12
2 Plasma Physics in the ICM	15
2.1 The Intra-Cluster Medium	15
2.2 Collisionless Shocks	16
2.3 Turbulence	17
2.4 Magnetic Fields	20
2.5 Particle Acceleration	28
2.6 Cosmic Rays	32
3 Non-Thermal Emission in the Large-Scale Structure of the Universe	35
3.1 Synchrotron Radiation	35
3.2 Diffuse γ -ray emission	44
4 Simulations	47
4.1 Large-Scale Structure Simulations	47
4.2 Including Magnetic Fields	49
4.3 Including Cosmic Rays	51
4.4 The Relevance of this Cosmic Ray Model	53

II	CRESCENDO	55
5	A Spectral Cosmic Ray Model for Cosmological Simulations	57
5.1	The Diffusion-Advection Equation	57
5.2	Spectral Parameters	58
5.3	Time Evolution	59
5.4	Boundary Conditions	64
5.5	Timestep Constraints	65
6	Sources	67
6.1	Shock Acceleration	67
6.2	Supernovae	78
7	Adiabatic Changes	81
7.1	Implementation	81
7.2	Tests	82
8	Cooling Processes	85
8.1	Synchrotron and IC Losses	85
8.2	Coulomb Losses	87
9	Fermi-II Re-acceleration	91
9.1	Momentum Diffusion Coefficient D_{pp}	91
9.2	Systematic Re-Acceleration	93
9.3	Stochastic Re-Acceleration	93
10	Spatial Propagation	95
10.1	Artificial Conduction	95
10.2	Isotropic Momentum Dependent Diffusion	96
10.3	Anisotropic Momentum Dependent Diffusion	97
10.4	Tests	98
11	Observables	103
11.1	Synchrotron Emission	103
11.2	Stokes Parameters	107
11.3	γ -ray Emission	109
12	Coupling to OPENGADGET3	115
12.1	Smoothed Particle Hydrodynamics	115
12.2	Cosmic Ray - Hydrodynamics	117

III Applications	119
13 Idealized Cluster Mergers	121
13.1 Initial Conditions	121
13.2 Magnetic Field Models	123
13.3 Simulations	124
13.4 Shock Fronts	126
13.5 The Northern Relic	126
13.6 The Southern Relic	132
13.7 Conclusions	135
14 Zoom-In Simulations: ‘Wrong Way’ Radio Relics	137
14.1 Introduction	137
14.2 Methods	139
14.3 Results	141
14.4 Discussion	148
14.5 Conclusion	150
15 SLOW - Synchrotron Emission from the Local Cosmic Web	151
15.1 Introduction	152
15.2 Methods	154
15.3 Full-Sky Projections	158
15.4 The Coma Filaments	165
15.5 Full Box	171
15.6 Discussion	175
15.7 Conclusions	182
16 SLOW - γ-ray Emission from the Local Universe	183
16.1 Introduction	183
16.2 Methods	185
16.3 Full-Sky Projections	190
16.4 Fermi-LAT limits	191
16.5 Coma, Virgo, Perseus and Fornax	193
16.6 Discussion	196
16.7 Conclusions	200
IV Outlook & Conclusion	201
17 Outlook	203
17.1 Ultra-Relativistic Limits	203
17.2 AGN jets	203
17.3 Odd Radio Circles	204
17.4 Radio Mega Halos	204

18 Conclusion	205
Bibliography	207
Acknowledgements	243
Appendix	245
A.1 Shocktube Tests	245
A.2 Non-Relativistic Limits	246

List of Acronyms

AGN Active Galactic Nucleus

AIC Alfvén Ion Cyclotron

CMB Cosmic Microwave Background

COM center-of-mass

CR Cosmic Ray

CR_e Cosmic Ray electron

CR_p Cosmic Ray proton

DM Dark Matter

DSA Diffusive Shock Acceleration

EFI Electron Firehose Instability

FDF Faraday Dispersion Function

GC Galaxy Cluster

HT de Hoffmann-Teller

ICM Intra-Cluster Medium

IC inverse Compton

IMF Initial Mass Function

ISM Interstellar Medium

PIC Particle-In-Cell

RH Radio Halo

RR Radio Relic

RM Rotation Measure

SDA Shock Drift Acceleration

SN Supernova

SPH Smoothed-Particle Hydrodynamics

LOS line-of-sight

LSS Large-Scale Structure

MHD Magneto Hydrodynamics

NFW Navarro, Frenk and White

ORC Odd Radio Circle

pc Parsec

kpc Kilo-parsec

Mpc Mega-parsec

WHIM Warm-Hot Intergalactic Medium

Part I

Introduction

1 | The Large-Scale Structure of the Universe

Understanding the origin and evolution of the structure of our Universe is one of the key questions in modern astrophysics. Ambitious surveys like 2DFGRS ([Colless et al., 2003](#)), 2MASS ([Jarrett et al., 2003](#)) and SDSS ([Tegmark et al., 2004](#)) established that, when looking at the clustering of galaxies, the Universe looks like a giant web on Mega-parsec (Mpc) scales, the so-called *Cosmic Web* (e.g. [Bond et al., 1996](#)). With modern simulations the astrophysical community has made great advances in reproducing this structure, as can be seen in Fig. 1.1.

This work is aimed towards a better understanding of one specific aspect of the Large-Scale Structure (LSS) of the Universe, namely what role relativistic particles, so-called Cosmic Rays (CRs) play in the formation of this LSS and what the non-thermal emission associated with these CRs can tell us about the underlying structure of the gas dynamics and magnetic fields that permeates the gas in the LSS.

In this chapter, we want to give a brief introduction to the physics behind cosmic evolution and the zoology of the components that make up the cosmic web.

1.1 Evolution of Cosmic Structure

Our current understanding of the origin of the Universe is that it emerged from a single event of energy release that generated space-time, the so-called *Big Bang*¹. Shortly after this Big Bang, there was a period of inflation that blew up causally connected quantum fluctuations into causally decoupled density fluctuations. These density fluctuations provided the seeds for cosmic structure formation.

First, we need to establish the framework of how we can even begin to describe cosmological structure formation. A natural step is to first identify a dominating force for this process. This force is easily identified as gravity, since it is the only force that, to the best of our current knowledge, cannot be shielded off and is infinitely far-reaching.

Since the introduction of a general theory of relativity by [Einstein \(1916\)](#) the most general way

¹Author's note: This (musical) typo has intentionally been left in, per explicit request by Prof. Harald Lesch.

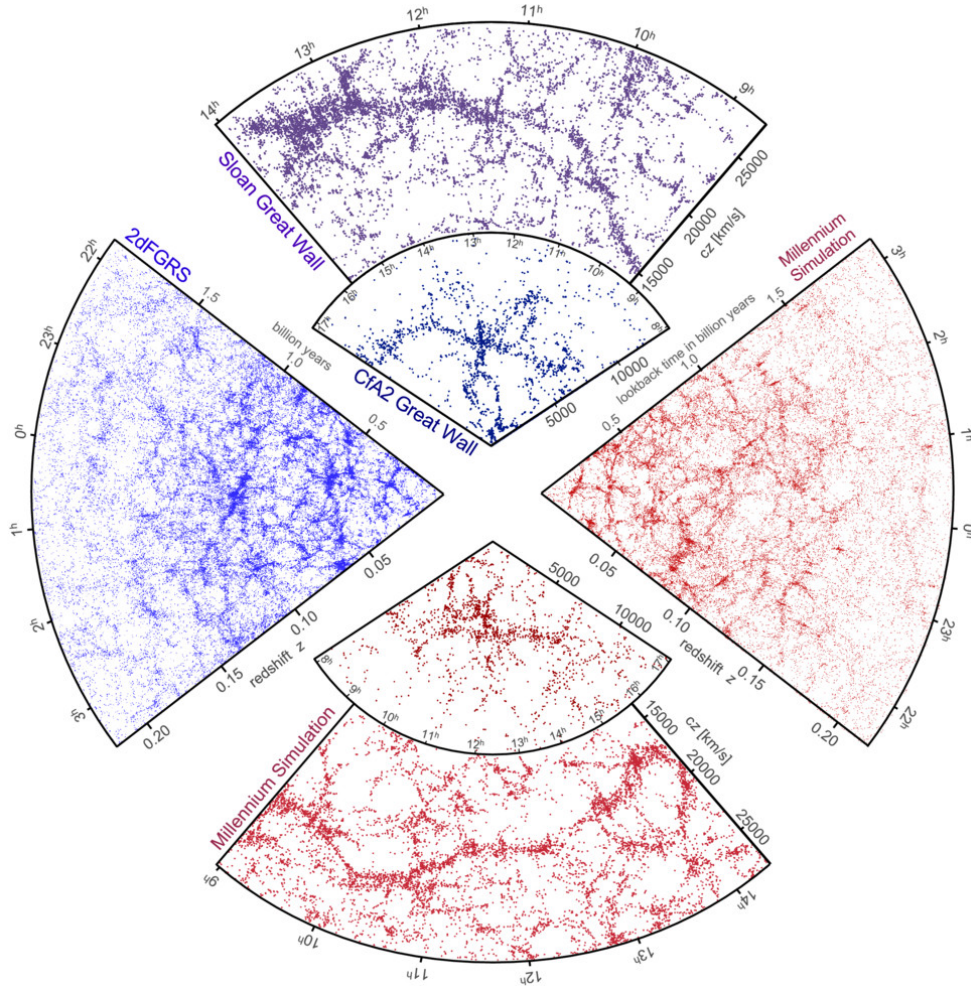


Figure 1.1: The large-scale structure of the Universe as observed (blue) and obtained from simulations (red). Adopted from [Springel et al. \(2006\)](#).

to describe gravitational interaction is via *Einstein's field equation*

$$\mathbf{G}_{\alpha\beta} = \frac{8\pi G}{c^4} \mathbf{T}_{\alpha\beta} + \Lambda \mathbf{g}_{\alpha\beta} \quad (1.1)$$

where $\mathbf{G}_{\alpha\beta}$ is the Einstein tensor, giving a description for a (curved) space-time, G the gravitational constant, c the speed of light, $\mathbf{T}_{\alpha\beta}$ is the energy-momentum tensor, Λ the so-called *cosmological constant* and $\mathbf{g}_{\alpha\beta}$ the metric tensor. We also used Einstein's sum convention where $\alpha\beta$ runs over the indices $0 \dots N_{\text{dim}}$. The metric tensor defines a way to measure distance in an arbitrary geometry. We can postulate that our position in space-time is not unique and the Universe has no preferential direction, this is known as the *cosmological principle*, which implies that on the largest scales, our Universe is *homogeneous* and *isotropic*. In such a homogenous and isotropic Universe, distance can be measured via the *Friedmann-Lemaître-Robertson-Walker* (commonly

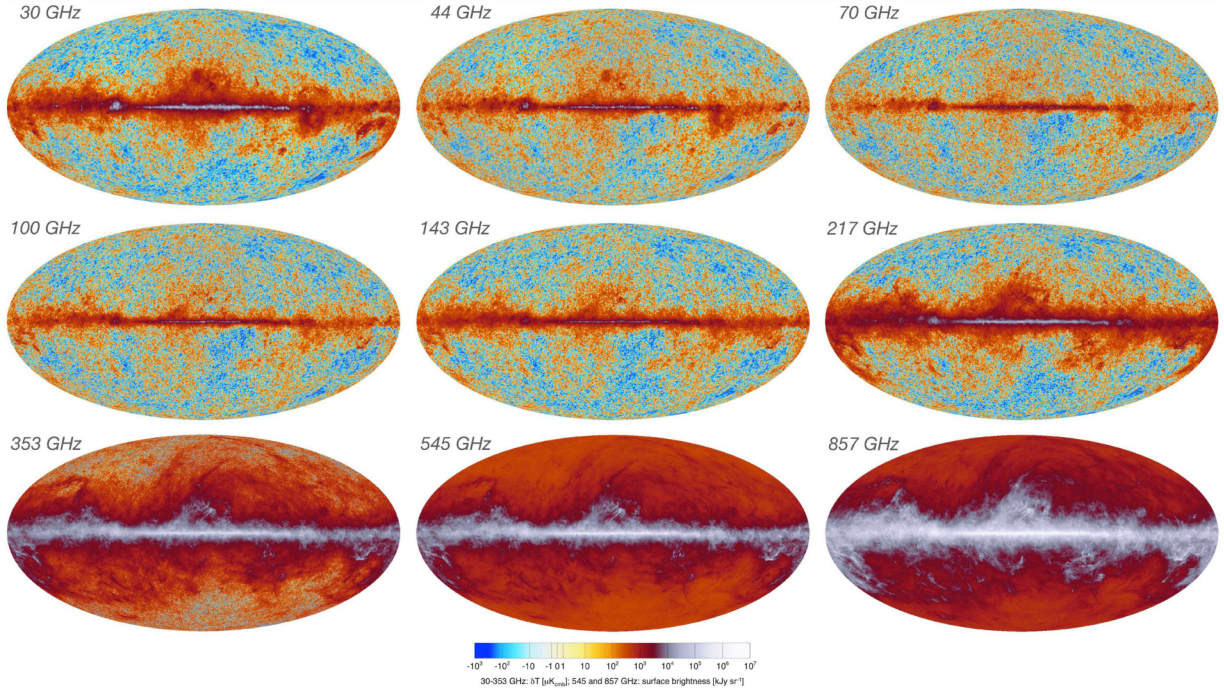


Figure 1.2: Temperature fluctuations in the CMB as observed at different frequencies by the PLANCK satellite at different frequencies, before the galactic foreground is removed. Adopted from [Planck Collaboration et al. \(2020a\)](#).

shortened to Roberston-Walker) metric

$$\mathbf{g}_{ij}dx^i dx^j = ds^2 = c^2 dt^2 - a^2(t) \left(\frac{dr^2}{1 - kr^2} + r^2 d\Omega^2 \right) \quad (1.2)$$

where $a(t)$ is the so-called *scale factor* of the Universe, $k = 0, \pm 1$ is its curvature, with $k = 0$ describing a flat Universe, $k = -1$ a saddle-shaped Universe and $k = 1$ a spherical Universe. The scale factor is chosen in such a way that we can define a coordinate system that is independent of cosmic expansion (which we will discuss later)

$$r_{\text{physical}} = a(t)r_{\text{comoving}} \quad (1.3)$$

Finally, $d\Omega^2 = d\theta^2 + \sin^2(\theta)d\phi^2$ is the angular component of the line-element in (comoving) spherical coordinates. By inserting this metric into Eq. 1.1, under the condition of an isotropic and homogeneous Universe, we can derive the so-called *Friedmann equations*

$$\frac{\dot{a}^2}{a^2} = \frac{8\pi G}{3}\rho - \frac{kc^2}{a^2} + \frac{\Lambda}{3} \quad (1.4)$$

$$\frac{\ddot{a}}{a} = -\frac{4\pi G}{3} \left(\rho + \frac{3p}{c^2} \right) + \frac{\Lambda}{3} \quad (1.5)$$

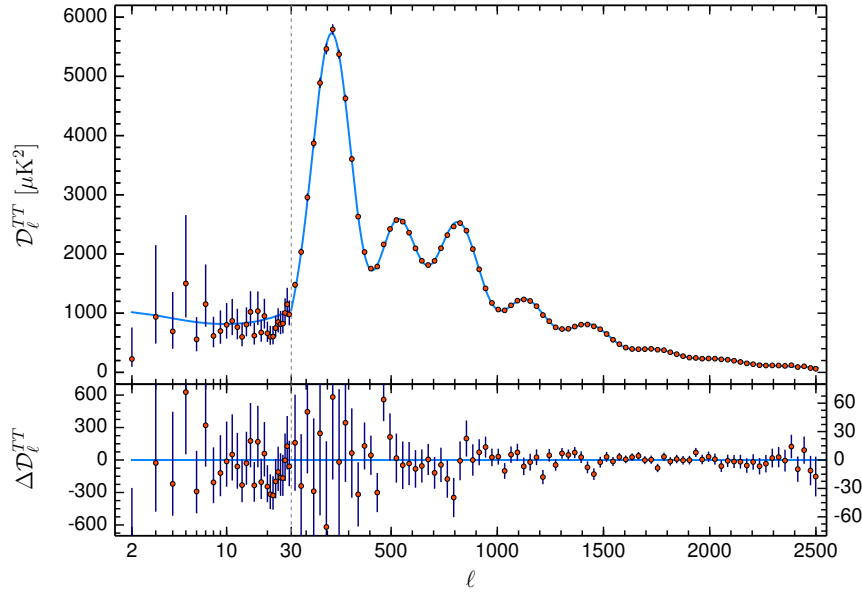


Figure 1.3: Temperature power spectrum obtained from the CMB. Adopted from [Planck Collaboration et al. \(2020b\)](#).

which describe the time evolution of the Universe, where Eq. 1.4 describes how the scale of the Universe changes and Eq. 1.5 describes how the rate of this change behaves. These equations have a number of implications, we will note two major ones. First, simply from our existence, we can infer that $\rho \neq 0$, so Eq. 1.4 implies that the Universe is not static, but instead either expanding or contracting, unless convenient values of Λ are found. Second, from Eq. 1.5 follows that unless $\Lambda \neq 0$ and $p \neq -c^2/3$ this expansion will decelerate over the time the Universe evolves.

By rearranging Eq. 1.4, performing a time derivative on both sides and substituting \ddot{a} via Eq. 1.5, we can further obtain a *third Friedmann equation*

$$\dot{\rho}c^2 = -3\frac{\dot{a}}{a}\left(\rho + \frac{P}{c^2}\right) \quad (1.6)$$

which essentially is an expression for the conservation of energy.

With the discovery by [Hubble \(1929\)](#) that distant galaxies are moving away from us at a velocity that is proportional to their distance, it was established that the Universe is indeed not static, but expanding. This was later confirmed by [Riess et al. \(2001\)](#) who found that the Universe is not only expanding, but doing so in an accelerated fashion. This gives Λ a physical interpretation as some sort of energy density that drives the current expansion of the Universe, typically referred to as *dark energy*. By introducing $H(t) = \dot{a}(t)/a(t)$ as the so-called *Hubble parameter* and in the case of a flat Universe $k = 0$ without a cosmological constant $\Lambda = 0$, we can solve Eq. 1.4 for the density

$$\rho_{\text{crit}}(t) = \frac{3H(t)}{8\pi G} \quad (1.7)$$

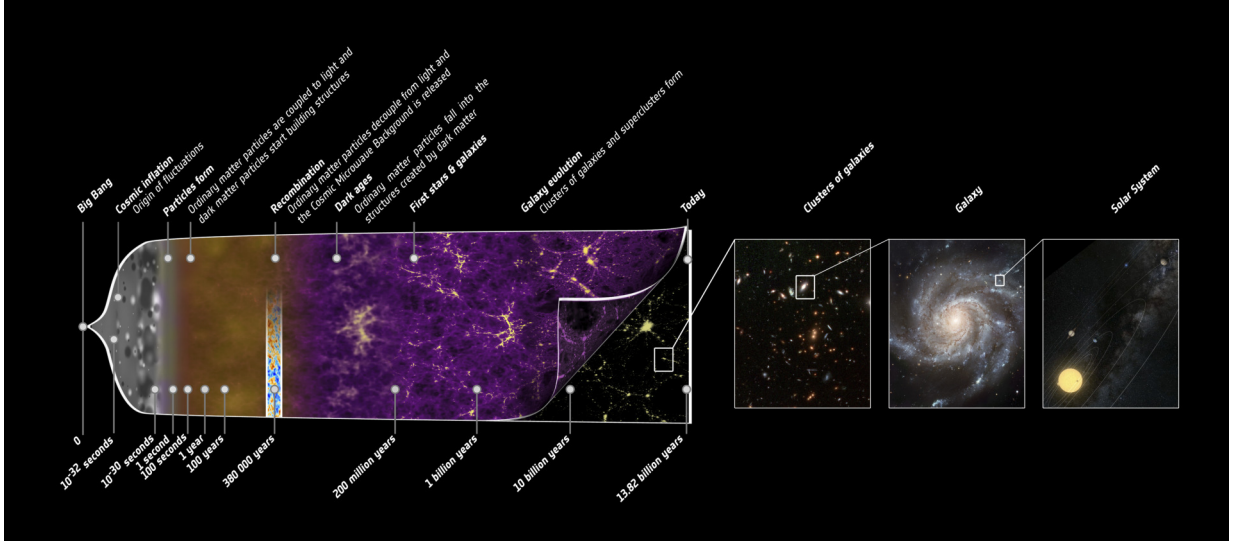


Figure 1.4: Schematic of the cosmic evolution, from the Big Bang to the current state of the Universe. Adopted from https://www.esa.int/ESA_Multimedia/Images/2013/03/Planck_history_of_Universe, last accessed November 22nd 2023.

and obtain an expression for the *critical density* of the Universe at a given time. More generally we can rewrite the components of the first Friedmann equation as ratios between the density at the current time t_0 and critical density as

$$\Omega_{i,0} \equiv \frac{\rho_{i,0}}{\rho_{\text{crit},0}}. \quad (1.8)$$

From primarily geometric and energy conservation considerations we can then rewrite the first Friedmann equation in terms of these (energy) densities

$$H^2(a) = H_0 \sqrt{\Omega_r a^{-4} + \Omega_m a^{-3} + \Omega_k a^{-2} + \Omega_\Lambda} \quad (1.9)$$

where Ω_r is the energy density due to radiation, Ω_m that of the total matter, Ω_k that of curvature and Ω_Λ that of dark energy. If we consider our Universe to be a closed system where no energy can be created or escape the different densities at the present time t_0 must sum up to

$$\Omega_{r,0} + \Omega_{m,0} + \Omega_{k,0} + \Omega_{\Lambda,0} = 1. \quad (1.10)$$

The relative ratios of these energy densities can be obtained from measurements of the Cosmic Microwave Background (CMB).

This CMB is a natural consequence of the concept of a Big Bang. Assuming that our Universe is expanding, [Gamow \(1946\)](#) proposed that it must have been smaller, more dense, and hence hotter at some earlier time. This concept can be brought to an extreme, where the Universe was little more than a sphere of hot, fully ionized plasma of elementary particles and photons.

In this period photons are efficiently scattered off free electrons via (inverse) Compton scattering and perform a random walk through the hot plasma, effectively making the medium fully opaque. Reversing this thought experiment and expanding the Universe from this state should lead to a cooling of the plasma and to a (re-) combination of electrons and protons to neutral hydrogen (as well as Helium and Lithium that can be generated through nucleosynthesis in the high temperatures of this early Universe, which was Gamow's primary motivation). The Compton cross-section of neutral hydrogen is three orders of magnitude smaller than that of free electrons, freeing the electrons from their random walk and making the Universe transparent. Under the assumption that the Universe is homogeneous and isotropic, this process should happen at the same time, everywhere in this early Universe. The freed photons should therefore be observable at every time, in the same way, from every point in the Universe.

If the Universe had been perfectly homogenous at all times, we would not be able to observe any structure formation. Hence there must have been some density perturbation at some time t

$$\delta(\mathbf{x}, t) \equiv \frac{\bar{\rho}(t) - \rho(\mathbf{x}, t)}{\bar{\rho}(t)} \quad (1.11)$$

that was able to survive corrective forces in the early Universe. As a side note, this also provides one of the strongest heuristical arguments for the existence of Dark Matter (DM), since density perturbations of purely baryonic matter would have been smoothed out by interaction with a background photon field on short timescales. We can assume that after inflation the density fluctuations were frozen in place and the hot plasma in the early Universe can be considered an ideal gas with a constant temperature. Small density fluctuations in a gas with constant temperature lead to pressure fluctuations, which again lead to sound waves. These sound waves, typically called *baryonic acoustic oscillations*, can be measured as imprints on the temperature fluctuations of the CMB, which have been measured with increasing sensitivity (the latest observation by [Planck Collaboration et al. \(2020a\)](#) can be seen in Fig. 1.2). The angular separation of temperature fluctuations with similar scales can be used to construct the power spectrum of temperature fluctuations, shown in Fig. 1.3. By modeling this power spectrum with different cosmological parameters Ω_i , the measured power spectrum can be fit, allowing a constraint on these parameters (for details see [Planck Collaboration et al., 2020b](#), and references therein). This provides a description of the energy content of the Universe with current values, $\Omega_{m,0} = 0.315$, $\Omega_{\Lambda,0} = 0.684$, $\Omega_{k,0} = 0.001$ ([Planck Collaboration et al., 2020b](#)). These parameters provide the basis for the to-date most successful cosmological model Λ CDM, where Λ is again the energy density of dark energy and CDM stands for cold dark matter, assuming that dark matter is a massive, dynamically cold particle whose exact nature is still unknown (see e.g. [Arbey & Mahmoudi, 2021](#), for a recent review).

Finally, we need a way to define time in a cosmological context. Since all current experiments indicate that the speed of light is constant and the absolute speed limit in the Universe, there is no simple way to agree on a fixed time t with a second observer somewhere else in the Universe. It is therefore convenient to define a common way to define time differences in a way that can be validated by any observer in the Universe to a common reference frame. Under the

assumption that the Universe is homogeneous and isotropic, we can identify the CMB as such a reference frame, since it should appear from each point in space in the same way. Photons in a curved space-time follow a so-called *null geodesic*, so that in Eq. 1.2 $ds^2 = 0$. This allows us to solve the metric under the assumption of two photons emitted at different times $t_e, t_e + \Delta t_e$ propagating along the same path through space-time experience a doppler-shift, or *redshift* z

$$\frac{\Delta t_0}{\Delta t_e} = \frac{\lambda_0}{\lambda_e} = \frac{v_e}{v_0} = \frac{a(t_0)}{a(t_e)} \equiv 1 + z, \quad (1.12)$$

which is caused by the expansion of space in the path of the propagating photon. This provides a more stable definition of time in a cosmological context.

With these ingredients, the growth of structure in the Universe can be motivated by simple arguments. Using the initial density perturbations (Eq. 1.11), the *Press & Schechter formalism* (Press & Schechter, 1974) provides a way to describe the formation of structures from a non-linear collapse of some critical overdensity δ_c into a (comoving) number density of haloes in a given mass range

$$n(M, z)dM = \sqrt{\frac{2}{\pi}} \frac{\bar{\rho}}{M^2} \frac{\delta_c}{\sigma} \exp\left(-\frac{\delta_c^2}{2\sigma^2}\right) \left| \frac{d \ln(\sigma)}{d \ln(M)} \right| dM \quad (1.13)$$

Within this formalism, we can relate the mass variance σ of a smoothed density field δ_s to the initial density field via the power spectrum $P(k)$

$$\sigma^2(M) = \langle \delta_s^2 \rangle = \frac{1}{2\pi^2} \int_0^\infty dk P(k) \tilde{W}^2(\mathbf{k}R) k^2, \quad (1.14)$$

where $\tilde{W}^2(\mathbf{k}R)$ is the Fourier transform of the window function. The power spectrum $P(k)$ can be obtained from CMB measurements and provides the basis for our understanding of density fluctuations in the Universe.

In over-dense regions, this leads to a growth of structure, namely Galaxy Clusters (GCs) and filaments, while in under-dense regions, also called *voids* the cosmic expansion is not inhibited by matter, so they can expand.

1.2 Galaxy Clusters

Galaxy clusters are the most massive, gravitationally bound structures in the Universe (see e.g. Kravtsov & Borgani, 2012, for a review).

Initially, these structures were observed in the optical band through their significant stellar brightness, stemming from hundreds to thousands of galaxies caught in the potential, dubbing the term GC. They were believed to be nebulae and part of our galaxy, until the detection of cepheids in M31 by Edwin Hubble in 1920 changed the picture of distances in the Universe and established that these galaxies in clusters were at distances of Mpc, instead of Kilo-parsec (kpc).

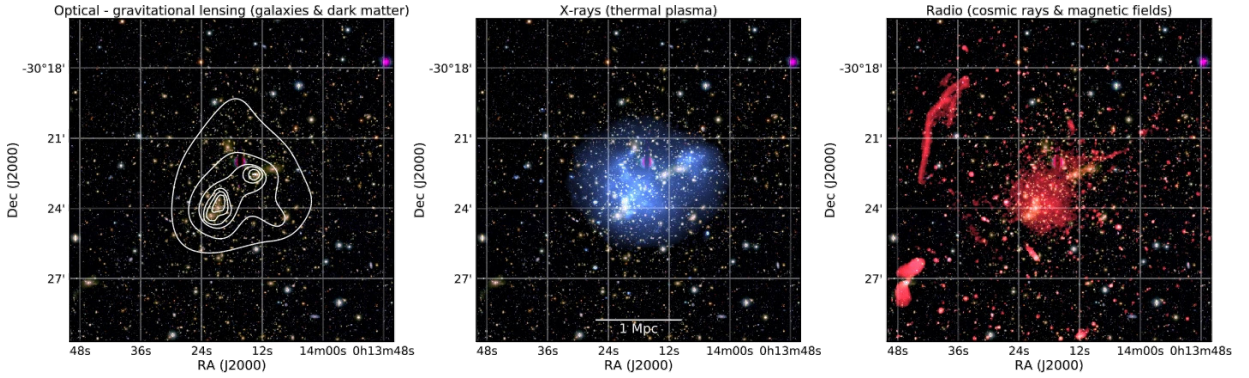


Figure 1.5: Multi-wavelength view of the cluster A2744, adopted from [van Weeren et al. \(2019\)](#). *Left*: Optical light, overlaid with contours for the surface density of DM. *Middle*: X-ray emission from the hot ICM. *Right*: Radio emission originating from CRs in the magnetized ICM.

The motion of galaxies within GCs lead [Zwicky \(1933\)](#) to postulate that significantly more mass must be present in galaxy clusters than is visible as stars in galaxies in order to keep them gravitationally bound.

Some of this additional mass was ultimately found beyond the optical band. X-ray observations revealed that the volume between galaxies is filled with hot plasma, emitting X-ray photons via thermal Bremsstrahlung (see Sec. 2.1 for more details). However, the combination of stellar mass and hot ICM still only accounted for $\sim 15 - 20\%$ of the mass required to bind the galaxies within the cluster.

The establishment of the theory of DM due to observations by [Rubin et al. \(1980\)](#) and others helped to solve this issue. By now gravitational lensing measurements (e.g. [Mehlert et al., 2001](#)) give strong indications that this DM is able to account for the remaining mass, even though the nature of DM is still strongly under debate (see e.g. [Arbey & Mahmoudi, 2021](#), for a review). With all components accounted for, GCs have typical masses of $M \sim 10^{14} - 5 \times 10^{15} M_{\odot}$.

Simulations find that the density profile of DM in GCs is universal and can be described by the so-called Navarro, Frenk and White (NFW) profile ([Navarro et al., 1996](#))

$$\rho_{\text{DM}}(r) = \rho_{\text{crit}} \frac{\delta_c}{\frac{r}{r_s} \left(1 + \frac{r}{r_s}\right)^2} \quad (1.15)$$

$$\delta_c = \frac{200}{3} \frac{c^3}{\ln(1+c) - c/(1+c)} \quad (1.16)$$

with the concentration parameter c and the critical density of the Universe $\rho_{\text{crit}} = 3H^2/8\pi G$.

Radio observations of Galaxy Clusters indicate the presence of relativistic Cosmic Ray electrons (CREs) in the ICM. These observations of the extended radio emission around galaxy clusters are paramount to obtain constraints on the cluster magnetic field strength (e.g. [Clarke](#)

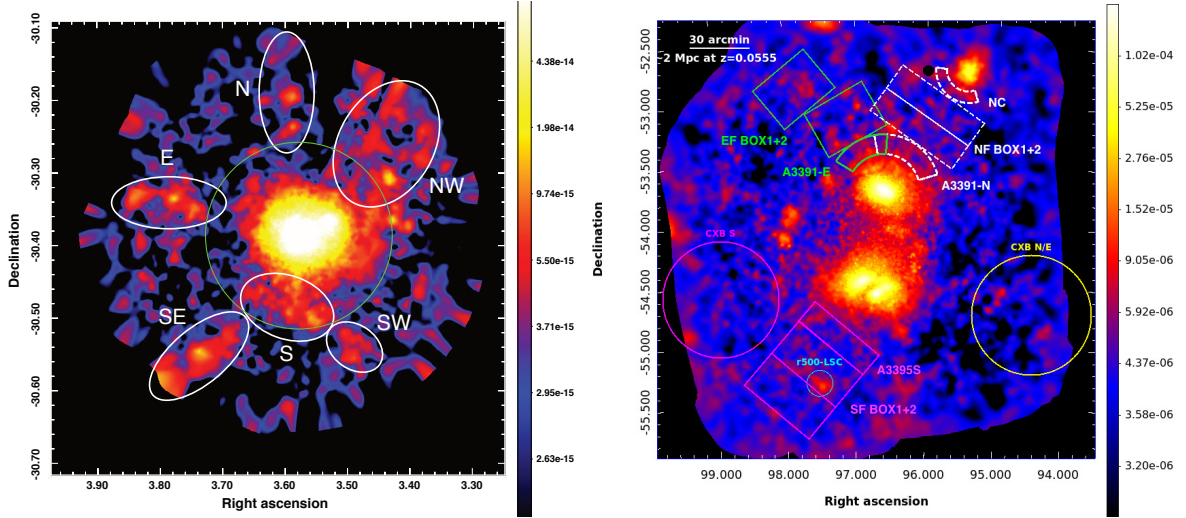


Figure 1.6: Examples of X-ray detected filaments. *Left*: Detection of X-ray emission from Cosmic Web filaments connected to A2744. Adopted from Eckert et al. (2015). They show the X-ray emission of the galaxy cluster Abell 2744 in the 0.5–1.2 keV band. The color bar shows X-ray brightness in units [$\text{erg s}^{-1} \text{cm}^{-2} \text{arcmin}^{-1}$]. The green circle indicates the position of the virial radius with $R_{\text{vir}} \sim 2.1h_{70}^{-1} \text{Mpc}$. *Right*: Most recent detection by Veronica et al. (2023). Here the color bar shows photon counts per second.

et al., 2001; Brüggén et al., 2012; Johnston-Hollitt et al., 2015). Galaxy cluster magnetic fields, on the other hand, are of outstanding importance for our understanding of thermal conduction and viscosity (see Sec. 2.4) and particle acceleration mechanisms (Sec. 2.5) which are likely the origin of two of the most common flavors of radio emission in merging GCs, Radio Halos (RHs) and Radio Relics (RRs). Both types of radio sources are extensively studied in the literature (see e.g. Feretti et al., 2012; Brüggén et al., 2012; van Weeren et al., 2019, for reviews). We will give an overview of their origin and properties in Sec. 3.1. We show a multi-wavelength view of the GC Abell 2744 in Fig. 1.5.

Today’s picture of the formation of galaxy clusters is that the strongest an-isotropies in the epoch of re-ionization after the Big Bang were able to form the earliest potential wells. These potential wells accrete mass in the form of DM, gas, and galaxies over cosmic time in a process called *hierarchical structure formation*. This accretion happens primarily along cosmic web filaments, which we will discuss in the next section. During this formation process the potential energy of the accreted mass is dissipated in the shape of shocks that head the ICM to $T \sim 10^8 \text{K}$, accelerate CRs and inject turbulence which amplifies the magnetic field in the ICM and leads to a re-acceleration of CRs.

1.3 Cosmic Web Filaments

Cosmic web filaments are the structures that inspired the name cosmic web (Bond et al., 1996). They were initially identified via galaxy clustering in large-scale surveys, so in the optical band.

Simulations find that the matter contained in these filaments and the outskirts of clusters, the so-called Warm-Hot Intergalactic Medium (WHIM), make up $\sim 30\% - 40\%$ of the total baryonic matter in the Universe, most of which has not yet been directly observed, coining the term *missing baryon problem* (see e.g. Cen & Ostriker, 1999; Davé et al., 2001; Shull et al., 2012).

Direct observations of the gas in filaments have been difficult to achieve, due to the expected low density and temperature of the WHIM. The main target band for direct observation of this WHIM is in X-ray, since even at this low temperature and density some thermal Bremsstrahlung is expected (see Sec. 2.1 for more details on this emission process). Indications for detection have been found for connecting filaments between clusters (also referred to as cluster bridges) (e.g. Werner et al., 2008; Akamatsu et al., 2017; Sarkar et al., 2022) and some filaments at the outskirts of clusters (e.g. Eckert et al., 2015; Bulbul et al., 2016; Bonamente et al., 2022). We show the detection by Eckert et al. (2015) and the latest detection by Veronica et al. (2023) in the left and right panel of Fig. 1.6, respectively.

These observations indicate that cosmic web filaments have densities of $n_e \sim 10^{-6} - 10^{-4} \text{ cm}^{-3}$ and temperatures in the range $T \sim 10^5 - 10^7 \text{ K}$ (see Nicastro et al., 2017, for a recent review).

1.4 Cosmic Voids

Cosmic Voids are significantly under-dense regions in the Universe, effectively identifiable as *holes* in the cosmic web in Fig. 1.1 (for a detailed review please see van de Weygaert & Platen, 2011, which provides the basis for this section).

Voids are approximately spherical regions of under-densities in the Universe. They have sizes of $L \sim 10 - 50 h^{-1} \text{ Mpc}$ with typical under-densities of $\rho \approx 0.2 \bar{\rho}$, where $\bar{\rho}$ is the mean density of the Universe and are bordered by filaments, or sheets of filaments and GCs. These voids account for roughly 95% of the total volume of the Universe (van de Weygaert & Platen, 2011, and references therein).

Cosmologically they can be viewed as the transition region where density regions have decoupled from the Hubble flow. At this transition region over-densities were able to collapse into filaments and clusters, while voids were expanding with the Hubble flow. In a void-centric view, this can also be interpreted as the voids *pushing* in their expansion against the filaments and galaxy clusters at their borders, compressing the matter between neighboring voids.

Due to their under-densities, they are the ideal regions to study imprints by primordial properties, like magnetic seed fields, or the formation of isolated galaxies. The reason for this is that in such low densities any processing mechanisms, such as dynamo processes, or pollution by astrophysical seed fields are likely to be negligible (we will discuss this further in Sec. 2.4).

Observations of local velocity fields by Tully et al. (2019) indicate that our home galaxy lies

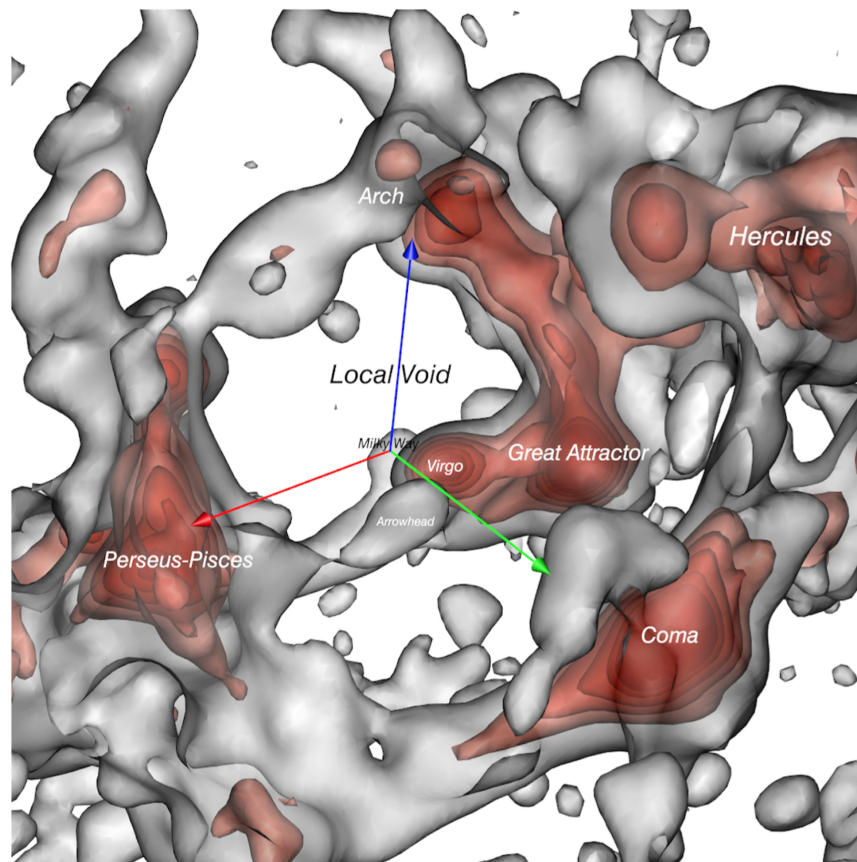


Figure 1.7: 3D visualization of the density distribution of the Local Universe. Adopted from [Tully et al. \(2019\)](#).

in the center of such a void. We show the density structure of the local Universe, as reconstructed from their observations in Fig. 1.7.

2 | Plasma Physics in the ICM

As discussed in the previous chapter, most of the baryonic matter in the universe exists in the state of ionized plasma. In this chapter, we will give a brief overview of the plasma physics governing the cosmological structures we are interested in this work. Since the overwhelming majority of non-thermal emission observed in the Universe originates from Galaxy Clusters (GCs) we will focus our description on the Intra-Cluster Medium (ICM), with brief excursions to the cosmic web where applicable. For a recent review of the plasma-physics in the ICM please see [Kunz et al. \(2022\)](#), which we will refer to frequently in this chapter.

2.1 The Intra-Cluster Medium

Most of our knowledge from the ICM stems from X-ray observations (see e.g. [Sarazin, 1986](#); [Böhringer & Werner, 2010](#), for reviews). Diffuse emission in GCs was first detected with the *Uhuhu* satellite mission ([Giacconi et al., 1972](#)), which established that GCs are filled with an atmosphere of hot, ionized plasma whose electrons emit X-ray emission via thermal Bremsstrahlung. Electrons emit Bremsstrahlung as they move through a plasma, due to them passing through the Coulomb potentials of thermal background protons. The opposite charge of electrons and protons deflects the electrons from their initial path as the electrons are attracted by the protons. This deflection for a population of thermal electrons with density n_e in a plasma with thermal ion density n_i leads to the emission of X-rays with total emissivity ([Rybicki & Lightman, 1979](#))

$$\frac{dE}{dt dV} \equiv j_X = \sqrt{\frac{2\pi k_B T}{3m_e}} \frac{2^6 \pi^2 e^6}{3\hbar m_e c^3} n_e n_i \bar{g}_B \quad (2.1)$$

$$= 1.4 \times 10^{-27} n^2 \sqrt{T} \bar{g}_B \quad [\text{erg s}^{-1} \text{ cm}^{-3}] \quad (2.2)$$

where k_B is the Boltzmann constant, m_e is the electron mass, e its charge, c is the speed of light and \bar{g}_B is the Gaunt factor with typical value $\bar{g}_B = 1.2$. In the last step we further assumed that the plasma is quasi-neutral, so $n = n_e = n_i$.

To obtain physical properties of the observed GCs it is typically assumed that GCs can be approximated as spheres of hot plasma that are unperturbed and in hydrostatic equilibrium. We can then follow e.g. [Evrard et al. \(1996\)](#) and define the binding mass of a sphere of gas in hydrostatic equilibrium as

$$M(r) = -\frac{k_B T(r)}{G \mu m_p} r \left[\frac{d \log \rho(r)}{d \log r} + \frac{d \log T(r)}{d \log r} \right] \quad (2.3)$$

where $T(r)$ is the temperature profile, G is the gravitational constant, m_p is the proton mass, μm_p is the mean molecular weight of the gas and $\rho(r)$ is the density profile. Assuming a density profile of an isothermal sphere from [Cavaliere & Fusco-Femiano \(1976\)](#)

$$\rho(r) = \rho_0 \left(1 - \frac{r^2}{r_c^2}\right)^{-\frac{3\beta}{2}} \quad (2.4)$$

where r_c is the core radius of the cluster, we can derive a functional form of the mass profile as (e.g. [Sarazin, 1986](#); [Evrard et al., 1996](#))

$$M(r) = \frac{3\beta k_B T_x r}{G \mu m_p} \frac{(r/r_c)^2}{1 + (r/r_c)^2} \quad (2.5)$$

$$= 1.13 \times 10^{15} \beta \frac{(r/r_c)^2}{1 + (r/r_c)^2} \left(\frac{T_x}{10 \text{ keV}}\right) \left(\frac{r}{\text{Mpc}}\right) [M_\odot]. \quad (2.6)$$

Here T_x is the spatially averaged temperature, which can be obtained from the X-ray spectrum and β and r_c can be estimated from X-ray imaging. We can then obtain the central density ρ_0 in Eq. 2.4 by equating the integral over the density profile with the total mass obtained from the mass profile. Similarly, the temperature profile can be found by solving Eq. 2.3 for the temperature, once the density profile is obtained.

In practice, the assumption of a hydrostatic equilibrium can be problematic, as many clusters are perturbed from equilibrium by mergers, gas sloshing, and Active Galactic Nuclei (AGN) feedback (e.g. [Forman et al., 2007](#); [Randall et al., 2015](#); [Fabian et al., 2016](#); [Sanders et al., 2016b,a](#); [Bulbul et al., 2019](#)). Further, the non-thermal pressure support by magnetic fields, turbulence, and Cosmic Ray protons (CRPs) is not yet fully constrained (see e.g. [Sayers et al., 2021](#), and references therein). For this reason, independent mass verification via gravitational lensing (e.g. [Hoekstra et al., 2013](#), for a review), or measurements of the Sunyaev–Zel’dovich (SZ) effect ([Sunyaev & Zeldovich, 1972](#)) is required (e.g. [Bocquet et al., 2015](#)).

2.2 Collisionless Shocks

Heating the plasma within the ICM to temperatures where thermal Bremsstrahlung can be observed in the X-ray band requires a substantial amount of energy. As we discussed in the first chapter, the primary source of energy in the LSS of the Universe is gravity. The gravitational energy released in the collision of two $M \sim 10^{15} M_\odot$ galaxy clusters is of the order $E \sim 10^{64}$ erg. Assuming that $\sim 10\% - 20\%$ of the total mass is contained in the ICM with a density of $n_e \sim 10^{-3} \text{ cm}^{-3}$ and a temperature $T \sim 10^8 \text{ K}$ gives a thermal energy of $E_{\text{th}} \sim 10^{63}$ erg, meaning the ICM can be heated to these temperatures via the release of potential energy. Efficient dissipation of energy within a gas typically happens via particle collisions, in the most extreme cases via supersonic flows, also known as shocks.

The low density and high temperature in the ICM leads to the medium being a strongly ionized

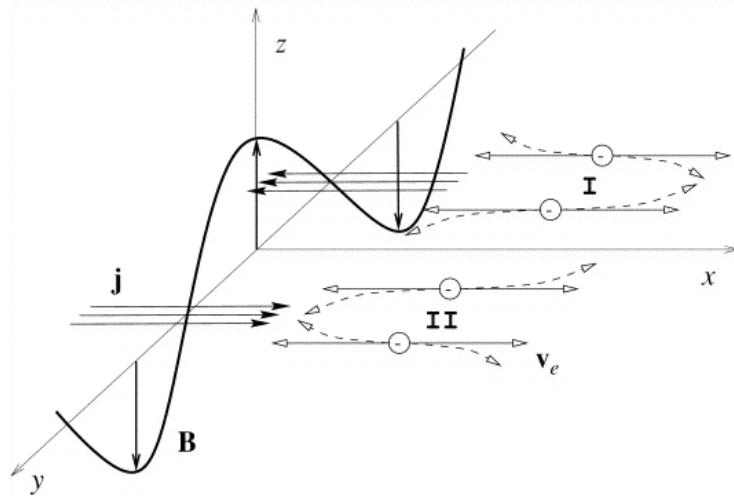


Figure 2.1: Formation of the Weibel instability due to particle deflection by an initial magnetic field perturbation. Adopted from [Medvedev & Loeb \(1999\)](#).

and weakly collisional plasma with a particle mean free path ([Spitzer, 1956a](#))

$$\lambda_{\text{MFP}} = \frac{3^{3/2} k_B^2 T^2}{4\sqrt{\pi} n_e Z^4 e^4 \ln \Lambda} \quad (2.7)$$

$$\approx 23 \text{ kpc} \left(\frac{\ln \Lambda}{30} \right) \left(\frac{T}{10^8 \text{ K}} \right)^2 \left(\frac{n_e}{10^{-3} \text{ cm}^{-3}} \right)^{-1}. \quad (2.8)$$

Here we assumed the elementary charge $Z = 1$ since we consider the plasma as an ideal plasma of electrons and protons. k_B refers to the Boltzmann constant and e is the elementary charge of an electron. Therefore, the low particle density in the ICM does not allow for enough pile-up of particles due to collisions, hence the process is referred to as collisionless (see [Krasnoselskikh et al., 2013](#), for a review on quasi-perpendicular collisionless shocks).

Instead, shocks in the ICM are formed from plasma instabilities, most prominently the Weibel instability ([Weibel, 1959](#)). In this process two colliding quasi-neutral streams of weakly magnetized plasma pass through each other. Assuming an initial magnetic field perturbation, the Lorentz force deflects the particles based on their trajectory and charge as shown in Fig. 2.1. This leads to the formation of current sheaths which amplifies the instability if particles propagate in the x -direction (see [Medvedev & Loeb, 1999](#), for a more detailed discussion). The deflection causes a pile-up of particles perpendicular to the shock propagation, which are subsequently swept along with the shock. This produces behavior analogous to that of a collision-dominated shock.

2.3 Turbulence

Turbulence in the ICM is a vast topic, whose exhaustive summary is beyond the scope of this chapter. To give a brief introduction in line with the topic of this work we will therefore follow the

introduction given in [Donnert et al. \(2018\)](#) and refer to further excellent reviews by [Subramanian et al. \(2006\)](#); [Schekochihin & Cowley \(2006\)](#); [Schekochihin \(2022\)](#) for more details.

As we discussed in the last chapter, GC form in the process of hierarchical structure formation by accreting smaller GCs, galaxy groups, and gas, primarily along cosmic web filaments. This process is highly chaotic and accretion events are almost never completely isolated, which can be interpreted as a random stirring of the ICM. From this we can assume that the velocity of individual pockets of gas is highly randomized within the cluster volume, leading to a velocity dispersion v . In the standard [Kolmogorov \(1941\)](#) (but see [Kolmogorov, 1991](#), for the translation) picture of turbulence these pockets (typically referred to as *eddies*) of plasma with size l break apart into two eddies of smaller size due to the convective term in the fluid equation ($\mathbf{v} \cdot \nabla \mathbf{v}$), which leads to an energy transfer from larger, to smaller scales. The rate at which this energy transfer takes place can be written as $k v$, with $k = 2\pi/l$ being the wave vector. This leads to a characteristic timescale at which this energy transfer takes place, the so-called *eddy turnover time* as $\tau_l = l/v_l$, with v_l being the velocity dispersion at scale l .

At some scale, k_v , also referred to as *inner scale*, or *dissipation scale*, this energy transfer to smaller scales is stopped by viscous forces and is dissipated. This dissipation happens in the form of heat if the viscous force is dominated by Coulomb collisions, or in the form of magnetic energy if the viscous force is driven by the Lorentz force.

If the injection of turbulent energy on large scales is happening at a constant scale, we can define it as an *outer scale*, *injection scale*, or *driving scale* k_0 .

Assuming that the energy density of the turbulence is isotropic and the medium is incompressible we arrive at the standard [Kolmogorov \(1941\)](#) description for the velocity spectrum of turbulence

$$I(k) \propto v_0^2 \frac{k_0^{2/3}}{k^{5/3}} \quad (2.9)$$

where v_0 is the velocity dispersion on top of the mean, at the outer scale k_0 . Naturally, this equation is only valid between the outer- and inner scale, typically referred to as *inertial range*. To better characterize plasma properties we can define the so-called *Reynolds number*

$$R_e = \frac{v_0}{k_0 \nu} = \frac{l_0 v_0}{\nu} \propto \left(\frac{l_0}{l_\nu} \right)^{4/3} \quad (2.10)$$

as a ratio between momentum transport and momentum diffusion, where we defined the *kinematic viscosity* ν and the viscous scale l_ν as the scale where this viscosity dominates.

This viscous scale can be estimated in the classical picture ([Spitzer, 1956a](#)) by assuming that the dissipation of energy is dominated by Coulomb collisions, which gives the viscosity of the ICM plasma as (see e.g. [Sijacki & Springel, 2006](#), for a detailed discussion)

$$\nu = 0.0406 \frac{m_p^{1/2} (k_B T)^{5/2}}{e^4 \ln \Lambda} . \quad (2.11)$$

This assumes that the characteristic length scale at which viscosity is relevant is larger than the mean-free path λ_{mfp} (e.g. [Sarazin, 1986](#)) of the particles. For a typical ICM plasma this results

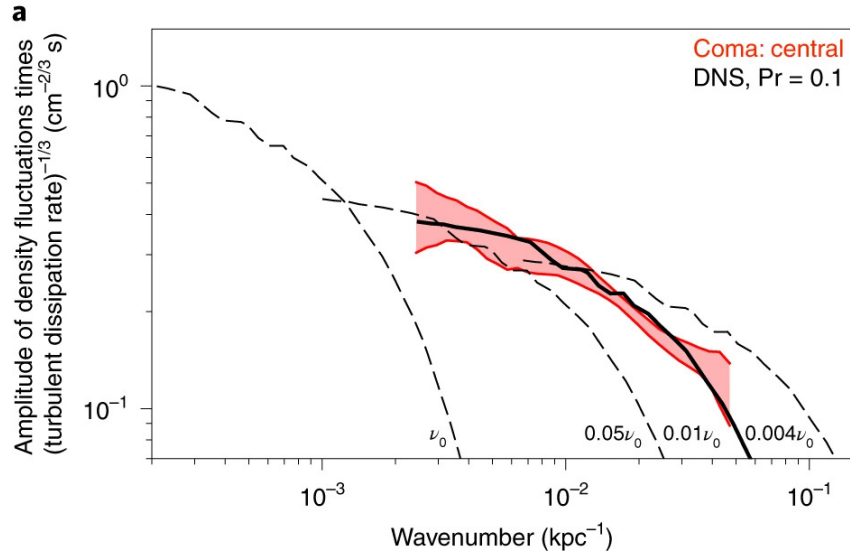


Figure 2.2: Probe for the turbulent power spectrum via density fluctuations in the Coma cluster obtained by [Zhuravleva et al. \(2019\)](#). The red band indicates the observations, while the dashed and solid lines show predictions for different values of suppression of the Spitzer viscosity to allow for the observed density fluctuation structure.

in a viscosity similar to that of honey, which would strongly suppress turbulence on small scales.

Observations can make assumptions about turbulence by measuring velocity structures via line-broadening in X-ray spectra, or inferring scales of fluctuations via magnetic field reversals from Rotation Measures (RMs) or density perturbations from X-ray emission (see [Inogamov & Sunyaev, 2003](#); [Lazarian, 2009](#); [Simionescu et al., 2019](#), for reviews). Observations by e.g. [Schuecker et al. \(2004\)](#); [Laing et al. \(2008\)](#); [Govoni et al. \(2010\)](#); [Kuchar & Enßlin \(2011\)](#); [Vacca et al. \(2012\)](#); [Hitomi Collaboration et al. \(2016\)](#); [Roncarelli et al. \(2018\)](#); [Zhuravleva et al. \(2019\)](#) find turbulent velocities of $v_{\text{rms}} \sim 200 \text{ km s}^{-1}$ and fluctuations on scales $l \sim 1 - 50 \text{ kpc}$. This leads to typical Reynolds numbers of

$$R_e \approx 52 \frac{v_0}{10^3 \text{ km s}^{-1}} \frac{l_0}{300 \text{ kpc}} \frac{n}{10^{-3} \text{ cm}^{-3}} \left(\frac{T}{8 \text{ keV}} \right)^{-5/2} \left(\frac{\log \Lambda}{40} \right) \approx 10 - 100 \quad (2.12)$$

for the canonical values of density and temperature in galaxy clusters, which would mean strong suppression of turbulence on small scales. This is however not observed (see Fig. 2.2 for the observations by [Zhuravleva et al., 2019](#), who find a suppression of the Spitzer viscosity by at least a factor ~ 100).

As we will see in the next section, this discrepancy can be attributed to magnetic fields.

2.4 Magnetic Fields

The time evolution of a magnetic field can be well described by the induction equation in the continuum limit of Magneto Hydrodynamics (MHD)

$$\frac{\partial \mathbf{B}}{\partial t} = \nabla \times (\nabla \times \mathbf{B}) + \eta \Delta \mathbf{B}, \quad (2.13)$$

where \mathbf{B} is the 3D magnetic field vector and η is the magnetic diffusivity. Most notable about this equation is the lack of a source term, so if $\mathbf{B} = \mathbf{0}$ at any time then it will remain zero for all time. The nature of a source for magnetic fields and its time evolution in the Universe has been the center of some debate in the literature (see e.g. [Widrow, 2002](#); [Carilli & Taylor, 2002](#); [Durrer & Neronov, 2013](#); [Donnert et al., 2018](#), for reviews).

Sources

The two most common theories of sources for magnetic fields are *primordial* magnetic fields and *astrophysical sources* for magnetic fields.

Primordial sources for magnetic fields refer to processes that can induce magnetic fields in the epoch before re-ionization, i.e. before the CMB. These come in two main flavors: either magnetic fields are generated by coupling to the evolution of space-time, or by phase-transitions in the early Universe.

The first can generate magnetic fields of up to

$$B_0 \sim 10^{-9} a^{-2} \quad [\text{G}], \quad (2.14)$$

but this leads to a number of problems, such as a strongly changing electron charge e over the time of inflation (which leads to a number of pitfalls, see discussion in Sec. 3.1.1 of [Durrer & Neronov, 2013](#), and references therein). With more conservative assumptions for the coupling and assuming that the maximum wave number of the magnetic field spectrum is the size of the Universe at reconnection this is reduced to

$$B_0 \sim 10^{-23} \quad [\text{G}]. \quad (2.15)$$

In the case of magnetic field generation from phase transitions in the early Universe, a part of the energy from the break of symmetry available for the generation of new particles is channeled into the generation of magnetic fields. This amounts to the generation of

$$B_0 \sim 10^{-29} - 10^{-23} \quad [\text{G}], \quad (2.16)$$

for the electro-weak and QCD phase transition, respectively.

Determining if primordial magnetic fields are relevant for the evolution of magnetic fields in the Universe requires measurements in regions where magnetic fields can not be affected by potential astrophysical seed fields, or by amplification processes. The ideal environment for this are cosmic

voids. Constraints on magnetic fields in voids are obtained via γ -ray observations, as we will discuss later in this section.

Primordial magnetic fields from the QCD transition phase at $z = 10^{12}$ could also be observed as gravitational waves since these fields can couple to the energy-momentum tensor in the early Universe. This could explain the stochastic gravitational wave background detected by NANOGrav (Neronov et al., 2021).

However, whether magnetic fields generated prior to re-combination can survive long enough in the hot plasma before recombination has been a matter of debate in the literature (see e.g. Lesch & Birk, 1998; Widrow, 2002, the latter for a review)

Astrophysical sources for magnetic fields most commonly discussed in the literature are the Biermann battery, Supernovae (SNe), and Active Galactic Nuclei (AGN).

The principle of a Biermann battery (after Biermann, 1950) is based on the different masses of electrons and protons. Due to these different masses, they are affected in different ways by Coulomb interaction or background photon fields, leading to a relative displacement between electrons and protons and with that a separation of charges in an initially neutral plasma. Charge displacement leads to an induction of current, which in turn induces a magnetic field. For a Biermann battery to work, a misalignment between pressure and density gradient in the plasma is required, which can be parametrized as (e.g. Davies & Widrow, 2000; Xu et al., 2008)

$$\frac{\partial \mathbf{B}}{\partial t} \propto \frac{\nabla P \times \nabla \rho}{\rho^2}. \quad (2.17)$$

This process could be acting in cosmological accretion shocks, (re-) ionization fronts, or cosmological over-densities and produce large-scale magnetic fields of the order $B \sim 10^{-25} - 10^{-18}$ G (see Kunz et al., 2022, and references therein).

In the SN scenario a pre-existing seed magnetic field is amplified within stars through dynamo processes or instabilities (e.g. Parker, 1955; MacDonald & Mullan, 2004) and fed back to the Interstellar Medium (ISM) once the star dies in a SN explosion. This produces magnetic fields with $B \sim 10^{-4}$ G in stars (see e.g. Beck et al., 2013, and references therein), which are adiabatically expanded and therefore diluted as the SN remnant is mixed with the ISM. Simulations show that this process can provide a seed field that can then be further increased in strength by amplification mechanisms (e.g. Beck et al., 2013; Garaldi et al., 2021).

A similar seeding process should be at work in accretion discs around AGN, where magnetic fields can be generated by a hydrodynamic battery, such as the Biermann battery, and quickly amplified by dynamo processes (e.g. Pariev et al., 2007) and subsequently injected into the ICM by strongly magnetized AGN jets with $B \sim 10^{-4}$ G (e.g. Xu et al., 2008).

Amplification

Independent of the physical source of the initial magnetic fields, their seeded strength is expected to be small. This indicates that there must be some efficient mechanisms to amplify seed fields with $B \sim 10^{-30} - 10^{-10}$ G to the observed field strengths of $B \sim 10^{-6}$ G (e.g. Bonafede et al., 2010).

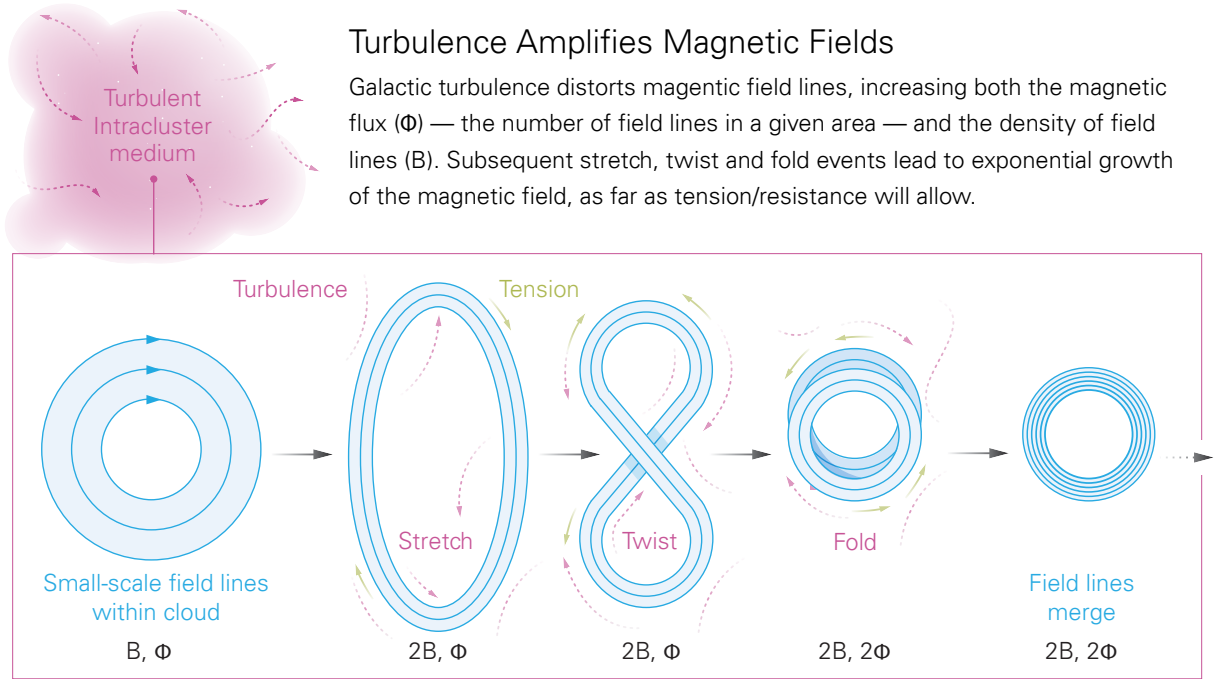


Figure 2.3: Schematic of magnetic field amplification via the stretch-twist-fold mechanisms in the turbulent dynamo process. Adopted from [Steinwandel et al. \(2023a\)](#).

There are two mechanisms believed to work in tandem that can amplify the magnetic field. One is adiabatic compression under flux conservation, which assumes that the magnetic field lines are frozen into the plasma and amplifies the magnetic field as

$$B \propto B_0 \left(\frac{\rho}{\rho_0} \right)^{\frac{2}{3}}. \quad (2.18)$$

This poses problems in galaxy clusters, where the over-density compared to the cosmic mean is $\delta\rho \sim 10^2 - 10^4$ (e.g. [Dolag et al., 2008b](#)), leading to a magnetic field amplification of $\delta B \sim 100$ and with that not nearly enough to explain the magnetic field amplification from cosmic seed fields. This amplification will, however, happen independently of plasma kinematics and magnetization, so it can always contribute to magnetic field amplification, which may be relevant in cosmic web filaments.

The second mechanism is amplification via dynamo processes (e.g. [Parker, 1955](#); [Ruzmaikin et al., 1988](#); [Kulsrud, 1999](#); [Brandenburg & Subramanian, 2005](#); [Kulsrud & Zweibel, 2008](#)). Fig. 2.3 shows a schematic of the magnetic field amplification process commonly referred to as *turbulent dynamo* (originally proposed by [Zel'dovich, 1970](#)). In this process magnetic field lines are stretched, twisted, and folded by the turbulent motions in the ICM. This continues until the folding requires more energy than is available in the turbulent motion, as the magnetic field pushes back against the folding. Once the energy density of the magnetic field is in equipartition with

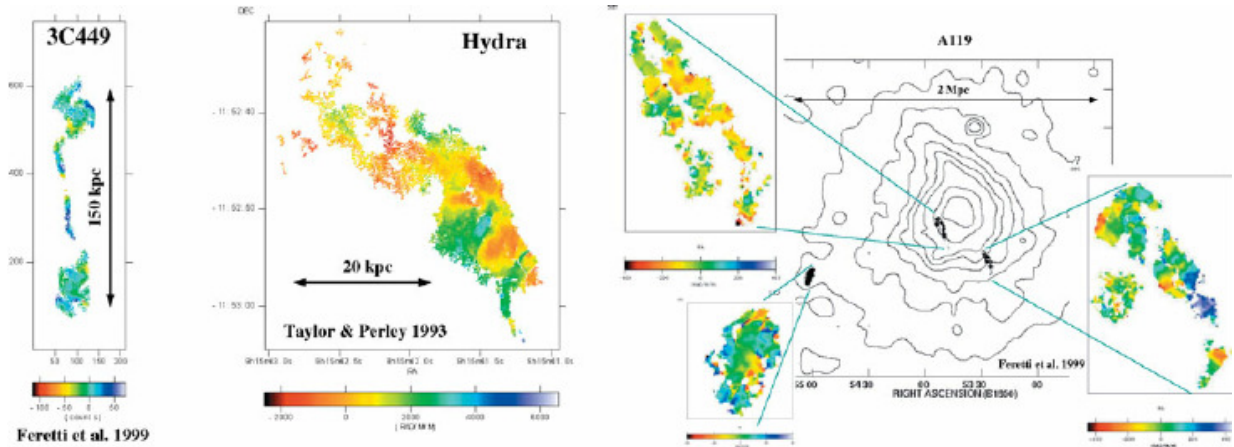


Figure 2.4: Visualisation of Faraday rotation measurements of AGN lobes within the cluster volume. Adopted from Dolag et al. (2009b).

the turbulent kinetic energy further folding is suppressed and the turbulent dynamo is commonly referred to as *saturated*. To better quantify this saturation it has been shown that the amplification is efficient until a critical magnetic Reynolds number $R_{m,crit}$ is undercut (see e.g. Schober et al., 2015, and references therein), where the magnetic Reynolds number is defined as

$$R_m = \frac{l_0 v_0}{\eta}, \quad (2.19)$$

with v_0 being the turbulent velocity on the forcing scale l_0 and η the magnetic diffusivity. The critical Reynolds number is found to be $R_{m,crit} \sim 100 - 3000$, depending on the underlying turbulence spectrum (please see Tab. 1 in Schober et al., 2015, for a list of critical Reynolds numbers for a number of different turbulence spectra).

This amplification process proceeds exponentially so that saturation in the ICM is found by $z \approx 4$ in high-resolution simulations (e.g. Vazza et al., 2018; Steinwandel et al., 2023a). Once the dynamo is saturated, the magnetic energy is transported to larger scales via the so-called inverse turbulent cascade, leading to a volume-filling magnetic field strength of $B \sim 0.1 - 10 \mu\text{G}$ in GCs (e.g. Bonafede et al., 2009a).

Observations

Magnetic fields in the Universe can by now be measured in a number of ways, however, there are two methods that are most relevant for the present work.

The first is via so-called Rotation Measure (RM) observations. This method makes use of the fact that linearly polarized emission can be viewed as a superposition of two opposite circular polarized photons. As these photons propagate along a magnetic field line towards the observer they experience different indices of refraction due to the fixed rotational direction of the background electrons along the same magnetic field line. This leads to a rotation of the angle of linear polarisation (ϕ), also referred to as the Faraday depth, depending on the wavelength of the

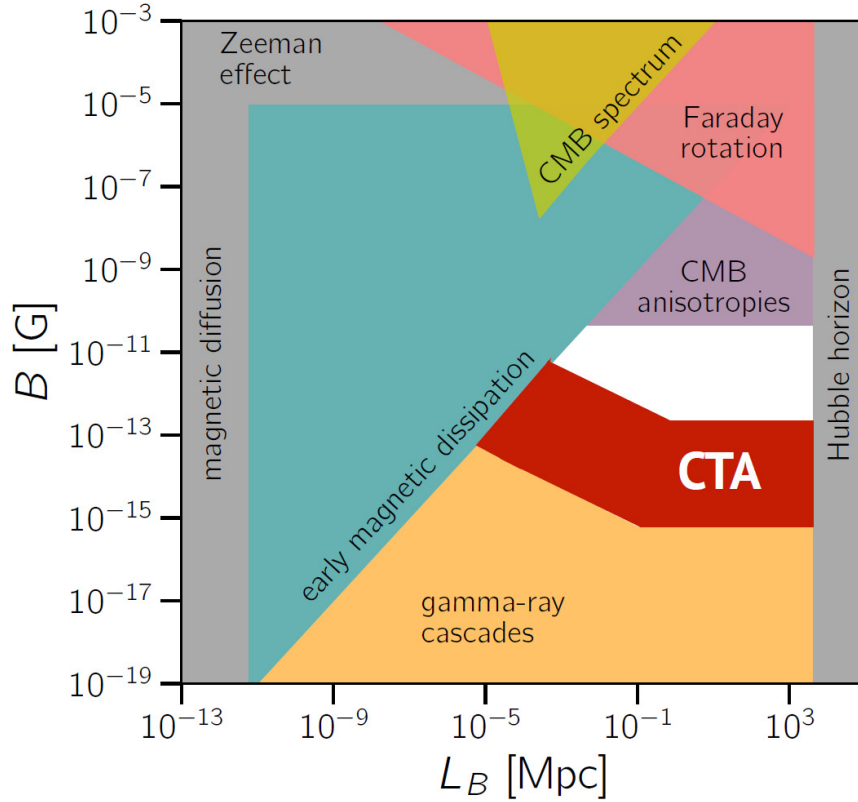


Figure 2.5: Current constraints on magnetic field strengths and coherence length in voids. Adopted from [Alves Batista & Saveliev \(2021a\)](#).

photons (λ) as $\phi = \psi \times \lambda^2$. Measuring these angles at different wavelengths allows us to solve for the RM as

$$\psi = \frac{\phi_1 - \phi_2}{\lambda_1^2 - \lambda_2^2} = \frac{e^3}{2\pi m_e^2 c^4} \int dl n_e B_{\parallel} \quad (2.20)$$

where m_e is the mass of an electron, c the speed of light, n_e the electron density and l the length along the line-of-sight (LOS). This allows the computation of the parallel component of the magnetic field B_{\parallel} if n_e and l are known. As discussed above, in galaxy clusters n_e can be obtained from X-ray emission and l can be calculated if the redshift of the polarized source is known. These polarized sources are typically AGN-jets, whose host-galaxy is within or behind the cluster volume, or a cosmic web filament. In galaxy clusters, given enough sources in the radial distance of the cluster, this can be used to find a magnetic field profile. See Fig. 2.4 for a visualization of typical sources for these measurements and their location in the cluster volume. For the Coma cluster, where the best observations are available, this profile is found to be closely tied to the density of the gas

$$B = B_0 \left(\frac{n_{\text{th}}}{n_0} \right)^{\eta}, \quad (2.21)$$

with $B_0 = 4.7\mu\text{G}$ and $\eta = 0.7$ (Bonafede et al., 2010).

This technique can be extended to perform a statistical analysis of a large observational field. For this one takes advantage of the fact that due to the finite resolution of the radio observations, the measured linearly polarized intensity ($P(\lambda^2)$) is the sum of all RMs within a beam and can be expressed as

$$P(\lambda^2) = \int_{-\infty}^{\infty} d\psi F(\psi) e^{2i\psi\lambda^2} \quad (2.22)$$

where $F(\psi)$ is a description for the distribution of polarized emission as a function of the Faraday depth, called the Faraday Dispersion Function (FDF). This FDF can be estimated via the *RM synthesis* technique (Burn, 1966; Brentjens & de Bruyn, 2005) and assuming only a single polarized source experiences RM along a given LOS it is equivalent to a measurement of the RM. With this technique and large-scale surveys performed with the LOFAR telescopes Carretti et al. (2022) were able to constrain the magnetization of cosmic web filaments to $B_0 \approx 30$ nG.

While these observations are the only ones that can actually constrain magnetic fields in galaxy clusters and filaments, they can constrain them only there, meaning that they trace magnetic fields in matter that has already been processed to some degree. This poses a problem when trying to distinguish between primordial and astrophysical origins of magnetic fields in galaxy clusters, although less so in cosmic web filaments (see e.g. Vazza et al., 2021a, for a discussion).

A second method of magnetic field measurement in the universe makes use of γ -ray emission by AGN (see e.g. Alves Batista & Saveliev, 2021a, for a recent review). With this technique, a distant γ -ray source, ideally a bright blazar, is observed. As the γ -rays have energies above the rest-mass of an electron they can spontaneously produce electron-positron pairs on their path from source to observer. These are charged particles that an ambient magnetic field could deflect. If they subsequently encounter a CMB photon this photon can be inverse Compton (IC) up-scattered to produce γ -rays with MeV-GeV energies, which can then propagate towards the observer from the deflected point of origin. This effect should produce a halo of γ -rays around the original point source. The shape and size of the halo could then provide insight into the strength and structure of the magnetic field in voids.

At the time of writing these halos have not yet been observed, putting a limit on magnetic fields in voids of $B \sim 10^{-16} - 10^{-15}$ G. We show the constraints on magnetic field strength and its coherence length in Fig. 2.5, which is adopted from Alves Batista & Saveliev (2021a).

The next generation of γ -ray observations with the Cherenkov Telescope Array (CTA) will push the constraints by another two orders of magnitude and hopefully lead to the first detection of the γ -ray halos. This would allow to further constrain primordial models for magnetic fields, since cosmic voids are expected to still retain the memory of the initial magnetic field, due to the lack of matter and turbulence to drive amplification processes (see e.g. Dolag et al., 2011, and references therein).

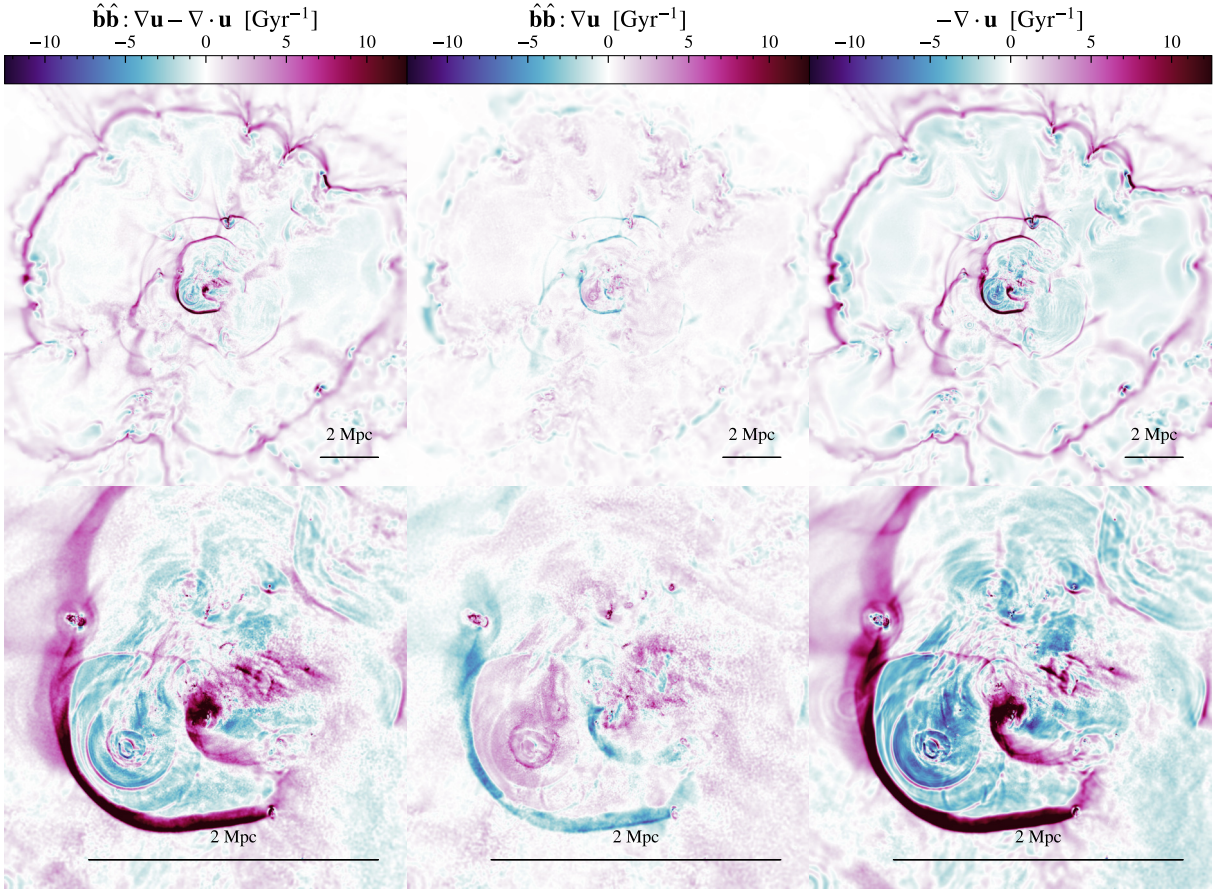


Figure 2.6: Components of the pressure anisotropy given in Eq. 2.29. Adopted from [Steinwandel et al. \(2023a\)](#).

Impact on Galaxy Clusters

As discussed above, the ICM can be characterised as a low density medium ($n \sim 10^{-3} \text{ cm}^{-3}$), with high temperatures ($T \sim 10^8 \text{ K}$, $E > 1 \text{ keV}$) that is weakly magnetized ($B \sim 0.1 - 10 \mu\text{G}$) (e.g. [Sarazin, 1986](#); [Carilli & Taylor, 2002](#)). This results in a typical plasma- β , where

$$\beta = \frac{P_{\text{th}}}{P_B} \propto \frac{n_e T}{B^2} \sim 50 - 1000, \quad (2.23)$$

meaning that the kinematic impact of the non-thermal pressure by magnetic fields is negligible on GC scales.

However, the magnetic field can nonetheless impact the properties of the cluster, by limiting the symmetry of plasma flow within the ICM. Due to the overwhelming majority of the gas in the ICM being fully ionized plasma, the propagation of the individual electrons and protons is impacted by the magnetic field.

For one, this has implications for thermal conduction, since the particles transporting the heat and with that kinetic energy will do so preferentially along magnetic field lines. This is commonly

referred to as anisotropic thermal conduction (see e.g. [Balbus & Potter, 2016](#), for a review). In a fully ionized plasma, the energy flux due to thermal conduction should be well described by ([Spitzer, 1956b](#))

$$\mathbf{Q} = -\kappa_{\text{SP}} \nabla T = 20 \left(\frac{2}{\pi} \right)^{3/2} \frac{(k_B T_e)^{5/2} k_B}{m_e^{1/2} e^4 Z \ln \Lambda} \nabla T. \quad (2.24)$$

However, observations of the ICM (e.g. [Ettori & Fabian, 2000](#); [Markevitch et al., 2003](#); [Richard-Laferrière et al., 2023](#)) indicate that this ideal conduction is suppressed by a factor of $\sim 3 - 5$. As a reason for that magnetic fields have been identified, due to the previously discussed preferential propagation of the charged, heat-carrying particles along magnetic field lines. When thermal conduction is treated in the anisotropic formulation

$$\mathbf{Q} = -\kappa \mathbf{b}(\mathbf{b} \cdot \nabla T) \quad (2.25)$$

where $\mathbf{b} = \mathbf{B}/|\mathbf{B}|$, the ideal conduction is suppressed perpendicular to the magnetic field lines, yielding results that are in better agreement with observations (see e.g. [Arth et al., 2014](#); [Berlok et al., 2021](#); [Steinwandel et al., 2020b](#); [Perrone et al., 2023](#), for simulations of this effect).

Second, it also has implications for the viscosity of the ICM. The isotropic formulation of viscosity can be written as (e.g. [ZuHone et al., 2015](#))

$$\mathbf{\Pi}_{\text{iso}} = -\nu \nabla \mathbf{v} \quad (2.26)$$

with ν the shear viscosity coefficient. In the isotropic case and hence in the absence of magnetic fields ν is governed by Coulomb interaction and one arrives at a shear viscosity for a fully ionized, unmagnetized plasma as described by Eq. 2.11. This disagrees with observations by e.g. [Zhuravleva et al. \(2019\)](#), who find significantly higher turbulence from density and temperature fluctuations than expected at such high viscosities.

Here magnetic fields again change the picture. In a collisionless, but magnetized medium, the dominating dissipative force is not Coulomb interactions between particles, but the Lorentz force, which becomes relevant at much smaller scales. This extends the inertial range from the thermal mean-free-path of the particles ($\lambda_{\text{mfp}} \approx 20$ kpc) down to their Lamour radius with

$$r_{\text{Lamour}} \approx 3 \times 10^{-12} \left(\frac{T}{10 \text{ keV}} \right) \left(\frac{B}{\mu\text{G}} \right)^{-1} \text{ [kpc]}, \quad (2.27)$$

allowing for much smaller eddies. This anisotropic viscosity can be parametrized as (e.g. [Berlok et al., 2020](#), and references therein)

$$\mathbf{\Pi} = -\Delta p \left(\mathbf{b}\mathbf{b} - \frac{\mathbf{1}}{3} \right), \quad (2.28)$$

with the pressure an-isotropy

$$\Delta p = \rho \nu_{\parallel} (3\mathbf{b}\mathbf{b} : \nabla \mathbf{v} - \nabla \cdot \mathbf{v})^2 \quad (2.29)$$

where ν_{\parallel} is the viscosity coefficient, usually dependent on density and temperature $\nu_{\parallel} \propto T^{5/2}/\rho$ (Spitzer, 1962; Braginskii, 1965; Sarazin, 1986) and \cdot is the double dot-product. We show a visualization of this pressure an-isotropy in an ultra-high resolution MHD simulation of a massive galaxy cluster in Fig. 2.6. See Steinwandel et al. (2023a) for a detailed discussion of how these components of the pressure an-isotropies affect magnetic field amplification in GCs.

Observations by Zhuravleva et al. (2019) indicate that in the Coma cluster the viscosity lies at least a factor $\sim 10 - 1000$ below the Spitzer viscosity (see Eq. 2.11). This suppression of viscosity has implications for the development of cold-fronts (e.g. Dursi & Pfrommer, 2008; ZuHone et al., 2015; Ghizzardi et al., 2010, the latter for a review), turbulence (e.g. Parrish et al., 2012; Zhuravleva et al., 2019; Schekochihin, 2022), the Kelvin-Helmholtz Instability (Churazov et al., 2001; Marin-Gilabert et al., 2022) and shocks (e.g. Dolag et al., 2005c) in the ICM.

Including both these effects into the description of MHD is referred to as Braginskii MHD, after Braginskii (1965). The next generation of galaxy cluster simulations will need to account for these effects, as the resolution reaches the coulomb collision scale in the majority of the cluster volume (Steinwandel et al., 2023a).

2.5 Particle Acceleration

A number of plasma instabilities in the proximity of shocks in the ICM induce MHD-turbulence and can cause individual electrons and protons to be scattered at the shock surface. These instabilities can be relevant in different parts of the shock region. Fig. 2.7 shows a schematic of the instabilities relevant at surfaces of cosmological shocks, overlaid on results from Particle-In-Cell (PIC) simulations by Ha et al. (2021), which we will use as a brief introduction to the concept of particle scattering at shocks.

In the so-called shock foot an anisotropy between the electron temperature parallel and perpendicular to the shock $T_{e,\parallel/\perp}$ can induce the Electron Firehose Instability (EFI) (see e.g. Guo et al., 2014). In this instability electrons *compress* magnetic field lines from two sides, leading to a bent morphology (like a firehose pushed at from two sides, hence the name) and the bending induces Alfvén waves. CRs can then scatter off these Alfvén waves and be deflected from their original path.

In the shock transition region, the Alfvén Ion Cyclotron (AIC) instability can be triggered by a similar temperature anisotropy of ions, which causes the confinement of particles in the waves excited parallel to the shock. This transition region has roughly the width of one Larmor radius of the ions in that region, making it efficient at confining electrons whose Larmor radius of the same energy is smaller by a factor of the mass ratios.

These scattering and confinement processes can lead to two forms of particle acceleration: Diffusive Shock Acceleration (DSA) and Shock Drift Acceleration (SDA), which we will briefly outline in this section.

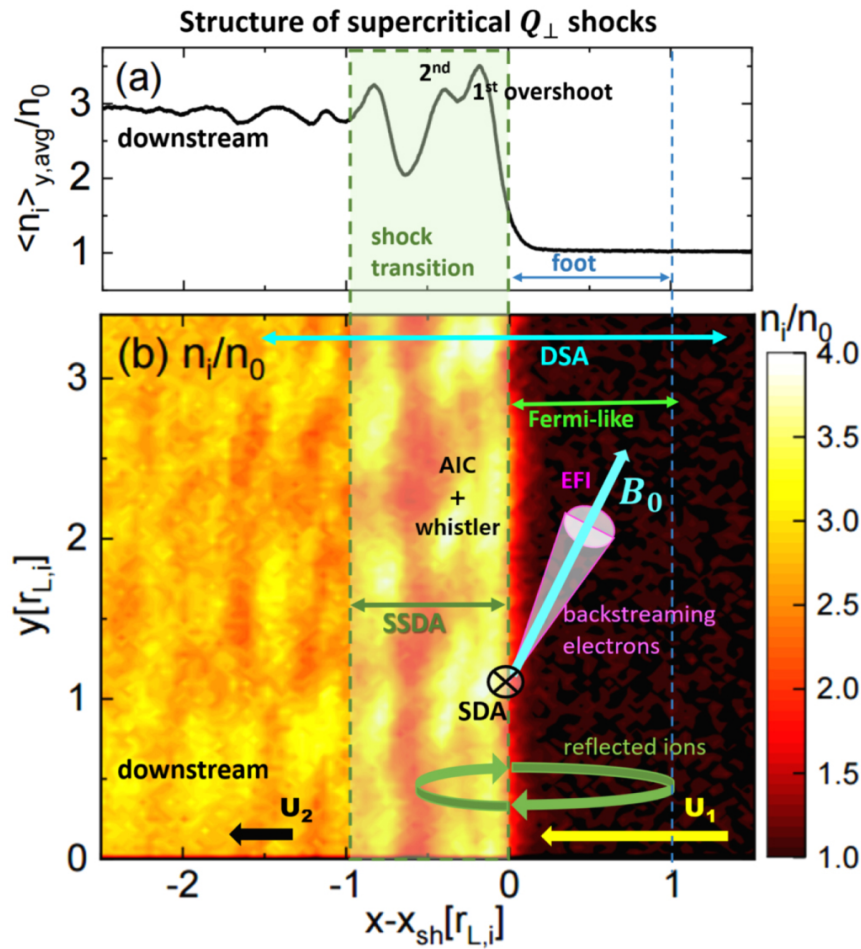


Figure 2.7: Schematic of the plasma-physics occurring at a cosmological shock. Adopted from Ha et al. (2021).

Diffusive Shock Acceleration (DSA)

DSA was first proposed by Fermi (1949), hence it is often referred to as *Fermi-I acceleration*. Fermi proposed that particles scattering off Alfvén waves behind a shock in the ISM have a statistical probability of being scattered back upstream of the said shock. From there they could cross the shock again and gain energy from the shock crossing. This theory has later been refined by Krymskii (1977); Bell (1978a,b); Blandford & Ostriker (1978) (see also Drury, 1983; Bykov et al., 2019, for reviews).

The process can be summarized as follows: In the rest frame of the particle, a shock wave propagates toward it with the shock speed v_s . As the particle crosses the shock it gains energy according to the fractional momentum change over the shock. In addition, the particle's streaming amplifies plasma instabilities, which confine it in the shock transition region. Given a large enough gyro radius of the particle, its confinement region is large enough to cross the shock again in the upstream region. In the upstream, again from the particle's rest frame as it is faster than

the ambient plasma, it feels approaching particles, leading to another (albeit weaker) momentum gain. In the upstream, it can again scatter off Alfvén waves to be reflected back across the shock into the downstream. The self-similarity of this acceleration mechanism produces a power-law in momentum space.

A derivation of this process can be either done in a macroscopic way via the general transport equation of CRs, or in a microscopic way via the test-particle approach (see e.g. Drury, 1983; Jones & Ellison, 1991; Blasi, 2013; Bell, 2013, or the Masters thesis by Daniel Karner¹ for a thorough derivation).

Heuristically it can be understood as follows: At every step of the previously discussed scattering process, the particle has a probability P_{esc} to escape the acceleration zone so that we can define the number of particles after k cycles as

$$N = N_0(1 - P_{\text{esc}})^k \quad (2.30)$$

where N_0 is the number of particles before the acceleration process starts. We can further assume an energy gain per shock crossing as $\Delta E = E - E_0 = \beta E_0$, which leads to an energy of the particle after k cycles

$$E = E_0(1 + \beta)^k \quad (2.31)$$

where E_0 is again the energy of the particle before the acceleration process. By taking the logarithm of these two equations we can eliminate k and define a particle spectrum as

$$N(E) = N_0 \left(\frac{E}{E_0} \right)^{\ln(1-P_{\text{esc}})/\ln(1+\beta)}, \quad (2.32)$$

i.e. a power-law in energy space.

By solving this problem in energy space, however, we lose information on the particle's direction or pitch angle (see Sec. 2.6 for more details). It is, therefore, more convenient, but also more elaborate, to solve the acceleration in momentum space, for this, we again refer to the previous references.

This approach also results in a power-law in momentum space with the particle distribution function

$$f(p) \propto p^{-q} \quad (2.33)$$

and it can be shown that

$$q = \frac{3r}{r+1} = \frac{4\mathcal{M}_s^2}{\mathcal{M}_s^2 - 1} \quad (2.34)$$

where r is the shock compression ratio and \mathcal{M}_s is the sonic Mach number.

However, the main complication with this process is that it is only effective once the gyroradius of the particle is comparable to the shock width and the particle can be scattered back upstream, allowing it to gain energy over multiple cycles. Especially for electrons this requires the particles to gain substantial energy before they can be efficiently accelerated by DSA. Otherwise, they simply cross the shock, gain energy, and are advected downstream before they can be scattered back into the upstream of the shock.

¹https://www.usm.uni-muenchen.de/CAST/wp/download/karner_msc.pdf, last accessed: November 22nd 2023.

Shock Drift Acceleration (SDA)

Small-scale plasma simulations with PIC and hybrid models have been used to find solutions for the problem of CR injection into a DSA-like process (e.g. [Caprioli & Spitkovsky, 2014](#); [Guo et al., 2014](#); [Park et al., 2015](#); [Caprioli et al., 2018](#); [Ryu et al., 2019](#); [Kobzar et al., 2021](#); [Ha et al., 2021](#)). It has been shown that particles can initially gain energy via (stochastic) SDA, where they gain energy from the gradient drift along the shock ramp until they reach a critical momentum p_{inj} which is enough to inject them into a Fermi-like process like DSA (e.g. [Ha et al., 2021](#), and references therein). SDA leads to an energy gain of

$$\frac{\Delta\gamma}{\gamma_i^{\text{up}}} \equiv \frac{2u_t (u_t - v_{i\parallel}^{\text{up}})}{c^2 - u_t^2} \quad (2.35)$$

per cycle ([Guo et al., 2014](#)), where γ_i^{up} is the Lorentz factor before the SDA cycle, $v_{i\parallel}^{\text{up}}$ is the particle velocity parallel to the magnetic field before SDA and u_t is the velocity required to boost from the upstream frame to the de Hoffmann-Teller (HT) frame ([de Hoffmann & Teller, 1950](#))

$$u_t = \sqrt{\frac{2\Gamma k_B T_e}{m_e}} \sqrt{\frac{m_e}{m_i}} \mathcal{M}_s \sec \theta_B. \quad (2.36)$$

Here T_e is the electron temperature, m_e is the electron mass, m_i the ion mass, \mathcal{M}_s the sonic Mach number of the shock and θ_B the shock obliquity. The onset of SDA (and with that DSA) is found to depend on the excitement of plasma instabilities and electromagnetic waves which require a critical sonic Mach number $\mathcal{M}_{s,\text{crit}} \approx 2.25$ ([Ha et al., 2018b](#)), and different magnetic field configurations to trigger electron or proton acceleration.

In this context it was found that CR protons are more efficiently accelerated by low obliquity shocks (e.g. [Caprioli & Spitkovsky, 2014](#); [Caprioli et al., 2018](#); [Ryu et al., 2019](#)), meaning shocks where the angle between magnetic field vector and shock normal are small, while electrons are more efficiently accelerated at high obliquity shocks (e.g. [Guo et al., 2014](#); [Ha et al., 2021](#); [Kobzar et al., 2021](#)).

However, see [Winner et al. \(2020\)](#); [Shalaby et al. \(2021, 2022\)](#) for discussions of this in the case of low- β SN remnants, who find efficient electron acceleration at quasi-parallel shocks.

Current theoretical problems

First, the acceleration efficiencies, i.e. the fraction of available energy dissipated by the shock that goes into the acceleration of CRs, required to reproduce the surface brightness of radio relics should also inject a significant population of CR protons. These should then interact with background gas and scatter into π^0 pions and from there γ -photons, which should be observable. This is ruled out by Fermi-LAT observations which place an upper limit to the CR proton energy density in clusters at a few percent of the thermal energy density (e.g. [Ackermann et al., 2014, 2015, 2016](#); [Vazza et al., 2016](#); [Adam et al., 2021](#), and references therein). We will discuss this in more detail in Sec. 3.2.

One possible solution to study this problem in simulations that has been proposed is the inclusion

of shock obliquity in the acceleration efficiency models (Ha et al., 2020; Wittor et al., 2020), which suppresses CRp acceleration at merger shocks. This does however not solve the problem of too-low CRe acceleration efficiencies (see e.g. Botteon et al., 2020a, for a discussion).

Second, the sonic Mach numbers obtained in X-ray observations of GC merger shocks are typically below the critical Mach number of $\mathcal{M}_{s,\text{crit}} \approx 2.25$ found in PIC simulations, which is required to accelerate CRs in the first place. For Mach numbers obtained from radio observations, this strain is less severe, as they are typically above this threshold (see Wittor et al., 2021, and references therein). This could indicate that thermal- and relativistic particle acceleration probes different parts of the shock (Wittor et al., 2021), or that multiple acceleration events are required to reach the required radio relic brightness (e.g. Inchingolo et al., 2022; Smolinski et al., 2023).

2.6 Cosmic Rays

Finally, we want to discuss the impact that CRs can have on the ICM. As we will see in Sec. 3.2, the pressure ratio between CRs and the thermal gas can be constrained by observations to

$$X_{\text{CR}} \equiv \frac{P_{\text{CR}}}{P_{\text{th}}} \lesssim 10^{-2}. \quad (2.37)$$

This indicates that the kinematic impact of CRs in the ICM is negligible. However, as was the case with the magnetic fields, CRs can have an impact on the ICM via various plasma instabilities. We will give a brief overview of the key processes and how they affect the ICM. For a recent review, please see Ruszkowski & Pfrommer (2023), which we will use as a basis for this section.

Most of the interaction between CRs and the thermal plasma is driven by Alfvén waves. Alfvén waves are plasma waves that are driven by oscillations of ions that feel a restoring force from the re-alignment with the background magnetic field. In a sense, Alfvén waves are to magnetic field oscillations what sound waves are to pressure oscillations in a gaseous medium. They propagate through a fully ionized at the Alfvén speed

$$v_A = \frac{B}{\sqrt{4\pi\rho}}. \quad (2.38)$$

In general the interaction between CRs and plasma is caused by the particle's helical motion around magnetic field lines and the coupling with circularly polarized MHD waves. There are two distinct ways in which this interaction can take place: A *resonant* and a *non-resonant* interaction.

In the resonant interaction the CR's gyro frequency

$$\Omega = \frac{qB}{\gamma mc} \quad (2.39)$$

with the charge of the particle q , magnetic field strength B , the Lorentz factor of the particle $\gamma = (1 - (v/c)^2)^{-1/2}$ at velocity v and its mass m , is a multiple of the rotation rate ω_r of a

circularly polarized plasma wave

$$k_{\parallel} \mu v - \omega_r = \pm N \Omega, \quad (2.40)$$

where k_{\parallel} is the component of the wave number parallel to the magnetic field and $\mu = \cos \theta = \mathbf{p} \cdot \mathbf{B} / (|\mathbf{p}| |\mathbf{B}|)$ is the cosine of the pitch angle between the magnetic field vector \mathbf{B} and the relativistic particle momentum \mathbf{p} .

If N is a natural number the particle feels a constant *pumping* by the Alfvén wave, leading to a net energy gain/loss, depending on the sign on the right-hand-side of Eq. 2.40. Eq. 2.40 can also result in a changing of v or μ as the particle's free parameters, if N is not a natural number, leading to the so-called *pitch-angle scattering*².

In the case $N = 0$, which is referred to as *Landau resonance*, the interaction is non-resonant, which is typically called *transit time damping*. Here the particle is confined by magnetic mirrors and *surfs* along the wave. This leads to a net energy gain because head-on interactions are more frequent than head-tail interactions.

These scattering processes also back-react to the plasma, as the energy transfer from Alfvén waves to CRs, or vice-versa, transfers energy between thermal plasma and CR population.

This back-reaction is mainly driven by the *cosmic ray streaming instability*, or *gyro-resonant streaming instability*, which describes the process of CRs exciting Alfvén waves as they propagate through the magnetized background plasma (see e.g. [Kulsrud & Pearce, 1969](#); [Skilling, 1975a,b,c](#); [Marcowith et al., 2021](#), the latter for a review). This is caused by the CRs typically propagating faster than the local Alfvén speed, which leads to a transfer of forward momentum from CRs to hydromagnetic waves, leading to their growth. The growth rate can be derived by equating the momentum densities of CRs and Alfvén waves (see e.g. Sec. 7.4 in [Longair, 2011](#), for a derivation) and leads to

$$\Gamma = \frac{eB}{m_p} \frac{N(E)}{N_p} \left(\frac{v}{v_A} \right) \quad (2.41)$$

in the case of CRps, where $N(E)$ is the number density at a given energy and v their velocity.

This instability leads to a self-confinement of CRs in an *Alfvén-cage*, which has three main effects on the CRs.

First, it isotropizes the pitch-angle μ of the CRs. Since the Alfvén waves in a realistic, turbulent plasma will interact with CRs from multiple directions, CRs will perform random walks by scattering off the complex grid of surrounding Alfvén waves. This leads to an isotropization of the propagation of individual CRs within this Alfvén-cage, i.e. a random walk.

Second, it can confine populations of CRs in a package of thermal plasma whose net-propagation velocity is reduced from nearly the speed of light c to the Alfvén speed v_A , due to the same random walk as before.

Third, energy transfer via adiabatic compression of the surrounding gas can be passed on to the

²Like [Ruszkowski & Pfrommer \(2023\)](#) we would like to refer to <https://svs.gsfc.nasa.gov/4649> for excellent visualization of this process.

confined CR population, leading to a net energy gain/loss from compression/expansion of the surrounding plasma.

3 | Non-Thermal Emission in the Large-Scale Structure of the Universe

The term "non-thermal emission" is somewhat loosely defined, given its frequent usage in high-energy astrophysics. Following Longair (2011) we use the definition that emission is non-thermal "if its spectrum cannot be accounted for by the spectrum of thermal Bremsstrahlung or black-body radiation", i.e. if the particles emitting the radiation are non-thermal.

In this chapter, we will focus on the main examples of non-thermal emission in the LSS and how they relate to our presented work. We will briefly outline the emission mechanisms and the most common classifications of observed structures but note that many of these structures have sub-classifications we will not discuss.

3.1 Synchrotron Radiation

The dynamics of charged particles in a magnetized medium are governed by the Lorentz force (see e.g. Chapter 7 in Longair, 2011, for a detailed derivation). This forces electrons to move along magnetic field lines in helical motions. The helical motion can be viewed as a constant deflection of the initial propagation direction of the electron. Electrons deflected from their initial path emit radiation as a dipole along and away from their velocity vector, in the rest-frame of the particle. Given that the electrons we are interested in are highly relativistic we need to account for Lorentz transformation between the particle's rest frame and our observer frame. This Lorentz transformation can be seen in Fig. 3.1, for a derivation see Chapter 8.3 in Longair (2011). It transforms the symmetric dipole emission in the rest frame to a beamed emission along the particle's trajectory in the lab frame. We can express the angle ϕ under which the radiation along the velocity vector is emitted as

$$\phi \approx \pm\gamma^{-1}, \quad (3.1)$$

where $\gamma = \sqrt{1 + \frac{v^2}{c^2}}$ is the Lorentz factor of the relativistic electrons.

Naturally, this emission does not come for free but leads to an energy loss rate for a single electron of

$$\left(\frac{dE}{dt}\right)_{\text{synch}} = \frac{4\sigma_T}{3m_e^2 c} \frac{B^2}{8\pi} \gamma^2 \sin^2(\alpha), \quad (3.2)$$

where σ_T is the Thompson cross-section, B is the magnetic field strength, α is the pitch angle between the magnetic field and particle propagation vector and we already accounted for the

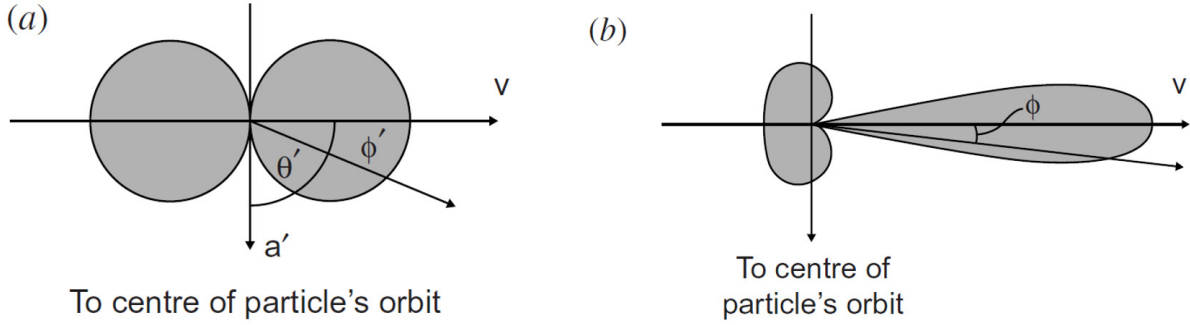


Figure 3.1: Emission of a relativistic electron moving around a magnetic field line. *Left*: Rest-frame of the particle. *Right*: Laboratory-frame of the observer. Adopted from Longair (2011).

ultra-relativistic limit (see Dolag & Enßlin, 2000).

From this energy loss rate, one can derive the spectrum of emitted photons from a single electron following Ginzburg & Syrovatskii (1965) as

$$j_{\perp}(\nu) = \frac{\sqrt{3}e^3 B \sin(\alpha)}{2m_e c} (\mathcal{F}(x) + \mathcal{G}(x)) \quad (3.3)$$

$$j_{\parallel}(\nu) = \frac{\sqrt{3}e^3 B \sin(\alpha)}{2m_e c} (\mathcal{F}(x) - \mathcal{G}(x)) \quad (3.4)$$

$$j(\nu) = j_{\perp}(\nu) + j_{\parallel}(\nu) \quad (3.5)$$

$$= \frac{\sqrt{3}e^3 B \sin(\alpha)}{2m_e c} \mathcal{F}(x) \quad (3.6)$$

where \perp and \parallel describe the perpendicular and parallel components, respectively. The functions $\mathcal{F}(x)$ and $\mathcal{G}(x)$ are commonly referred to as the first and second synchrotron functions, with

$$\mathcal{F}(x) = x \int_x^{\infty} dz K_{5/3}(z) \quad (3.7)$$

$$\mathcal{G}(x) = x K_{2/3}(x) \quad (3.8)$$

where we used the modified Bessel functions $K_a(x)$ at the ratio between observer- and critical frequency

$$x \equiv \frac{\nu}{\nu_c} = \frac{4\pi m_e^3 c^3 \nu}{3eB(t) \sin \alpha E^2}. \quad (3.9)$$

In the systems we are interested in, we typically do not find synchrotron emission from individual electrons. Instead, we find a population of CRes following a power-law energy spectrum as

$$N(E)dE \propto E^{-\alpha} dE. \quad (3.10)$$

Fig. 3.2 shows that the emission is strongly peaked around $x \approx 1$, so we can closely match the energy radiated away in a frequency band $\nu + d\nu$ to an energy band of the emitting electrons in

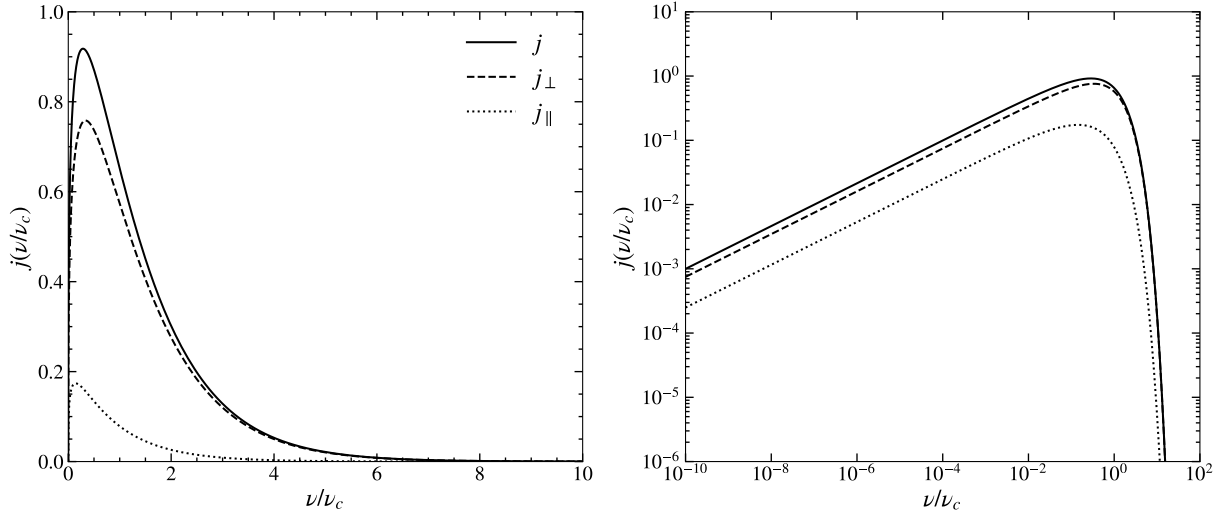


Figure 3.2: Spectra of a single electron emitting synchrotron radiation, i.e. the synchrotron kernel. Solid lines show total emission, dashed lines perpendicular polarisation, and dotted lines parallel polarization. In all cases the prefactors for Eqs.3.3-3.6 are set to one.

the range $E + dE$ as

$$J(\nu)d\nu = \left(-\frac{dE}{dt} \right)_{\text{synch}} N(E)dE . \quad (3.11)$$

Using the definitions for E , dE and $\left(-\frac{dE}{dt} \right)_{\text{synch}}$ in Longair (2011), Sec. 8.5, one finds an expression for the synchrotron emission of a power-law spectrum of electrons in energy space as

$$J(\nu) \propto B^{(\alpha+1)/2} \nu^{-(\alpha-1)/2} . \quad (3.12)$$

It is common to express this as $J(\nu) \propto \nu^{-\alpha_\nu}$ where $\alpha_\nu = (\alpha - 1)/2$ is the spectral index of the synchrotron spectrum.

In realistic systems, Eq. 3.11 will not hold for all frequencies. As high-energy CRes with $E \sim 10$ GeV have cooling times of $\tau_{\text{synch}} \approx 200$ Myrs, the high energy end of the power-law distribution of electrons will cool off quickly, leading to a steepening of the energy spectrum. This leads to fewer electrons remaining in this energy band and therefore less synchrotron emission in this frequency band, resulting in a steepening of the synchrotron spectrum at higher frequencies. No analytical solution for a synchrotron spectrum of an arbitrary electron spectrum exists in the literature.

In Sec.11.1 we will therefore show our numerical solution to obtain synchrotron emission from arbitrary electron spectra.

Finally, it is worth noting that this emission mechanism is highly ordered if the magnetic fields are highly ordered. Highly ordered emission leads to polarized emission, which therefore provides a powerful probe in the magnetic field structure of objects emitting synchrotron emission.

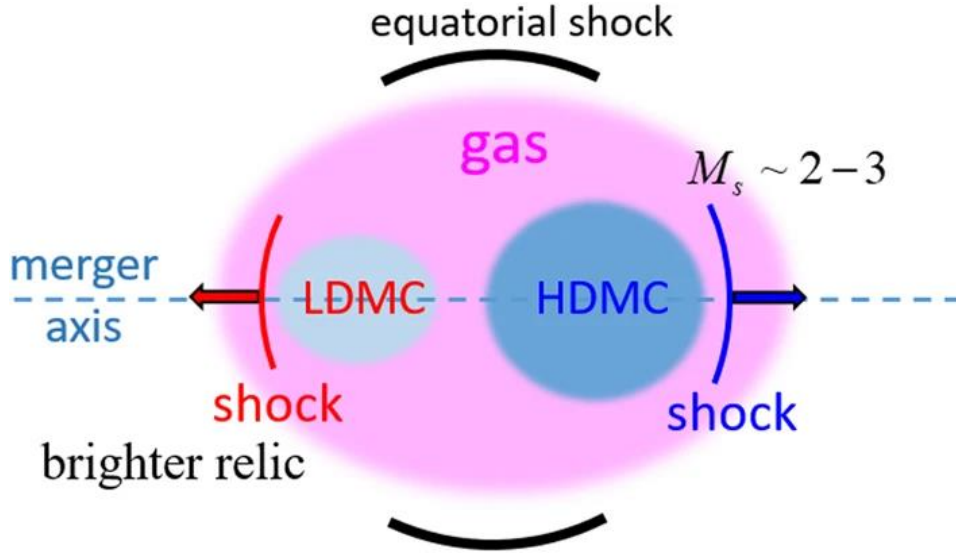


Figure 3.3: Schematic of the shock origin of radio relics. Adopted from [van Weeren et al. \(2019\)](#).

As we discussed in Ch. 2 the ICM can be described as a weakly magnetized, collisionless plasma with $T \sim \text{keV}$. It is therefore an ideal environment for synchrotron emission.

For a recent and extensive review of synchrotron emission in galaxy clusters please see [van Weeren et al. \(2019\)](#), which we will refer to frequently in this chapter.

3.1.1 Radio Relics

Radio Relics (RRs) can be characterized as roughly Mpc sized elongated structures observable at radio wavelengths. They are mostly located in the outskirts of galaxy clusters where they are typically observed as giant radio arcs, bowing out from the cluster center.

The canonical picture for their origin is that they are caused by shock waves, driven by galaxy cluster mergers. These mergers dissipate $E \sim 10^{62} - 10^{64}$ erg, mostly into thermal particles, heating the ICM to temperatures of $T \sim 10^8$ K (e.g. [Sarazin, 2002](#)). A part of this energy is however also channeled into the acceleration of thermal protons and electrons to relativistic speeds in a process called Diffusive Shock Acceleration (DSA), as we discussed in Sec. 2.5. The electrons can then emit the observed synchrotron emission, given the magnetic field strength in the relic is high enough. We show a schematic of this merger process in Fig. 3.3, which is taken from the review by [van Weeren et al. \(2019\)](#).

In this simple picture, a head-on merger between two GCs drives four shock waves. The most prominent shock is being driven by the lighter merging cluster. As the lighter cluster (LDCM in Fig. 3.3) falls into the deeper potential well of the heavier cluster (HDMC) it gains significant kinetic energy. Once the lighter cluster has passed through the heavier cluster it drives a strong bow shock, which is typically visible as a bright radio relic.

As the heavier cluster (HDMC) is also displaced from its initial position, due to the formation of a common center-of-mass (COM), it also drives a shock wave in the infall direction of the lighter

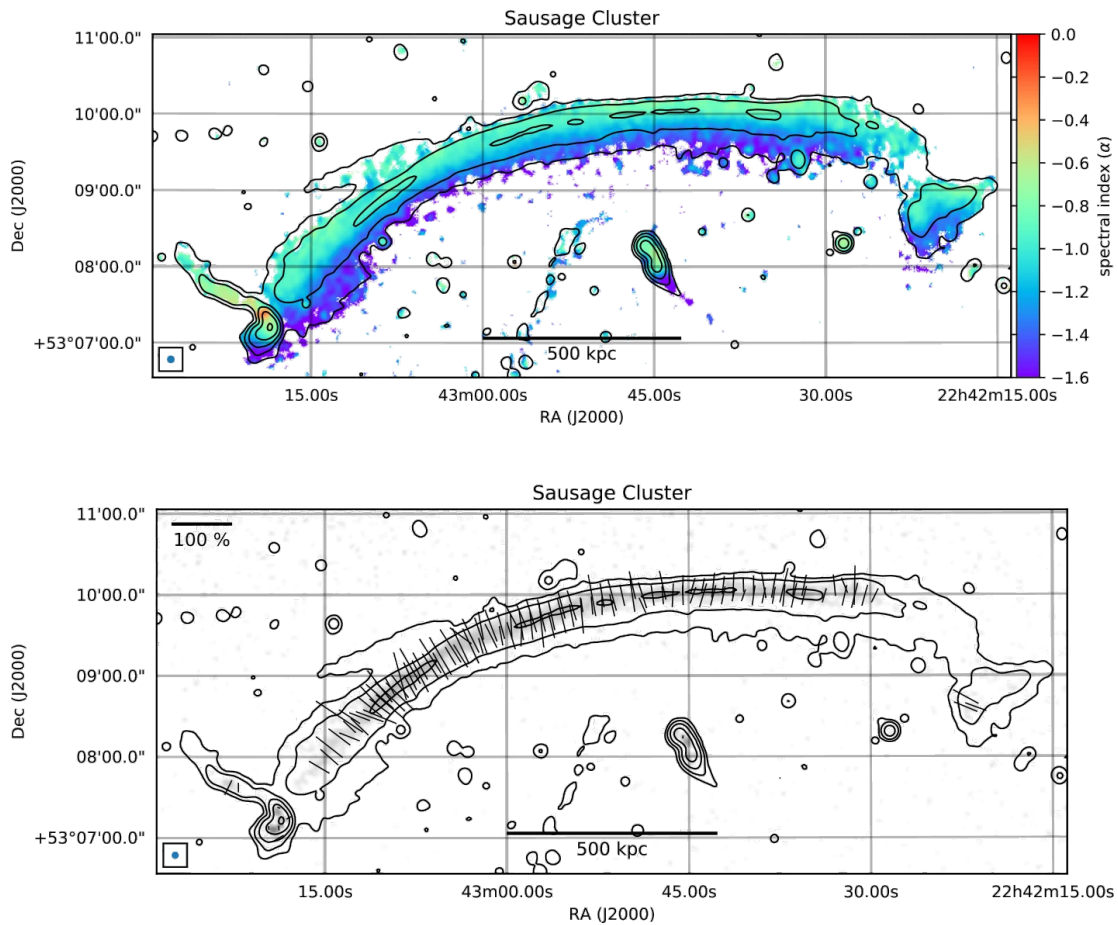


Figure 3.4: Observations of the "Sausage Relic". Taken from [van Weeren et al. \(2019\)](#). *Top*: Spectral index map between 150 MHz and 3 GHz (from [Di Gennaro et al., 2018](#)). *Bottom*: Polarized intensity at 3 GHz. Contours show the total intensity, and lines indicate the electric field vectors corrected for Faraday Rotation (published in [Di Gennaro et al., 2021](#)).

cluster. These counter shocks are typically weaker with lower sonic Mach numbers. As discussed in Sec. 2.5 this results in less efficient acceleration of electrons and with that a lower synchrotron brightness. Of the ~ 60 systems with observed relics to date, only 22 are double-relic systems ([Bonafede et al., 2009b, 2017](#); [de Gasperin et al., 2014](#); [Stuardi et al., 2022](#)), meaning that the countershock is only observable in 1/3 of all cases.

The final two shocks are equatorial shocks expected to propagate perpendicular to the merger axis. These shocks are predicted from simulations (e.g. [Springel & Farrar, 2007](#); [van Weeren et al., 2011a](#); [Donnert, 2014](#); [Donnert et al., 2017](#); [Molnar & Broadhurst, 2017, 2018](#); [Ha et al., 2018a](#)) however rarely observed (see e.g. [Hoang et al., 2022](#)).

RRs typically show a steepening of the synchrotron spectrum towards the cluster center. A resolved synchrotron spectrum map of the sausage relic can be seen in the top panel of Fig. 3.4. The relic shows the typical behavior of a flatter synchrotron spectral index at one edge of the relic

and a steeper index at the opposite edge. It is commonly assumed that this originates from the aforementioned cooling of the electron population that leads to a steepening of the synchrotron spectrum. This allows us to infer a propagation direction of the underlying shock, which in the case of the sausage relic looks to propagate away from the cluster center, as expected for an underlying shock driven by a previous merger event.

From these observations [Di Gennaro et al. \(2018\)](#) found that the spectral index between 150 MHz and 3 GHz obtained at the northern edge of the relic is $\alpha_\nu = -0.86 \pm 0.05$. If the resolved spectral index at the shock front is available one can estimate the sonic Mach number of the shock via ([Drury, 1983](#))

$$\mathcal{M} = \sqrt{\frac{2\alpha_{\text{inj}} + 3}{2\alpha_{\text{inj}} - 1}} \quad (3.13)$$

where α_{inj} is the spectral index of the freshly injected synchrotron spectrum at the leading edge of the relic. In the case of the sausage relic, this leads to a Mach number of $\mathcal{M} \approx 2.6$, in good agreement with the Mach number obtained by calculating the temperature jump from X-ray observations ([Akamatsu et al., 2015](#)).

This agreement is however not common, with many relics showing a strong disagreement between the Mach number obtained from Radio- and X-ray observations (see [Wittor et al., 2021](#), and references within). In most cases, the Mach number obtained from X-ray observations is found to be lower than that of Radio observations. Simulations by [Hong et al. \(2015a\)](#); [Wittor et al. \(2021\)](#) indicate that this is caused by Radio- and X-ray observations probing different parts of the shock surface.

Most RRs emit strongly polarized synchrotron radiation, with a typical polarisation fraction $\Pi \sim 30\%$ at 1.4 GHz (e.g. [Rajpurohit et al., 2022a](#)), but some relics have been observed to show regions of up-to 60% polarisation (e.g. [Di Gennaro et al., 2018](#); [Stuardi et al., 2021](#)). Observations of the polarisation vector of RRs give insight into the magnetic field morphology at the surfaces of merger shocks (e.g. [de Gasperin et al., 2022](#)). This can be seen in the bottom panel of Fig. 3.4. The black lines indicate the direction of the E-vectors, which in turn means that the magnetic field vectors are parallel to the shock surface. These observations can be understood as the magnetic field lines being swept up by the shock, which leads to compression and with that amplification of the magnetic field component parallel to the shock surface (see e.g. [Wittor et al., 2017](#)). This leads to an alignment of the magnetic field vector with the shock surface, i.e. to a 90° angle between the shock normal and the magnetic field vector, meaning a high obliquity shock. As we discussed in Sec. 2.5 these high obliquity shocks favor CRe acceleration.

A number of recent observations indicate that the medium the shocks that power radio relics expand into is highly complex and turbulent. This leads to relics with complex surface brightness variations over their surface ([Rajpurohit et al., 2020b](#); [de Gasperin et al., 2022](#); [Chibueze et al., 2023](#)), or deformation from the poster-child arc-shaped radio relic ([van Weeren et al., 2010](#); [Stroe et al., 2013, 2016](#); [Hoang et al., 2017](#); [Di Gennaro et al., 2018](#); [Dwarakanath et al., 2018](#); [HyeongHan et al., 2020](#); [Botteon et al., 2021, 2022](#); [Riseley et al., 2022](#)). We will study this in

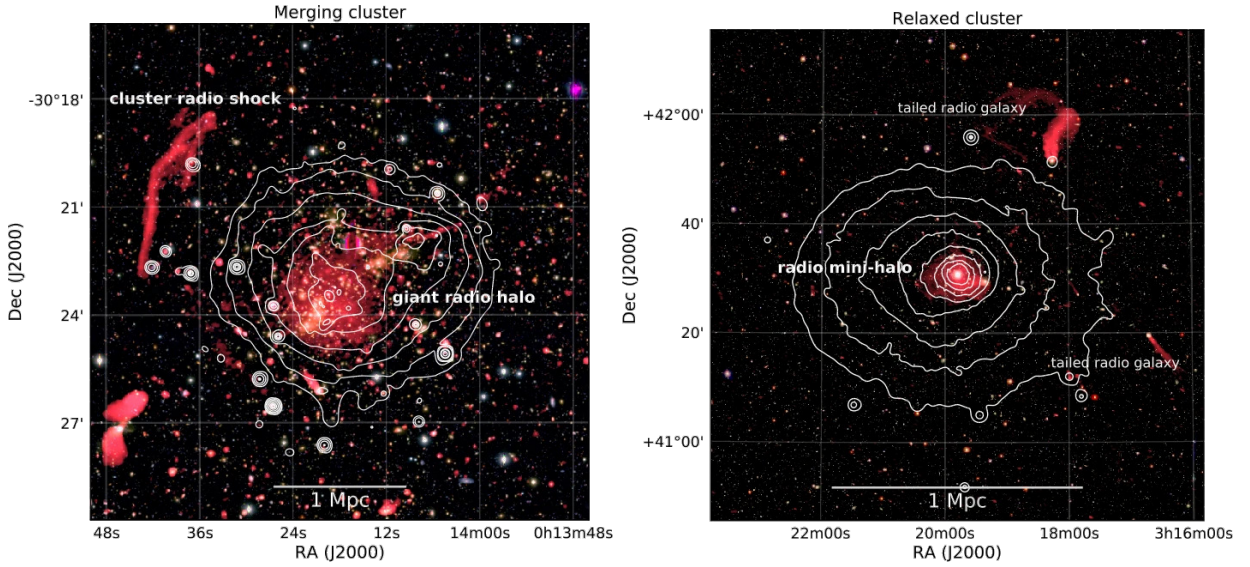


Figure 3.5: Examples for a radio halo and radio mini halo, adopted from [van Weeren et al. \(2019\)](#). Both images show radio emission in red, optical emission in color, and contours show the X-ray surface brightness. *Left*: Abell 2744 ([Pearce et al., 2017](#)). *Right*: Perseus cluster ([Gendron-Marsolais et al., 2017](#))

more detail in Ch. 14.

3.1.2 Radio Halos

Radio Halos can be classified as diffuse radio emission at the center of GCs, roughly following the thermal structure of the ICM (i.e. the X-ray emitting hot gas). They have diameters of up to 2 Mpc, their morphology largely follows the overall structure imprinted on ICM-scales (for example in the Coma cluster [Large et al., 1959](#); [Willson, 1970](#); [Giovannini et al., 1993](#); [Thierbach et al., 2003](#); [Brown & Rudnick, 2011](#); [Bonafede et al., 2022](#)) and they can be detected out to large redshifts (e.g. El-Gordo [Menanteau et al., 2012](#)). The spectral index of the integrated synchrotron emission is in good agreement with the power-law index range of $\alpha \approx -1.4 \sim -1.1$ (e.g. [Giovannini et al., 2009](#)), which is steeper than that of RRs, indicating weak shocks, or older CRe populations.

While the underlying physical origin is still under debate, there is strong observational evidence that these halos correlate with recent merger activity ([Cassano et al., 2010](#); [Feretti et al., 2012](#), and references therein) which can lead to an increase in the turbulent motions in the ICM and with that re-acceleration of CRes (e.g. [Cassano & Brunetti, 2005](#); [Brunetti & Lazarian, 2007](#); [Brunetti, 2016](#); [Brunetti & Lazarian, 2016](#); [Eckert et al., 2017](#); [Stuardi et al., 2019](#); [Wong et al., 2020](#)).

Another possible explanation is a hadronic origin, where long-lived CRps scatter with the background plasma to produce charged π^\pm -ons, which decay into secondary electrons/positrons (e.g.

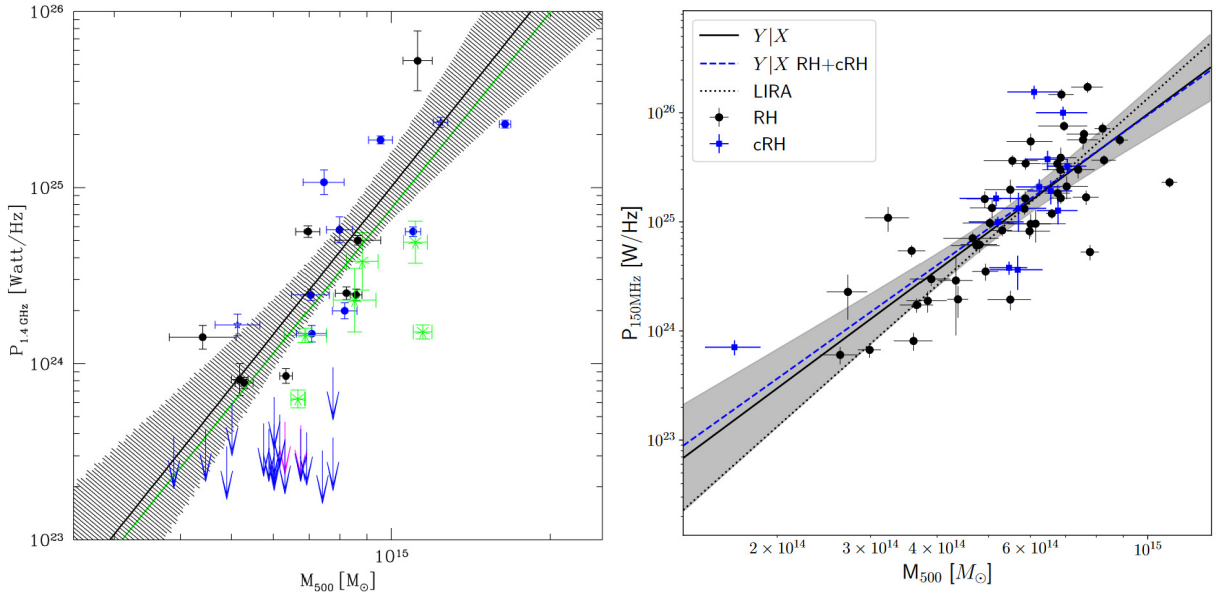


Figure 3.6: Scaling relations of observed radio halos with host cluster mass. *Left*: Scaling at 1.4 GHz, adopted from [Cassano et al. \(2013\)](#). *Right*: Scaling at 150 MHz, adopted from [Cuciti et al. \(2023\)](#).

[Dolag & Enßlin, 2000](#); [Pfrommer & Enßlin, 2004](#)). However, to explain large radio halos purely from a hadronic scenario, the ratio between thermal- and CR proton pressure needs to be of the order $4\% \leq X_{\text{cr}} \leq 14\%$. This is ruled out by the non-detection of diffuse γ -ray emission in galaxy clusters, which we will discuss in Sec. 3.2.

For smaller radio halos, so-called Radio Mini Halos, the hadronic scenario could however explain observations like the unbroken spectral index up to very high energies in the halo center observed by [Perrott et al. \(2021\)](#).

We show a comparison between a giant radio halo and a radio mini-halo in Fig. 3.5, which we adopted from [van Weeren et al. \(2019\)](#). As the name suggests the main difference in the radio morphology is the extent of the emitting region. Giant radio halos have extents of up to Mpc-size, while mini halos are defined to be smaller than $r_{\text{mH}} < 0.2r_{500}$ (e.g. [Giacintucci et al., 2017](#)). Taking into account dynamical considerations, classical RHs tend to correlate with ongoing or recent merger activity, while radio mini-halos are typically found in relaxed clusters.

The total luminosity of RHs is found to strongly correlate with the cluster mass and its X-ray luminosity over a wide range of masses, redshifts, and radio frequencies (e.g. [Brunetti et al., 2009](#); [Cassano et al., 2013](#); [Cuciti et al., 2021b,a, 2023](#)). An example of these observed scaling relations can be found in Fig. 3.6. Ultimately this relation traces the release of potential energy during structure formation into turbulent energy and its dissipation on smaller scales. This

strongly supports the turbulence scenario as a source for radio halos (e.g. [Brunetti & Lazarian, 2007](#)). With this correlation persisting over a wide range of frequencies it allows us to conclude that sufficient turbulence is present also in less massive clusters, given it is currently undergoing any sort of merger event ([Cuciti et al., 2023](#)).

Around 100 RHs have been reported in the literature at this point ([van Weeren et al., 2019](#)). Most of them show only weakly polarized emission (up-to ten percent in Coma and upper limits of less than five percent in other clusters [Feretti & Giovannini, 1998](#); [Liang et al., 2000](#); [Feretti et al., 2001](#); [Bacchi et al., 2003](#)). From this we can infer that the underlying magnetic field structure is chaotic and turbulent, which leads to randomized emission of the CRes and complex Faraday Rotation of the polarized emission as it moves through the ICM, causing gradual depolarization along the LOS. This fits the concept of the emitting electrons being re-accelerated in a turbulent medium.

Only three RHs have so far been observed to show polarized emission: A2255 ([Govoni et al., 2005](#)), MACS J071.5+3745 ([Bonafede et al., 2009a](#)) and A523 ([Girardi et al., 2016](#); [Vacca et al., 2022b,a](#)). While the origin of the polarized emission is under debate in all cases, they each show complex dynamical states. [Govoni et al. \(2005\)](#) suggest that the polarized emission could originate from the interaction of an aged electron population with pressure waves that align the magnetic field, or that the polarized emission stems from foreground structures with minimal RM between emitting region and observer. [Vacca et al. \(2022a\)](#) discuss different scenarios for the polarized emission in A523. Most prominently they suggest that the observed halo could be driven by a secondary merger which either re-accelerates the still young electron population from the primary merger, or from recent AGN activity, or drives a relic that is seen in projection. Whatever the scenario for this uncommon polarized diffuse emission may be, it shows that even with the current generation of radio telescopes disentangling different formation scenarios is difficult and requires complementary numerical modeling to explore different scenarios.

3.1.3 Radio Mega Halos

A new class of RHs has recently been found by [Cuciti et al. \(2022\)](#) and dubbed *radio mega halos* since the diffuse emission extends significantly further from the cluster center than in previously known RHs. They find a number of clusters whose radial profile of synchrotron surface brightness initially falls off exponentially, like a typical radio halo, but then saturates to a stable value at $r \sim 500$ kpc and extends up to $0.5r_{500}$ of the cluster. This extended emission shows steep synchrotron spectra with $\alpha_\nu \approx -1.6$, indicating an old electron population. We show Fig. 2 of [Cuciti et al. \(2022\)](#) in Fig. 3.7. The inset plot shows the radial drop of synchrotron surface brightness, indicating a saturation level roughly one order of magnitude below the central surface brightness peak of the classical Radio Halo.

These observations imply a significant volume-filling population of relativistic electrons further from the cluster center than previously expected. This poses a number of problems for theoretical models, namely: What is the initial source of these electrons? How can these electrons remain synchrotron-bright? Are radio mega halos common and our instruments are just

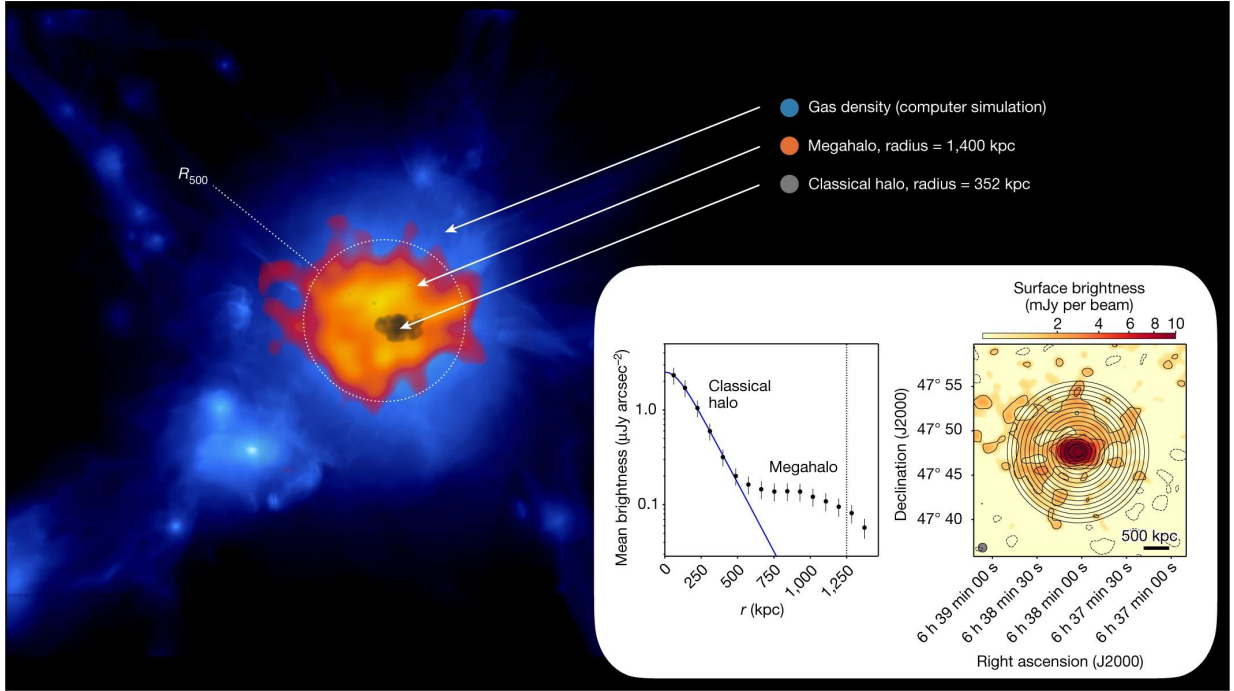


Figure 3.7: Fig. 2 of [Cuciti et al. \(2022\)](#), showing the schematic and observation of a Radio Mega Halo.

now sensitive enough to detect them?

First numerical simulations by [Beduzzi et al. \(2023\)](#) strongly support that efficient re-acceleration by turbulence can explain the origin of radio mega halos. However, further studies are required to improve our understanding of this process.

3.2 Diffuse γ -ray emission

The second non-thermal emission process relevant for the present work is γ -ray emission originating from hadronic interactions between Cosmic Ray protons (CRPs) and the thermal background gas. This process was initially proposed by [Fermi \(1950\)](#) and later refined by e.g. [Stecker \(1970\)](#); [Stephens & Badhwar \(1981\)](#); [Dermer \(1986\)](#); [Pfrommer & Enßlin \(2004\)](#); [Kafexhiu et al. \(2014\)](#); [Yang et al. \(2018\)](#).

In the most simplified picture, a primary CRp beyond a threshold momentum of $p_{\text{th}} = 0.78 \text{ GeV}/c$ impacts a thermal proton, and the impact partners produce pions, $\Delta_{2/3}$ isobars and other secondary particles ([Blasi et al., 2007](#))

$$p_{\text{CR}} + p_{\text{th}} \rightarrow \pi^0 + \pi^+ + \pi^- + \text{anything} . \quad (3.14)$$

Depending on the charge of the resulting π -on they decay into

$$\pi^\pm \rightarrow \mu^\pm + \nu_\mu/\bar{\nu}_\mu \rightarrow e^\pm + \nu_e/\bar{\nu}_e + \nu_\mu + \bar{\nu}_\mu \quad (3.15)$$

$$\pi^0 \rightarrow 2\gamma \quad (3.16)$$

with the latter process being the one we are primarily interested in for this work.

This second decay channel has a multiplicity of $\sim 20\%$, i.e. every fifth interaction between CRp and thermal protons results in this scattering (see e.g. [Mannheim & Schlickeiser, 1994](#)). These interactions directly result in a cascade of γ -rays for primary CRps, making the process very efficient at producing high-energy photons (we will discuss the resulting γ -ray cascade in more detail in Sec. 11.3.1).

The remaining $\sim 80\%$ of the scattering events can however still contribute indirectly to high-energy γ -rays by IC up-scattering of CMB photons via the produced secondary electrons and positrons. This process is however expected to be subdominant in the case of diffuse γ -ray emission in GCs, so we will address it in future work.

[Pfrommer & Enßlin \(2004\)](#) introduced a parametrization for the source function of γ -ray photons from a power-law energy spectrum of protons with slope α_p as

$$q_\gamma(E_\gamma, X_{\text{cr}}) dE_\gamma dV \approx c\sigma_{\text{pp}} n_H \tilde{n}_{\text{CR}}(X_{\text{cr}}) \frac{2^{4-\alpha_\gamma}}{3\alpha_\gamma} \quad (3.17)$$

$$\times \left(\frac{m_{\pi^0}c^2}{\text{GeV}}\right)^{-\alpha_\gamma} \left[\left(\frac{2E_\gamma}{m_{\pi^0}c^2}\right)^{\delta_\gamma} + \left(\frac{2E_\gamma}{m_{\pi^0}c^2}\right)^{-\delta_\gamma} \right]^{\frac{-\alpha_\gamma}{\delta_\gamma}} \quad (3.18)$$

$$\times \frac{dE_\gamma}{\text{GeV}} dV \quad (3.19)$$

where $\sigma_{\text{pp}} = 32 \times (0.96 + e^{4.4-2.4\alpha_\gamma})$ mbarn is the effective cross section for the pp-process, $\alpha_\gamma = 4.3(\alpha_p - 1/2)$ is the slope of the γ -ray spectrum and $\delta_\gamma = 0.14\alpha_\gamma^{-1.6} + 0.44$ is the so-called shape parameter. The CR proton number density \tilde{n}_{CR} relates to the thermal energy density ϵ_{th} via Eq. 8 in [Pfrommer & Enßlin \(2004\)](#) as

$$\tilde{n}_{\text{CR}}(X_{\text{cr}}) = X_{\text{cr}}\epsilon_{\text{th}} \frac{2(\alpha_p - 1)}{m_p c^2} \left(\frac{m_p c^2}{\text{GeV}}\right)^{\alpha_p - 1} \left[\mathcal{B}\left(\frac{\alpha_p - 2}{2}, \frac{3 - \alpha_p}{2}\right) \right]^{-1} \quad (3.20)$$

where $\mathcal{B}(x, y)$ is the beta-function. This allows to compute the total γ -ray luminosity in the energy band $E \in [E_1, E_2]$ as a function of thermal to CRp energy density X_{CR} via

$$L_\gamma(X_{\text{CR}}) = \int_{\Omega} dV \int_{E_1}^{E_2} dE E^2 q_\gamma(E, X_{\text{CR}}) . \quad (3.21)$$

Constraining X_{CR} allows to confirm or rule out a hadronic origin for RHs and poses limits on CRp acceleration models. It is further important for background estimation for the aforementioned

magnetic field measurement method, as well as detection of DM interaction ([Cherenkov Telescope Array Consortium et al., 2023](#)). Finally, constraining X_{CR} is relevant for the hydrostatic equilibrium assumption needed to infer GC masses from X-ray observations.

Due to the non-detection of diffuse γ -ray emission from GCs with EGRET, it was possible to limit $X_{\text{CR}} < 20\%$ ([Reimer et al., 2003](#); [Pfrommer & Enßlin, 2004](#)), which was still in agreement with a hadronic origin for RHs. Newer observations with Fermi-LAT still fail to find direct detection of diffuse γ -ray emission in GCs, which further constrains $X_{\text{CR}} < 1\%$ ([Pinzke et al., 2011](#); [Ackermann et al., 2014, 2015, 2016](#)). Recent results from stacking Fermi-LAT data claim a detection ([Adam et al., 2021](#)), these results are however debated in the literature (see e.g. [Cherenkov Telescope Array Consortium et al., 2023](#), for a discussion). The increased sensitivity of the CTA will further allow to constrain $X_{\text{CR}} < 5 \times 10^{-3}$ in the case of non-detection of diffuse γ -ray emission. We will show predictions for diffuse γ -ray emission in GCs and cosmic web filaments in Ch. 16.

4 | Simulations

All observations previously discussed in this work lack one fundamental physical quantity: Time. Typical dynamical times in GCs are of the order $\sim 10^2 - 10^3$ Myrs and with that considerably longer than observation times. On top of that observations can only provide us with a two-dimensional view of the Universe, with some indications for properties of the third dimension via velocity measurements. This is where simulations of Large-Scale Structure (LSS) formation come into play. In this chapter, we will give a brief overview of simulations of LSS and where our work fits into this context.

4.1 Large-Scale Structure Simulations

The first simulation of cosmological structure formation within a Dark Matter (DM) dominated Universe was performed by [Davis et al. \(1985\)](#). This established that the clustering of galaxies in the observable Universe can be reproduced with a (Λ) CDM cosmology. Since then these simulations have been improved in scale, resolution, numerical implementation of gravity and baryonic physics, and updated with more accurate values for cosmological parameters. A complete historical overview is beyond the scope of this work, instead, we will give a brief introduction to different kinds of simulations of the LSS and refer to [Dolag et al. \(2008a\)](#); [Somerville & Davé \(2015\)](#); [Naab & Ostriker \(2017\)](#); [Donnert et al. \(2018\)](#); [Vogelsberger et al. \(2020\)](#); [Angulo & Hahn \(2022\)](#) for reviews on LSS simulations.

Simulations of the LSS can be broadly separated into three categories: *idealized simulations*, *zoom-in* simulations, and *cosmological volumes/boxes*. Since we will use all three of these in this work in that order through Chapters 13-16 we will give a brief introduction here.

Idealized Simulations

This class takes objects from the LSS, represents them via a simplified model (e.g. a radial DM and gas density profile), and performs an idealized experiment where most of the parameters can be controlled.

For this work, the relevant example of this is a simulation of a merger between GCs, where velocity and impact parameters are fixed to study the development of merger shocks. Prominent examples of these simulations were performed by [Roettiger et al. \(1999\)](#); [Springel & Farrar \(2007\)](#); [van Weeren et al. \(2010, 2011b\)](#); [ZuHone et al. \(2010, 2013\)](#); [Walker et al. \(2017\)](#); [Donnert \(2014\)](#);

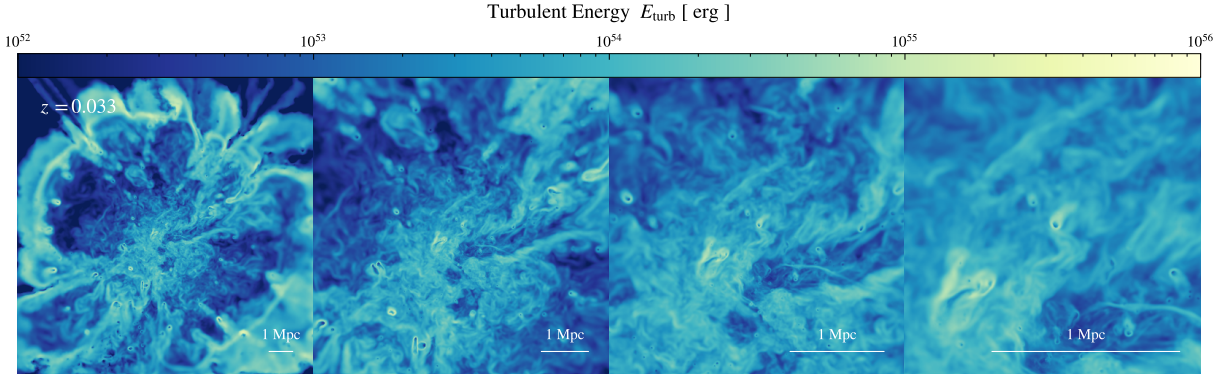


Figure 4.1: Example of the dynamic range achievable in modern zoom-in simulations. Each panel shows a zoom-in by a factor of two on the turbulent energy structure of the $M \approx 2 \times 10^{15} M_{\odot}$ galaxy cluster used in [Steinwandel et al. \(2023a\)](#); [Böss et al. \(2023b\)](#).

[Donnert et al. \(2017\)](#); [Lee et al. \(2020, 2022\)](#); [Biffi et al. \(2022\)](#) to study shocks, cold-fronts, velocity structures and turbulence in clusters, as well as turbulence scenarios for RHs. We refer to [ZuHone & Su \(2022\)](#) for a more detailed overview of this class of simulations.

Zoom-In Simulations

In zoom-in simulations, an object of interest, such as a galaxy cluster or galaxy, is identified in a cosmological volume simulation at the target redshift. This object is then extracted from the initial condition of the cosmological volume, up-sampled in resolution in the central region, and padded with lower-resolution DM particles to retain the long-range gravitational forces (see e.g. Appendix A in [Bonafede et al., 2011](#), for an example of how this is done).

This allows to reach resolutions for the central regions of the object of interest that could not be reached in a full cosmological volume, while still obtaining a realistic system at the end of the simulation.

Here examples of galaxy cluster simulations were performed by [Dolag et al. \(1999\)](#); [Bonafede et al. \(2011\)](#); [Ha et al. \(2023\)](#); [Nelson et al. \(2023\)](#); [Steinwandel et al. \(2023a\)](#) to study magnetic fields, turbulence, and CRs in a cosmological context. See Fig. 4.1 for a visualization of the dynamic range in resolution that is possible with state-of-the-art zoom-in simulations.

Cosmological Volumes

Simulations of cosmological volumes are set up by defining a grid of particles/cells at a given starting redshift and perturbed from the grid positions to satisfy the matter power spectrum obtained from a given cosmology (e.g. [Planck Collaboration et al., 2020b](#)). Depending on the size of the simulated volume varying numbers of modes of the power spectrum can be represented in the box, leading to the formation of larger structures in larger simulated volumes. These volumes (also referred to as *boxes*) are then evolved in time under periodic boundary conditions.

Their benefit is that they provide a statistical sample of galaxies and GCs at the cost of significant

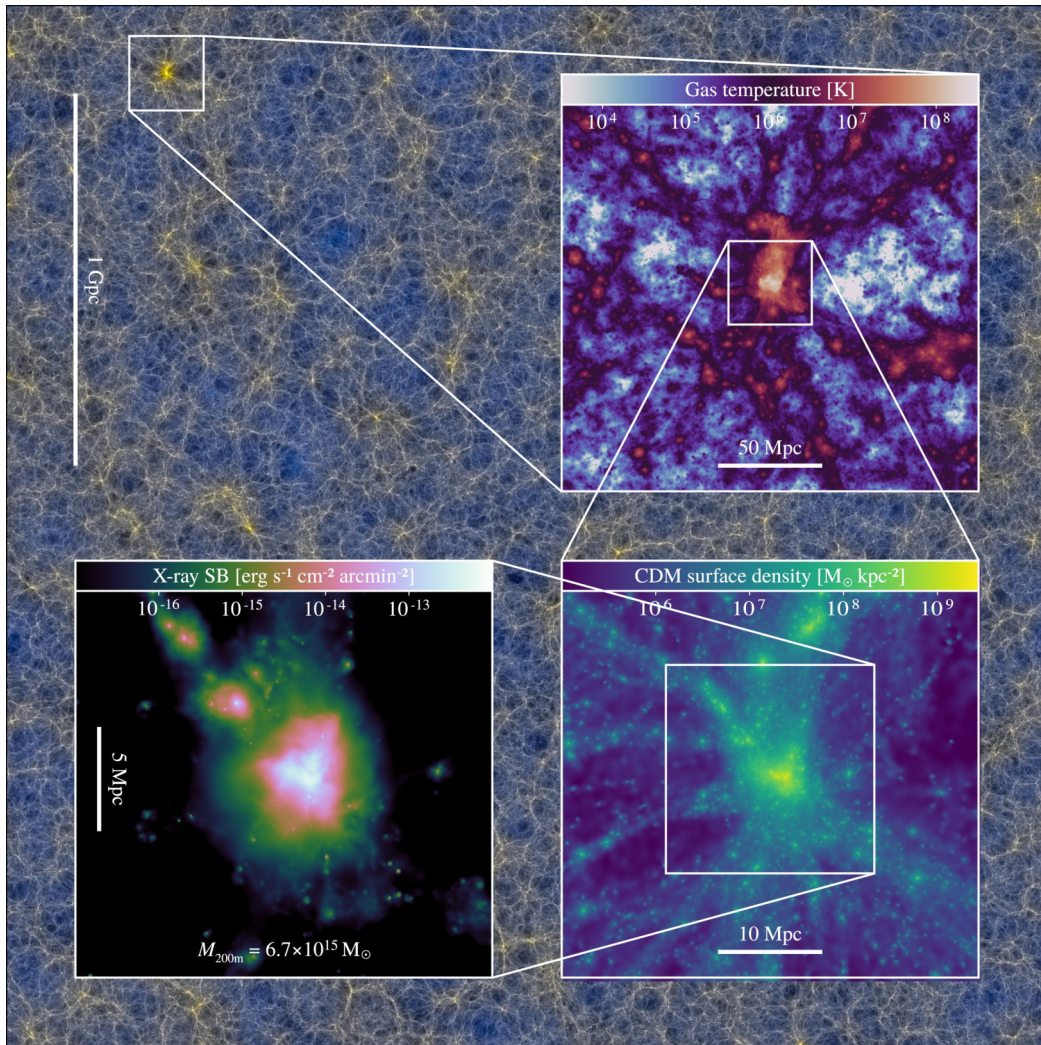


Figure 4.2: Example of the sample size and dynamic range in the largest volume of the FLAMINGO simulation set. Adopted from [Schaye et al. \(2023\)](#).

computational expense and lower resolution per object, compared to idealized or zoomed-on simulations.

Here prominent cases were presented by [Navarro et al. \(1997\)](#); [Springel et al. \(2005\)](#); [Vogelsberger et al. \(2014\)](#); [Miniati \(2014\)](#); [Dolag et al. \(2016\)](#); [Springel et al. \(2018\)](#); [Pillepich et al. \(2018\)](#); [Schaye et al. \(2023\)](#); [Dolag et al. \(2023b\)](#) to study the formation of galaxies and galaxy clusters under various aspects.

4.2 Including Magnetic Fields

The inclusion of magnetic fields in simulations of cosmological structure formation is a necessary step towards simulations that include CRs. We will list a number of relevant works that lead

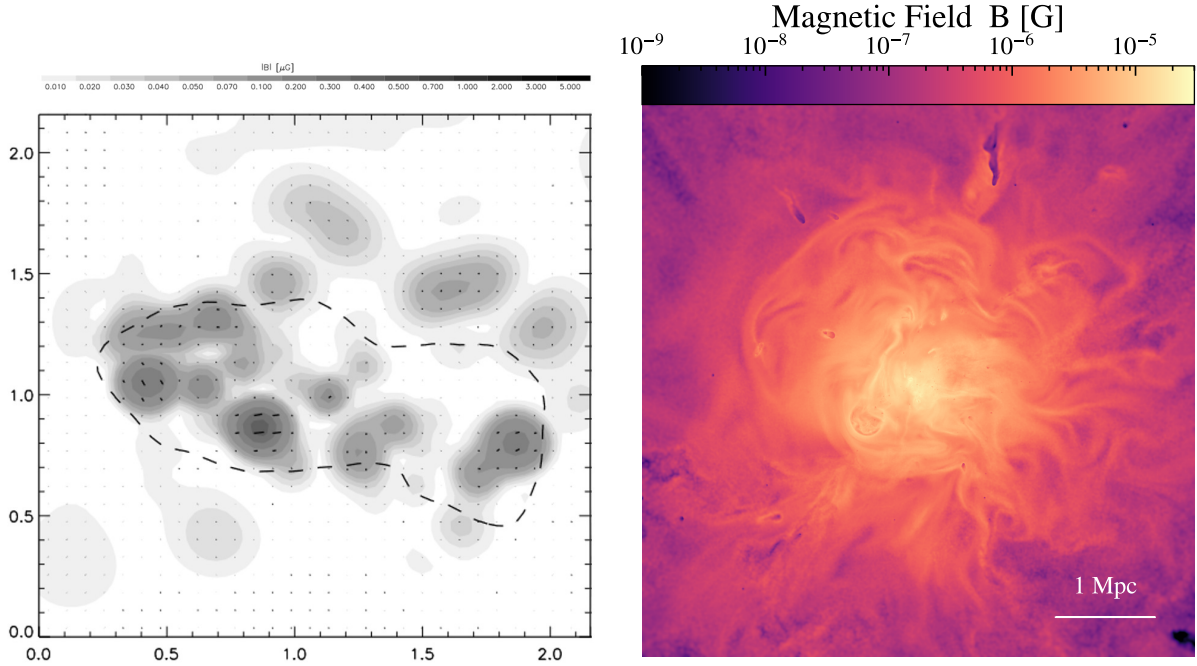


Figure 4.3: Slices through the magnetic field in the cluster center. *Left*: Simulation by Dolag et al. (1999). *Right*: Simulation by Steinwandel et al. (2023a).

the way towards CR-MHD simulations and refer to Donnert et al. (2018) for a more complete historical overview.

The first full 3D MHD simulations of magnetic fields in galaxy clusters were performed by Roettiger et al. (1999); Dolag et al. (1999, 2001). This pioneering work led to improved understanding of RHs (Dolag & Enßlin, 2000; Donnert et al., 2010a,b; Bonafede et al., 2011; Marinacci et al., 2018), deflection of ultra-high energy CRs (Dolag et al., 2005a) and fast radio bursts (Dolag et al., 2015).

A number of studies were performed to test amplification of seed fields of varying strengths to the $\sim \mu\text{G}$ magnetic fields observed in clusters (Bonafede et al., 2013; Vazza et al., 2014, 2018; Domínguez-Fernández et al., 2019; Steinwandel et al., 2022) and found general agreement that a turbulent dynamo can efficiently amplify the magnetic field within GCs to realistic values, while the dominant mechanism that impacts magnetic fields in filaments and voids is adiabatic compression/expansion. Further work was performed to study magnetic field seeding by SNe (Donnert et al., 2009; Beck et al., 2013; Marinacci et al., 2015; Vazza et al., 2021b) or AGN (Xu et al., 2008, 2011) who similarly found that turbulent motions can amplify astrophysical seed fields to realistic values.

The inclusion of magnetic fields allowed to obtain a better understanding of thermal conduction (e.g. Arth et al., 2014) and viscosity (e.g. ZuHone et al., 2015) in galaxy clusters. To the best of our knowledge, the highest resolution MHD simulation of a galaxy cluster to date are the ones presented in Steinwandel et al. (2023a); Böss et al. (2023b), which reach maximum spatial resolutions of $\Delta x_{\min} \approx 1 \text{ kpc}$. This allows for an unprecedented insight into the complex structure

of ICM magnetic fields. To visualize this immense progress we show a comparison between Dolag et al. (1999) and Steinwandel et al. (2023a) in Fig. 4.3.

4.3 Including Cosmic Rays

Simulations of LSS lack the resolution to simulate CR physics from first principles, like PIC and hybrid models do. However, a number of groups bridged this gap by implementing so-called sub-grid models to include CR physics into simulations of galaxy- or structure formation.

For galaxy formation these simulations typically couple CRs to the star formation model and with that SN rate, as SNe are expected to be the sources that feed enough CRs into the ISM to reach energy equipartition between magnetic-, turbulent-kinetic- and CR-pressure (Beck, 2015).

For GC simulations, CR injection at supersonic shocks can be implemented by adopting mach number dependent efficiency models obtained in thermal leakage models, PIC or hybrid simulations (e.g. Kang & Jones, 2007; Kang & Ryu, 2013; Caprioli & Spitkovsky, 2014; Ryu et al., 2019; Kang, 2020).

Bridging the gap between PIC and large scale MHD simulations will be one of the challenges of the upcoming simulation sets including CR physics in galaxy clusters (for simulations of intermediate scales see e.g. Vaidya et al., 2018; Dominguez-Fernandez et al., 2021; Domínguez-Fernández et al., 2021).

Large-scale simulations that study CRs can broadly be separated into three categories.

Post-Processing

The first is pure post-processing of dynamically decoupled CRs.

These CRs can be modeled as a single energy budget following a strict power-law distribution in energy and have been used to study galaxy cluster radio haloes and intra-cluster shocks (e.g. Ensslin et al., 1998; Dolag & Enßlin, 2000; Kang & Jones, 2007; Hoeft & Brüggén, 2007; Hoeft et al., 2008; Hong et al., 2014a,b; Wittor et al., 2017; Banfi et al., 2020; Ha et al., 2020; Lee et al., 2023). In these simulations either a shock-finder is employed to detect merger and accretion shocks in the simulation (e.g. Kang & Jones, 2007; Hoeft et al., 2008; Vazza et al., 2019; Banfi et al., 2020; Ha et al., 2020), or a CR population is imposed based on some model for thermal to non-thermal energy density (Ensslin et al., 1998; Dolag & Enßlin, 2000; Pinzke & Pfrommer, 2010; Pinzke et al., 2011). Then observables from CRs are “painted on” in post-processing to study radio relics, radio halos and diffuse γ -ray emission from clusters. We show an application of this to simulations of radio emission from cosmic web filaments in Fig. 4.4, which is adopted from Vazza et al. (2019).

As processes such as energy losses of CRs are energy dependent, a simple power-law approach can limit the descriptive capability of these models. To this end Jones et al. (1999) extended the treatment of CR electrons in their work to represent a population of particles distributed in momentum space following a piece-wise power-law. Miniati (2001); Miniati et al. (2001)

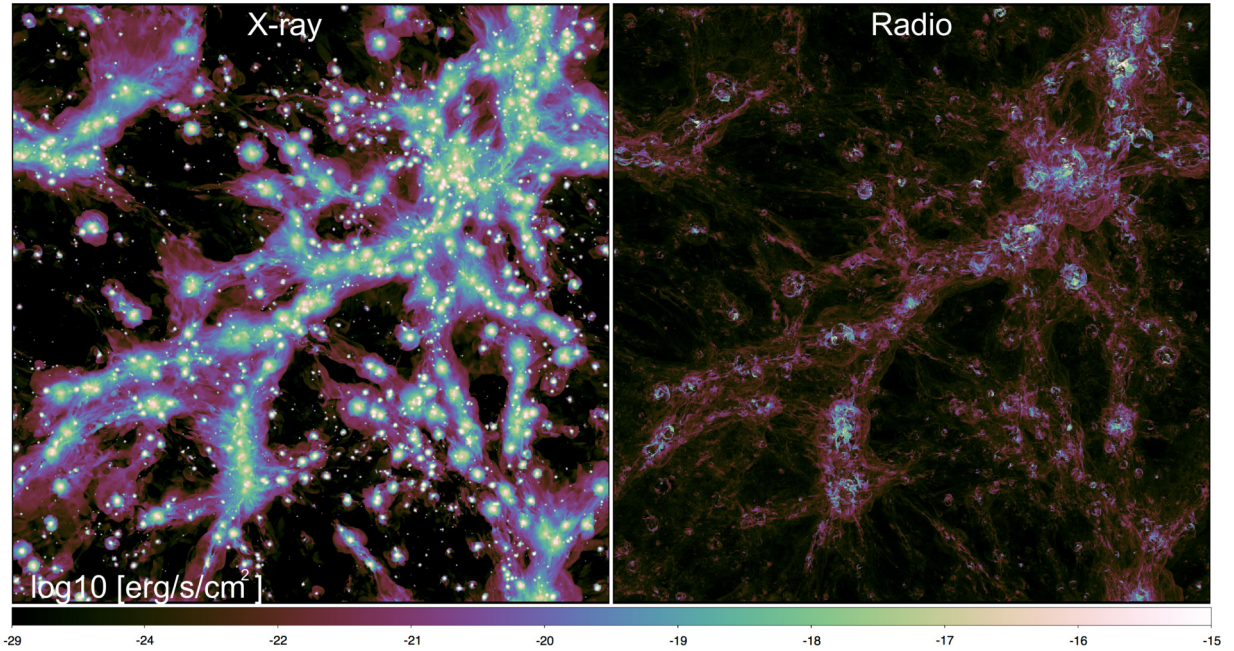


Figure 4.4: Mock observations of X-ray surface brightness and synchrotron flux of the cosmic web. Adopted from [Vazza et al. \(2019\)](#).

extended this further to a spectral model for both protons and electrons. [Jones & Kang \(2005\)](#) further improved upon this, including CR propagation in a method they labeled "Coarse-Grained Momentum finite Volume" (CGMV). The distribution function of these CRs can then be evolved in time using a Fokker-Planck solver ([Pinzke et al., 2013, 2017](#); [Donnert & Brunetti, 2014](#); [Wittor et al., 2017](#); [Winner et al., 2019, 2020](#); [Vazza et al., 2021b](#)) to obtain more realistic spectra and with that improved predictions for synchrotron emission. In grid-based codes, these models typically introduce lagrangian tracer particles in a sub-volume of the simulation, which store properties like shock strength, density changes, and magnetic field of the cells they encounter.

These post-processing approaches are however limited in information by the number of output snapshots and interpolations between those outputs, or the number of tracer particles in the simulation.

Gray Models

The second category is an on-the-fly implementation of CRs. This requires a large surrounding code infrastructure with descriptions for shock finding, star formation, or AGN as CR sources, as well as an accurate treatment of turbulence and magnetic fields. For these reasons, it has been a significant computational challenge.

To reduce the computational cost of the CR component itself it has mainly been treated as an additional energy budget coupled to the hydrodynamical equations as an ideal, relativistic gas.

This approach is also referred to as *one bin approach* or *gray model* (e.g. [Girichidis et al., 2016](#))

and has been used to model the impact of CRs on galaxy formation (e.g. [Hanasz & Lesch, 2003](#); [Jubelgas et al., 2008](#); [Girichidis et al., 2016](#); [Pfrommer et al., 2017](#); [Ruszkowski et al., 2017b](#); [Butsky & Quinn, 2018](#); [Butsky et al., 2020](#); [Kim et al., 2020](#); [Semenov et al., 2021](#); [Chan et al., 2019, 2021](#); [Weber et al., 2022](#)), AGN jets (e.g. [Sijacki et al., 2008](#); [Guo & Mathews, 2011](#); [Ruszkowski et al., 2017a](#)) and structure formation (e.g. [Enßlin et al., 2007](#); [Pfrommer et al., 2007, 2008, 2017](#); [Vazza et al., 2012, 2016](#)).

Spectral Models

Finally, the most elaborate, but also most computationally costly, way of adding CR physics to simulations is to again represent spectra of CRs and evolve them on the fly in the simulation.

This allows to more accurately model fast radiative loss processes of electrons as well as adiabatic changes, injection, and propagation, as they are not limited by the time resolution of the outputs. More recently [Yang & Ruszkowski \(2017\)](#); [Girichidis et al. \(2020\)](#); [Ogrodnik et al. \(2021\)](#); [Hopkins et al. \(2022a\)](#) revisited spectral CR models for novel implementations in current state-of-the-art cosmological MHD codes used in simulations of galaxy formation.

This allowed them to study Fermi-Bubbles ([Yang et al., 2018, 2022](#)), galactic outflows ([Girichidis et al., 2022, 2023](#)) and synchrotron spectra from galaxies ([Ponnada et al., 2023](#)) at unprecedented fidelity.

4.4 The Relevance of this Cosmic Ray Model

To the best of our knowledge, there are currently four independent groups with an implementation for an on-the-fly spectral CR model in a simulation code capable of running CR-MHD simulations of galaxy- and structure formation.

Two of these groups treat only electrons ([Yang & Ruszkowski, 2017](#); [Ogrodnik et al., 2021](#)), one group only protons ([Girichidis et al., 2020](#)) and only [Hopkins et al. \(2022a\)](#) accounts for more than one CR species.

All groups use their models only in the context of galaxy formation.

The spectral CR model in this work is the first one tailored towards CR physics in massive Galaxy Clusters (GCs), while accounting for Cosmic Ray protons (CRps) *and* Cosmic Ray electrons (CRes). We model CR injection at structure formation shocks, adiabatic changes, and high-energy losses of CRes, to study Radio Relics (RRs). Adding re-acceleration of CRs via turbulence allows us to study Radio Halos (RHs) and extended emission in cosmic web filaments. The feedback of the CR component on the thermal gas allows us to study the potential impact of CRps on structure formation. Finally, we can directly obtain observables such as synchrotron- and γ -ray emission from the evolved CR spectra, allowing us to reproduce key observables such as spectral steepening in RR and make predictions for the detectability of γ -rays in GCs.

Part II

CRESCENDO

5 | A Spectral Cosmic Ray Model for Cosmological Simulations

Our aim is to study the impact of CR protons on structure formation processes and obtain observables from CR electrons and protons. As the mass of typical resolution elements in cosmological simulations is 60-70 orders of magnitude above individual proton and electron masses and the typical size of a resolution element is 30 orders of magnitude above characteristic length-scales in CR physics, we need to implement a *sub-grid model* to treat whole populations of these particle species.

We dubbed this model **CRESCENDO**: *Cosmic Ray Evolution with SpeCtral Electrons aND prOtons* and introduced it in [Böss et al. \(2023c\)](#). In this part, we will repeat the implementation steps and their tests, and introduce some not yet published components.

5.1 The Diffusion-Advection Equation

In principle CRs are distributed in phase-space according to their momentum \mathbf{p} and their position \mathbf{x} at time t in the distribution function $F(\mathbf{p}, \mathbf{x}, t)$. This makes describing the distribution function a 7-dimensional problem. As mentioned previously the scale of the plasma physics relevant in the evolution of CRs is significantly below the resolution limits of cosmological simulations. This holds especially for the momentum vector \mathbf{p} of the CRs.

Assuming a *sufficiently stochastic* ([Drury, 1983](#)) scattering process, e.g. the scattering and self-confinement by Alfvén waves triggered by the CR streaming instability (e.g. [Kulsrud & Pearce, 1969](#); [Wentzel, 1974](#); [Skillington, 1975a,b,c](#)), we can infer that the particle movement is random on small scales and treat the distribution of the CRs as isotropic in momentum space and drop the vector description of the momentum.

This simplifies the phase-space from $F(\mathbf{p}, \mathbf{x}, t)$, to only depend on absolute momenta

$$F(\mathbf{p}, \mathbf{x}, t) \rightarrow 4\pi p^2 f(p, \mathbf{x}, t) \tag{5.1}$$

The time evolution of this distribution function can then be described by the diffusion-advection equation (see e.g. [Skilling, 1975a](#); [Drury, 1983](#); [Schlickeiser, 2002](#), for a derivation)

$$\frac{Df(p, \mathbf{x}, t)}{Dt} = \nabla \cdot (\kappa(p) \nabla f(p, \mathbf{x}, t)) \quad (5.2)$$

$$+ \left(\frac{1}{3} \nabla \cdot \mathbf{u} \right) p \frac{\partial f(p, \mathbf{x}, t)}{\partial p} \quad (5.3)$$

$$+ \frac{1}{p^2} \frac{\partial}{\partial p} \left(p^2 \left[\sum_l b_l f(p, \mathbf{x}, t) + D_{pp} \frac{\partial f(p, \mathbf{x}, t)}{\partial p} \right] \right) \quad (5.4)$$

$$- \frac{f(p, \mathbf{x}, t)}{t_c(p)} \quad (5.5)$$

$$+ j(\mathbf{x}, p, t), \quad (5.6)$$

where the individual terms describe; Advection (l.h.s. side of Eq. 5.2), which we express in Lagrangian form by using: $\frac{Df}{Dt} = \frac{\partial f}{\partial t} + \mathbf{u} \cdot \nabla f$, spatial diffusion (r.h.s of Eq. 5.2), adiabatic compression/expansion of the surrounding gas (Eq. 5.3), energy losses (first term of Eq. 5.4) where we used

$$\sum_l b_l \equiv \left| \frac{dp}{dt} \right|_c + \left| \frac{dp}{dt} \right|_{\text{rad}} \quad (5.7)$$

for energy losses due to coulomb interaction and radiative losses, respectively. Diffusion in momentum space, or Fermi-II re-acceleration is described by the second term of Eq. 5.4. Catastrophic losses are given via Eq. 5.5 and sources of CRs are described by Eq. 5.6.

5.2 Spectral Parameters

In order to evolve Eq. 5.2 in time, we need to choose a numerical discretization. Similar to [Yang & Ruszkowski \(2017\)](#); [Girichidis et al. \(2020\)](#); [Ogrodnik et al. \(2021\)](#) we follow the approach by [Miniati \(2001\)](#) and parameterize the spectrum with four parameters: For a momentum bin p_i we follow the spectral norm f_i , spectral slope q_i , CR number N_i and CR energy E_i .

Since observations (e.g. [Abdo et al., 2009](#); [Aguilar et al., 2013](#)) show the CR spectrum as a (broken) power-law in energy or momentum over many orders of magnitude, a logical choice is to discretize the initial spectrum as a power-law in momentum space, split up in i momentum bins of equal size. This way the spectrum takes the functional form

$$f(p) = f_i \left(\frac{p}{p_i} \right)^{-q_i} \quad (5.8)$$

where f_i and q_i are the norm and slope of the spectrum at momentum p_i .

Compared to a piece-wise constant discretization this piece-wise power-law approach has the additional advantage of spanning the high dynamical range with fewer momentum bins and thus saving on memory while maintaining a better representation of the spectral shape.

Once this discretization has been set we can obtain the number of CRs per bin by performing a simple volume-integral in momentum space in shells where the width corresponds to the bin-widths.

$$N_i = \frac{1}{\rho} \int_{p_i}^{p_{i+1}} dp 4\pi p^2 f(p) = \frac{4\pi f_i p_i^3}{\rho} \frac{\left(\left(\frac{p_{i+1}}{p_i}\right)^{3-q_i} - 1\right)}{3-q_i} \quad (5.9)$$

The energy contained in each bin can be obtained by assuming that every CR particle carries the kinetic energy

$$T(p) = \sqrt{p^2 c^2 + m_i^2 c^4} - m_i c^2 \approx pc \quad (5.10)$$

where we used that the CRs we are interested in are relativistic and m_i represents the rest mass of the individual particle species. Including this in our volume integral gives

$$E_i = \frac{1}{\rho} \int_{p_i}^{p_{i+1}} dp 4\pi T(p) p^2 f(p) \approx \frac{1}{\rho} \int_{p_i}^{p_{i+1}} dp 4\pi c p^3 f(p) \quad (5.11)$$

$$= \frac{4\pi c f_i p_i^4}{\rho} \frac{\left(\left(\frac{p_{i+1}}{p_i}\right)^{4-q_i} - 1\right)}{4-q_i} \quad (5.12)$$

Both these equations contain a $\frac{1}{\rho}$ term due to the Lagrangian reference frame in which we discretize the equations, which represent these quantities per unit mass.

To avoid a division by 0 for $q_i = 3$ and $q_i = 4$ we introduce a slope softening parameter $\epsilon = 10^{-6}$ and interpolate, as an example for N_i

$$N_i = \frac{4\pi f_i p_i^3}{\rho} \left(\frac{q_i - 3}{\epsilon} + \log\left(\frac{p_{i+1}}{p_i}\right) \left(1 - \frac{q_i - 3}{\epsilon}\right) \right). \quad (5.13)$$

To simplify and unify the descriptions for CR electrons and protons we choose to represent the momentum in dimensionless units, meaning $\hat{p} \equiv \frac{p}{m_i c}$.

Evolving both CR number and energy is commonly referred to as a *two-moment approach* (see e.g. [Hanasz et al., 2021](#), for a review on different approaches). We use this two-moment approach for both electrons and protons. For electrons, this is required to accurately capture rapid cooling processes. For protons the second moment is often neglected based on the assumption of a quasi-stationary spectrum or a spectrum of constant curvature ([Miniati, 2001](#)). However, this can lead to numerical instabilities if energy is injected only into one part of the spectrum (see [Girichidis et al., 2020](#), for a detailed discussion of this problem).

5.3 Time Evolution

We evolve Eq. 5.2 in time by use of operator splitting. For this, we treat the individual terms as independent where necessary and combined where possible. We will give a brief derivation of this process in the following sections.

5.3.1 Particle Number and Energy Changes

The key point of evolving the distribution function is to trace the changes in number- and energy density as a function of time. For simplicity we follow the approach by [Miniati \(2001\)](#) and show this for adiabatic changes and radiative losses.

The part of Eq. 5.2 governing those effects is

$$\frac{Df}{Dt} = \frac{1}{3} \frac{\partial u}{\partial x} p \frac{\partial f}{\partial p} + \frac{1}{p^2} \frac{\partial}{\partial p} (p^2 b_l f) . \quad (5.14)$$

By multiplying both sides of Eq. 5.14 with $4\pi p^2/\rho$ to be able to associate the l.h.s. with Eq. 5.9 and integrating both sides over the bin with index i yields:

$$\frac{DN_i}{Dt} = \frac{1}{\rho} \left\{ \left(\frac{1}{3} \frac{\partial u}{\partial x} p + b_l(p) \right) 4\pi p^2 f(p) \right\}_{p_i}^{p_{i+1}} . \quad (5.15)$$

As proposed by [Miniati \(2001\)](#) we can integrate this in time and can identify the r.h.s. as the time-averaged fluxes over the momentum boundaries. This gives a number density of bin i after a timestep Δt

$$N_i^{t+\Delta t} = N_i^t + \frac{1}{\bar{\rho}} \left(F_{N_{i+1}}^m - F_{N_i}^m \right) \quad (5.16)$$

where $F_{N_{i+1}}^m$ and $F_{N_i}^m$ are the CR number fluxes into and out of the bin respectively and $\bar{\rho}$ denotes the mean density over the timestep.

Similarly, to obtain the energy after a timestep we multiply Eq. 5.14 with $4\pi c p^3/\rho$ to be able to associate the l.h.s. with Eq. 5.12 and perform the same integral as before. This gives

$$\frac{DE_i}{Dt} = \frac{1}{\rho} \left\{ \left(\frac{1}{3} \frac{\partial u}{\partial x} p + b_l(p) \right) 4\pi c p^3 f(p) \right\}_{p_i}^{p_{i+1}} \quad (5.17)$$

$$- \left(\frac{4}{3} \frac{\partial u}{\partial x} E_i + \frac{1}{\rho} \int_{p_i}^{p_{i+1}} dp b_l(p) 4\pi c p^2 f(p) \right) . \quad (5.18)$$

To simplify this equation we can introduce the quantity $R_i(q_i, p_i)$ for the energy loss integral per bin

$$R_i(q_i, p_i) = \frac{4 - q_i}{p_{i+1}^{4-q_i} - p_i^{4-q_i}} \int_{p_i}^{p_{i+1}} dp p^{2-q_i} \left(\frac{1}{3} \frac{\partial u}{\partial x} + \sum_l^{N_{\text{losses}}} b_l(p) \right) . \quad (5.19)$$

Here again $\frac{1}{3} \frac{\partial u}{\partial x}$ denotes the adiabatic changes and $\sum_l^{N_{\text{losses}}} b_l(p)$ the individual energy loss processes. In most cases, these factors cannot be solved in one step, but need to be split up into individual processes. As in [Miniati \(2001\)](#) we can express the energy in a bin after the timestep Δt as

$$E_i^{t+\Delta t} \left(1 + \frac{\Delta t}{2} R_i(q_i, p_i) \right) = E_i^t \left(1 - \frac{\Delta t}{2} R_i(q_i, p_i) \right) + \frac{1}{\bar{\rho}} \left(F_{E_{i+1}}^m - F_{E_i}^m \right) \quad (5.20)$$

with $\bar{\rho}$ being the mean density over the timestep, $F_{E_{i+1}}^m$ the energy flux into the bin and $F_{E_i}^m$ the energy flux out of the bin.

5.3.2 Fluxes Between Momentum Bins

We can now identify the first term of the integral by parts as the time-averaged fluxes over one bin boundary as

$$F_{N_i}^m = \int_t^{t+\Delta t} dt' b_l(p) 4\pi p^2 f(t', p)|_{p_i} \quad (5.21)$$

$$F_{E_i}^m = \int_t^{t+\Delta t} dt' b_l(p) 4\pi c p^3 f(t', p)|_{p_i} \quad (5.22)$$

This is a consequence of our fixed momentum boundaries. A particle of momentum p_u gains, or loses momentum over a timestep Δt and arrives at momentum p_i . Since we use fixed momentum boundaries we cannot move those boundaries to account for this change and instead need to calculate a flux over the boundary into a higher, or lower bin (for an alternative lagrangian approach to bin boundaries see [Mimica et al., 2009](#)).

If we consider the definition of our momentum changes

$$\frac{dp}{dt} = b_l(p) \quad (5.23)$$

we can solve this for dt and substitute dt' in Eq. 5.22. This gives an equation for the fluxes only dependent on p

$$F_{N_i}^m = \int_{p_i}^{p_u} dp 4\pi p^2 f^m(p) \quad (5.24)$$

$$F_{E_i}^m = \int_{p_i}^{p_u} dp 4\pi c p^3 f^m(p), \quad (5.25)$$

with

$$f^m(p) = \begin{cases} f_i \left(\frac{p}{p_i}\right)^{-q_i} & \text{if } p_u > p_i \\ f_{i-1} \left(\frac{p}{p_{i-1}}\right)^{-q_{i-1}} & \text{if } p_u \leq p_i, \end{cases} \quad (5.26)$$

and p_u being the momentum a particle needs to have to yield the momentum p_i after a timestep Δt . To solve this integral we use the separation of variables in Eq. 5.23

$$\Delta t = \int_{p_i}^{p_u} \frac{dp}{b_l(p)}. \quad (5.27)$$

Identifying Δt as the timestep of our simulation and p_i as the momentum bin i we only need to calculate adiabatic changes and radiative losses, respectively to find p_u and with that the lower boundary of the flux integral.

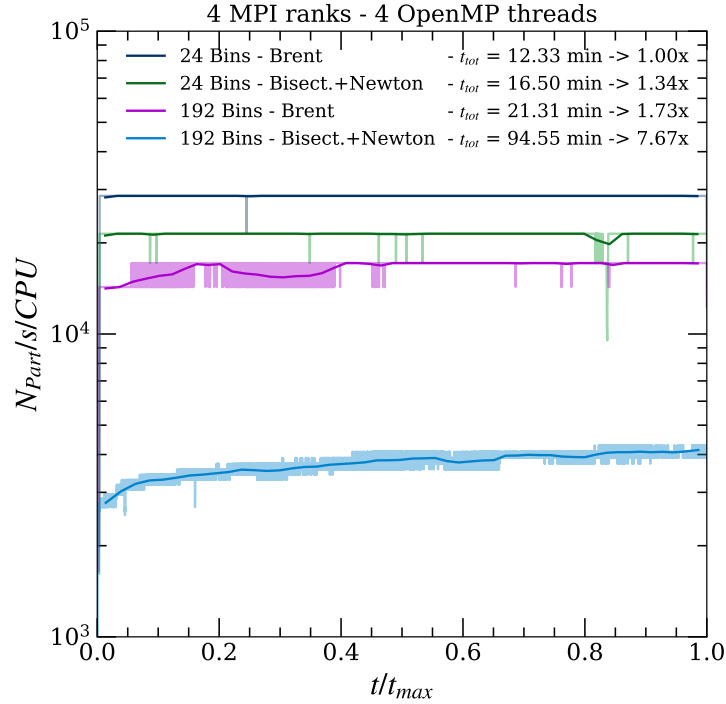


Figure 5.1: Performance comparison for a simple cooling test using either a Bisection+Newton method for root finding or the fiducial Brents' method.

5.3.3 Spectral Cut Update

As we will discuss in Sec. 5.4 we chose to keep the upper boundary of our distribution closed and allow no in- or outflux. This leads to a right shift of the cutoff momentum of the distribution in the case of energy gains and a left shift in the case of energy losses. The spectral cutoff needs to be updated at every step of the spectral evolution.

Similar to the fluxes the spectral cutoff can be updated by solving for the integration boundaries in Eq. 5.27. Here we assume that the cutoff is the momentum at which the most energetic particles arrive after a timestep Δt by setting $p_{cut} = p_u$ and solving Eq. 5.23 for p_i .

5.3.4 Slope Update

As a next step, we need to update the slope of each momentum bin. Solving Eqs. 5.9 and 5.12 for f_i gives an equation only dependent on E_i , N_i and q_i .

$$\frac{E_i}{N_i p_i c} = \frac{3 - q_i \left(\frac{p_{i+1}}{p_i} \right)^{4-q_i} - 1}{4 - q_i \left(\frac{p_{i+1}}{p_i} \right)^{3-q_i} - 1} \quad (5.28)$$

Having calculated E_i and N_i in the previous steps we can solve Eq. 5.28 for q_i with any suitable root-finding method. The root-finding is usually performed via the Newton-Rhapson method (e.g.

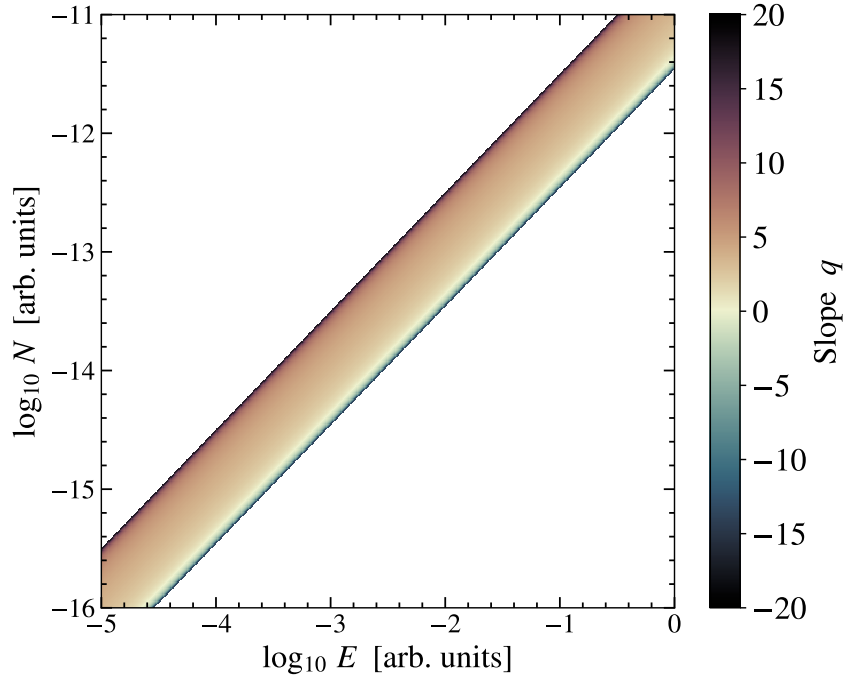


Figure 5.2: Allowed values for the slope q_i in a parameter space of N_i and E_i .

Miniati, 2001; Girichidis et al., 2020; Ogrodnik et al., 2021), which shows fast convergence, but requires an initial guess. This guess can either be provided in tabulated form as in Girichidis et al. (2020) and Ogrodnik et al. (2021) or has to be found in a preparation step e.g. by a bracketing method which can prove to be expensive.

In this work, we find faster convergence using Brent’s method at the same accuracy. As this is the most expensive computational step of the scheme we get a substantial performance boost from this choice. We show the performance impact in the right panel of Fig. 5.1.

To further reduce the cost of this step we introduce a finite search range for the root-finding with $q \in [-20, 20]$. As bins with a slope $|q| > 20$ will contribute very little to the overall number- and energy density we accept this artificial error for the benefit of reduced computational cost. Fig. 5.2 shows the band of convergence for these values of allowed q_i . We find that this band is considerably larger for positive than for negative values of q_i . This has implications for the numerical stability of low-momentum energy losses, which we will discuss briefly in Sec. 8.2.

5.3.5 Norm Update

With all other variables updated, we can update the normalization of the distribution function. This can in principle be done by solving either of Eq. 5.9 or 5.12 for f_i .

In practice, it is slightly cheaper to solve Eq. 5.9 so that the new normalization of bin i can be

computed from

$$f_i = \frac{\rho N_i}{4\pi p_i^3} \frac{3 - q_i}{\left(\frac{p_{i+1}}{p_i}\right)^{3-q_i} - 1} \quad (5.29)$$

Ideally, one could also solve both Eqs. and construct an interpolation scheme between the two to reduce errors. This could be tested for potential benefits in future work.

5.4 Boundary Conditions

To decouple the CR component from the non-relativistic gas we need to set the boundary conditions of our distribution function accordingly.

We choose \hat{p}_{\min} and \hat{p}_{\max} arbitrarily to best fit the requirements of the simulation and do not necessarily want to cover the full scale of relativistic energies. This allows us to save on memory and computational cost in cases where we are only interested in the high-energy range of the distribution function. Therefore, we have to handle the treatment of CRs that move out of this range.

For the presented work we choose open boundaries at the lower end of the distribution function and closed boundaries at the upper end. The physical motivation for this is that as CRs cool and loose energy they smoothly transition to the non-relativistic thermal background of particles. For our purposes, we assume a gap in the transition between the Maxwell-Boltzmann distribution of particles and the power-law high-energy tail. By doing so we can treat our implementation as a two-component fluid with distinct equations of state with a sharp jump between the two and thus work around the problem of an intermediate state.

The upper end of the distribution function is chosen to have a closed boundary. In order to achieve this we employ a movable upper boundary that also works as a cutoff of the distribution function p_{cut} . This parameter needs to be updated at *every* time step.

Here the physical motivation is that particles can be further accelerated beyond the arbitrarily chosen initial upper limit of the distribution function. Numerically we avoid an artificial pile-up of energy and particles in the last momentum bin. In the case of electrons, this treatment also leads to a more accurate description of the cooling spectrum. As electrons lose energy, the high-momentum end of the distribution function is depopulated. Since we cannot assume that over a time step of our simulation, a whole bin is depopulated, we need to be able to represent the distribution function with partially filled bins. To accomplish this we can employ the spectral cut and solve the number- and energy density integrals between the lower bin boundary and the cutoff within the bin.

5.5 Timestep Constraints

Similar to [Miniati \(2001\)](#); [Yang & Ruszkowski \(2017\)](#); [Ogrodnik et al. \(2021\)](#) we find that the common approach to limit the timestep within the solver so that one bin is not fully depleted within one timestep is not sufficient in the case of fast cooling electrons.

Like the previous authors, we therefore employ

$$\Delta t_{\max} \leq 0.1 \tau_{i,\text{cool}} \quad (5.30)$$

with $\tau_{i,\text{cool}}$ being the cooling time of each energy loss process.

To avoid computational overhead wherever possible we sub-cycle the solver and update the distribution function at the end of the simulation timestep.

6 | Sources

To inject CRs into our model we need three parameters: $E_{\text{inj}}^{\text{CR}}$ as the energy to be injected, p_{inj} as the momentum at which the injected power-law starts, and q_{inj} , the slope of this power-law. We can then insert these parameters into Eq. 5.12 and solve for the normalization of the distribution function at the injection momentum

$$f_{\text{inj}} = \frac{E_{\text{inj}}^{\text{CR}}(4 - q_{\text{inj}})}{\frac{4\pi c \hat{p}_{\text{inj}}^4}{\rho} \left(\left(\frac{\hat{p}_{\text{max}}}{\hat{p}_{\text{inj}}} \right)^{4 - q_{\text{inj}}} - 1 \right)} \quad (6.1)$$

where \hat{p}_{max} is the (arbitrarily chosen) upper boundary of the distribution function. This is typically $\hat{p}_{\text{max}} \sim 10^5 - 10^6$.

For strongly magnetized shocks this strict power-law injection is softened by an exponential cut-off for high momenta in the electron population. In weakly magnetized ICM shocks this can be neglected (see the discussion in Kang, 2020).

The other normalizations can then be interpolated from the power-law shape by using Eq. 5.8. With the normalization f_i and slope q_{inj} of every bin calculated we can inject CR number and energy per bin by solving Eq. 5.9 and Eq. 5.12 respectively. The spectral cutoff of the distribution is either reset to p_{max} if it was below that before the injection or kept as is if it was above p_{max} . To preserve the total energy we subtract the energy injected into the CR component by the shock from the entropy change of the gas component. Once the energy and CR number of every bin is updated we update the total distribution function by first solving the slope of the individual bins with Eq. 5.28 and then recalculating the normalization f_i using Eq. 5.29.

In this chapter, we will present how the injection parameters are obtained for our models of CR injection by DSA and SNe.

6.1 Shock Acceleration

To bridge the gap between the small-scale physics of DSA and large-scale shocks in the ICM we take the result from hybrid and PIC simulations and include them in a subgrid description. We quantify this as different models of acceleration efficiencies η that depend on the sonic mach number \mathcal{M}_s , the ratio between upstream thermal and CR pressure $X_{\text{CR}} \equiv \frac{P_{\text{CR,u}}}{P_{\text{th,u}}}$ and the angle

between magnetic field and shock normal θ_B .

Generally, the energy injected into a CR population behind a shock can be written as (e.g. Kang & Jones, 2007)

$$E_{CR,2} = \eta(\mathcal{M}_s, X_{cr}) \eta(\theta_B) E_{sh} \quad (6.2)$$

Here E_{sh} is the energy dissipated at the shock and the two efficiency functions $\eta(\mathcal{M}_s, X_{cr})$ and $\eta(\theta_B)$ describe which fraction of that shock energy is injected due to the strength of the shock $\eta(\mathcal{M}_s, X_{cr})$ and the geometry between magnetic field vector and shock normal $\eta(\theta_B)$.

We use two different methods to obtain the shock energy. One is via the on-the-fly shock finder

$$E_{sh} = \frac{1}{2} u_{sh}^3 \frac{\Delta t}{2h_i} \quad (6.3)$$

where u_{sh} is the shock speed obtained from the shock finder, Δt is the time step and h_i is the hydrodynamic smoothing length. This denotes the shock energy per timestep, normalized to conserve the total energy the shock dissipates as it runs through the region broadened by the Smoothed-Particle Hydrodynamics (SPH) kernel. This works well in idealized simulations such as shock tubes but is prone to numerical noise and limitations from the shock finder in resolution-limited cases. As the shock is numerically broadened and detected slightly in front of the actual shock front, the injection also happens in the pre-shock region. This in turn leads to a precursor wave of CR gas which can lead to a runaway effect for high CR injection efficiencies. This is often remedied by saving the shock energy and injecting it after a delay time into the post-shock region (e.g. Pfrommer et al., 2006, 2017; Dubois et al., 2019) which in turn reduces the temporal resolution of the injection mechanism.

As an alternative method, we compute the shock energy from the entropy change per timestep.

$$E_{sh} = \frac{\Delta S}{(\gamma - 1)\rho^{\gamma-1}} \Delta t \quad (6.4)$$

This has the advantage of being numerically self-consistent as it represents the actual energy dissipated as computed in the hydro solver, instead of the shock finder. The downside is again that the shock finder detects the shock slightly in front of the actual shock front, which leads to the injection process not capturing the whole shock time. For Mach number dependent acceleration efficiencies this has the additional disadvantage of only capturing the decaying flank of the broadened shock, which leads to an additional under-prediction of the acceleration efficiency. Nonetheless, both these effects can be countered by tuning on shock tubes, which makes the entropy injection method more stable than the shock speed injection method in our tests.

6.1.1 Mach Number Dependent Efficiency Models

For this work we implemented four different Mach number dependent efficiency models introduced by Kang & Jones (2007); Kang & Ryu (2013); Caprioli & Spitkovsky (2014) and Ryu et al. (2019) for physical systems and the constant injection efficiency used by Pfrommer et al. (2017) and Pais et al. (2018) for test problems. To the best of our knowledge only Kang & Jones (2007)

Table 6.1: From left to right we report the name, the ratio between thermal and CR pressure to use for the interpolation between acceleration and re-acceleration, the values for the parameters of Eq. 6.5 and the critical sonic Mach number from the different efficiency models.

Model	$X_{\text{cr},0}$	b_0	b_1	b_2	b_3	b_4	$\mathcal{M}_{\text{s,crit}}$
KR07	0	5.46	-9.78	4.17	-0.33	0.57	1
KR07r	0.3	0.24	-1.56	2.8	0.51	0.56	1
KR13	0	-2.87	9.67	-8.88	1.94	0.18	2
KR13r	0.05	-0.72	2.73	-3.29	1.34	0.19	2
Ryu19	0	-1.53	2.40	-1.25	0.22	0.03	2.25
Ryu19r	0.05	-0.72	2.73	-3.29	1.34	0.19	2.25

provide a fitting function to their data with

$$\eta(\mathcal{M}_s) = \begin{cases} 1.96 \cdot 10^{-3} (\mathcal{M}_s^2 - 1) & \text{for } \mathcal{M}_s \leq 2 \\ \sum_{n=0}^4 b_n \frac{(\mathcal{M}_s - 1)^n}{\mathcal{M}_s^4} & \text{for } \mathcal{M}_s > 2 \end{cases} \quad (6.5)$$

for initial acceleration and only the equation for $\mathcal{M}_s > 2$ for re-acceleration. We find that these equations also provide a good basis for fitting to the remaining Mach number dependent acceleration functions. Table 6.1 gives a reference for all the values of b_n used in our description of the different acceleration models¹, which we obtained from fitting their published data.

The model by [Kang & Ryu \(2013\)](#) for initial acceleration (KR13) can be well described with

$$\eta(\mathcal{M}_s) = \begin{cases} c + d\mathcal{M}_s^e & \text{for } 2 \leq \mathcal{M}_s \leq 5 \\ \sum_{n=0}^4 b_n \frac{(\mathcal{M}_s - 1)^n}{\mathcal{M}_s^4} & \text{for } 5 < \mathcal{M}_s \leq 15 \\ 0.211 & \text{for } \mathcal{M}_s > 15 \end{cases} \quad (6.6)$$

with $c = -5.95 \cdot 10^{-4}$, $d = 1.88 \cdot 10^{-5}$ and $e = 5.334$. We also introduced a saturation value of $\eta_{\text{max}} = 0.211$ for $\mathcal{M}_s > 15$. Their re-acceleration model (KR13r) is well fit by the $\mathcal{M}_s > 2$ form of Eq. 6.5 with the parameters given in Tab. 6.1. Both these models assume that only shocks with $\mathcal{M}_s > 2$ can efficiently accelerate particles.

We do not explicitly list the values of [Caprioli & Spitkovsky \(2014\)](#) (CS14), as we take the same approach as [Vazza et al. \(2016\)](#) and assume that the efficiency is half that of KR13 and KR13r. [Ryu et al. \(2019\)](#) performed their study only for sonic Mach numbers relevant for intra-cluster shocks in the range of $2.25 \leq \mathcal{M}_s \leq 5$ where only supercritical shocks can accelerate CRs (motivated by the findings of [Ha et al., 2018b](#)). To be able to account for higher Mach number shocks we interpolate their data up to higher Mach numbers assuming a similar functional form as the re-acceleration model KR13r with a maximum efficiency of $\eta_{\text{max}} = 0.035$. We find that both initial acceleration (Ryu19) and re-acceleration (Ryu19r) are well described by using the

¹We also provide a public version of the DSA models at <https://github.com/LudwigBoess/DiffusiveShockAccelerationModels.jl>

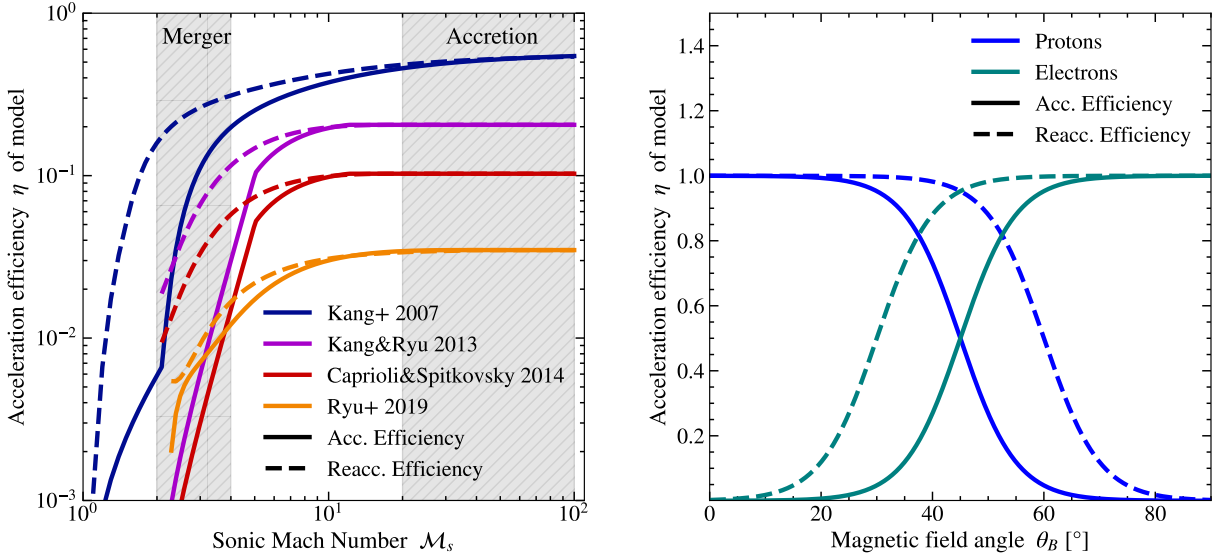


Figure 6.1: *Left*: Mach number dependent efficiency models present in our model. The x-axis shows the Mach number and the y-axis the fraction of shock energy that is being injected into the CR component. Solid lines indicate initial acceleration, dashed lines indicate re-acceleration. Gray areas mark Mach number ranges for typical merger shocks and expected accretion shocks. *Right*: Magnetic field angle dependent acceleration efficiency model for protons and electrons. Again solid lines indicate initial and dashed lines re-acceleration.

values for b_n listed in Tab. 6.1 and show the efficiency models in the left panel of Fig. 6.1. We interpolate between acceleration and re-acceleration models based on the CR to thermal pressure ratio present in the SPH particle. As a basis for this, we use the seeded CR population of the underlying models $X_{\text{cr},0}$ (given in Tab. 6.1) and interpolate linearly between the two models according to X_{cr} contained in the particle.

6.1.2 Magnetic Field Geometry Dependent Efficiency Models

As noted above, the magnetic field morphology at the shock plays a vital role in the triggering of instabilities and with that the acceleration efficiency. Unfortunately, these instabilities are significantly below the resolution limits of current large-scale MHD simulations. Most recent work treats these processes as sub-grid models and use a statistical approach to give an additional efficiency parameter (e.g. [Vazza et al., 2016](#)), or just allow CR injection in a specific angle range and switch acceleration on and off (e.g [Banfi et al., 2020](#)).

In this work, we take the same approach as [Pais et al. \(2018\)](#); [Dubois et al. \(2019\)](#) and introduce an additional factor $\eta(\theta_B)$ in our total acceleration efficiency. This parameter was obtained by [Pais et al. \(2018\)](#), who use the values by [Caprioli & Spitkovsky \(2014\)](#) to fit a functional form to their data as

$$\eta(\theta_B) \approx \frac{1}{2} \left[\tanh \left(\frac{\theta_{\text{crit}} - \theta_B}{\delta} \right) + 1 \right] \quad (6.7)$$

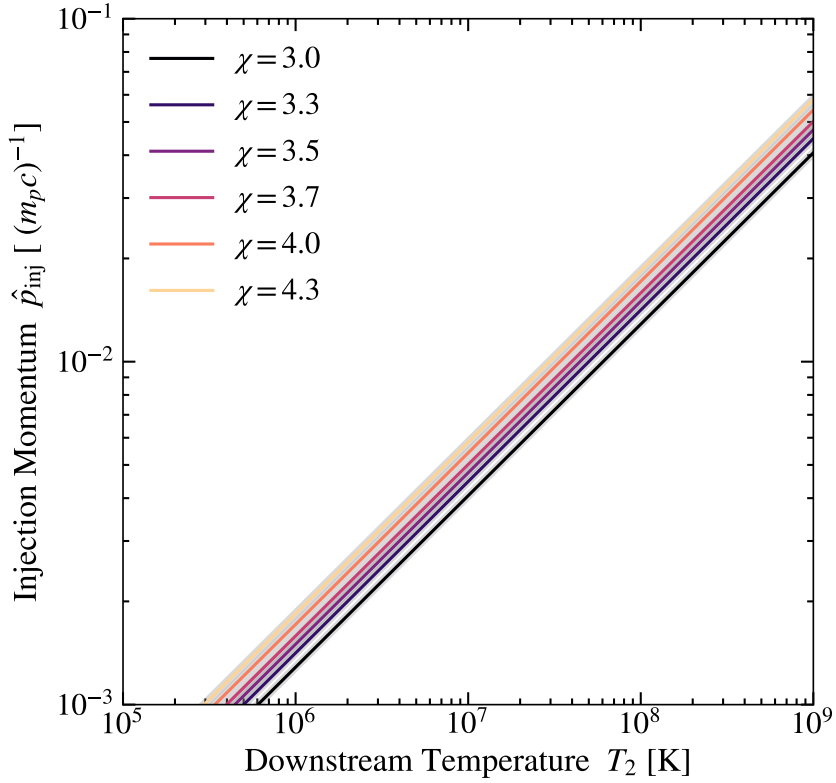


Figure 6.2: Injection momentum as defined in Eq. 6.8 as a function of downstream temperature for different values of χ .

with $\delta = \pi/18$ and $\theta_{\text{crit}} = (\pi/4; \pi/3)$. $\theta_{\text{crit}} = \pi/4$ corresponds to a shock without and $\theta_{\text{crit}} = \pi/3$ to a shock with pre-existing CR component (from Caprioli & Spitkovsky, 2014; Caprioli et al., 2018, respectively). These efficiencies were modeled for ions, for which DSA should be most effective at quasi-parallel shocks. For electrons, quasi-perpendicular shocks should be the main driver of acceleration, as outlined above. We therefore take the simple approach of shifting the efficiency model by 90° for electrons for the purpose of this work.

The efficiency model is shown in the right panel of Fig. 6.1.

6.1.3 Injection Momentum

Since we arbitrarily set our lower momentum boundary we need to pay attention to the connection between thermal and non-thermal components. With a fixed lower boundary the spectral connection between the Maxwell-Boltzmann distributed thermal gas and the non-thermal power-law tail is not necessarily represented.

We remedy this by again using the results from PIC simulations (e.g. Caprioli & Spitkovsky, 2014; Ryu et al., 2019) who find the momentum p_{inj} at which the MBD transitions to a power-law

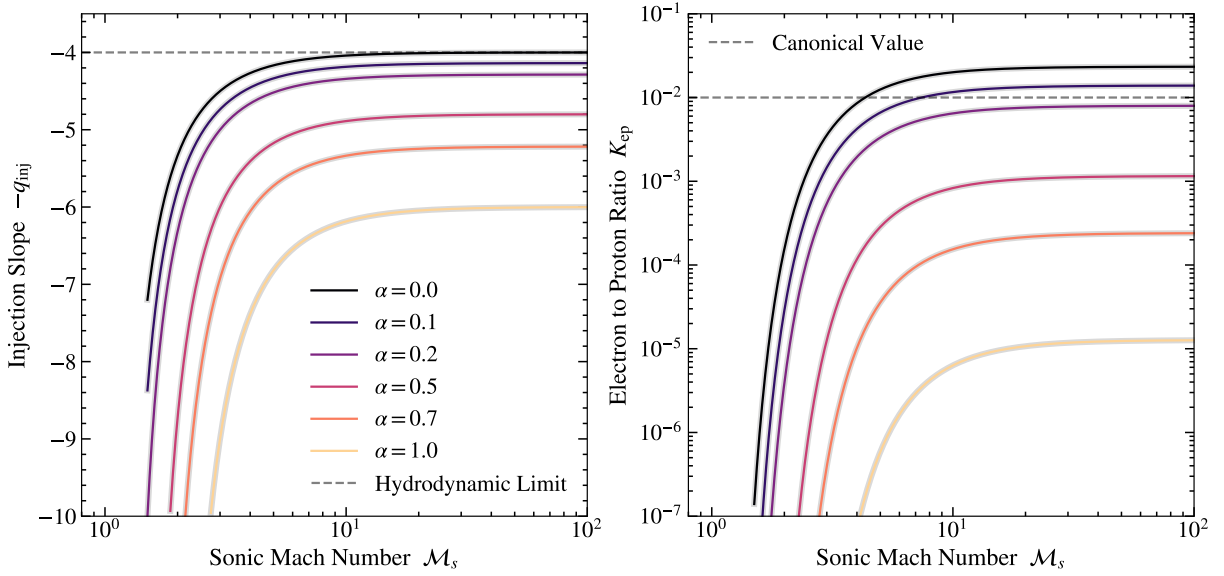


Figure 6.3: *Left*: Injection slope as defined in Eq. 6.10 as a function of sonic Mach number for a shock with negligible CR injection. Colors correspond to different values of α . *Right*: The resulting electron to proton injection ratio for the spectral slopes in the left panel, as defined by Eq. 6.11.

to be a multiple χ of the momentum of the thermal protons downstream of the shock

$$p_{\text{inj},p} = \chi p_{\text{th}} = \chi \sqrt{2m_p k_B T_2} \quad (6.8)$$

where χ is a free parameter found in the simulations and T_2 denotes the gas temperature downstream of the shock. We employ $\chi = 3.5$ and assume that electrons are injected at the same dimensionless momentum as protons. The injection momentum as a function of downstream temperature is shown in Fig. 6.2 for a range of values of χ . In cosmological simulations, the choice of χ is of limited importance, as the uncertainty in acceleration models is significantly larger than the scatter between the different choices for χ .

For electrons, the injection momentum is given by e.g. in Kang et al. (2019); Vazza et al. (2021a); Ha et al. (2023) as

$$p_{\text{inj},e} \approx 3 \sqrt{\frac{m_e}{m_p}} p_{\text{th},p}, \quad (6.9)$$

which we will employ for future work.

6.1.4 Spectral Slope

In the classic picture of particle acceleration via DSA the acceleration is a self-similar process that converges to a power-law distribution of the particles, in general agreement with observations. A caveat of the standard DSA model (as pointed out by e.g. the review of Drury, 1983) is that it is

based on a purely hydrodynamical shock, while the scattering processes clearly require magnetic fields and with that a MHD treatment, as outlined above. A recent set of hybrid simulations by [Caprioli et al. \(2020\)](#) (followed up by a further investigation by [Diesing & Caprioli, 2021](#)) showed that the shock develops a magnetosonic post-cursor wave that can scatter a large fraction of high-energy CRs out of the acceleration zone. This leads to a steepening of the spectrum which they parameterize with

$$q = \frac{3r}{r - 1 - \alpha}; \quad \alpha \equiv \frac{v_{A,2}}{u_2} \quad (6.10)$$

where $v_{A,2} = B_2/\sqrt{4\pi\rho_2}$ and u_2 are downstream Alfvén speed and gas velocity, respectively. They refer to this new description as non-linear diffusive shock acceleration (NLDSA). It follows trivially that Eq. 6.10 reduces to the standard DSA slope for a non-MHD shock.

We added the computation of α to our on-the-fly shock finder to optionally account for this process. In the left panel of Fig. 6.3 we show q as a function of sonic Mach number if we assume the CR injection to be inefficient and with that not significantly altering the compression ratio of the shock.

6.1.5 Proton to Electron Injection Ratio

The total energy budget provided by the shock acceleration needs to be distributed over electrons and protons, following some energy ratio. Unfortunately this ratio is poorly constrained with $\frac{f_e}{f_p} \equiv K_{e,p} \sim 0.01 - 0.025$ (e.g. [Beck, 2015](#); [Park et al., 2015](#)). As an alternative, for the current work, we can calculate the electron-to-proton ratio as found in the semi-analytic approach by [Kang \(2020\)](#)

$$K_{e,p} = \left(\frac{m_e}{m_p}\right)^{(3-q_{\text{inj}})/2} \quad (6.11)$$

For a typical injection slope of $q_{\text{inj}} \approx 4 - 5$ this leads to $K_{e,p} \sim 10^{-2} - 10^{-3}$ (see [Inchingolo et al., 2022](#), for an analogous approach).

6.1.6 Tests

To test our model against an analytic solution we extended the analytic solution derived by [Pfrommer et al. \(2006\)](#) to account for Mach number and magnetic field geometry-dependent acceleration efficiencies. We solve the Riemann problem to first order, higher order solutions would require multiple iterative solution steps for the high-efficiency models. As the inclusion of a CR fluid with considerable contribution to the total post-shock energy density slows down the shock (see e.g. [Pfrommer et al., 2006, 2017](#); [Dubois et al., 2019](#)) this leads to a lower Mach number and with that a lower acceleration efficiency, which again results in smaller CR component in the post-shock region and a higher Mach number in the next iteration of the solution. As the more recent acceleration models point to efficiencies below 10 percent, this effect becomes considerably smaller than the uncertainty of the models themselves.

We list the parameters for all shock tubes used in this section in Table A.1.

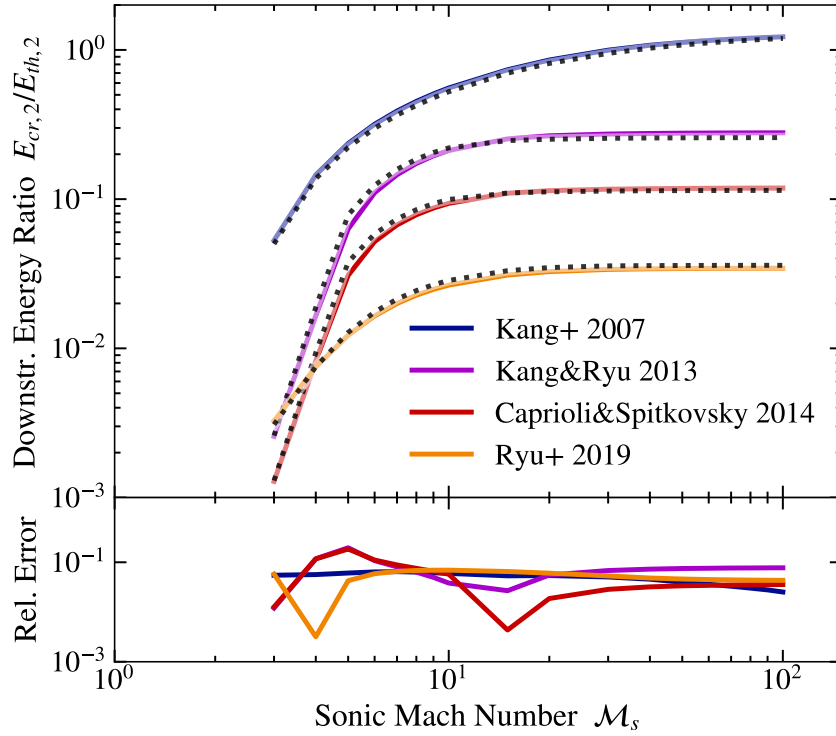


Figure 6.4: We show the results of the injection tests. The upper panel displays the ratio between downstream CR and thermal energies for a shock with sonic Mach number \mathcal{M}_s and the lower panel displays the relative error to the analytic solution. Solid lines indicate the injection method based on entropy change and dotted lines show the analytic solution. The colors refer to the same efficiency models as shown in Fig. 6.1. In general, we find excellent agreement with the analytic solution for the entropy changed based injection model.

Mach Number Dependent Efficiency Models

As a test for the accuracy of our Mach number dependent efficiency $\eta(M)$ we set up a series of Sod shock tubes (following Sod, 1978). We used the canonical density jump of $\rho_L/\rho_R = 8$, kept the left-sided temperature fixed, and varied the right-side temperature to obtain resulting shocks with Mach numbers in the range $\mathcal{M}_s \in [3, 100]$. We ran these shock tubes with all efficiency models shown in Fig. 6.1 and with only the proton component switched on. Fig. 6.4 shows the result of these tests. The entropy-dependent acceleration method captures the analytic solution quite accurately, with a relative error of 10% percent and below. This is especially evident in the relevant low Mach number regime. The excellent agreement over all efficiency models together with the little work required to implement them gives us the chance to test upcoming efficiency models in the context of cosmological simulations, as these models become available.

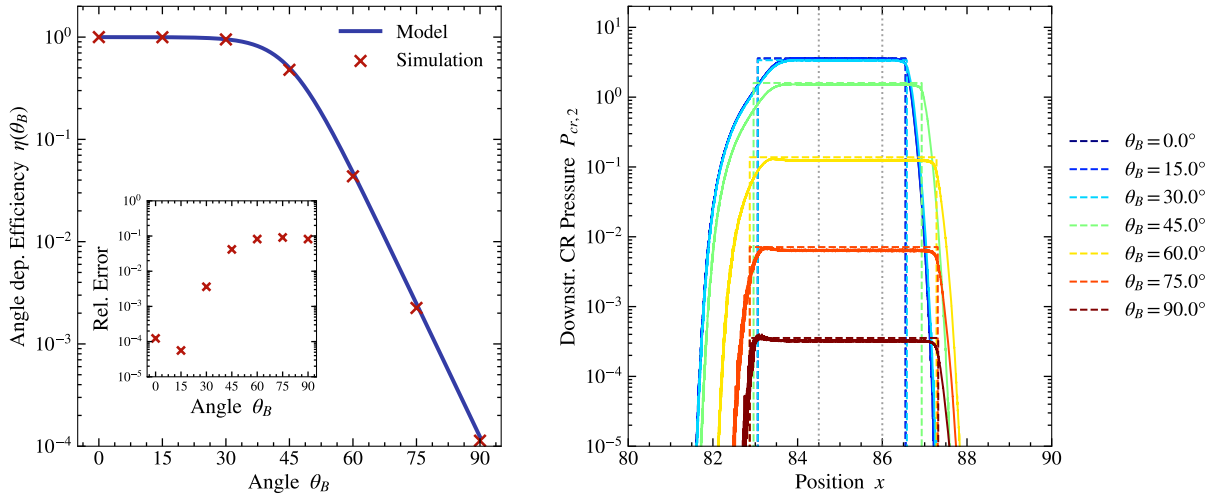


Figure 6.5: Tests for the accuracy of the magnetic field geometry dependent injection. *Left:* Functional form of the dependency parameter and simulation data taken from the mean values of the post-shock region indicated by vertical dotted lines in the RHS plot. The inset plot shows the corresponding relative errors. *Right:* CR proton pressure component in the post-shock region. Colors indicate the ideal angle θ_B between shock normal and magnetic field vector. Dashed lines show the analytic solution, while solid lines show the simulation output. Values of all particles are shown.

Magnetic Field Angle Dependent Efficiency Models

To test how accurately we can model the magnetic field angle dependent acceleration model we followed the approach by [Dubois et al. \(2019\)](#) and set up a series of shock tube tests with negligible, but constant magnetic field at a given angle to the shock propagation. This allows us to capture the angle θ_B between \hat{n}_s and \mathbf{B} while avoiding a kinetic impact of the magnetic field on the development of the shock. The results of these tests for the proton component can be seen in Fig. 6.5. The blue line in the l.h.s. of the figure shows Eq. 6.7 with $\theta_{\text{crit}} = \pi/4$. The red crosses show the results of our simulation. We obtained these values by taking the mean value of the post-shock region indicated by the dashed vertical lines on the r.h.s. The small inset plot shows the corresponding relative error. The r.h.s. shows the injected CR proton pressure component in the post-shock region. Dashed lines indicate the analytic solution, while solid lines show the values of all SPH particles containing injected CRs. Colors correspond to the angle between the shock normal \hat{n}_s and the magnetic field \mathbf{B} . In general, we find excellent agreement with the analytic solutions. The solutions stay numerically stable with very low numerical noise.

Spectral slope

As the shock front is smoothed out by the SPH kernel we systematically under-predict the compression ratio of the shock. Since the velocity jump is equally smoothed out the two effects cancel out and the error of the Mach number estimate at the shock center is on a sub-percent

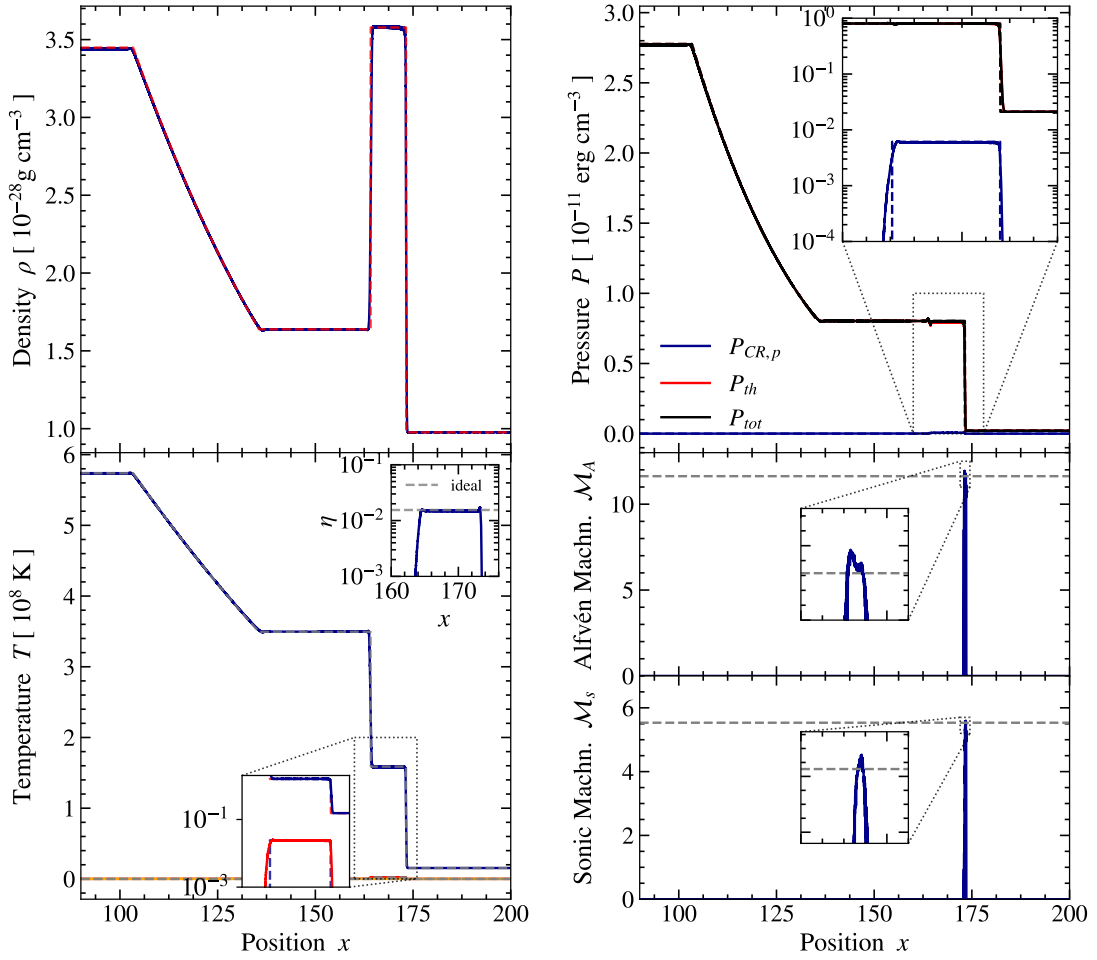


Figure 6.6: Final state of the shock tube test with galaxy cluster properties. Values of all particles are shown with solid lines to include numerical noise. In all plots, the analytic solutions are indicated with dashed lines. *Top left*: Density, *Top right*: Pressure with total pressure in black lines, CR proton pressure in blue lines and thermal pressure in red lines. The inset plot shows a zoom-in on the injection region with logarithmic scaling. *Bottom left*: Temperature and CR energy. The upper inset plot shows the energy ratio in the injection region, while the lower one gives a zoom-in on the injection region with logarithmic scaling. *Bottom right*: Alfvén- and sonic Mach number. Inset plots zoom in on the peak of the shock. The horizontal dashed line shows the analytic solution.

level (see Beck et al., 2016a). To remedy this behaviour we optionally recalculate the shock compression ratio based on the Mach number from the Rankine–Hugoniot conditions as

$$x_s = \frac{(\gamma + 1)\mathcal{M}_s^2}{(\gamma - 1)\mathcal{M}_s^2 + 2} \quad (6.12)$$

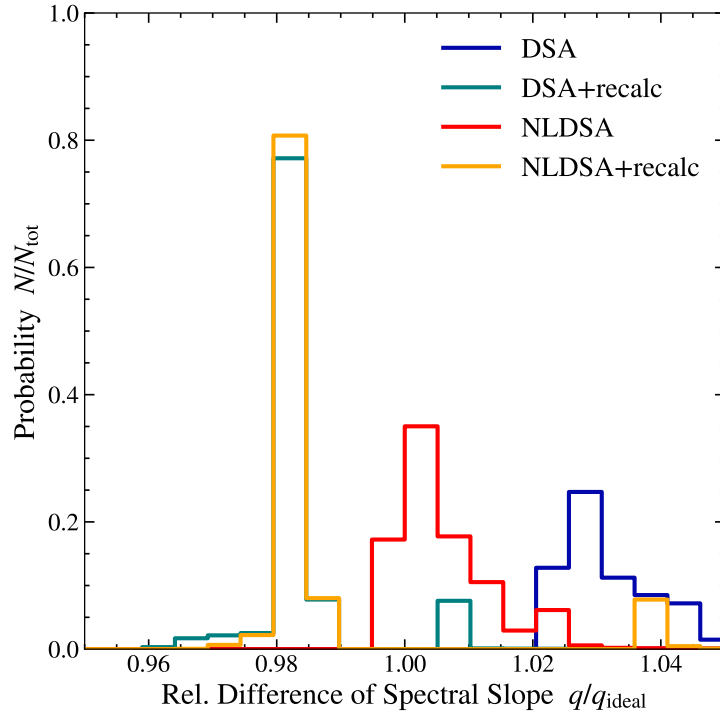


Figure 6.7: Histograms of the ratio between injected and ideal spectral slopes. Colors represent standard DSA and NLDSA description with and without recalculation of the shock compression ratio.

where $\gamma = 5/3$ is the adiabatic index of an ideal gas and M_s is the Mach number of the shock. This approach holds only with a small CR component and is therefore only justified for usage in structure formation shocks where the CR pressure component is expected to be small (as discussed above) and not e.g. in resolved ISM simulations with SNe, where the CR pressure component can be a significant fraction of the total pressure and will therefore modify the shock properties (e.g. Beck, 2015).

To test the accuracy of capturing the correct slope of the injected spectrum we set up a series of shock tubes with properties similar to those found in galaxy cluster shocks. Table A.1 gives the properties of the shock initial condition and Fig. 6.6 shows the result of the simulation.

As can be seen, the quantities agree nicely with the analytic solution and the capture of the Alfvén Mach number and with that the capture of the Alfvén speed needed for the non-linear correction to DSA agrees very well with the analytic solution. We ran four different simulations with each DSA, DSA plus recalculation of compression ratio according to Eq. 6.12, NLDSA and NLDSA with recalculation. We then compared the obtained injection slopes with the ideal slopes in Fig. 6.7. The recalculation shows promising results, as it is less broadened and in the case of DSA more accurate. For NLDSA recalculation introduces a larger error, but nonetheless stays less broadened. We therefore accept this discrepancy for now.

6.2 Supernovae

The most prominent source of high-energy CRs within our galaxy are SNe. This contribution is so significant that CRs in our galaxy are found to be in equilibrium with the magnetic and turbulent kinetic pressure components (Beck, 2015). Work by Hanasz & Lesch (2003); Pfrommer et al. (2006, 2017); Butsky & Quinn (2018); Ji et al. (2020); Fielding et al. (2020); Hopkins et al. (2021); Hopkins et al. (2022a); Girichidis et al. (2022, 2023) find that the inclusion of CR physics in simulations of galaxy evolution can amplify magnetic fields, mediate star formation and drive powerful galactic winds.

To prepare CRESCENDO for simulations of galaxy formation and evolution we therefore implemented a model for CR injection at SNe. This model is however very simplistic and still needs to undergo improvements to be used in such simulations. We nonetheless report the current state here, to facilitate future improvements.

This work will be continued by MSc. Daniel Karner.

6.2.1 Effective Model

As an initial attempt, we implemented a simplified SN seeding model, based on the *effective model* by Springel & Hernquist (2003) and the magnetic SN seeding model by Beck et al. (2013). In this model the CR energy injected due to SNe, per SPH particle, per timestep can be expressed as

$$E_{\text{CR,inj}}^{\text{SN}} = \eta E_{\text{SN}} \sqrt{N_{\text{SN}}^{\text{eff}}} \xi \quad (6.13)$$

where η is the efficiency, or how much energy of the SN is available for CR acceleration, $E_{\text{SN}} = 10^{51}$ erg, $N_{\text{SN}}^{\text{eff}}$ is the effective number of SNe per timestep and ξ is what we refer to as a mixing term. η is typically taken as a canonical value of $\eta \approx 0.1$ (see e.g. Ackermann et al., 2013; Helder et al., 2012; Morlino & Caprioli, 2012, and references therein). The effective number of SNe per timestep can be computed as

$$N_{\text{SN}}^{\text{eff}} = \alpha \left(\frac{M_c}{M_\odot} \right) \left(\frac{\Delta t}{t_*} \right). \quad (6.14)$$

Here $\alpha = 0.008$ is the number of SNe per solar mass formed, which is based on the fraction of formed stars that are above $M_* > 8M_\odot$ and are therefore able to explode as core-collapse SNe. Since we do not form individual stars in our simulation due to resolution limitations (unlike Steinwandel & Goldberg, 2023), but rather deal with stellar populations, this fraction depends on how the stellar populations are sampled. The sampling of stellar populations in OpenGadget3 is done via the Initial Mass Function (IMF) by Chabrier (2003), which results in the given value for α . t_* describes the star formation timescale, which in the model by Springel & Hernquist (2003) is defined via a density threshold ρ_{thr} beyond which cloud collapse and with that star formation can take place, with

$$t_* = t_{*,\text{max}} \left(\frac{\rho_{\text{thr}}}{\rho} \right) \quad (6.15)$$

and $t_{*,\max}$ is a free parameter with typical value $t_{*,\max} \approx 1.5$ Gyrs. Depending on resolution, $N_{\text{SN}}^{\text{eff}}$ will be smaller than one in most cases. If $N_{\text{SN}}^{\text{eff}} < 1$ we draw a random number and based on the result set $N_{\text{SN}}^{\text{eff}}$ to 1, or 0.

This gives at least a stochastic chance of SNe occurring in our simulation, even if the timestep is too small to allow for a cloud collapse to occur. Last, we need to account for the difference in resolution between the size of a supernova and our resolution elements. For this, we defined the mixing term

$$\xi \equiv \left(\frac{r_{\text{SN}}}{r_{\text{SB}}} \right)^{\frac{4}{3}} \left(\frac{r_{\text{SB}}}{h_{\text{sml}}} \right)^2 \quad (6.16)$$

where r_{SN} is the size of the SN, $r_{\text{SB}} = 25$ pc is the size of the SN bubble and h_{sml} is the smoothing length of our SPH particle. The physical motivation behind this is that the CRs are accelerated at the SN and subsequently adiabatically expanded over the size of the SN bubble. This bubble is then advected and mixed in the volume of the SPH particle.

Eq. 6.13 gives us a total energy injected per SPH particle. This energy then needs to be distributed over its neighbors

$$E_{i,\text{CR},\text{inj}} = \sum_{j=0}^{N_{\text{ngb}}} E_{j,\text{CR},\text{inj}} \frac{m_j}{\rho_j} W(\vec{r}_i - \vec{r}_j, h_i) \quad (6.17)$$

to be consistent with the SPH formalism.

The resulting energy is then injected at the end of the timestep by calculating the normalization at the injection momentum, following Eq. 6.1. In this case, the injection momentum $p_{\text{inj}} = 0.1$ is a free parameter. We inject with a slope $q_{\text{inj}} = 4.3$, to mimic the observed CR slope in the solar neighborhood (see [Drury, 1983](#); [Caprioli & Spitkovsky, 2014](#), and references therein). As in the case of DSA, we inject a fixed ratio of $K_{\text{ep}} = 0.01$ of CR electrons to protons (see again [Park et al., 2015](#)). This may however be too low by a factor \sim ten to match the results by [Lacki et al. \(2010\)](#).

6.2.2 Supernova Yields and Realistic Spectra

Models of emission from supernova remnants indicate that the underlying CR spectrum may deviate significantly from a simple power-law (see e.g. Fig. 7 in [Allen et al., 2008](#)). While the acceleration via DSA produces a power law as was the case for merger shocks, in the case of SNe we need to account for CR energy losses due to the stronger magnetic field and adiabatic expansion of the SN remnant.

In future work, we will therefore inject escape spectra, instead of in-situ spectra, following the models by [Cristofari et al. \(2021\)](#); [Morlino & Celli \(2021\)](#). They also account for different escape spectra for various SN types. This can then be coupled to the model for different SN types and yields by [Tornatore et al. \(2007\)](#).

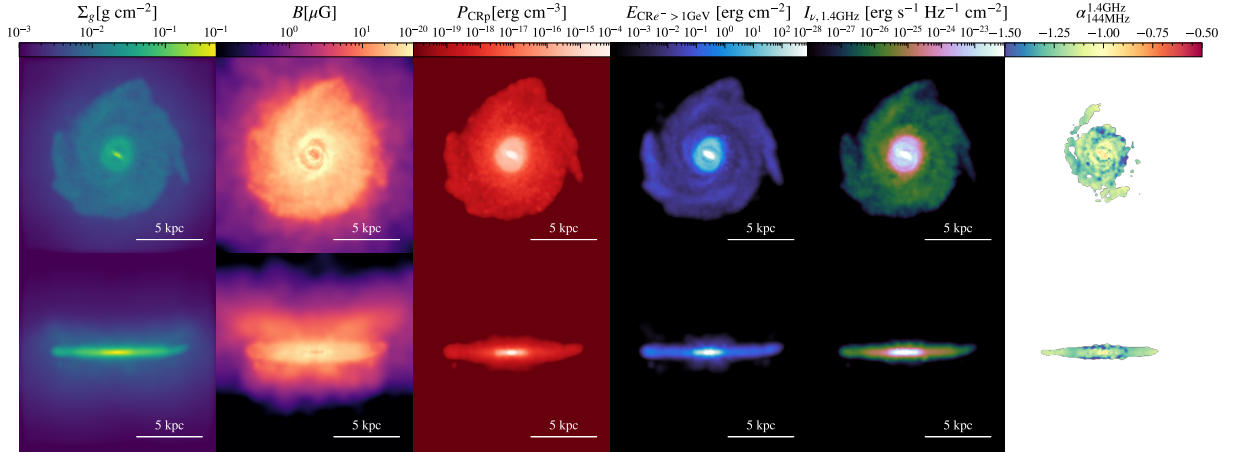


Figure 6.8: Isolated galaxy simulation with the simple SN-source model. The top panels show the face-on, bottom panels the edge-on projection. From left to right we show the gas surface density, magnetic field strength, CR proton pressure, the energy contained in CR electrons with energies above $E > 1$ GeV, synchrotron surface brightness at 1.4 GHz, and the synchrotron slope between 144 MHz and 1.4 GHz.

6.2.3 Test Run

Fig. 6.8 shows an initial test run with the effective model. We used an initial condition for a dwarf galaxy with a realistic hot halo (see [Steinwandel et al., 2020a](#), for a detailed discussion of these setups). The resolution of this simulation is $m_{\text{gas}} = 4.9 \times 10^5 M_{\odot}$ and $m_{\text{DM}} = 9.7 \times 10^6 M_{\odot}$ for gas and DM particles, respectively.

From left to right we show the gas surface density, magnetic field strength, CR proton pressure, the energy contained in CR electrons with energies above $E > 1$ GeV, synchrotron surface brightness at 1.4 GHz and the synchrotron slope between 144 MHz and 1.4 GHz. The top panels show the face-on projection, while the bottom panels show edge-on projections.

While the overall injected energy is too low, i.e. the CR protons are not in pressure equilibrium with the magnetic and turbulent kinetic pressure, we find morphologically promising results. We find that CRs are preferentially accelerated in the spiral arms, consistent with observations (e.g. [Mulcahy et al., 2014](#)). This can be seen in the synchrotron intensity maps and the resolved synchrotron spectrum maps in the last two columns of Fig. 6.8.

7 | Adiabatic Changes

The next mechanism to consider is how the distribution function of CRs changes due to adiabatic expansion or compression of the surrounding gas. With CRs being confined within the surrounding gas by the CR streaming instability due to their scattering at (self-excited) Alfvén waves (e.g. [Kulsrud & Pearce, 1969](#); [Wentzel, 1974](#); [Skillling, 1975a,b,c](#)) they are dynamically coupled to this gas. As this Alfvén rest frame is compressed, the CRs gain energy based on the PdV work of the gas. Given that the Alfvén waves have sufficiently high modes this process should be self-similar, so every particle should gain the same amount of energy. In the case of a power-law distribution of particles this should contain the power-law shape and only shift to higher energies and momenta respectively. This leaves the problem of how to handle the lower end of the distribution. In previous works this has been addressed by setting a lower cut (e.g. [Winner et al., 2019](#); [Ogrodnik et al., 2021](#)) or a larger 0th bin as a buffer zone with open lower boundary conditions (e.g. [Girichidis et al., 2020, 2022](#)).

7.1 Implementation

As discussed in Section 5.4 we choose to keep an open boundary condition at the lower end of the spectral distribution. The influx can be achieved by interpolating the lowest momentum boundary to a “ghost bin” (p_g) and solving the flux over the lowest boundary

$$p_g = p_0 \cdot 10^{-\Delta p} \quad (7.1)$$

where p_g is the boundary of the ghost bin, p_0 is the boundary lowest bin and Δp is the bin-width of the spectrum. The normalization of the ghost bin can then be interpolated as

$$f_g = f_0 \left(\frac{p_0}{p_g} \right)^{q_0} \quad (7.2)$$

where again f_0 is the norm and q_0 is the slope of the lowest bin.

The momentum change due to adiabatic expansion or compression of the surrounding gas can be described by

$$\left(\frac{\partial p}{\partial t} \right)_{\text{adiab.}} = -\frac{1}{3} \frac{\partial u}{\partial x} p = -\frac{1}{3} \ln \left(\frac{\rho}{\rho_0} \right) \frac{p}{\Delta t} . \quad (7.3)$$

Integrating this by parts, as described in Section 5.3.2, and solving the momentum integral for the upper boundary yields

$$p_u = p_i \left(\frac{\rho_t}{\rho_{t+\Delta t}} \right)^{1/3}. \quad (7.4)$$

This boundary can then be inserted into the flux integrals in Eqs. 5.24 and 5.25 to compute the number- and energy-density fluxes between momentum bins.

7.2 Tests

We test the quality of the adiabatic changes as implemented in our model based on its capability of keeping the spectral slope, as well as its ability to conserve energy throughout every completed model cycle. For completeness, we use two versions of the model, a stand-alone version for testing as well as the direct implementation of that model into our code `OPENGADGET3`.

Convergence

For comparison with other implementations, we performed the same test as [Girichidis et al. \(2020\)](#) and modeled a sinusoidal density wave moving through a single SPH particle.

For this, we set up a single power-law spectrum with a slope of $q = 4.5$ over six orders of magnitude in momentum. We then set a time-dependent density field as

$$\rho(t) = \rho_0 \left(1 + \frac{\sin(2\pi t)}{2} \right) \quad (7.5)$$

and evolve the spectrum for 100 cycles. In addition, we run the test with two spectral resolutions, 12 bins and 192 bins, or 2 bins/dex and 32 bins/dex, respectively. The result of the L_1 error for CR energy/number density and reconstructed slope after every cycle is shown in Fig. 7.1. We find stable behavior and comparable accuracy to the implementation by [Girichidis et al. \(2020\)](#), with the caveat that we find an increasing error after every cycle, while their model appears to stabilize after a number of cycles.

Further investigation shows that this stems from our ghost-bin interpolation. A small error in the slope reconstruction of the 0-th bin also affects the ghost bin. Since the 0-th bin by design contains the most CR energy/number this error can become problematic. We can counter this in future work by either applying a closed lower boundary in simulations where only the upper part of the distribution function is relevant, e.g. in simulations of cosmological structure formation, or by adding low-momentum energy loss processes in simulations of galaxy formation.

For the purpose of this work, we accept this behaviour as is, since the overall error is very small. We only show the result for 12 bins in Fig 7.1, as we find no significant difference in the CR energy and number errors to the 192 bin run, as is expected due to the nature of the test problem. Since we set up a single power-law spectrum and adiabatic changes should not change the shape of the spectrum the resolution should not be relevant. However, in principle more bins have the potential for more numerical inaccuracies, so we find this consistent behavior to be reassuring.

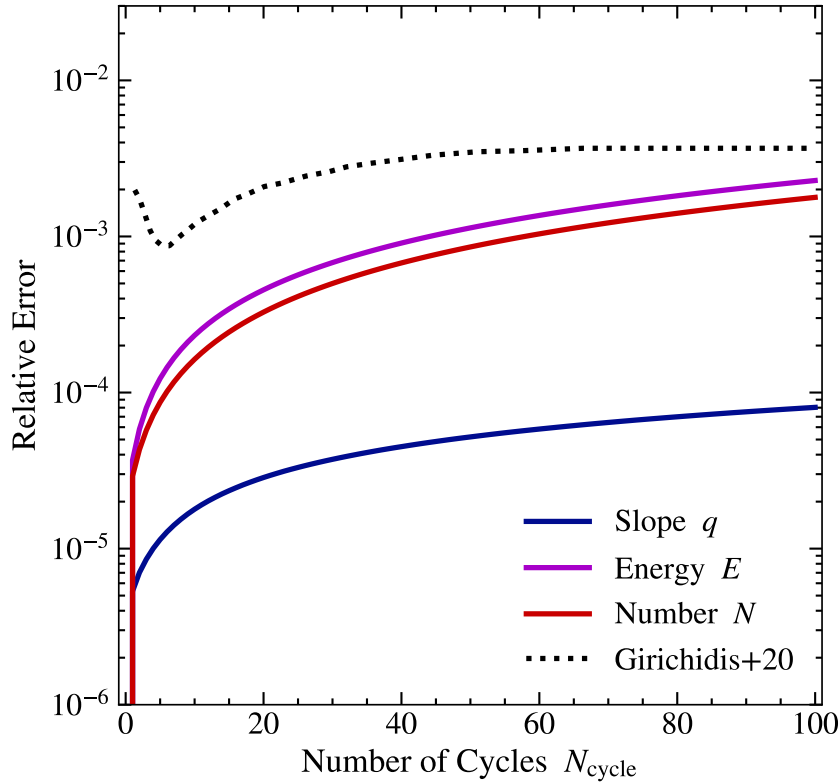


Figure 7.1: Relative errors for CR energy and number, as well as the reconstructed slope in the sine-wave test for a single SPH particle. We represent the spectrum with 2 bins/decade to test a worst-case scenario. The dotted line indicates the upper limit of the error from [Girichidis et al. \(2020\)](#), Fig. 9 for their piece-wise power-law implementation. We find similar accuracy, but note that while [Girichidis et al. \(2020\)](#) find a stable solution after a number of circles, our errors keep increasing over the course of the test.

Decaying Sinewave

In order to test the stability of the adiabatic changes within `OPENGADGET3` we set up a sinusoidal density profile within an isothermal periodic box. We set up a CR energy density as one-third of the thermal energy density and let it evolve until the resulting pressure wave had completed approximately three modes. The CR spectra were set up as a simple power-law with a constant slope $q_0 = -4.5$.

Fig. 7.2 shows the time evolution of the density in the left panel and the spectral evolution of two tracer particles in the right panels. For the tracer particles, we chose the particles with the highest density (large points) and lowest density (large X) at t_0 to observe the behavior under primarily adiabatic expansion and compression, respectively.

We plot the particle distribution functions multiplied by p^{q_0} to visually emphasize discrepancies from the initial slope in a bin. Since the distribution functions experience a self-similar shift due to adiabatic changes the slope should not change over the course of the simulation and should

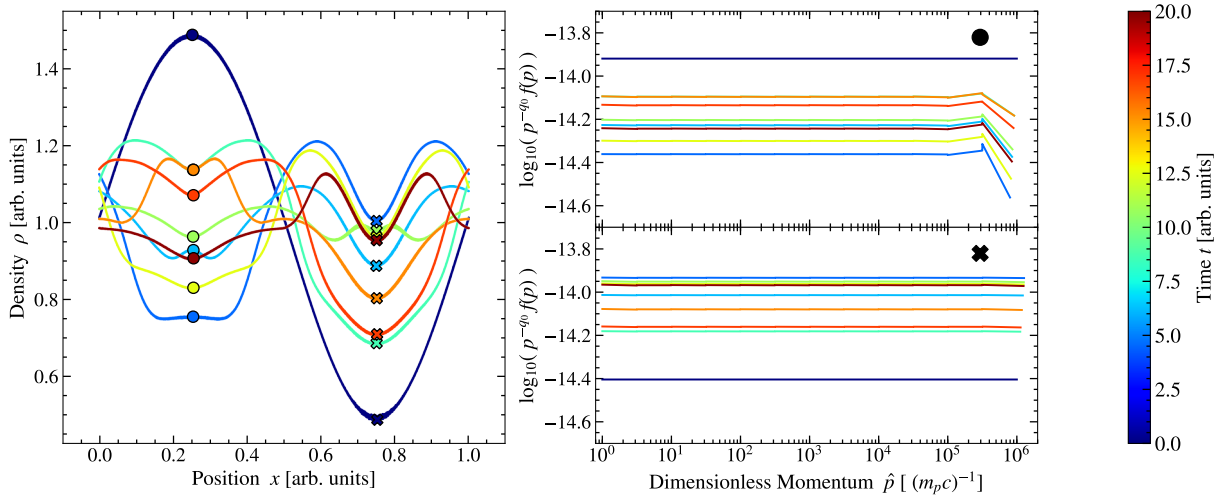


Figure 7.2: Test simulation of a sinus density profile in an isothermal periodic box. *Left*: Time evolution of the density profile. *Right*: Spectra of the particles with the maximum (upper panel) and minimum (lower panel) density at the beginning of the simulation. The corresponding particles are marked by the corresponding markers in the upper right corner of the spectrum plots. As desired the spectra stay flat over the course of the simulation with only the highest momentum bin showing a deviation under adiabatic expansion due to the spectral cut-off moving into the bin.

remain flat. We see consistent flat spectra at the low momentum and only see a deviation from this for the highest momentum bin in the particle that experiences adiabatic expansion. This is expected as the spectral cutoff moves in the center of the bin. Furthermore, it introduces only a small error, since the bulk of the energy is contained in the low-momentum end of the spectrum. The stability of the distribution function is especially evident in the upper spectral panel for $t \approx 8.6$ (cyan line) and $t \approx 15.3$ (orange line). As can be seen on the density plot on the left the density of the particle is virtually identical. At the same times, the spectral lines lie almost perfectly on top of each other, even though the particles have experienced one step of expansion and compression between the two data points.

8 | Cooling Processes

The CRs accelerated within GCs will experience energy losses due to a number of processes. In this chapter, we will give an overview of the implementation of energy losses for CRs, as these are the most relevant to obtain realistic observables within GCs.

We will leave the implementation of energy losses for CRps to future work, due to their energy loss mechanisms being very inefficient within GCs (see e.g. Fig. 7 in [Brunetti & Lazarian, 2007](#)).

8.1 Synchrotron and inverse Compton Losses

For the high momentum end of the CR electron distribution, the dominant loss mechanisms are IC scattering of electrons on CMB photons and synchrotron losses due to the surrounding magnetic field. These loss mechanisms both scale with p^2 and only depend on the energy density of the background photon field and the magnetic field, respectively. This makes it convenient to combine them into one loss process.

8.1.1 Implementation

The momentum change for a particle due to IC scattering and synchrotron losses can be written as

$$\left(\frac{dp}{dt}\right)_{\text{Synch+IC}} = \frac{4}{3} \frac{\sigma_T}{m_e^2 c^2} (U_{\text{IC}} + U_{\text{B}}) p^2 = \beta p^2 \quad (8.1)$$

where we introduced

$$\beta = \frac{4}{3} \frac{\sigma_T}{m_e^2 c^2} (U_{\text{IC}} + U_{\text{B}}) \quad (8.2)$$

for convenience. Following the steps in Section 5.3 we can solve this for the upper integration boundary as

$$p_u = \frac{p_i}{1 - \beta p_i \Delta t}, \quad (8.3)$$

and update the spectral cut as

$$p_{\text{cut},t+\Delta t} = \frac{p_u}{1 + \beta p_{\text{cut},t} \Delta t}. \quad (8.4)$$

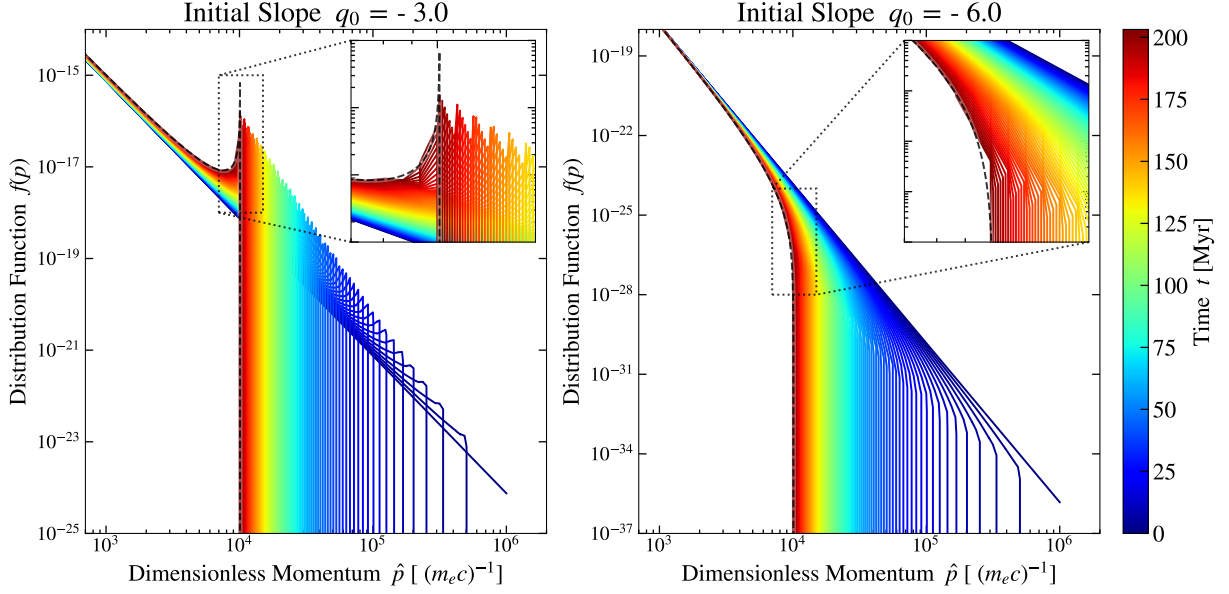


Figure 8.1: Test particle spectra with 32 bins per order of magnitude in momentum under constant inverse Compton scattering off CMB photons at $z = 0$. *Left*: Cooling for a spectrum with an initial slope of $q_0 = -3.0$. *Right*: Cooling for a spectrum with an initial slope of $q_0 = -6$. We only show the upper half of the distribution function, as IC losses are only relevant in the high-momentum end. The simulation was run until the cooling time for particles of momentum $\hat{p}_{\text{cool}} = 10^4$ was reached. Colors indicate the spectra at the respective time. The dashed line indicates the analytic solution at the final time. We find excellent agreement with the analytic solution and note that the agreement is only limited by spectral resolution.

With that we can solve the flux integrals (Eq. 5.25 and 5.24) and the number density update (Eq. 5.9). To evolve the energy density we also need to solve Eq. 5.19 per bin as

$$R_i(q_i, p_i) = \beta \frac{4 - q_i}{p_{i+1}^{4-q_i} - p_i^{4-q_i}} \frac{p_{i+1}^{5-q_i} - p_i^{5-q_i}}{5 - q_i} \quad (8.5)$$

8.1.2 Tests

To test our model under radiative cooling we set up a small box of SPH particles and switched off all contributions to the spectral evolution except for radiative cooling due to IC scattering of electrons on CMB photons at $z = 0$. We initialized the particle spectra as a single power-law with slopes $q_0 = -3.5$ and $q_0 = -6$ in the range $\hat{p} \in [1, 10^6]$ represented by 192 bins, or 32 bins/dex. We evolve the simulation until the cooling time of electrons with momentum $\hat{p} = 10^4$ is reached.

Accuracy

For testing the accuracy of our radiative cooling implementation we follow [Kardashev \(1962\)](#) who provides an analytic solution for an initial power-law spectrum experiencing radiative cooling from synchrotron radiation and inverse Compton scattering. This can be written in terms of the distribution function $f(p)$ as in [Ogrodnik et al. \(2021\)](#)

$$f(p, q, t) = \begin{cases} f(p, t_0) (1 - \beta t p)^{q-4} & \text{for } p < \frac{1}{\beta t} \\ 0 & \text{for } p > \frac{1}{\beta t} \end{cases} \quad (8.6)$$

where $\beta = \frac{4}{3} \frac{\sigma_T}{m_e^2 c^2} (U_{IC} + U_B)$ as in Eq. 8.1. This solution indicates a difference in spectral shape for spectra with $q < 4$ and $q > 4$. For $q < 4$ the high-momentum end on the spectrum is so densely populated that cooling particles pile up in lower momentum bins and lead to a flattening and even increase of the spectrum, while for $q > 4$ the high momentum electrons cool off fast enough to lead to a simple steepening of the spectrum. It also predicts a sharp cutoff of the distribution function at $p = \frac{1}{\beta t}$.

The result of this test can be seen in Fig. 8.1 where we only show the relevant upper half of the spectra. We can see the expected upturn of the spectrum for $q = -3$ and a steepening of the spectrum for $q_0 = -6$ and find excellent agreement with the analytic solution (dashed) that is only limited by the spectral resolution of the model.

Convergence

In order to study the convergence of our model under different spectral resolutions we can rewrite Eq. 8.6 to represent the spectral slope per bin as a function of time

$$q(p, t) = -\frac{\partial \ln f}{\partial \ln p} = q_0 + (q_0 - 4) \frac{t p / (\tau_{p_n} p_n)}{1 - t p / (\tau_{p_n} p_n)} \quad (8.7)$$

where τ_{p_n} is the cooling time for the radiative loss mechanisms. We repeat the previously described test with different spectral resolutions between 12 bins (2/dex) to 768 bins (128/dex). The results are shown in Fig. 8.2. We find a good convergence trend, with 24 bins (or 4/dex) being the minimum number of bins we consider acceptable to model CR electron cooling due to synchrotron and IC losses. We note that the discrepancy of the higher resolution models below $\hat{p} = 10^4$ stems from our limit on the slope per bin. As noted above, we ran the simulation until the cooling time of $\hat{p} = 10^4$ is reached and our spectral cutoff also reached that value with very high accuracy. The actual spectrum however should steepen below $q = -20$ and connect to p_{cut} at $q \rightarrow -\infty$. This would increase our computing time significantly due to the root-finding step, as previously discussed. The bins are therefore artificially set to $q = -20$. We performed the same test for initial slopes of $|q_0| < 4$ and found identical convergence behavior.

8.2 Coulomb Losses

For lower-energy CRs the dominant energy loss mechanism is Coulomb interaction with the fully ionized background plasma in the ICM (see e.g. [Longair, 2011](#), for a more detailed introduction).

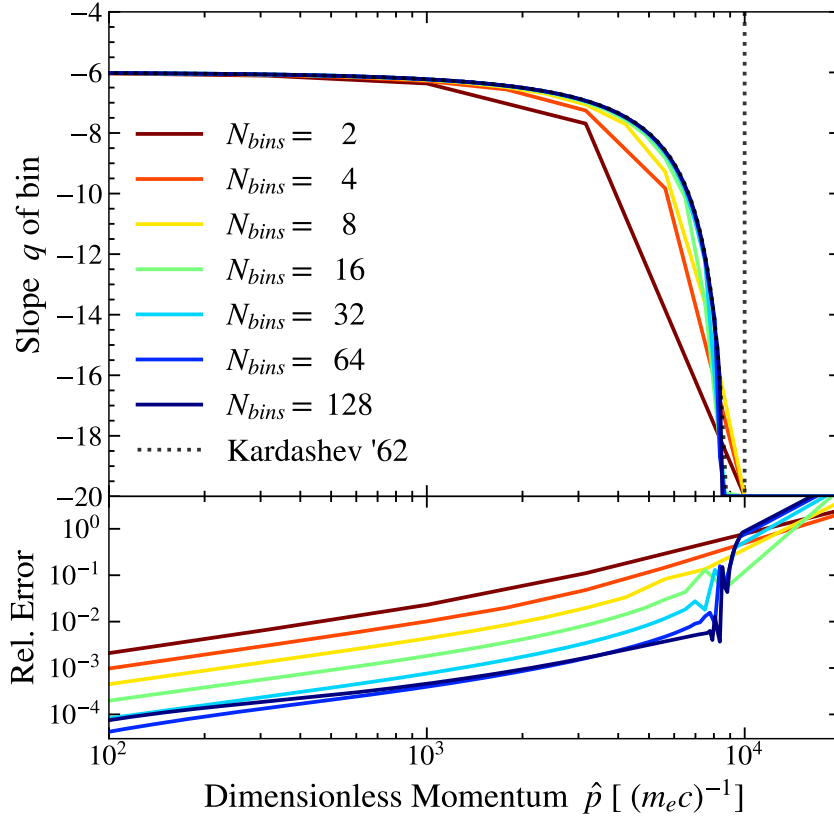


Figure 8.2: Results of the convergence tests for high-momentum radiative cooling. The top panel shows the analytic (dotted) and simulated (solid) slopes for each momentum bin. The dotted vertical line indicates the position of the spectral cutoff. The bottom panel shows the corresponding relative error. Colors refer to the different number of CR bins per order of magnitude in momentum. We find good convergence to the cooling solution for a spectral resolution of 8 bins per order of magnitude and above.

As these CRs move through the ICM they interact electrostatically with the thermal protons and electrons making up the plasma in the ICM. There they are deflected from equally charged particles and attracted to opposite charged particles. This deflection again introduces an energy loss rate, proportional to the density of the background plasma and inversely proportional to the CR energy.

As we are mainly interested in non-radiative emission of CRs and the kinematic impact of CRs is expected to be negligible on Galaxy Cluster (GC) scales we have not yet prioritized the implementation of Coulomb losses into the model. The inclusion of CRESCENDO in simulations of galaxy formation and evolution will however make it necessary to account for these loss mechanisms.

In the current state, there is an as-of-yet untested implementation of Coulomb losses for electrons in the solver. We will outline the implementation steps in this section nonetheless, to facilitate

future work on this aspect of the code.

The momentum loss rate for electrons due to coulomb collisions can be described as (see [Gould, 1972](#); [Winner et al., 2019](#))

$$\left(\frac{dp}{dt}\right)_{\text{Coulomb}} = -\frac{3\sigma_T n_e c}{2\beta^2} \left[\ln\left(\frac{m_e c^2 \beta \sqrt{\gamma - 1}}{\hbar \omega_{\text{pl}}}\right) + \ln(2) \left(\frac{\beta^2}{2} + \frac{1}{\gamma} \right) + \frac{1}{2} + \left(\frac{\gamma - 1}{4\gamma} \right) \right], \quad (8.8)$$

with the dimensionless CRe velocity $\beta = p(1 + p^2)^{-\frac{1}{2}}$, their Lorentz factor $\gamma = \sqrt{1 + p^2}$ and the electron density of the thermal background gas n_e . The plasma frequency can be calculated as $\omega_{\text{pl}} = \sqrt{4\pi e^2 n_e / m_e}$ and the Thomson cross-section is $\sigma_T = 8\pi e^4 / [3(m_e c^2)^2]$.

As in [Pinzke et al. \(2013\)](#) we can approximate Eq. 8.8 using

$$\left(\frac{dp}{dt}\right)_{\text{Coulomb}} \approx -\frac{3\sigma_T n_e c}{2} \ln\left(\frac{m_e c^2}{\hbar \omega_{\text{pl}}}\right) (1 + p^{-2}) \equiv b_c (1 + p^{-2}). \quad (8.9)$$

As was the case for synchrotron and IC losses we need to solve Eq. 5.27, which following [Winner et al. \(2019\)](#) can be approximated as

$$\int_{p_i}^{p_u} dp \left(\frac{dp}{dt}\right)_{\text{Coulomb}}^{-1} = -\frac{1}{b_c} [p - \arctan(p)] \approx -\frac{1}{b_c} \left(\frac{p^3}{3 + p^2} \right). \quad (8.10)$$

This can again be solved for p_u as

$$p_u = \frac{1}{3} \left[a + \left(a^3 + \frac{9}{2} \sqrt{4a^4 + 81a^2} + \frac{81a}{2} \right)^{\frac{1}{3}} + a^2 \left(a^3 + \frac{9}{2} \sqrt{4a^4 + 81a^2} + \frac{81a}{2} \right)^{-\frac{1}{3}} \right] \quad (8.11)$$

using the short-hand $a = p^3 / (3 + p^2) - b_c \Delta t$. With this, we can solve the fluxes between momentum bins. To solve the total energy change we also need to compute the quantity $R_i(q_i, p_i)$ in Eq. 5.19 as

$$R_{\text{Coulomb},i}(q_i, p_i) = \frac{4 - q_i}{p_{i+1}^{4-q_i} - p_i^{4-q_i}} \int_{p_i}^{p_{i+1}} dp p^{2-q_i} b_c (1 + p^{-2}) \quad (8.12)$$

$$= \frac{4 - q_i}{p_{i+1}^{4-q_i} - p_i^{4-q_i}} b_c \left(\frac{1}{3 - q_i} (p_{i+1}^{3-q_i} - p_i^{3-q_i}) + \frac{1}{1 - q_i} (p_{i+1}^{1-q_i} - p_i^{1-q_i}) \right) \quad (8.13)$$

With these equations, the loss mechanism can be solved within our model.

However, using these equations as-is holds a number of problems. First and foremost, in this formulation, we solve the Coulomb losses in the ultra-relativistic limit, which for the parts of the distribution function where they are relevant is no longer justified. This only concerns Eq. 8.13 however. In the next step, we will need to abandon the ultra-relativistic limit and use either a

different approximation or Taylor-expand the individual terms to a desired order. See Sec. 17.1 for a discussion.

Second, depending on where we decide to start our injection we may also need to introduce a lower momentum cutoff, as in [Ogrodnik et al. \(2021\)](#). In the case of efficient Coulomb losses of CRes and a distribution function modeled down to $\hat{p} \sim 0.01$, we may completely cool away the lower momentum bins over the course of the simulation. To accurately treat the spectra within a bin we need to be able to prescribe partially filled bins, as was the case with synchrotron and IC losses.

Third, the inclusion of Coulomb losses leads to negative values of q in the distribution function. For negative q our root-finding method to reconstruct the current slope per bin has a significantly smaller zone of convergence (see left panel of Fig. 5.2). This introduces a problem with numerical stability that needs to be handled with care.

9 | Fermi-II Re-acceleration

CRs change their momentum, not only due to energy losses but also energy gain mechanisms. The most prominent of those gain mechanisms leads back to the concept introduced by [Fermi \(1949\)](#), where he postulated that CRs can gain energy by stochastically scattering within ISM clouds. This can lead to a net energy gain from the energy transfer of the thermal gas to the CRs via the excited Alfvén waves. Hence this (positive) diffusion in momentum space is often referred to as *Fermi-II acceleration*, or *second order Fermi acceleration*.

The relevant part of the Fokker-Planck equation governing this process is

$$\frac{Df}{Dt} = \frac{\partial}{\partial p} \left(-\frac{2}{p} D_{pp}(p) f \right) + \frac{\partial}{\partial p} \left(D_{pp}(p) \frac{\partial f}{\partial p} \right) \quad (9.1)$$

where the first term on the right-hand side describes what is sometimes referred to as the systematic component and the second term as the stochastic component of re-acceleration.

The momentum diffusion coefficient $D_{pp}(p)$ describes the rate of re-acceleration as a function of momentum. This momentum dependence is not yet exhaustively explored in the literature.

9.1 Momentum Diffusion Coefficient D_{pp}

Following [Cassano & Brunetti \(2005\)](#) the change in momentum due to turbulent re-acceleration per timestep can be expressed as

$$\left(\frac{dp}{dt} \right)_{\text{acc}}^{\text{sys}} = -\chi p \approx -2 \frac{D_{pp}}{p}, \quad (9.2)$$

with the additional minus sign to match our formalism. For an isotropic distribution of wave and particle momenta and $v_A < v_M$, with v_A being the Alfvén velocity and

$$v_M^2 \approx \frac{4}{3} v_{\text{ion}}^2 + v_A^2 \quad (9.3)$$

the momentum diffusion coefficient D_{pp} is given by [Eilek \(1979\)](#) as

$$D_{pp}(p, t) \approx 4.45 \pi^2 \frac{v_M^2 p^2}{c B^2} \int_{k_{\min}}^{k_{\max}} dk k \mathcal{W}_k^B(t) \quad (9.4)$$

$$= D_0(t) p^2 \quad (9.5)$$

This assumes that the infall of substructure causes plasma instabilities and turbulence which in turn drives magneto-sonic (MS) waves. These instabilities lead to the systematic second-order Fermi re-acceleration process. The integral on the r.h.s. of Eq. 9.4 is therefore the integral over the spectrum of the MS waves. The boundaries of this integral are defined by the minimum and maximum wave numbers of the underlying turbulence spectrum.

Explicitly solving $D_0(t)$ proves difficult due to the integral on the r.h.s. of Eq. 9.4. The time evolution of $W_k(t)$, the modified spectrum of the MS waves, depends on wave-wave interaction and wave-particle interaction and is therefore very expensive to solve. [Cassano & Brunetti \(2005\)](#) use an approximation that simplifies the form of W_k to only depend on the injection spectrum of the waves $I(k)$, which for this purpose is assumed to be a simple power-law $I(k) = I_0 k^{-a}$, and the most prominent dampening mechanism, the dampening by thermal electrons $\Gamma_{\text{th},e}(k)$

$$W_k \simeq \frac{I(k)}{\Gamma_{\text{th},e}(k)}, \quad (9.6)$$

with

$$\Gamma_{\text{th},e}(k) = \sqrt{32\pi^3} \rho \sqrt{m_e k_B T} \left(\frac{v_M}{B} \right)^2 \frac{W_k^B}{W_k} \mathcal{I}(x) k, \quad (9.7)$$

and

$$\mathcal{I}(x) = 2 \int_1^\infty dx \left(\frac{1}{x} - \frac{1}{x^3} \right) \exp \left[-x^2 \left(\frac{v_M}{v_{\text{th}}} \right)^2 \right]. \quad (9.8)$$

Here v_M^2 is given by Eq. 9.3 and $v_{\text{th}}^2 = \frac{2k_B T}{m_e}$ is the thermal velocity of the electrons (please see Sec. 4.2 of [Cassano & Brunetti, 2005](#), for more details). To explicitly solve D_0 at *every* timestep we express it as

$$D_0(t) = \frac{4.45\pi^2}{c \sqrt{32\pi^3} m_e k_B} \frac{\eta_t a_k E_{\text{turb}}}{n_e V_p \sqrt{T} \Delta t \mathcal{I}(x)}, \quad (9.9)$$

where η_t is the free parameter introduced by [Cassano & Brunetti \(2005\)](#) with $\eta_t = 0.2$ in this model, E_{turb} is the turbulent energy, V_p is the kernel volume of a particle and a_k is the turbulent scale factor

$$a_k = \frac{k_{\text{max}}^{-2/3} - k_{\text{min}}^{-2/3}}{k_{\text{mps}}^{-2/3} - k_{\text{h}}^{-2/3}}. \quad (9.10)$$

The different components of this are k_{min} and k_{max} as the integral limits for Eq. 9.4, the wavelength of the mean particle separation $k_{\text{mps}} = N_{\text{ngb},i}^{1/3}/(2h_i)$ and the maximum wavelength within a kernel of smoothing length h_i , $k_{\text{h}} = 1/(2h_i)$. k_{min} and k_{max} are free parameters in this model and can be expressed as the inverse of the injection and dampening scale of the MS waves which for the purpose of this work take the values

$$\begin{aligned} k_{\text{min}} &= (\Lambda_{\text{inj}})^{-1} = (200 \text{kpc})^{-1} \\ k_{\text{max}} &= (\Lambda_{\text{damp}})^{-1} = (0.1 \text{kpc})^{-1} \end{aligned} .$$

9.2 Systematic Re-Acceleration

To model the systematic component of the re-acceleration we use the so-called ‘unified cooling approach’. This extends the $b_l(p)$ term in Eq. 5.4 to include the systematic component of the re-acceleration

$$\sum_l b_l(p) \equiv \left(\frac{dp}{dt} \right)_{\text{cool}}^{\text{synch}} + \left(\frac{dp}{dt} \right)_{\text{cool}}^{\text{IC}} + \left(\frac{dp}{dt} \right)_{\text{acc}}^{\text{sys}} . \quad (9.11)$$

Combining Eq. 9.2 and Eq. 9.5 gives the short form of

$$\left(\frac{dp}{dt} \right)_{\text{acc}}^{\text{sys}} = -2D_0(t) p . \quad (9.12)$$

With Eq. 9.12 this leads to an upper integration boundary of

$$p_u = p_i \cdot e^{-2D_0\Delta t} \quad (9.13)$$

and a spectral cut update of

$$p_{\text{cut},t+\Delta t} = p_{\text{cut},t} \cdot e^{2D_0\Delta t} . \quad (9.14)$$

Solving Eq. 5.19 with Eq. 9.12 gives

$$R_{D_{\text{pp}}} = -2D_0, \quad (9.15)$$

as all prefactors cancel out.

We note that this approach is a simplification and neglects the stochastic component of the turbulent re-acceleration. It does however counter the radiative loss processes of high-momentum electrons and with that provides the basis for studying the stabilisation of radio haloes in galaxy clusters against the cooling times of their electrons.

The exponential dependency on D_0 and the timestep Δt puts a significant timestep constraint on the simulation and needs to be handled with care. We therefore subcycle the solver if $D_0\Delta t > 10^{-5}$.

9.3 Stochastic Re-Acceleration

The stochastic part of Fermi-II re-acceleration can be written as

$$\frac{Df}{Dt} = \frac{1}{p^2} \frac{\partial}{\partial p} \left(p^2 D_{\text{pp}} \frac{\partial f}{\partial p} \right) \quad (9.16)$$

$$= D_0 \frac{1}{p^2} \frac{\partial}{\partial p} \left(p^4 \frac{\partial f}{\partial p} \right) \quad (9.17)$$

where we again used $D_{\text{pp}} = D_0 p^2$.

By multiplying Eq. 9.17 with $4\pi/\rho p^2$ for CR number and $4\pi/\rho c p^3$ for CR energy, as we did for

adiabatic changes and energy losses, we arrive at

$$\frac{DN_i}{Dt} = -\frac{4\pi D_0}{\rho} q_i f_i p_i^3 \left[\left(\frac{p_{i+1}}{p_i} \right)^{3-q_i} - 1 \right] \quad (9.18)$$

$$\frac{DE_i}{Dt} = -\frac{4\pi c D_0}{\rho} q_i f_i p_i^4 \frac{3-q_i}{4-q_i} \left[\left(\frac{p_{i+1}}{p_i} \right)^{4-q_i} - 1 \right] \quad (9.19)$$

as the rate of change of CR number and energy of bin i over a timestep Δt .¹

Please note that this component of re-acceleration is not yet implemented, nonetheless, we list it here for completeness and to facilitate a future implementation.

¹We thank Sebastian Nuza for confirming this derivation.

10 | Spatial Propagation

The propagation of CRs in physical space and the physical processes involved have been the matter of quite some debate (for a recent review see [Hanasz et al., 2021](#)).

The two main ideas discussed in the literature are *CR diffusion* and *CR streaming*.

In CR diffusion, the particles propagate along magnetic field lines with a constant, or energy-dependent diffusion coefficient. The value of this diffusion coefficient and its energy dependence is highly uncertain and may be different between the ISM and ICM. With diffusion an initially Gaussian spatial distribution of CRs will remain Gaussian, but broaden its width over time.

In CR streaming the particles stream down a CR pressure gradient with a streaming velocity v_{st} . This streaming velocity generally depends on the magnetic field strength and density in the medium and is of the order of the Alfvén, or sound speed (see e.g. [Enßlin et al., 2011](#), for a detailed discussion). With streaming an initially Gaussian spatial distribution of CRs will flatten and expand in a top-hat-like shape.

However, recent results from plasma simulations by [Reichherzer et al. \(2023\)](#) show that CRs with energies $E < 1$ TeV can be efficiently confined by magnetic micromirrors in pockets of plasma within the ICM. This would indicate that CRs are frozen into the plasma of the ICM like magnetic fields and transported primarily via advection.

In this chapter, we will discuss the currently implemented models of CR transport. The spatial diffusion model is not yet finished at the time of this writing. We will nonetheless discuss the model here and show preliminary tests, in order to use this work as a basis for future improvements. For future improvements, we refer to the extensive derivation of a general CR transport formalism for spectral CR models by [Hopkins et al. \(2022b\)](#).

10.1 Artificial Conduction

We adopted a simplified version of an isotropic diffusion model to counter numerical noise introduced by the shock finder in simulations where no physical diffusion is required. This is for example the case in the idealized cluster merger simulation in Chapter 13, where only initial acceleration is modeled and propagation times are longer than the relevant cooling times of synchrotron bright CR electrons.

In the case of simplified diffusion, we update the quantity Q of particle i based on the neighboring

particles j with

$$\frac{dQ_i}{dt} = \sum_j \frac{m_j}{\rho_i \rho_j} \kappa_c v_{\text{sig}} (Q_j - Q_i) \nabla_i W_{ij} \quad (10.1)$$

where κ_c is a constant diffusion coefficient and v_{sig} is the signal velocity of the CRs, which in the simplest case is equal to the Alfvén velocity. For the work in Chapter 13 we use $\kappa \approx 5 \times 10^{26} \frac{\text{cm}^2}{\text{s}}$ and the Alfvén velocity in the ICM is typically of the order $v_A = \frac{B}{\sqrt{\rho}} \approx 10^2 \frac{\text{km}}{\text{s}}$. We find that even this simple approach conserves the total energy to a relative error of only 0.2 percent over 1 Gyr.

10.2 Isotropic Momentum Dependent Diffusion

CRs are expected to diffuse along the CR pressure gradient with a momentum dependent diffusion coefficient κ . This gives an expression for the CR flux

$$\vec{j}_{\text{CR}} = -\kappa \nabla P_{\text{CR}} \quad (10.2)$$

as used e.g. in [Hanasz & Lesch \(2003\)](#). In "gray models", where only a total energy density of CRs is modeled, κ typically takes a fixed value for the total momentum range of the order $\kappa \sim 10^{26} - 10^{30} \text{ cm}^2 \text{ s}^{-1}$ (e.g. [Pfrommer et al., 2017](#); [Butsky & Quinn, 2018](#)).

However, in our case, we resolve a momentum distribution of CRs, hence we need to account for $\kappa(p)$ (possibly) being momentum dependent. With our spectrum being discretized in momentum, we also need to discretize $\kappa(p)$ in momentum.

For this work, we follow the approach of "bin-centered diffusion" (as in [Girichidis et al., 2020](#); [Ogrodnik et al., 2021](#)). In this approach, the diffusion coefficient is calculated at the logarithmic center of the bin and applied to the quantity $Q_i(\hat{p})$ in the whole bin. We compute the diffusion coefficient relative to a reference coefficient κ_{10k} at the dimensionless momentum $\hat{p} = 10^4$ as

$$\kappa(\hat{p}) = \kappa_{10k} \left(\frac{\hat{p}}{10^4} \right)^{\alpha_\kappa} \quad (10.3)$$

where the momentum dependence is added via the free parameter α_κ . With this the diffusion can be based on thermal conduction formulated for SPH ([Jubelgas et al., 2004](#)) as

$$\frac{dQ_i(\hat{p})}{dt} = \sum_j \frac{m_j}{\rho_i \rho_j} \frac{\kappa_{ij}(\hat{p})(Q_j(\hat{p}) - Q_i(\hat{p}))}{|\mathbf{x}_{ij}|^2} \mathbf{x}_{ij} \nabla_i W_{ij} \quad (10.4)$$

where i and j are the quantities for the SPH particle i and j , respectively. m and ρ are particle mass and density, respectively. $\mathbf{x}_{ij} \equiv \mathbf{x}_j - \mathbf{x}_i$ is the vector between the respective particle positions and W_{ij} is the kernel value of particle i at the position of particle j .

For $\kappa_{ij}(\hat{p})$ we use the arithmetic mean between $\kappa(\hat{p})$ of each particle. In most cases, this mean will be the same values for both particles i and j . Only in cases where a bin is partially filled and the diffusion coefficient is calculated as the mean between lower momentum bin boundary and spectral cutoff, or where the cutoff moves to higher momenta than the initial \hat{p}_{max} (due to

adiabatic compression or Fermi-II re-acceleration) this should of relevance.

Finally, $Q_i(\hat{p})$ is the quantity that is to be diffused, i.e. either CR number or energy in a bin.

One problem arising from a bin-centered diffusion model is that the distribution functions are no longer smooth. As both moments diffuse with the same diffusion coefficient the slope within the bin stays constant, while the normalization of the bin may increase, or decrease. This leads to a step-like morphology of the distribution functions. [Girichidis et al. \(2022\)](#) remedy this behavior by reverting to a 1-moment approach and only diffusing E . This is followed by a reconstruction step of f_i which is only based on energy and connects the normalizations of neighboring bins. That connection is then used to recompute a slope and from that N can be reconstructed by accepting an artificial error in N .

10.3 Anisotropic Momentum Dependent Diffusion

In the case of anisotropic CR diffusion, we employ the bi-conjugate gradient solver used by [Petkova & Springel \(2009\)](#) and implemented as anisotropic thermal conduction into `OpenGadget3` by [Arth et al. \(2014\)](#). Here we only outline the solver in broad strokes, for a more detailed derivation please see [Arth et al. \(2014\)](#).

First, we rewrite the diffusion coefficient in its proper anisotropic form as

$$\kappa_{ij}(p) = \kappa_{\perp}(p) \delta_{ij} + (\kappa_{\parallel}(p) - \kappa_{\perp}(p)) b_i b_j \quad (10.5)$$

where $b_i = B_i/|\mathbf{B}|$ and

$$\kappa_{\parallel}(p) = \kappa_{10k} \left(\frac{p_i}{10^4} \right)^{\alpha_{\kappa}}; \quad \kappa_{\perp} = 0.01 \kappa_{\parallel} \quad (10.6)$$

as in [Ogrodnik et al. \(2021\)](#). We then rewrite Eq. 10.4 in the conjugate gradient formalism

$$\frac{dQ_i}{dt} \rightarrow \frac{\Delta Q_i}{\Delta t} = \frac{Q_i^{n+1} - Q_i^n}{\Delta t} \quad (10.7)$$

where

$$Q_i^{n+1} = Q_i^n + \sum_{j=1}^{N_{\text{NGB}}} c_{ij} (Q_i^{n+1} - Q_j^{n+1}). \quad (10.8)$$

c_{ij} are the matrix elements of the interaction matrix, with

$$c_{ij} = -\kappa_{ij}(p) \frac{m_j \Delta t}{\rho_i \rho_j} \frac{\vec{x}_{ij}^T}{|\vec{x}_{ij}|^2} (\tilde{A}_i + \tilde{A}_j) \nabla_i W_{ij} \quad (10.9)$$

where the subscripts i and j correspond to the quantities of SPH particle i and j , respectively. $\kappa_{ij}(p)$ is the arithmetic mean of the anisotropic, momentum-dependent diffusion coefficient, following Eq. 10.6. Here we again need to be cautious when computing $\kappa_{ij}(p)$ between partially

filled bins, or extended distribution functions.

This allows us to write the diffusion as a matrix problem

$$\mathbf{C} \cdot \mathbf{x} = \mathbf{b} \quad (10.10)$$

where

$$C_{ij} = \delta_{ij} \left(1 - \sum_k c_{ik} \right) + c_{ij} \quad (10.11)$$

$$x_j = Q_j^{n+1} \quad (10.12)$$

$$b_i = Q_i^n \quad (10.13)$$

Knowing the initial quantities Q_i^n and explicitly calculating the matrix elements of C_{ij} , allows to effectively solve the diffusion step backward. This is done by inverting the matrix C from Eq. 10.10 using a bi-conjugate gradient solver. This inverted matrix is then applied to the initial quantities to obtain the updated quantities after a timestep Δt .

In the current state, we solve the anisotropic CR diffusion by computing the interaction matrix and its inversion for CR number and energy per bin individually, for protons and electrons. With our most common discretization for the CR distribution functions with 12 bins for protons and 48 bins for electrons this results in having to solve the anisotropic CR diffusion 120 times per timestep. Given that anisotropic thermal conduction, which only needs to be solved once per timestep, adds a factor of \sim two to the overall run time of the simulation, this makes a production run with our current implementation impossible.

One potential solution could be to reformulate the anisotropic CR diffusion to diffuse all quantities at once, effectively turning \mathbf{x} and \mathbf{b} in Eq. 10.10 into matrices and \mathbf{C} into a tensor. The interaction tensor could then be filled in a single process, drastically reducing the number of required tree walks and MPI communications in the code. Inverting the tensor \mathbf{C} could then be done in individual matrices, like a Rubik's Cube. GPUs are designed to perform highly efficient matrix and tensor operations, so porting the solver to a GPU could result in a significant performance boost. The anisotropic thermal conduction has the option to be run on a GPU, with significant performance improvements (Ragagnin et al., 2020). This implementation can be used as a basis for future work.

10.4 Tests

Due to the significant computational cost of our diffusion model, it has not been finished as of the time of this writing. For completeness, we will nevertheless show the initial tests as a basis for future work. Please note that these tests are only meant to be qualitative to show the behavior of CR diffusion.

Following Hanasz & Lesch (2003); Ogrodnik et al. (2021) we set up a pseudo canonical SN

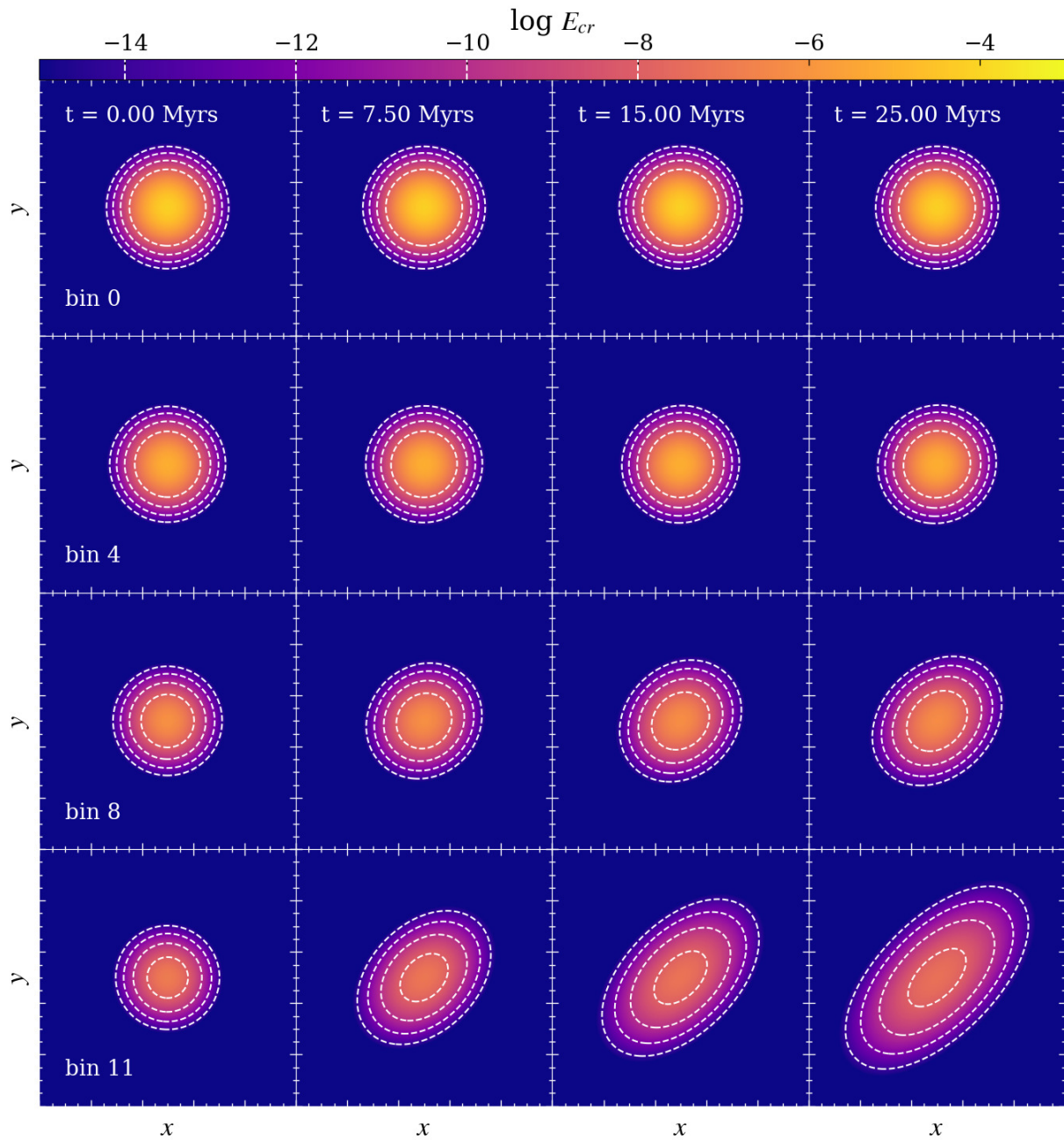


Figure 10.1: Anisotropic diffusion along a diagonal magnetic field in xy -direction. Colors show the CR energy per bin in code units, with contours indicating $\log_{10} E_{cr} \in [-14, -12, -10, -8]$ for clarity. *Top to bottom*: A selection of spectral bins with increasing momentum. *Left to right*: The time evolution of the diffusion.

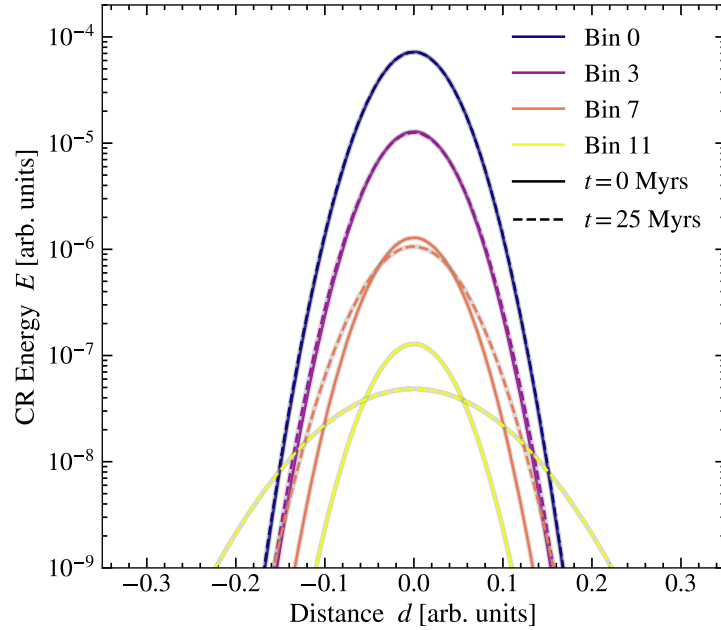


Figure 10.2: Profiles for Fig. 10.1, obtained from a diagonal slice in xy -direction. Colors correspond to the bins shown in the previous figure. Solid lines indicate the initial state, and dashed lines show the system after 25 Myrs.

explosion where we inject a fraction of the thermal energy into the CR component with a Gaussian profile

$$E_{\text{CR}} = \frac{K_{\text{ep}} \eta_{\text{SN}} E_{\text{SN}}}{\pi^{3/2} r_0^3} \times \exp\left(-\frac{||\Delta\vec{r}'||^2}{r_0^2}\right). \quad (10.14)$$

The gas component is set back to the ambient temperature and the CR component is scaled down according to some arbitrary efficiency η_{SN} to avoid a kinematic impact of the CRs on the surrounding gas. This gives a well-defined test bed for the different streaming/diffusion models. To test the anisotropic bin-centered diffusion we set up an additional magnetic field. The magnetic field is oriented diagonally in the positive xy -direction.

Following [Ogrodnik et al. \(2021\)](#), the time evolution of such a system can be expressed as

$$E_i(r_D, t) = \frac{K_{\text{ep}} \eta_{\text{SN}} E_{\text{SN}}}{\pi^{3/2} r_0^3} \frac{E_i(r_D, 0)}{E_{\text{tot},0}} \times \quad (10.15)$$

$$\sqrt{\frac{r_0^2}{r_0^2 + 4\kappa_{\parallel}(p)t}} \exp\left(\frac{-r_D^2}{r_0^2 + 4\kappa_{\parallel}(p)t}\right). \quad (10.16)$$

In Fig. 10.1 we show the qualitative behavior of our diffusion model. Top to bottom show bins with increasing momentum. In this case, we set up 12 momentum bins in the range $\hat{p} \in [1, 10^6]$. From left to right we show the time evolution of the spectral bins. The color map shows the CR energy per bin in code units, with the contours indicating $\log_{10} E_{\text{cr}} \in [-14, -12, -10, -8]$ for

clarity. We can clearly see how the CRs only diffuse along the diagonal magnetic field and do so faster with increasing momentum. This can be seen easiest in the lowest row of Fig. 10.1, which shows CRs in the momentum range $\hat{p} \in [3.16 \times 10^5, 10^6]$ of our highest momentum bin and with that the highest diffusion coefficient.

In Fig. 10.2 we show the profiles obtained from the same simulation. For these profiles, we take a diagonal cut in the image plane shown in Fig. 10.1 and sort the particles by distance from the image center. Solid lines show the initial state of the simulation, and dashed lines show the state after 25 Myrs. We find the expected behavior of CR diffusion, namely that the initial Gaussian profile is preserved and broadens. The rate of this broadening depends on the momentum at the bin center, due to our momentum dependence of $\kappa(p)$.

11 | Observables

One of the key advantages of a spectral CR model is the possibility of obtaining observables of the population directly from the simulation output. In this chapter, we will show how we compute the synchrotron emission from our CR spectra and the γ -ray emission from our CRp spectra.

11.1 Synchrotron Emission

As discussed in Sec. 3.1, high energy electrons emit synchrotron radiation as they gyrate around magnetic field lines in the ICM. In this section, we will show how to obtain the total and polarized synchrotron emission for a spectrum of electrons simulated with our model.

11.1.1 Emissivity

To calculate the synchrotron emission of our distribution function we take the same approach as [Donnert et al. \(2016\)](#); [Mimica et al. \(2009\)](#) and follow [Ginzburg & Syrovatskii \(1965\)](#). With this the synchrotron emissivity j_ν in units of [$\text{erg cm}^{-3} \text{s}^{-1} \text{Hz}^{-1}$] for a distribution function of CR electrons in dimensionless momentum space $f(\hat{p}, t)$ can be expressed as

$$j_\nu(t) = \frac{\sqrt{3}e^3}{m_e^2 c^3} B(t) \sum_{i=0}^{N_{\text{bins}}} \int_0^{\pi/2} d\theta \sin^2 \theta \int_{\hat{p}_i}^{\hat{p}_{i+1}} d\hat{p} 4\pi \hat{p}^2 f(\hat{p}, t) \mathcal{F}(x) \quad (11.1)$$

where e is the elementary charge of an electron, c is the speed of light, \hat{p} is the dimensionless momentum and $\mathcal{F}(x)$ is the first synchrotron function

$$\mathcal{F}(x) = x \int_x^\infty dz K_{5/3}(z) \quad (11.2)$$

using the Bessel function $K_{5/3}$ at a ratio between observation frequency ν and critical frequency ν_c

$$x \equiv \frac{\nu}{\nu_c} = \frac{\nu}{C_{\text{crit}} B(t) \sin \theta \hat{p}^2}; \quad C_{\text{crit}} = \frac{3e}{4\pi m_e c} \quad (11.3)$$

We solve the momentum integrals by employing the Simpson rule, which constructs a mid-point by interpolating the simulated spectrum and the pitch angle integrals with a trapeze integration.

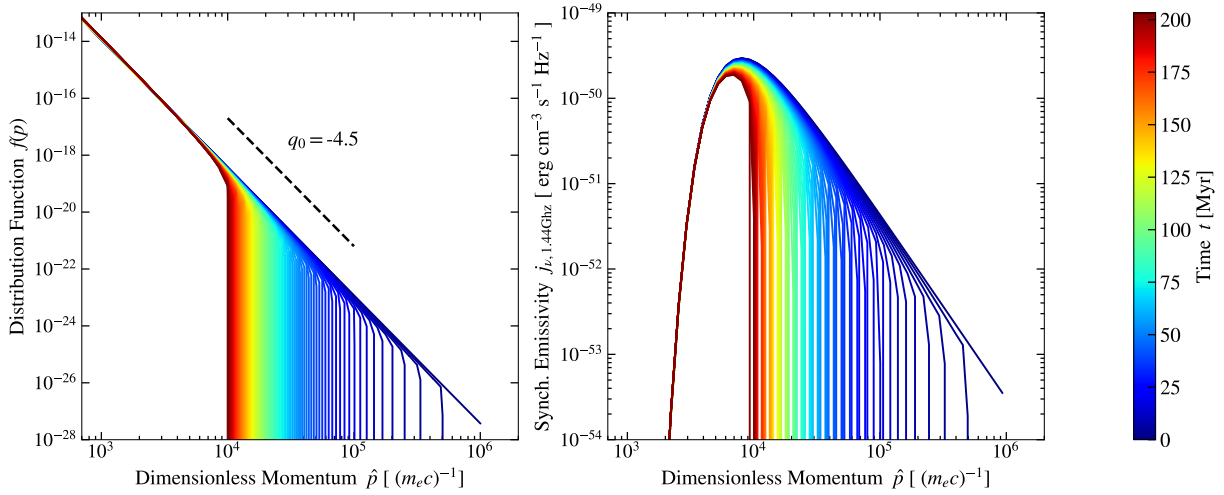


Figure 11.1: We show the spectral distribution and emissivity per bin of a CR electron population undergoing IC cooling by CMB photons. As the spectrum cools we can see that the contribution to the total emissivity at 1.4 GHz decreases for the higher bins. Dashed lines show the analytic solution of the slopes of a spectrum without cooling.

11.1.2 Intensity

The fraction of the total synchrotron intensity a SPH particle contributes to is found via

$$I_\nu = \int dz j_\nu \quad (11.4)$$

where dz is the depth of the particle along the LOS. In practice, it is most useful to map the SPH particles onto a grid and integrate the emissivity along the LOS in this process. This produces mock observations at grid-resolution and can be smoothed with a Gaussian beam at the size of the telescope's beam, to compare with observations.

11.1.3 Luminosity

From Eq. 11.1 we can compute a synchrotron luminosity per SPH particle by integrating the emissivity over the particle volume.

$$P_\nu = \int_\Omega dV j_\nu \quad (11.5)$$

where $\int_\Omega dV \equiv \frac{m_i}{\rho_i}$ is the volume of the SPH particle i . The total luminosity of the object is found by summing up the contribution of all relevant particles.

11.1.4 Flux

The flux relates to luminosity as

$$F_\nu = \frac{P_\nu}{4\pi D_L^2} \quad (11.6)$$

where D_L is the luminosity distance. This can be used to convert from total luminosity in [P_ν] = [W Hz^{-1}] to total flux in [Jy].

In most cases, one will want to compare to observed flux in units [Jy beam^{-1}]. For this, it is most convenient to first map the emissivity to a 2D grid as in Eq. 11.4. We then obtain an image with units [$\text{erg s}^{-1} \text{Hz}^{-1} \text{cm}^{-2}$] consisting of pixels with side-length Δx . In the first step, we need to convert the beam size in units ["] to units [kpc] at the image redshift. This conversion can be performed via

$$d_{\text{beam}} = \frac{2\pi}{360} \left(\frac{D_A}{\text{kpc}} \right) \left(\frac{\theta_{\text{beam}}}{3600''} \right) \quad (11.7)$$

where D_A is the angular diameter distance. We then obtain the synchrotron luminosity per pixel by multiplying the intensity maps with the pixel area

$$P_\nu(\text{pix}) = I_\nu(\text{pix}) \times (\Delta x)^2 \times 10^{-7} [\text{WHz}^{-1}] \quad (11.8)$$

where the extra factor 10^{-7} accounts for the conversion from [erg s^{-1}] to [W]. We then convert the synchrotron power per pixel to a flux, using Eq. 11.6 and compute the observed flux per beam via

$$F_\nu(\text{pix}) = \frac{P_\nu(\text{pix})}{4\pi D_L^2} \times \left(\frac{\pi d_{\text{beam}}^2}{(\Delta x)^2} \right) \quad (11.9)$$

which gives an image in units [mJy beam^{-1}] for each pixel.

11.1.5 Synchrotron Spectra

A population of CRes with an initial slope q_0 in momentum space generates a synchrotron spectrum with spectral index

$$\alpha_0 = \frac{q_0 - 3}{2} \quad (11.10)$$

for a given magnetic field strength B . We find that we recover this relation with very high accuracy, to an error below 0.1%, and show our obtained relation in Fig. 11.2. As the CR population cools and higher momentum bins depopulate we observe spectral steepening, in agreement with the observations in radio relics (e.g. [Di Gennaro et al., 2018](#)). Additionally the emissivity scales with the magnetic field B as

$$j_\nu \propto B^{\alpha_0+1} \nu^{-\alpha_0} \quad (11.11)$$

which indicates a strong scaling of synchrotron emission with $j_\nu \sim B^2$ for typical synchrotron spectra with $\alpha_0 \sim 0.75 - 1.2$. This strong scaling should be taken into account when comparing simulated radio spectra with observations, as magnetic fields in simulations tend to be strongly resolution dependent (see e.g. the resolution study in [Steinwandel et al., 2022](#)). We show our

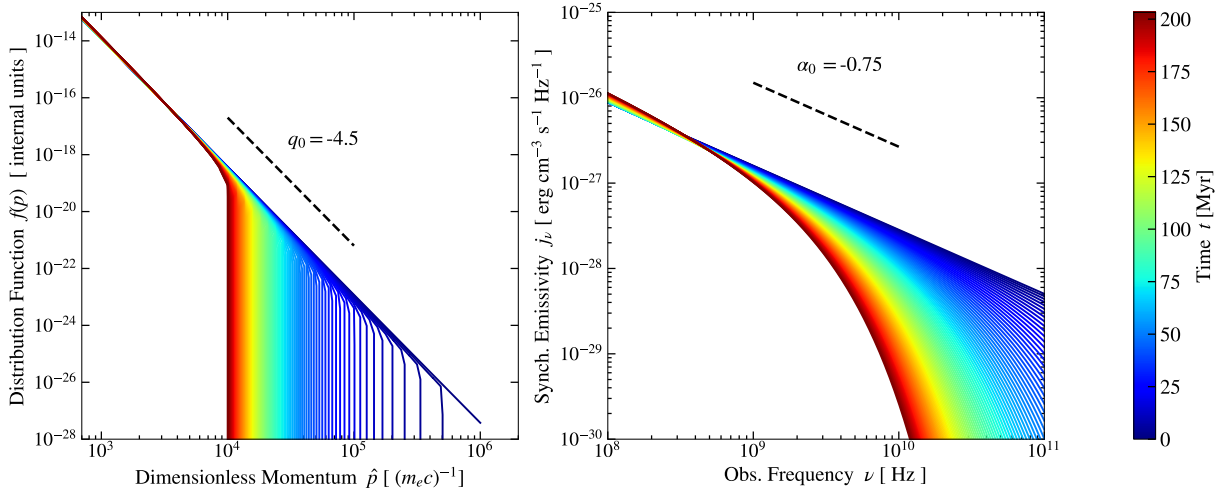


Figure 11.2: We show the spectral distribution and the synchrotron emissivities of a CR electron population undergoing cooling due to IC scattering off CMB photons as a function of observational frequency. Dashed lines show the analytic solution of the slopes of a spectrum without cooling. We nicely recover the analytic slope of the synchrotron spectrum and observe the spectral steepening of the aging population.

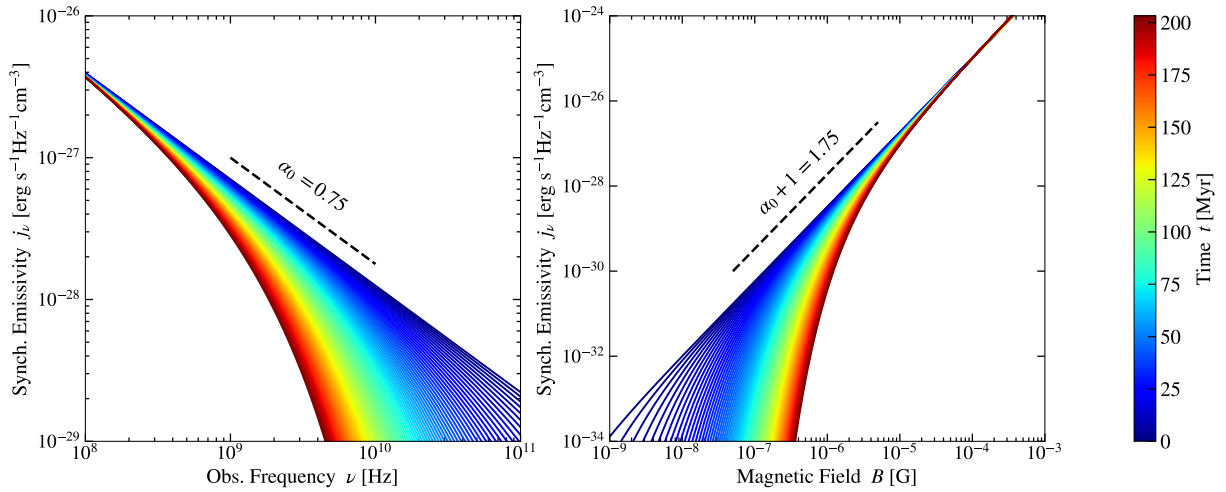


Figure 11.3: We show the synchrotron emissivities of a CR electron population undergoing cooling due to IC scattering off CMB photons as a function of observational frequency and magnetic field. Dashed lines show the analytic solution of the slopes of a spectrum without cooling.

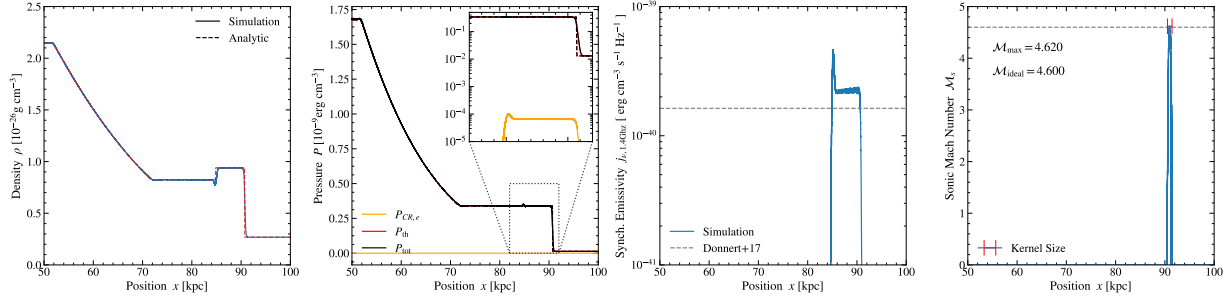


Figure 11.4: Idealized shock tube using the parameters for CIZA provided in [Donnert et al. \(2016\)](#). We find excellent agreement to the analytic solution of the Riemann problem and shock capturing. For the synchrotron emissivity, we employ a fixed magnetic field of $B = 5\mu\text{G}$. This emissivity agrees well with the emissivity reported in [Donnert et al. \(2017\)](#).

agreement with the analytic solution in Fig. 11.3 and again find excellent agreement. Only in the $B \sim 10^{-9}$ G regime do we find a slight under-prediction of our calculation.

11.1.6 Tests

We show the results of the CIZA shocktube discussed in Sec. 13.5.4 in Fig. 11.4. Initial parameters are given in Tab. A.1 and are obtained from [van Weeren et al. \(2010\)](#); [Ogrea et al. \(2014\)](#); [Akamatsu et al. \(2015\)](#) as gathered by [Donnert et al. \(2017\)](#). We find overall excellent agreement with the analytic solution (dashed lines in density, pressure, and Mach number), as well as the result for emissivity at 1.4GHz by [Donnert et al. \(2017\)](#).

11.2 Stokes Parameters

In addition to the total synchrotron emissivity we can also calculate only the polarized component of the synchrotron emissivity. Following [Ginzburg & Syrovatskii \(1965\)](#) we define the polarized emission as

$$j'_\nu(t) = \frac{\sqrt{3}e^3}{c} B_\perp(t) \sum_{i=0}^{N_{\text{bins}}} \int_0^{\pi/2} d\theta \sin^2 \theta \int_{\hat{p}_i}^{\hat{p}_{i+1}} d\hat{p} 4\pi \hat{p}^2 f(\hat{p}, t) \mathcal{G}(x) \quad (11.12)$$

where $B_\perp(t) \equiv |\mathbf{B}(t) \times \hat{n}_{\text{los}}|$ is the component of the magnetic field in the image plane,

$$\mathcal{G}(x) = xK_{2/3}(x) \quad (11.13)$$

is the second synchrotron function with $K_{2/3}$ being a Bessel function and x is given in Eq. 11.3 (here we only take into account the planar component of the magnetic field $B_\perp(t)$). The Stokes parameters Q_ν and U_ν , describing the polarisation of the synchrotron emission, can now be

obtained by integrating along the line of sight of the image

$$Q_\nu = \int dz j'(\nu, x, y, z) \cos 2\hat{\chi} \quad (11.14)$$

$$U_\nu = \int dz j'(\nu, x, y, z) \sin 2\hat{\chi} \quad (11.15)$$

taking into account the local polarisation angle $\hat{\chi}$ (see Fig. 3 in [Domínguez-Fernández et al., 2021](#), for an instructive visualisation of the angles involved).

11.2.1 Polarized Emission

Having computed the Stokes parameters we can now obtain the polarized component of the synchrotron emission. The degree of (linear) polarization, also canonically referred to as *polarisation fraction* can be obtained from the Stokes parameters as

$$\Pi = \frac{\sqrt{Q_\nu^2 + U_\nu^2}}{I_\nu} \quad (11.16)$$

where I_ν is the total synchrotron intensity as computed with Eq. 11.4. Similarly, we can construct the polarisation angle ψ from

$$\psi = \frac{1}{2} \arctan\left(\frac{U_\nu}{Q_\nu}\right) \quad (11.17)$$

As shown by e.g. [Westfold \(1959\)](#), the polarisation angle ψ is always perpendicular to the angle of the magnetic field in the sky plane (θ) and it, therefore, follows trivially that $\psi = -\theta$. This angle undergoes Faraday rotation, as the integration along the LOS proceeds and must be continuously rotated accordingly (we again refer to Fig. 3 in [Domínguez-Fernández et al., 2021](#)). In principle also redshift dependent Faraday rotation effects must be taken into account, as the photons propagate towards earth ([Vallee, 1975](#)). However, due to constraints on the strength of magnetic fields in voids, these effects are typically ignored.

11.2.2 Tests

We test Eq. 11.18 by applying the computation of the Stokes parameters to a single spectrum and show the result in the left panel of Fig. 11.5. We find nearly perfect agreement over the tested range, except for a slight over-prediction of slopes harder than $q \approx 3.8$. As DSA however, only produces spectra steeper than $q = 4$ this error is generally not a problem in the systems we consider.

The maximum polarization for a perfectly planar magnetic field scales with energy slope s or momentum slope q as (see e.g. [Longair, 2011](#))

$$\Pi_{\max} = \frac{s+1}{s+\frac{7}{3}} = \frac{q-1}{q+\frac{1}{3}} \quad (11.18)$$

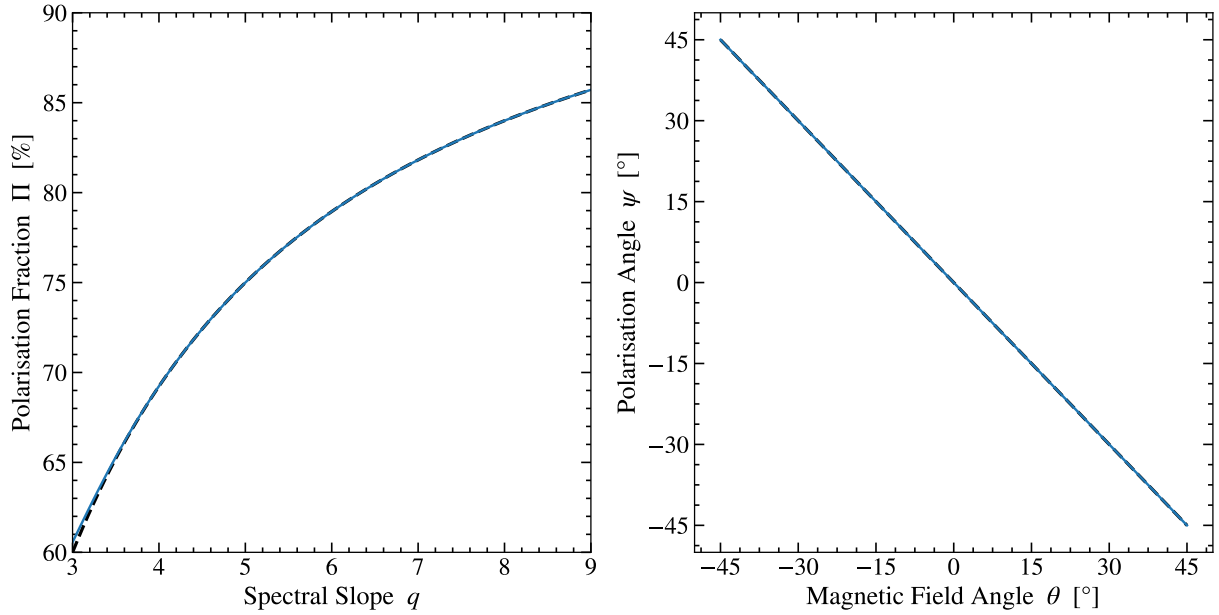


Figure 11.5: *Left:* Polarisation fraction for a planar magnetic field as a function of spectral slope. *Right:* Polarisation angle ψ for a planar magnetic field with angle θ in the xy -plane. In both plots dashed lines indicate the analytic solution and solid lines show the result from our calculations.

so for a constant magnetic field the maximum polarisation increases as the spectral slope increases. This has implications for radio relics which typically show a polarisation fraction at 1.4 GHz of $\sim 30\%$ (e.g. [Rajpurohit et al., 2020b](#)).

In the right panel of Fig. 11.5 we tested our computation of Eq. 11.17 for the same CRe spectrum and found agreement with the analytic solution, up to machine precision.

11.3 γ -ray Emission

The second non-thermal emission process relevant for observations of GCs is γ -ray emission by CRps scattering off thermal background protons. We discussed this emission mechanism in Sec. 3.2 and will now show how to calculate it from our simulated CRp spectra.

11.3.1 Parametrization

In this work, we follow the parametrization by [Kafexhiu et al. \(2014\)](#) (similar to [Werhahn et al., 2021](#), described in detail in their Appendix A1). As is the case in any interaction between particles the core concept is the differential cross-section of the process, which describes how large the interaction surface of the process is and from that gives a rate at which such processes can occur in media of a certain density. In the case of the interaction between relativistic and

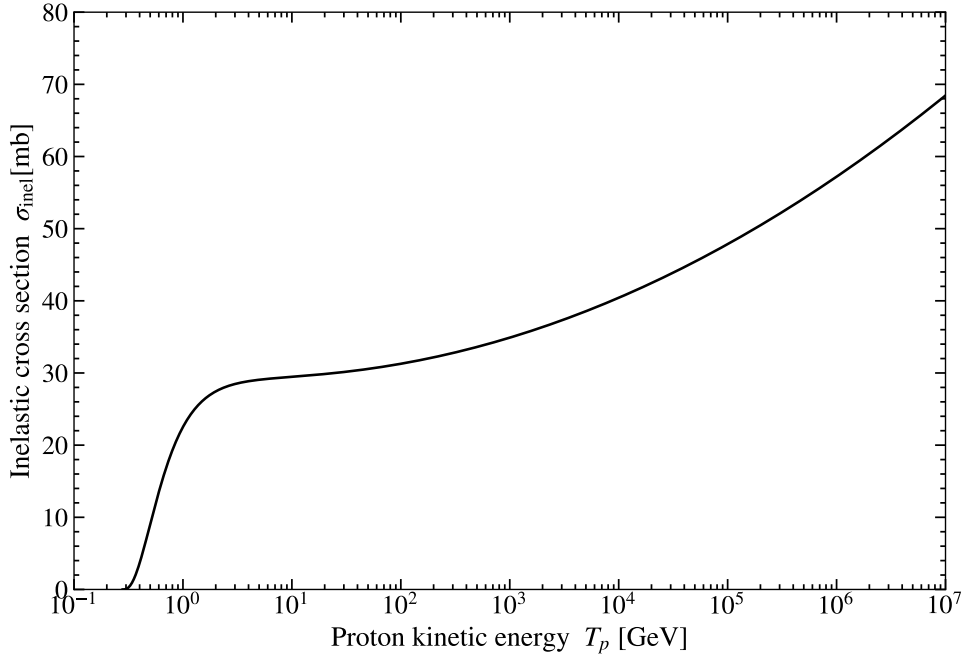


Figure 11.6: Total inelastic cross-section as a function of proton energy.

thermal protons which produces neutral π -ons, this is given as

$$\frac{d\sigma_\gamma(E, E_p)}{dE} = 2 \int_{E_{\pi, \min}}^{E_{\pi, \max}} dE_\pi \frac{d\sigma_\pi(E_p, E_\pi)}{dE_\pi} f_{\gamma, \pi}(E, E_\pi) \quad (11.19)$$

where the factor 2 stems from the production of two photons per decay event. The normalized energy distribution $f_{\gamma, \pi}(E, E_\pi)$ is a Green's function which describes the probability for a pion at energy E_π to produce a γ photon at energy E . Following [Stecker \(1971\)](#) it is given as

$$f_{\gamma, \pi}(E, E_\pi) = \frac{1}{\sqrt{E_\pi^2 - E_{\pi, 0}^2}} \quad (11.20)$$

with $E_{\pi, 0}$ being the rest-mass energy of a π -on.

There is no exhaustive analytic description of Eq. 11.19 currently in the literature, however, there are parametrizations from experiments and numerical models available. As mentioned before we used the parametrization by [Kafexhiu et al. \(2014\)](#) who provide fits to various numerical modeling tools. We use their fits to the data obtained with the GEANT4 toolkit ([Agostinelli et al., 2003](#); [Allison et al., 2006](#)).

They parametrize Eq. 11.19 with

$$\frac{d\sigma_\gamma(E, E_p)}{dE} = A_{\max}(E_p) F(E_p, E) \quad (11.21)$$

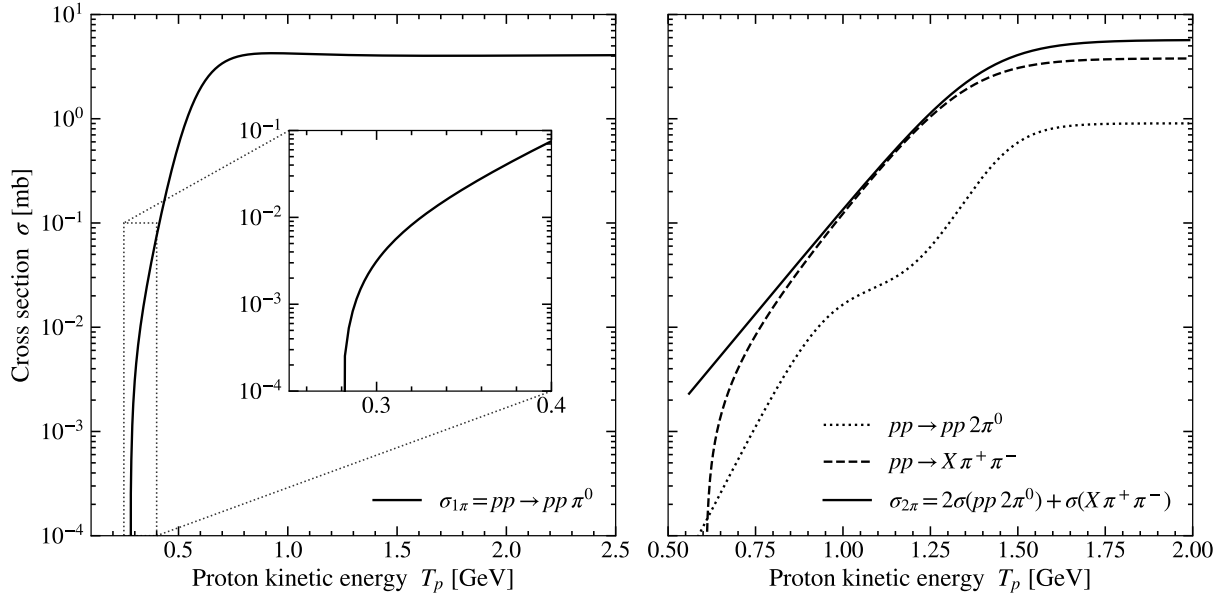


Figure 11.7: Cross sections for the different pp interaction channels for the very low energy range.

where $A_{\max}(E_p)$ describes the peak of the γ -ray cascade and $F(E_p, E)$ is a complex fit formula that describes the shape of the resulting cascade spectrum. $A_{\max}(E_p)$ can be expressed as

$$A_{\max}(E_p) = \left\{ \begin{array}{ll} b_0 \times \frac{\sigma_{pp,\text{inel}}(E_p)}{E_{\pi}^{\max}}, & \text{for } E_p^{\text{th}} \leq E_p \leq 1 \text{ GeV} \\ b_1 \theta_p^{-b_2} \exp(b_3 \log^2(\theta_p)) \times \frac{\sigma_{pp,\text{inel}}(E_p)}{E_{p,0}}, & \text{for } E_p \geq 1 \text{ GeV} \end{array} \right\} \quad (11.22)$$

where b_i are fit parameters, which we omit here for brevity, E_{π}^{\max} is the maximum π -on energy in the lab frame allowed by the kinematics and $E_{p,0}$ is the proton rest mass. Finally $\sigma_{pp,\text{inel}}(E_p)$ is the inclusive π^0 production cross section given as

$$\sigma_{pp,\text{inel}}(T_p) = \left[30.7 - 0.96 \log\left(\frac{T_p}{T_{p,\text{th}}}\right) + 0.18 \log^2\left(\frac{T_p}{T_{p,\text{th}}}\right) \right] \quad (11.23)$$

$$\times \left[1 - \left(\frac{T_p}{T_{p,\text{th}}}\right)^{1.9} \right]^3 \text{ mb} \quad (11.24)$$

where T_p is the kinetic energy of the proton in the lab frame and $T_p = 2m_{\pi}c^2 + m_{\pi}^2c^4/(2m_p c^2) \approx 0.2797$ GeV is the threshold proton kinetic energy in the particle lab frame. Eq. 11.24 is shown in Fig. 11.6. Inclusive here refers to the cross-section including production channels from single- and two π -on production channels for π^0 . These channels are

$$pp \rightarrow pp \pi^0 \quad (11.25)$$

$$pp \rightarrow pp 2\pi^0 \quad (11.26)$$

$$pp \rightarrow \{pn, D\} \pi^+ \pi^0 \quad (11.27)$$

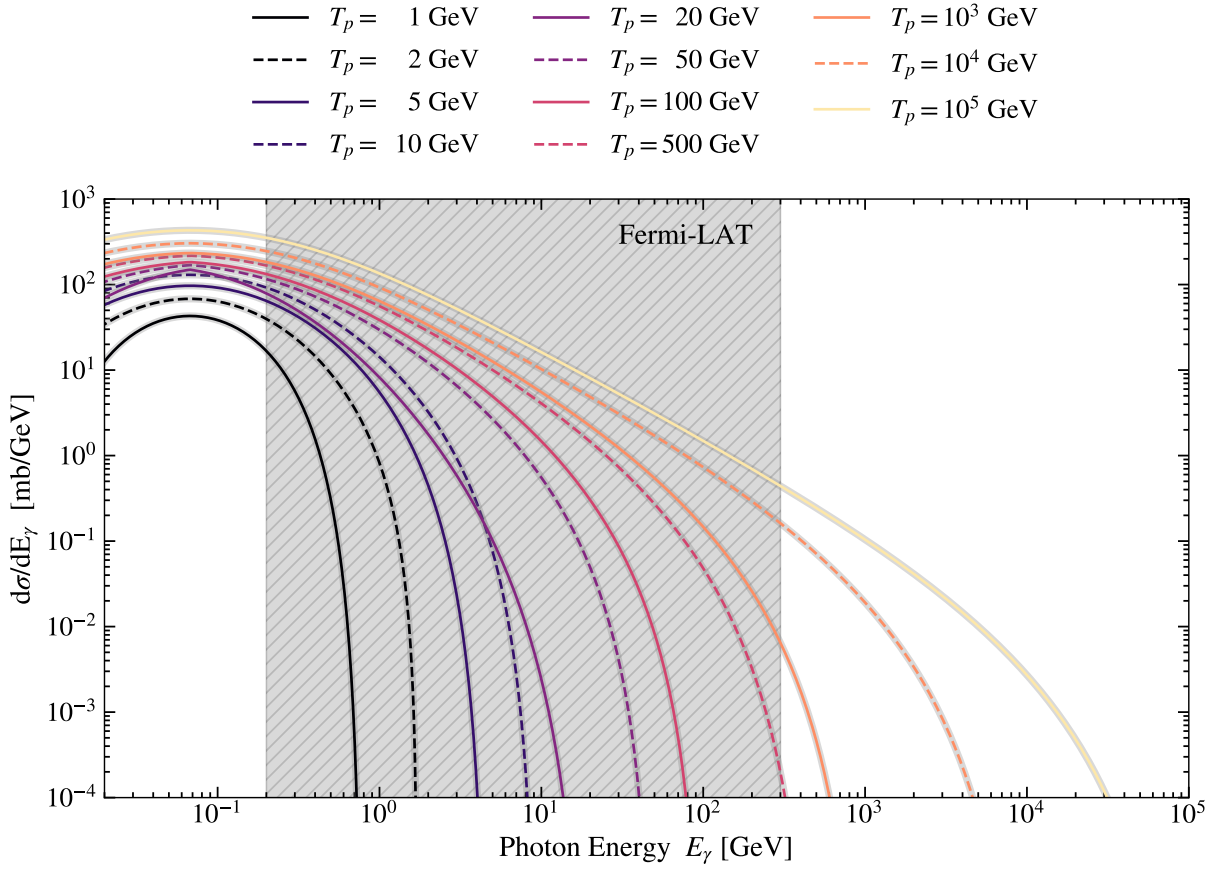


Figure 11.8: The differential energy cross-section as a function of photon energy for a wide range of proton energies. The gray area indicates the sensitivity range of Fermi-LAT. This is a simplified reproduction of Fig. 10 in Kafexhiu et al. (2014).

We show the cross-sections and their sum for these channels in Fig. 11.7.

The fit formula $F(E_p, E)$ in Eq. 11.21 can be written as

$$F(E_p, E_\gamma) = \frac{\left(1 - X_\gamma^{\alpha(E_p)}\right)^{\beta(E_p)}}{\left(1 + \frac{X_\gamma}{C}\right)^{\gamma(E_p)}} \quad (11.28)$$

where $\alpha(E_p)$, $\beta(E_p)$, and $\gamma(E_p)$ are elaborate fit functions that depend on the proton energy in the lab frame E_p . X_γ is a ratio between the energy of the emitted γ -photon, the maximum allowed γ -photon energy and the rest-mass of a π -on.

With this parametrization of Eq. 11.21 we can compute for every primary CR proton with energy E_p a cascade of photons originating from the interaction with a thermal background proton. We show this cascade in Fig. 11.8 for a number of different primary proton energies. The sensitivity region of Fermi-LAT is given as the gray shaded area.

11.3.2 Source Function

Having obtained a parametrization for the differential cross-section in Eq. 11.21, we can now compute a source function for the photon production from a CRp spectrum. This function in units of [$\gamma \text{ s}^{-1} \text{ cm}^{-3} \text{ GeV}^{-1}$] takes the form

$$q_\gamma(E_\gamma) = \frac{4\pi n_H}{m_p} \int_{\hat{p}_{\min}}^{\hat{p}_{\max}} d\hat{p} \hat{p}^2 f(\hat{p}) \frac{d\sigma_\gamma(E_\gamma, \hat{p})}{dE} \quad (11.29)$$

where n_H is the number density of the background gas, m_p is the proton mass and $f(\hat{p})$ is the distribution function or CRp in dimensionless momentum space. \hat{p}_{\min} and \hat{p}_{\max} are the minimum and maximum momentum boundary of the distribution function.

Similar to the solution of the synchrotron emission we solve Eq. 11.29 by numerically integrating over the distribution function using the Simpson rule. For this we evaluate Eq. 11.21 at the beginning, middle, and end of each momentum bin and interpolate $f(\hat{p})$ to each of these points via Eq. 5.1.

To reduce computational costs we skip bins where the upper momentum boundary is below the threshold energy for π -on production. If the threshold energy lies within a bin, we interpolate $f(\hat{p})$ to the threshold energy and solve the integral over the remaining bin.

11.3.3 Luminosity and Flux

The source function Eq. 11.29 is not directly observable. What we are interested in instead is a photon flux a telescope would capture from an object at distance d . As was the case for synchrotron emission we compute these quantities per SPH particle and then obtain the desired results by either summing up the contributions from all particles or mapping the data onto a 2D grid to produce mock observations.

To compute the photon flux from distance d to the observer in an energy band $E \in [E_1, E_2]$ that a single SPH particle contributes to we solve

$$F_\gamma = \frac{1}{4\pi d^2} \int_{\Omega} dV \int_{E_1}^{E_2} dE q_\gamma . \quad (11.30)$$

Here $\int_{\Omega} dV \equiv \frac{m_i}{\rho_i}$ is the volume of the SPH particle and E is given in GeV. This gives the photon flux in units [$\gamma \text{ s}^{-1} \text{ cm}^{-2}$] that a single SPH particle contributes to.

From Eq. 11.29 we can obtain an emissivity per photon energy E_γ in units [$\gamma \text{ s}^{-1} \text{ cm}^{-3}$] as

$$j_\gamma(E_\gamma) = E_\gamma q_\gamma . \quad (11.31)$$

This relates to the luminosity in units [GeV s^{-1}] via

$$L_\gamma = \int_{\Omega} dV \int_{E_1}^{E_2} dE E j_\gamma \quad (11.32)$$

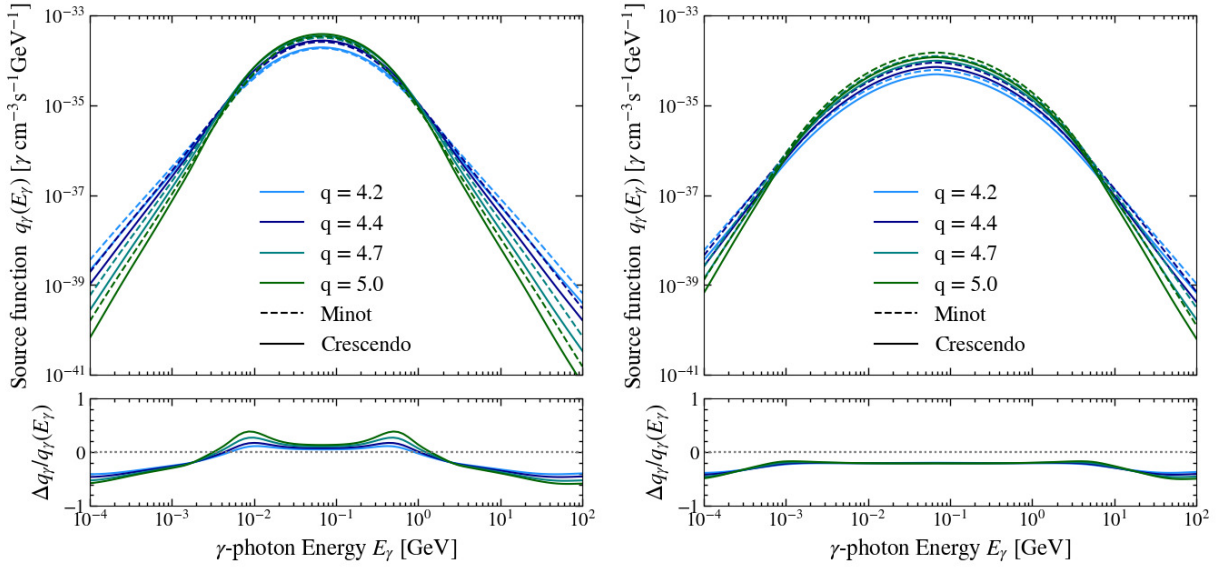


Figure 11.9: We compare our calculations of the γ -ray source function to the one by the MINOT package. For both plots, we set up a power-law in momentum space with an energy density of $\epsilon_{\text{CR},p} = 1 \text{ erg cm}^{-3}$ and vary the minimum momentum of the power-law p_{min} . *Left:* $p_{\text{min}} = 1 \frac{\text{GeV}}{c}$. *Right:* $p_{\text{min}} = 10 \frac{\text{GeV}}{c}$.

where we again have to use the volume of the SPH particle to solve the volume integral. The total luminosity of the object can then again be obtained by summing up the contribution of the individual SPH particles.

11.3.4 Tests

We test our implementation against results obtained with the MINOT package (Adam et al., 2020) and show the results in Fig. 11.9. To compare our results we set up CRp distribution functions with a fixed total energy density contained in the CRps of $\epsilon_{\text{CR},p} = 1 \text{ erg cm}^{-3}$ and a fixed upper momentum boundary $\hat{p}_{\text{max}} = 10^5 \frac{\text{GeV}}{c}$. We vary the lower momentum boundary between $p_{\text{min}} = 1 \frac{\text{GeV}}{c}$ in the left panels of Fig. 11.9 and $p_{\text{min}} = 10 \frac{\text{GeV}}{c}$ in the right panels. The top panels show the source function defined in Eq. 11.29 as a function of photon energy E_γ . Different colors correspond to different slopes of the distribution function. Solid lines are our results and dashed lines show the result obtained with MINOT. The lower panels show the relative errors.

In general, we find reasonable, although not perfect agreement. Further tests indicate that this is partially driven by the number of CRp bins, hinting towards the origin of the discrepancy lying in the numerical integration scheme of Eq. 11.29.

This warrants further future investigation, however for the current work where CR injection parameters and numerical resolution have a significantly stronger impact on the results we accept this small numerical error.

12 | Coupling to OPENGADGET3

We implemented CRESCENDO into OPENGADGET3 (Groth et al., 2023), a cosmological Tree-SPH code based on GADGET2 (Springel, 2005). In this section, we will give a brief outline of solving hydrodynamics with SPH and how this needs to be extended to account for a two-component fluid of thermal gas and CRs.

12.1 Smoothed Particle Hydrodynamics

We will first give a very brief overview on solving hydrodynamics with SPH, for details please see Price (2012), which our summary is based on.

As with any hydrodynamics code, we need to find a way to solve the Euler equations

$$\partial_t \rho + \nabla \cdot (\rho \mathbf{v}) = 0 \quad (12.1)$$

$$\partial_t (\rho \mathbf{v}) + \rho \mathbf{v} \cdot \nabla \mathbf{v} + \nabla P = 0 \quad (12.2)$$

$$\partial_t (\rho U) + \nabla \cdot [(\rho E_{\text{tot}} + P) \mathbf{v}] = 0 \quad (12.3)$$

where ∂_t is the partial time derivative with respect to time, ρ is the density of a fluid element, \mathbf{v} its velocity, E_{tot} its total energy and P its pressure.

In an initial step, one needs to decide how to define the density of a numerically discretized fluid element ρ . From the definition of $\rho = \frac{m}{V}$, it follows that one can either discretize the mass of a fluid element and find a way to define its volume, or one discretizes its volume and finds a way to define its mass. These two approaches are called *Eulerian* if volume is discretized, or *Lagrangian* if mass is discretized.

SPH is a *Lagrangian* method, discretizing mass in the shape of “SPH particles” which act as tracer particles for the fluid quantities. As such we need to find a reasonable way to define the volume of a particle. This is done by defining a normalized kernel function $W(r)$ as

$$\int_V dV' W(\mathbf{r}' - \mathbf{r}_i, h) = 1 \quad (12.4)$$

where the volume integral is evaluated over a finite radial extent h_{sml} . This finite extent is set to avoid having to compute the interaction between all particles in the simulation and reduce it to only an approximately fixed number of neighboring particles.

The kernel function should follow a number of properties:

- The weighting should be positive, decrease monotonically with relative distance, and have two well-behaved derivatives.
- It should be symmetric with respect to distance.
- The central part of the kernel should be flat, to avoid strong impacts in small relative position changes of close neighbors.
- The Fourier transformation should be positive definite to ensure stabilization against the tensile (pairing) instability.
- Its numerical form should be computationally cheap to solve.

For this work we typically use a Wendland C_4 kernel with 200 neighbors and bias correction as proposed by [Dehnen & Aly \(2012\)](#).

With this kernel function, we can compute the density from a weighted summation over nearby particles as

$$\rho(\mathbf{r}_i) = \sum_j^{N_{\text{ngb}}} m_j W(\mathbf{r}_i - \mathbf{r}_j, h_i) . \quad (12.5)$$

All other fluid quantities X_i are computed simply by summing up the quantities of all neighboring particles, weighted with the kernel evaluated at their distance from particle i

$$X_i = X(\mathbf{r}_i) = \sum_j \frac{m_j}{\rho_j} X_j W(\mathbf{r}_i - \mathbf{r}_j, h_i) . \quad (12.6)$$

In a similar fashion, we can calculate the gradient of the quantity X_i by acknowledging that only the kernel depends on the particle i , which simplifies the gradient ∇X_i to the gradient of the kernel

$$\nabla X_i = \nabla X(\mathbf{r}_i) = \sum_j \frac{m_j}{\rho_j} X_j \nabla W(\mathbf{r}_i - \mathbf{r}_j, h_i) \quad (12.7)$$

and the same holds for the curl or divergence of the fluid field. To obtain equations for the time evolution of the particles we derive the equations of motion from the Lagrangian

$$L = \int dV [\rho v^2 - \rho U(\rho, s)] \quad (12.8)$$

via the least action principle to get

$$\frac{\partial L}{\partial \mathbf{v}_i} = m_i \mathbf{v}_i \quad ; \quad \frac{\partial L}{\partial \mathbf{r}_i} = - \sum_j m_j \frac{\partial U_j}{\partial \rho_i} \Big|_s \frac{\partial \rho_j}{\partial \mathbf{r}_i} . \quad (12.9)$$

The internal energy U_j can be found via the first law of thermodynamics (although in modern SPH entropy is evolved instead of internal energy, see [Springel & Hernquist, 2002](#), for details) and together with an expression of the density gradient this gives a function for the acceleration a particle experiences due to the hydrodynamic forces exerted on it by its neighboring particles

$$\mathbf{a}_{\text{hydro}} = \frac{D\mathbf{v}_i}{Dt} = - \sum_j m_j \left(\frac{P_i}{\rho_i^2} + \frac{P_j}{\rho_j^2} + \Pi_{ij} \right) \nabla_i W(\mathbf{r}_i - \mathbf{r}_j, h_i) \quad (12.10)$$

where P is the total pressure the particle feels and Π_{ij} is the (artificial) viscosity required to capture shocks in SPH. For a detailed description of the SPH implementation we refer to [Beck et al. \(2016b\)](#).

We further omit a description of the implementation of MHD implementation, for the sake of brevity and refer to [Dolag et al. \(2009a\)](#); [Bonafede et al. \(2011\)](#).

12.2 Cosmic Ray - Hydrodynamics

Due to the Lagrangian nature of SPH, the update of the hydrodynamical quantities is driven by the total pressure. To this end we add the CR pressure to the thermal pressure of the particles and use this to update Eq. 12.10.

At the end of each time step, we have updated the spectral distribution due to the previously described energy gain and loss mechanisms. We can now compute the comoving CR pressure component by integrating over the spectrum

$$P_{\text{CR},c} = \frac{4\pi}{3} a^4 \int_{p_{\text{min}}}^{p_{\text{cut}}} dp p^2 T(p) f(p) \quad (12.11)$$

$$\approx \frac{1}{3} a^4 \int_{p_{\text{min}}}^{p_{\text{cut}}} dp 4\pi c p^3 f(p) \quad (12.12)$$

where the r.h.s. of Eq. 12.12 can readily be identified as an energy integral over the whole distribution function. Since we solve the update of the distribution function in physical space for cosmological simulations we introduce the conversion from physical to comoving frame as in [Pfrommer et al. \(2017\)](#) at this point, where a is the cosmological scale factor. Here we again used the approximation of purely relativistic particles. This pressure component is then added to the total pressure, which goes into the hydrodynamic acceleration of the SPH particles.

We note that this only provides a lower limit to the total CR pressure, due to the simplification $T(p) \approx pc$. As we are mainly interested in the high-energy emission of electrons and the observational constraints on CR proton pressure are quite strict, we accept this limitation for the current work. We will discuss ways to remedy this in Sec. 17.1 and leave the implementation to future work.

SPH uses the sound speed within the kernel as a way to limit the timestep. In a two-component fluid of gas and CRs the sound speed is defined as

$$c_s = \sqrt{\frac{\gamma_{\text{eff}} P_{\text{tot}}}{\rho}} \quad (12.13)$$

with

$$\gamma_{\text{eff}} = \frac{\gamma_{\text{cr}} P_{\text{cr}} + \gamma_{\text{th}} P_{\text{th}}}{P_{\text{cr}} + P_{\text{th}}} \quad (12.14)$$

as the effective adiabatic index of the composite fluid. We added this modification to the calculation of the sound speed to account for a change in the adiabatic index of the CR and thermal gas composite.

To conserve the total energy in the fluid, even as CRs are injected, it is important to subtract the energy injected into the CR fluid from the thermal energy. In the current implementation, this is done by subtracting the energy used for CR acceleration from the entropy change over the timestep. This subtraction needs to be performed before the second *kick* of the time integration since the entropy integration happens at this kick. Please note that this is currently solved by injecting the power-law spectrum within the hydro loop, shortly after the shock finder is evaluated. Since the actual time evolution of the CR spectrum happens at the end of the timestep this means that the injected spectrum is also always cooled over one timestep. This may need to be reconsidered in the future, as it does not allow us to study very high-frequency synchrotron emission e.g. $\nu > 4$ GHz, since we always write a cooled, hence curved, spectrum into the snapshot. As typical simulation timesteps are many orders of magnitude larger than observation times, we are therefore not able to reproduce unbroken power-laws in synchrotron emission up to very high frequencies.

Part III

Applications

13 | Idealized Cluster Merger

Co-Authors: Ulrich P. Steinwandel, Klaus Dolag and Harald Lesch

To introduce the model we chose to apply it to a set of idealized GC mergers. These results have been published in [Böss et al. \(2023c\)](#).

Idealized galaxy cluster mergers have been studied previously with great success to model X-ray emission of dynamical clusters (e.g. [Donnert et al., 2017](#)) and to study the origin of observed cold fronts (e.g. [Springel & Farrar, 2007](#); [ZuHone et al., 2010, 2013](#); [Walker et al., 2017](#)) as well as velocity structures in merging clusters ([Biffi et al., 2022](#)), or to model radio observations from relics (e.g. [van Weeren et al., 2010, 2011b](#); [Lee et al., 2020, 2022](#)) and secondaries (e.g. [ZuHone et al., 2013](#); [Donnert, 2014](#)). For a recent review on GC merger simulations see [ZuHone & Su \(2022\)](#).

We performed a series of idealized galaxy cluster mergers following the best-fit parameters for CIZA J2242.4+5301-1 obtained in [Donnert et al. \(2017\)](#). Specifically, we use the high Mach number scenario of the Red model, which gives the Mach number closest to that obtained by radio observations, while also matching the X-ray observations. This allows us to compare the result directly to their work and well-studied radio observations of the sausage relic (e.g. [Stroe et al., 2014, 2016](#); [Di Gennaro et al., 2018](#); [van Weeren et al., 2019](#)).

All these simulations are non-radiative, run with `OPENGADGET3` using the improvements to SPH presented in [Beck et al. \(2016b\)](#), higher order C_6 -kernels with 295 neighbors, non-ideal MHD ([Dolag & Stasyszyn, 2009](#); [Bonafede et al., 2011](#)), on-the-fly shock finder ([Beck et al., 2016a](#)) and thermal conduction ([Jubelgas et al., 2004](#); [Arth et al., 2014](#)).

13.1 Initial Conditions

To construct the initial conditions for the galaxy cluster merger we employ a slightly modified version of the `TOYCLUSTER` code (see [Donnert & Brunetti, 2014](#), for details) with improvements presented in [Donnert et al. \(2017\)](#). The code sets up DM and gas spheres for galaxy clusters and places them on a colliding orbit. For the purpose of this work, we will only outline the key components of the ICs setup here and refer the interested reader to the aforementioned papers.

`TOYCLUSTER` uses rejection sampling to set up the positions of equal-mass DM particles following a NFW profile

$$\rho_{\text{DM}} = \frac{\rho_{0,\text{DM}}}{\frac{r}{r_s} \left(1 + \frac{r}{r_s}\right)^2} \left(1 + \frac{r^3}{r_{\text{sample}}^3}\right)^{-1} \quad (13.1)$$

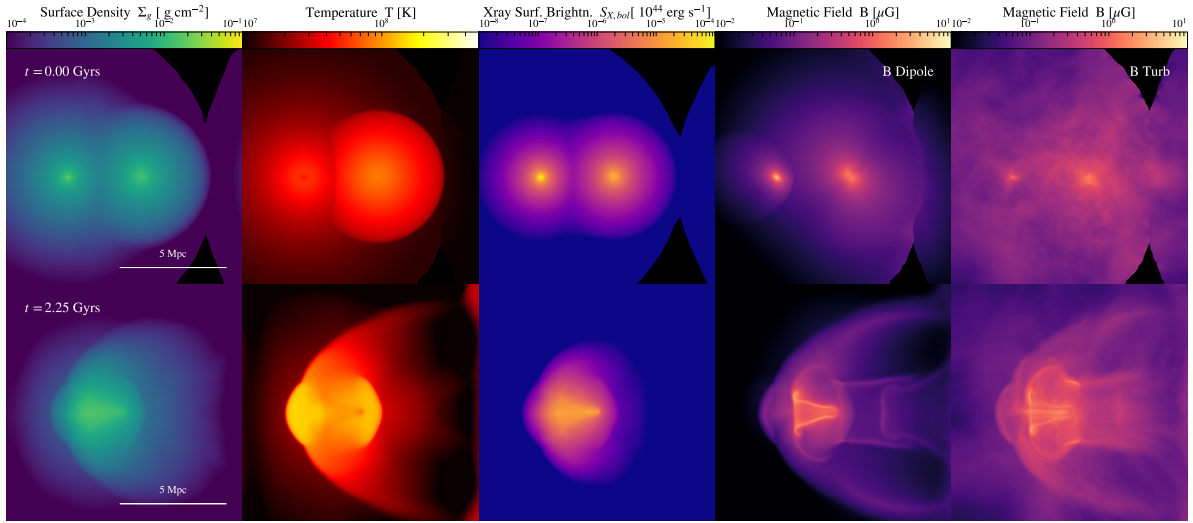


Figure 13.1: *Upper panels:* Initial conditions for the galaxy cluster mergers. From left to right we show gas surface density, temperature, bolometric X-ray surface brightness, magnetic field strength of the dipole setup, and magnetic field strength of the turbulent setup. *Lower panels:* Simulation output at $t = 2.25$ Gyrs as both shock waves have developed. This output time was used to obtain the results for the shock front and CR component analysis. Left and right shocks correspond to the northern and southern relics, respectively. The three left panels show the gas quantities of the B Dipole run. For all runs the plasma-beta is $\beta \gg 1$, which leads to a negligible impact on the gas dynamics from the magnetic field.

where $\rho_{0,\text{DM}}$ is the central DM density, r_s is the NFW scale radius and r_{sample} is the sample radius for the DM distribution. We employ $r_{\text{sample}} = 1.7r_{200}$ (see Sec 3.1 in [Donnert et al., 2017](#), for a discussion about the choice of this value).

The corresponding particle energies and from that the velocities to obtain a stable halo are then found by sampling from the particle distribution function $f(E)$. With the added complexity of an embedded gas halo within the DM halo $f(E)$ must be obtained by numerically solving the Eddington equation ([Eddington, 1916](#)).

$$f(E) = \frac{1}{\sqrt{8\pi}} \int_0^E \frac{d\Psi}{\sqrt{E-\psi}} \frac{d^2\rho}{d\Psi^2} \quad (13.2)$$

where ψ is the potential energy, E the kinetic energy and ρ the total density profile.

The positions of the gas particles are found with a weighted Voronoi tessellation method ([Diehl et al., 2012](#); [Arth et al., 2019](#)). This method defines a maximum density as a function of position, in this case, a β -model ([Cavaliere & Fusco-Femiano, 1976](#))

$$\rho_{\text{gas}}(\mathbf{x}) = \rho_{0,\text{ICM}} \left(1 + \frac{r^2(\mathbf{x})}{r_{\text{core}}^2}\right)^{-\frac{3}{2}\beta} \left(1 + \frac{r^3(\mathbf{x})}{r_{\text{cut}}^3}\right)^{-1} \quad (13.3)$$

where $\rho_{0,\text{ICM}}$ is the central ICM density, r_{core} is the core radius and r_{cut} is the cut-off radius of the gas-halo sampling. Initially, we sample a Poisson distribution.

The actual density at the particle position \mathbf{x} is then found with a SPH loop and from that a displacement for the particle can be computed which will lead to a better agreement to the analytic density model. That process is repeated until the error between analytic and SPH density is below 5 percent.

Finally, the gas temperature and from that the internal energy of particles is found by calculating the hydrostatic equilibrium temperature

$$T(r) = \frac{\mu m_p}{k_B} \int_r^{R_{\text{max}}} dr' \frac{\rho_{\text{gas}}(r')}{r'^2} M_{\text{tot}}(< r') \quad (13.4)$$

where $\mu \approx 0.6$ is the mean molecular mass of the ICM plasma and k_B, m_p are Boltzmann constant and proton mass, respectively. To model cool-core and non-cool-core clusters r_{core} is set to $r_{\text{core}} = r_s/9$ for cool-core and $r_{\text{core}} = r_s/3$ for non-cool-core models (see [Donnert, 2014](#)).

A final parameter is the in-fall velocity of the merging clusters as a function of the energy contained in the orbits (X_E) if the clusters are at rest at an infinite distance. In this parametrization $X_E = 1$ is the maximum energy available to the system and $X_E = 0$ would mean the clusters are at rest if they are placed so that their virial radii r_{200} touch.

For the current work, we employ the high Mach number scenario with $X_E = 0.5$ and the parameters of the Red model from [Donnert et al. \(2017\)](#), which we sampled with 10^7 gas and DM particles each. This leads to a mass resolution of $m_{\text{gas}} = 5.1 \cdot 10^7 M_\odot$ and $m_{\text{DM}} = 2.1 \cdot 10^8 M_\odot$ with a gravitational softening of $\epsilon = 3.4 \text{ kpc}$.

13.2 Magnetic Field Models

We employ two magnetic field configurations: A dipole field and a turbulent field. For the dipole field, we used the standard configuration of `TOYCLUSTER` to set up a divergence-free magnetic field from a vector potential. Here we follow the magnetic field model by [Bonafede et al. \(2011\)](#) and define a vector potential as

$$\mathbf{A}(\mathbf{x}) = A_0 \left(\frac{\rho(\mathbf{x})}{\rho_0} \right)^\eta \quad (13.5)$$

with $A_0 = 5 \mu\text{G}$ as the central field strength and $\eta = 0.5$ as the scaling parameter. We then compute the magnetic field components by explicitly solving the curl of the vector potential over the neighboring SPH particles.

For the turbulent magnetic field, we set up a power spectrum in Fourier space with an amplitude $P(k) \propto k^\alpha$, where $\alpha = -11/3$. We then sample randomly from this spectrum on a 3D grid and transform this grid into real space. In real space, we can then normalize the magnetic field to the desired field strength, again $5 \mu\text{G}$, and apply a density weighting as in the previous case. The normalized B-field grid is then again transformed into Fourier space for divergence cleaning, following the method described in [Ruszkowski et al. \(2007\)](#). The divergence-free grid is then

Table 13.1: Configuration of the different simulation runs. From left to right we list the name of the run. Whether it was run with the dipole magnetic field setup or the turbulent magnetic field setup. Which Mach number dependent acceleration model was used. If the magnetic field geometry-dependent efficiency was used. How p_{inj} was defined. How the ratio between CRp and CRe injection K_{ep} was set. And if it was run with turbulent re-acceleration.

Model	B Dipole	B Turb	$\eta(\mathcal{M}_s)$	$\eta(\theta_B)$	p_{inj}	K_{ep}	α
KR13d θ_B	✓		Kang & Ryu (2013)	✓	0.1	0.01	0
KR13t		✓	Kang & Ryu (2013)		0.1	0.01	0
KR13t θ_B		✓	Kang & Ryu (2013)	✓	0.1	0.01	0
Ryu19t		✓	Ryu et al. (2019)		0.1	0.01	0
Ryu19t θ_B		✓	Ryu et al. (2019)	✓	0.1	0.01	0
Ryu19t $\theta_B p_{\text{inj}}$		✓	Ryu et al. (2019)	✓	Eq. 6.8	Eq. 6.11	0
Ryu19t $\theta_B p_{\text{inj}} q_\alpha$		✓	Ryu et al. (2019)	✓	Eq. 6.8	Eq. 6.11	Eq. 6.10

transformed back into real space. From there the magnetic field can be mapped to the SPH particles by Nearest Grid Point interpolation. Both these methods result in small values for $\nabla \cdot \mathbf{B}$ with a mean relative divergence of $|\nabla \cdot \mathbf{B}|h_i/|\mathbf{B}| \approx 10^{-6}$ in the case of the dipole setup and $|\nabla \cdot \mathbf{B}|h_i/|\mathbf{B}| \approx 10^{-4}$ in the case of the turbulent setup over the course of the simulations. We find that these values are acceptable for our simulation efforts.

13.3 Simulations

We ran a total of seven different simulations to study the impact of the different components of our model. We summarize the runs in Tab. 13.1 and will give a brief overview of the different setups and the naming convention, as well as their motivation in this section.

First, we distinguish between the different Mach number dependent acceleration efficiency models. For these runs, we use the models by [Kang & Ryu \(2013\)](#) and [Ryu et al. \(2019\)](#), denoted by KR13 and Ryu19 respectively. The most simple run is KR13t with only the sonic Mach number dependent acceleration efficiency employed, a fixed injection momentum $\hat{p}_{\text{inj}} = 0.1$ and a fixed electron to proton injection of $K_{\text{ep}} = 0.01$ (as in e.g. [Hong et al., 2015b](#)). We use this as a baseline to see the impact of a Mach number dependent efficiency model and use the magnetic field only for the synchrotron analysis in Sec. 13.5.2.

Next, we keep the previous parameters and include shock obliquity dependent acceleration efficiencies. We test this for the ordered, dipole magnetic field and the turbulent magnetic field in KR13d θ_B and KR13t θ_B respectively. A visualization of the initial conditions with dipole and turbulent magnetic field can be seen in the two upper right panels of Fig. 13.1.

We then switched to the [Ryu et al. \(2019\)](#) efficiency model where we use the turbulent setup to first test only the effect of switching to this more modern Mach number dependent efficiency model in Ryu19t and then include magnetic field geometry dependent acceleration in Ryu19t θ_B . The next simulation again uses the more modern Ryu19 efficiency, shock obliquity dependent injection, and on-the-fly calculation of \hat{p}_{inj} and K_{ep} . We use this to study how our model behaves

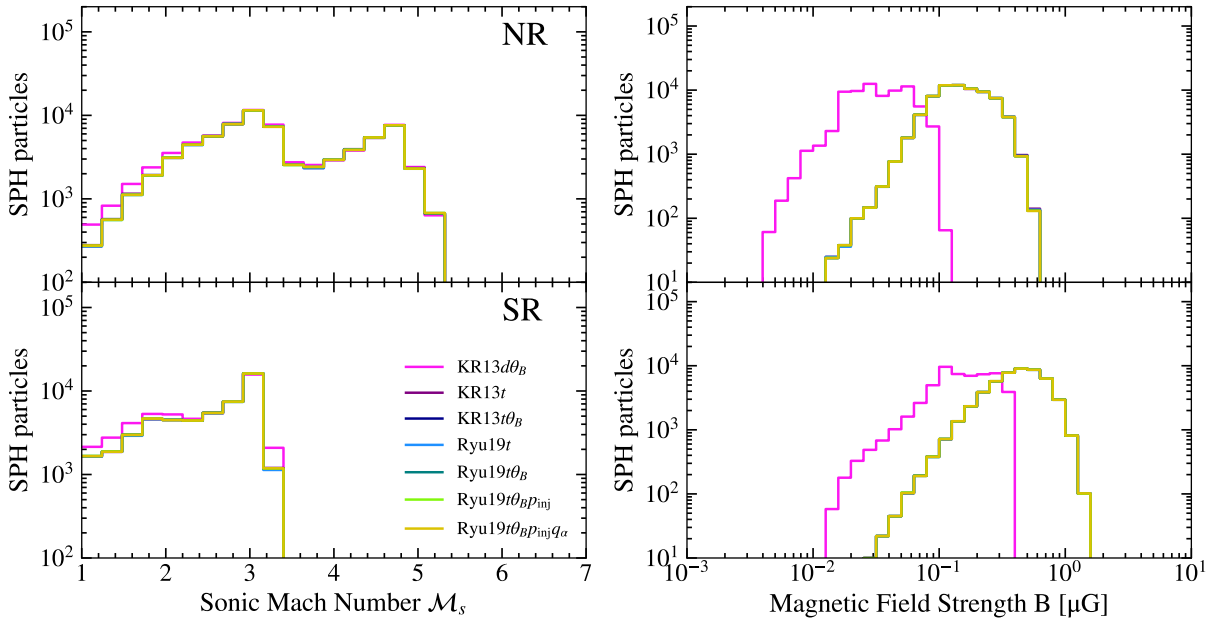


Figure 13.2: Shock properties of the northern relic (NR, top panels) and southern relic (SR, lower panels) in our simulations. *Left:* Histograms of sonic Mach number distribution of all shocked SPH particles. As expected the Mach number distribution does not differ significantly between the runs. Even for the run with the highest efficiency (KR13t) *Right:* Magnetic field strength distribution of all shocked particles. The magnetic field strength of the NR is significantly below common values of $2 - 5 \mu\text{G}$ commonly found in cluster shocks (see tables in [van Weeren et al., 2019](#)). As the SR expands into the wake of the larger cluster the magnetic field is stronger.

with a more modern injection efficiency and more complex parameter combinations for the distribution functions in run $\text{Ryu19t}\theta_B p_{\text{inj}}$.

Last, we reuse all settings from the previous simulation but also include the computation of a slope based on non-linear DSA following Eq. 6.10.

All simulations were run with CR distributions in the range $\hat{p} \in [10^{-1}, 10^5]$. This represents the full range of the spectrum in the case of a fixed \hat{p}_{inj} and makes it easy to compare these results to the simulations with an on-the-fly calculation of \hat{p}_{inj} .

However this puts strain on our approximation $T(p) \approx pc$, as particles with $\hat{p} \approx 10^{-1}$ can not be considered ultra-relativistic and the transition between $\gamma = \frac{4}{3}$ and $\gamma = \frac{5}{3}$ occurs around $\hat{p} \approx 10^{-1} - 10^1$ (see Fig. 2 in [Girichidis et al., 2022](#)). This leads to our pressure estimates being a lower limit.

We resolve the CR proton spectrum with 12 bins (2 bins/dex) and the electron spectrum with 96 bins (16 bins/dex) for each of our 10^7 resolution elements.

13.4 Shock Fronts

For the rest of the paper, we will study the shocks moving along positive and negative x -direction. Here the left moving shock corresponds to the northern relic (NR) and the right moving shock to the southern relic (SR) in [Donnert et al. \(2017\)](#). We show the state of the simulation at 2.25 Gyrs, which we will use for the following analysis of the NR in the bottom panels of Fig. 13.1. For the analysis of the SR, we use an earlier snapshot at 1.96 Gyrs, as at the later time the shock has already extended further into the track of the larger cluster and has been deformed by the boundaries of this track.

Fig. 13.2 gives a histogram of sonic Mach number and magnetic field strength distribution in the shock fronts. The distribution of Mach numbers shows good agreement between the different setups. This makes for good comparisons of the runs.

A larger discrepancy can be found in the distribution of magnetic field strengths of the shocked particles, where the KR13 $d\theta_B$ model shows half dex lower magnetic field strengths. As the shock is detected slightly ahead of the density and temperature jump the magnetic field amplification by the shock is not completed in the shocked particles either. This means that the shocked particle primarily probes the upstream magnetic field, which is stronger in the turbulent setup. In addition to that, we find that the downstream magnetic field is lower in our simulation, compared to typical observational values of $2 - 5\mu G$ commonly found in cluster shocks (see tables in [van Weeren et al., 2019](#)). We will discuss the implications of this for the synchrotron emission we obtain directly from the electron population in our particles in Sec. 13.5.4.

13.5 The Northern Relic

First, we will focus on the CR pressure component, synchrotron emission, and the time evolution of the spectral distributions of protons and electrons of the northern relic (NR). We will discuss the southern relic in the next section.

13.5.1 Injection

We show the injected pressure component of CR protons and electrons, as well as the ratio between proton and thermal pressure in the first three columns of Fig. 13.3. As discussed above, our approximation of $T(p) \approx pc$ only provides a lower limit here.¹

The top panels show the results for the model KR13 $d\theta_B$. In the dipole magnetic field case, the shock expands into a lobe of the dipole setup, causing a very oblique magnetic field geometry over the entire shock surface. This strongly suppresses the injection of CR protons. In the electron case this leads to a preferential acceleration and with that a smoothly injected electron component

¹We also note that for the electrons Coulomb losses at the lowest end of our distribution function are efficient enough to cool away a substantial amount of the total energy density and it would be more consistent to only show the energy density of the synchrotron and ICs dominated part of the spectrum. However, we show the total pressure component here to illustrate the difference in injection, which would be less visible if only the fast-cooling part of the spectrum was considered.

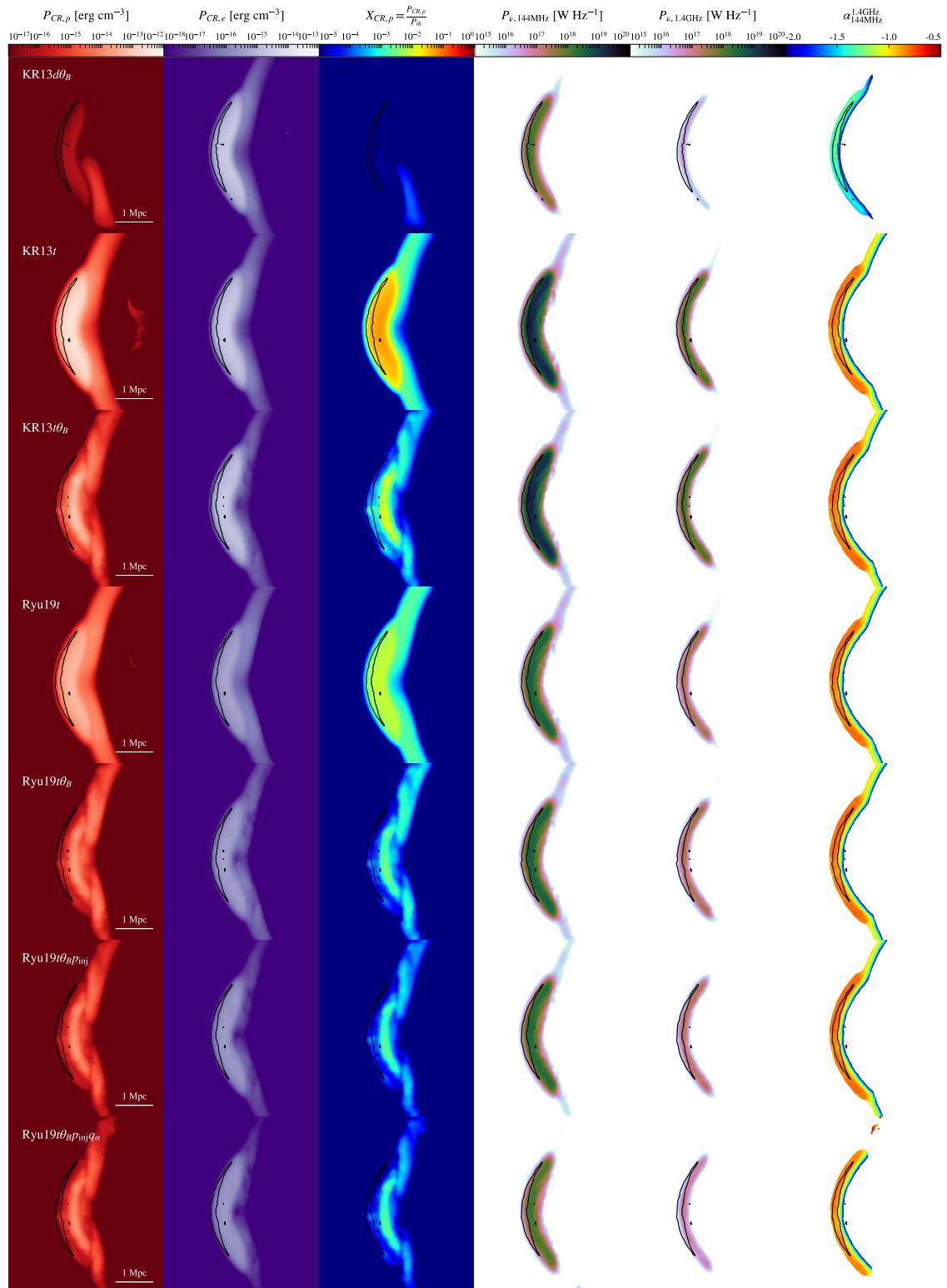


Figure 13.3: Simulation results for the northern relic (NR). We show, from left to right, the proton and electron pressure components, the ratio between proton and thermal pressure, synchrotron power at 144 MHz, synchrotron power at 1.4 GHz, and the spectral slope obtained by a single power-law fit between those frequencies. The images contain the average values in a 200kpc slice, centered on the shock. The black contours show the SPH particles in the shock with a sonic Mach number $\mathcal{M}_s > 4.5$ which corresponds to the center of the shock.

whose energy density surpasses that of the protons. As a result of this, the ratio between CR proton and thermal pressure is negligible and produces no stress on the observational constraints. In the KR13 t model, which does not use the shock obliquity dependent acceleration efficiency, we find a smooth injection of both components and an energy ratio that strictly follows the fixed $K_{ep} = 0.01$. The CR proton to thermal pressure ratio is significantly higher than in the previous run at 5% and with that surpasses the observational limit, which we expect to become a problem with a more realistic setup that also includes multiple shocks and the more efficient re-acceleration models. Including $\eta(\theta_B)$ in the run KR13 $t\theta_B$ results in a more varying CR component behind the shock, for protons. We can see a decrease in proton pressure where the shock propagated through regions of varying shock obliquity and find a structure behind the shock with increased proton pressure. This is also evident in the map of thermal to CR proton pressure ($X_{CR,p}$), where the maximum ratio behind the shock, caused by a pocket of perpendicular magnetic field does approach the observational limits, but there are also regions of significantly lower CR proton pressure.

Once we switch to the most modern Ryu19 efficiency models we always obtain CR proton pressure components in agreement with the observational limits. The Ryu19 t run shows smooth injection at the shock front for both electrons and protons, as expected with an injection scheme only dependent on Mach number. The values of $X_{CR,p}$ stay below 1%, however in a full cosmological simulation with multiple shocks and re-acceleration this picture could change. Once the magnetic field angle dependent acceleration efficiency in Ryu19 $t\theta_B$ is switched on however, CR proton acceleration is suppressed further, making this our favored model for CR proton acceleration. Including on-the-fly calculation of \hat{p}_{inj} and NLDSA slopes does not significantly alter this picture. The CR proton to thermal pressure ratio lies well below observational limits. This is for one caused by the lower efficiency and for another by the fact that not all of the energy available for injection is represented by our CR population and therefore remains in the thermal gas component. Nevertheless, we expect this efficiency model to behave like in other studies in a full cosmological simulation and suppress acceleration and re-acceleration of CR protons enough to be consistent with observations.

13.5.2 Radio Relic Morphology

We applied the calculation of synchrotron emissivity to the CRe populations injected at the bow shock. After calculating the emissivity per particle we mapped the particles to a 2D image, following the algorithm described in Dolag et al. (2005a). We do not smooth the images with a radio beam to retain the intrinsic information, for simplicity. The result can be seen Fig. 13.3. For this section, we will address the morphology of the synchrotron emission shown in columns four and five.

In all cases, the 144 MHz emission shown in the fourth panel still closely follows the total CRe pressure component, albeit we can see that the absolute emission behind the shock is decreasing by more than 2 orders of magnitude due to the cooling of the electron population. This is especially evident in the KR13 $d\theta_B$ run where the magnetic field is significantly smoother behind the shock, indicating that the decrease in emission is mainly caused by the cooling electrons. With the turbulent magnetic field models, we see the imprints of the turbulent field behind

the shock in the low-frequency emission for models KR13t - Ryu19t $\theta_B p_{inj} q_\alpha$. As seen in the suppression of the CR proton component the shock has a predominantly large obliquity and with that favors CR electron acceleration. Since the morphology of the magnetic field in the medium the northern shock travels through is not very complex, however, it has little impact on the relic morphology in this case. For the 1.4 GHz emission images in the fifth column of Fig. 13.3 we see a significantly narrower emission zone behind the shock, caused by the much shorter cooling times of the radio bright electrons at this frequency. The run KR13d θ_B shows again very smooth synchrotron emission at the shock front, which gradually decreases and also shows a smooth structure behind the shock. Including the turbulent setup, but switching off $\eta(\theta_B)$ gives a somewhat similar smooth synchrotron surface at the shock, as the shock travels through a fairly homogeneous medium apart from the magnetic field structure. This repeats for the remaining models. Again including the inclusion of p_{inj} computation does not significantly alter this image. The inclusion of the q_α -model does decrease the synchrotron emission significantly, however, as the shock is only very weakly magnetized. This causes α in Eq. 6.10 to approach zero and with that the slope follows the standard DSA prediction.

13.5.3 Spectral Steepening

One distinct feature of radio relics is the steepening of the synchrotron spectrum behind the estimated shock front. This is in the literature commonly attributed to the cooling of high energy, synchrotron bright electrons due to their synchrotron emission and inverse Compton scattering off background photons (van Weeren et al., 2019). This steepening has been studied with toy models (e.g. Donnert et al., 2017) as well as with idealized simulations (e.g. Stroe et al., 2016). In our simulations, we can obtain the spectral steepening directly from the aging electron population within every resolution element. For this, we construct images by calculating the emissivity per particle and integrating along the line of sight, as described in the previous section. Taking the intensity of the same pixel at two frequencies $\nu \in [144, 1400]$ MHz and fitting a single power-law between the results gives the spectral slope of the synchrotron spectrum. The results of this can be seen in the right panels of Fig. 13.3. We chose color range and map to closely resemble Fig. 4 in Di Gennaro et al. (2018). Generally, we find reasonable agreement with the spectral morphology apart from the KR13d θ_B model. At the shock front, we see a constant spectral slope of $\alpha \sim [-0.8, -1.0]$ in agreement with observations. We note that this region is broader than the observed counterpart as this is still contained in the numerical acceleration region. For this reason, a constant power-law is injected resulting in a constant spectral slope. We note therefore that the actual spectral image should be considered starting from the center of the Mach number contour and to the right from there. Behind the shock, we observe a clear gradual steepening up to and in principle beyond $\alpha = -2.0$. We chose to cut the image off at that slope for reasons of comparability to observations. We note however that the regions of steep radio spectra $\alpha \approx -1.5 \sim -2.0$ are smaller than in observations. Additional tests show that we can extend these zones by choosing deeper slices through the relic. Since the shocks in these simulations are nearly perfectly bowl-shaped and have a very even Mach number distribution this leads to more projection effects introduced by this only somewhat realistic setup.

We find that the spectral discrepancy in the KR13d θ_B run is most likely caused by the magnetic

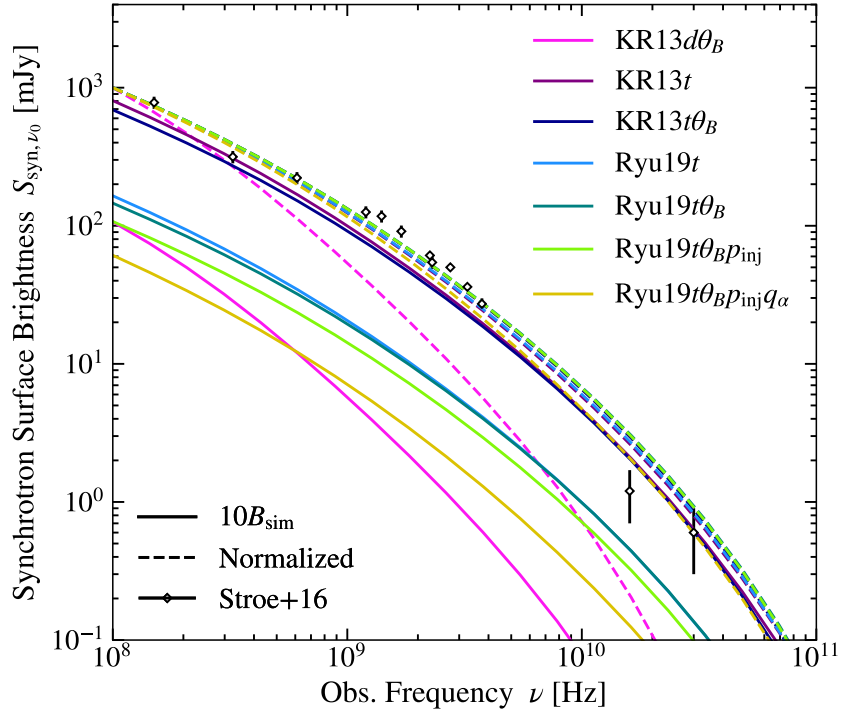


Figure 13.4: Synchrotron spectra as a function of observational frequency for the different models. Solid lines indicate the synchrotron power computed from 10 times the intrinsic magnetic field, to compensate for the too small magnetic field in the post-shock region. Dashed lines show the same spectra but normalized to 1 Jy at 100 MHz to compare spectral shapes. Diamonds with error bars indicate the observations from [Stroe et al. \(2016\)](#).

field morphology and will discuss this in more detail in the next section. The underlying morphological resemblance to the sausage relic for all other models however gives us confidence to further study radio relic morphologies in large-scale simulations of galaxy clusters with more realistic merger shocks.

13.5.4 Synchrotron Surface Brightness

We show the total synchrotron surface brightness of the NR as a function of observational frequency in Fig. 13.4. As our idealized simulation is not cosmological we assume a Planck 2018 cosmology ([Planck Collaboration et al., 2020b](#)) and place the relic at $z = 0.1921$ for the conversion between our intrinsic radio power to observable surface brightness. As mentioned above we find the downstream magnetic field associated with this emission is roughly one order of magnitude below observations. The resulting total synchrotron brightness is very sensitive to the magnetic field as well as the free parameters of relic volume and injection efficiency due to the shock Mach number. To remedy this we multiply the intrinsic magnetic field with a factor of 10 and recalculate the synchrotron spectra. This is shown with the solid lines. To account for

relic volume and injection discrepancy we normalized the spectra to 1 Jy at 100 MHz, the result is shown in the dotted lines. This allows us to compare the total spectral shape.

We find good agreement for the KR13 t and KR13 $t\theta_B$ models. Both the absolute surface brightness and the shape of the spectrum match observations well. Only above 10 GHz the spectrum proves to be slightly too shallow, which can easily be attributed to the lack of synchrotron cooling due to a lower magnetic field in the simulation. All Ryu19 models lie significantly below the observed spectrum, which follows trivially from the lower injection efficiency. However once the spectra are normalized to 1 Jy their spectral shapes agree very well, with the observations with the Ryu19 $t\theta_B p_{inj} q_\alpha$ run showing the best agreement due to its steeper spectrum. To rule out a systematic error in the injection we performed a shock tube test with the observational properties obtained by [van Weeren et al. \(2010\)](#); [Ogrea et al. \(2014\)](#); [Akamatsu et al. \(2015\)](#) as used in the analytic approach by [Donnert et al. \(2017\)](#) to analyze the origin of discrepancy of our results. We employ the same parameters for the CR model as in the analytic work with the KR13 acceleration model, $K_{ep} = 0.01$ and $\hat{p}_{inj} = 0.1$. The results of this test are shown in Fig. 11.4. We obtain the analytic solution for density, pressure, and the target Mach number with high accuracy. We then calculated the synchrotron emissivity per particle for a fixed magnetic field of $B = 5\mu G$. The results match the emissivity shown in Fig. 3 of [Donnert et al. \(2016\)](#) (indicated by the horizontal gray line) quite well. This result, combined with the normalization approach above leads us to believe, that the discrepancy in the radio emission is mainly driven by the magnetic field strength.

13.5.5 Spectral Evolution of a Tracer Particle

To show the spectral evolution of our tracer particles we randomly picked one particle in the NR at $t = 1.96$ Gyrs in the Ryu19 $t\theta_B p_{inj} q_\alpha$ model, as it best reproduces the synchrotron spectrum of the sausage relic. We show the evolution of said particle in Fig. 13.5. The light green line shows the onset of the CR injection. With the steeper slope than the later spectrum and the lower normalization of the distribution function, this suggests that the particle sat at the increasing flank of the numerically broadened shock at the output time of the snapshot. The subsequent snapshot already sees the fully injected spectrum. This supports the previous point of a limiting description in the case of a purely post-processed CR model. A spectrum that is injected only based on the initial snapshot will significantly under-predict CR related observables for this tracer particle. After the injection both protons and electrons experience adiabatic expansion as they pass the shock and the gas expands again in the outskirts of the cluster. The electron population experiences free cooling due to synchrotron and ICs losses. The steepening of the particle distribution function is less pronounced compared to the right panel of Fig. 8.1 due to the flatter spectrum, attributed to the strong shock. This shock leads to injection slopes of $q \sim -4$ and with that the fringe case of Eq. 8.7 where a spectrum with this slope contains its power-law shape up until the spectral cutoff. Even in this numerically challenging case and in a production simulation we find that the spectrum stays stable. We note that, as discussed above, the current implementation lacks low-momentum cooling for protons and electrons and therefore over-estimates the CR pressure component at late times. We accept this limitation for the current work, as we are interested in injection and high-momentum cooling of electrons at this point.

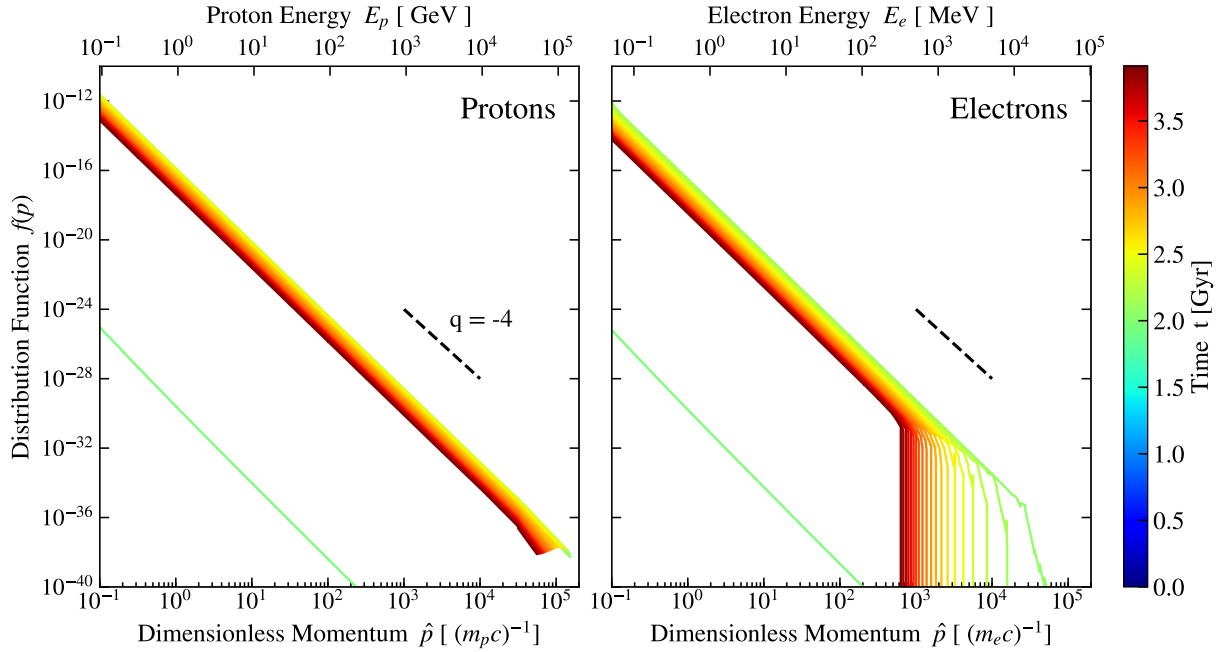


Figure 13.5: We show the time evolution of the proton- and electron distribution function of an arbitrarily chosen tracer particle. *Left*: proton distribution function. *Right*: electron distribution function. We can see the onset of the acceleration in light green and how it differs from the fully injected spectrum. The proton population shows adiabatic expansion after the injection with the spectral cutoff moving into the upper-most bin. The electron population shows adiabatic expansion and free cooling due to synchrotron emission and inverse Compton scattering. Both distribution functions stay numerically stable.

13.6 The Southern Relic

The southern relic (SR), the shock moving towards the right in our simulations, provides an excellent testbed for the different components of our acceleration model. Since this shock moves through a more perturbed medium, originating from the movement of the southern progenitor through the gas halo of the northern one, we can more clearly observe the impact of the different parts of the model.

13.6.1 Injection

We will again study the injected CR components first, shown in the first through third column in Fig. 13.6.

As was the case for the NR the shock of the SR in the KR13 $d\theta_B$ run expands into a pocket of a dipole from the dipole setup leading to a strongly oblique shock. This significantly suppresses the CR proton injection, while favoring the electron injection, which leads to a negligible CR proton to thermal pressure ratio. In KR13 t , the turbulent setup without θ_B computation, the injection

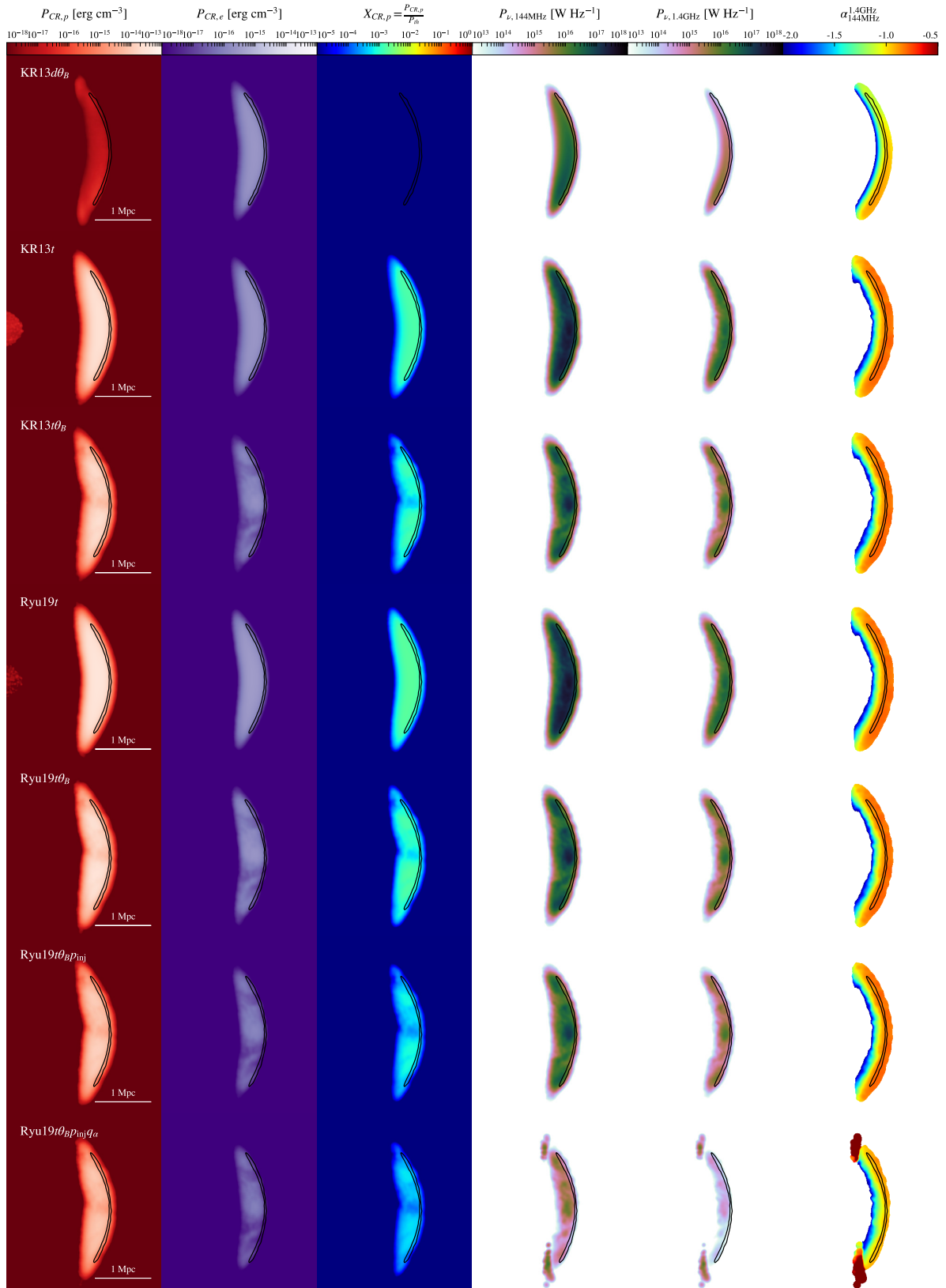


Figure 13.6: We show the same quantities as in Fig. 13.3 for the southern relic. The black contours show the SPH particles in the shock with a sonic Mach number $\mathcal{M}_s > 3$ which corresponds to the center of the shock.

is very smooth and again closely follows the fixed $K_{\text{ep}} = 0.01$ ratio. Including the obliquity dependent acceleration leads to a more complex morphology of the injected component as the efficiency fluctuates due to pockets of large and small obliquity. We can also see how this leads to complementary behavior between proton and electron injection in the KR13 $t\theta_B$ and Ryu19 $t\theta_B$ runs. In both KR13 runs the ratio between CR proton and thermal pressure is below 1%, however again this picture could change with multiple shocks and re-acceleration. This persists in the Ryu19 t run, as both efficiency models lie within a factor of ~ 2 of each other at $\mathcal{M}_s \approx 3$. Including $\eta(\theta_B)$ in the injection model again reduces the proton injection enough to account for this potential problem. As was the case with the NR including p_{inj} and q_α computation does not change the result significantly for protons. We find that the discrepancy in CR electron injection stems mainly from the on-the-fly calculation of K_{ep} , which leads to a significant decrease in this weaker shock.

13.6.2 Radio Relic Morphology

Considering the synchrotron surface brightness of the SR in the fourth and fifth panels of Fig. 13.6 gives a strong insight into the effect of the different components of our acceleration model. The KR13 $d\theta_B$ run again shows a very smooth emission due to the smooth injection and the less turbulent magnetic field behind the shock. While the injection of the CR electron component in the KR13 t run is similarly smooth we can see the imprint of the more turbulent magnetic field in the synchrotron emission at 144 MHz. Including $\eta(\theta_B)$ in this setup gives rise to the complex morphology with radio brighter nodes in the radio relic which can be observed in a number of observed examples (see [Dominguez-Fernandez et al., 2021](#); [Domínguez-Fernández et al., 2021](#), for a deeper analysis of the origin of substructure in relics). As discussed above the inclusion of p_{inj} and K_{ep} calculation in the run Ryu19 $t\theta_B p_{\text{inj}}$ reduces the CR electron injection significantly and with that reduces the synchrotron emission. The synchrotron emission is further reduced by including q_α and with that steepening the spectrum of the electron population, leaving fewer high-energy electrons to produce synchrotron emission. In all runs the synchrotron emission is at least two orders of magnitude below that of the NR. This puts strong observational constraints on the synchrotron brightness of these relics, providing an explanation for the occurrence of single-relics, as discussed in [van Weeren et al. \(2010\)](#).

13.6.3 Spectral Steepening

As was the case for the NR, the SR shows significant spectral steepening following the shock propagation. Again the Mach number contours are shown in black, indicating the center of the shock, behind which electron aging can set on. The KR13 t and Ryu19 t runs, with the exception of Ryu19 $t\theta_B p_{\text{inj}} q_\alpha$, show very consistent results. In the KR13 $d\theta_B$ run we find steeper spectra which we find to stem from the magnetic field morphology, as was the case in the NR. The steeper spectrum in the Ryu19 $t\theta_B p_{\text{inj}} q_\alpha$ run follows trivially from the steeper injection spectrum caused by our accounting for NLDSA. This shock seems to deform the outward moving shock and could be a site of electron re-acceleration. We will study this concept in future work with cosmological

simulations, which contain more complex systems that allow for colliding shocks and multiple shock scenarios.

13.7 Conclusions

We introduced a novel implementation of an on-the-fly Fokker-Planck solver for spectrally resolved CR physics included in the cosmological Tree-SPMHD code `OPENGADGET3`. We showed that the solver performs well for test cases and reproduces CR injection at shocks, spectral changes due to adiabatic changes of the surrounding gas, and high-energy cooling of CR electrons with high accuracy and good numerical stability.

We also applied the model to an idealized galaxy cluster merger to show that it is performant enough to be used in production runs. The results of these simulations can be summarized as follows

1. The subgrid modeling of CR proton injection is consistent with the lack of direct γ -ray observations in shocks due to the addition of shock obliquity dependent and the latest Mach number dependent injection models.
2. Spectral treatment of CR electrons allows to calculate observables such as synchrotron emission directly from the time-evolved CR population.
3. The injection models reproduce the complex radio relic morphology present in the CIZA relics.
4. Ageing of the electron population leads to a steepening of the radio spectrum of the relic, which can be obtained directly from the simulation data.
5. We can reproduce the shape of the synchrotron spectrum, albeit the absolute strength of the synchrotron emission is not reached. Cross-checking this against a shock tube test with realistic cluster shock parameters agrees well with previous results by other authors however, leading us to the opinion that the strength of the radio spectrum is most likely limited by the magnetic field strength over the whole relic.

In upcoming work, we will apply this model to high-resolution zoom-in simulations of galaxy clusters to study synchrotron and γ -ray emission of galaxy clusters.

14 | Zoom-In Simulations: 'Wrong Way' Radio Relics

Co-Authors: Ulrich P. Steinwandel and Klaus Dolag

As a next step, we applied the model to cosmological zoom-in simulations of a massive galaxy cluster to study Radio Relics (RRs). This work has been published in [Böss et al. \(2023b\)](#).

Abstract

Radio Relics are typically found to be arc-like regions of synchrotron emission in the outskirts of merging clusters. They typically show synchrotron spectra that steepen toward the cluster center, indicating that they are caused by relativistic electrons being accelerated at outwards traveling merger shocks. A number of radio relics break with this ideal picture and show morphologies that are bent the opposite way and spectral index distributions that do not follow expectations from the ideal picture. We propose that these 'Wrong Way' Relics can form when an outwards traveling shock wave is bent inwards by an in-falling galaxy cluster or group. We test this in an ultra-high resolution zoom-in simulation of a massive galaxy cluster with an on-the-fly spectral Cosmic Ray model. This allows us to study not only the synchrotron emission at colliding shocks but also their synchrotron spectra to address the open question of relics with strongly varying spectral indices over the relic surface.

14.1 Introduction

Radio Relics are roughly Mpc-size regions of radio emission in galaxy clusters, typically with an arc-like morphology, which shows strong polarisation (typically $\sim 30\%$ at 1.4 GHz, e.g. [Rajpurohit et al., 2022a](#)), steep integrated radio spectra ($L_\nu \propto \nu^\alpha$, where $\alpha \sim -1.1$) and a steepening of these spectra toward the cluster center (see [van Weeren et al., 2019](#), for a recent review). They are typically associated with ongoing mergers between massive galaxy clusters (see e.g. [Ensslin et al., 1998](#); [Roettiger et al., 1999](#); [Enßlin & Brüggen, 2002](#); [Brüggen et al., 2012](#); [Brunetti & Jones, 2014](#)). These mergers dissipate a large fraction of their potential energy in the form of shocks that heat the intra-cluster medium (ICM) to $\sim 10^8$ K. This can be observed as thermal X-ray emission of the fully ionized plasma (e.g. [Böhringer & Werner, 2010](#), for a review). A smaller part of the shock energy is dissipated into the acceleration of Cosmic Ray (CR) electrons and protons in a process called "diffusive shock acceleration" (DSA, see e.g., [Bell, 1978a,b](#); [Blandford & Ostriker, 1978](#); [Drury, 1983](#), the latter for a review). In this process

(supra-)thermal particles cross a shock front and are scattered by MHD turbulence from the downstream of the shock back into the upstream. They gain energy at every crossing until their gyro-radii are large enough to escape from the acceleration region or they are advected away downstream of the shock. Hybrid and PIC plasma simulations of shock fronts show that this process can efficiently accelerate protons in low- β supernova shocks (e.g. [Caprioli & Spitkovsky, 2014](#); [Caprioli et al., 2018](#); [Caprioli et al., 2020](#); [Pohl et al., 2020](#), the latter for a review) and high- β structure formation shocks (e.g., [Ryu et al., 2019](#); [Ha et al., 2023](#)). For electrons, it is found that this process is harder to trigger, as their gyro-radii are smaller at equivalent magnetic field strength, and with that, it is more difficult to start a cyclical DSA process and with that efficient acceleration of thermal electrons to the GeV energies expected from synchrotron emission by radio relics. They require an efficient pre-acceleration process such as (stochastic) shock-drift acceleration (SDA), or a seed population stabilized against cooling, to efficiently part-take in a DSA process (see e.g., [Guo et al., 2014](#); [Park et al., 2015](#); [Kang et al., 2019](#); [Tran & Sironi, 2020](#); [Kobzar et al., 2021](#); [Amano & Hoshino, 2022](#); [Tran et al., 2023](#)). On top of that the acceleration efficiency is found to be dependent on the shock obliquity, the angle between shock propagation, and magnetic field vector. Typically it is found that protons are more efficiently accelerated at quasi-parallel shocks (see e.g., [Kang & Ryu, 2013](#); [Caprioli & Spitkovsky, 2014](#); [Ryu et al., 2019](#)), while electrons are more efficiently accelerated at quasi-perpendicular shocks (e.g., [Guo et al., 2014](#); [Kang et al., 2019](#); [Ha et al., 2021](#); [Amano & Hoshino, 2022](#)). The results from small-scale plasma simulations have been adopted in cosmological simulations to model emission originating from structure formation shocks (see e.g., [Hoefl et al., 2008](#); [Pfrommer, 2008](#); [Pfrommer et al., 2007, 2008, 2017](#); [Skillman et al., 2013](#); [Vazza et al., 2012, 2016](#); [Wittor et al., 2017](#); [Banfi et al., 2020](#); [Wittor, 2021](#); [Ha et al., 2023](#)). However, the efficiencies found in plasma simulations are not sufficient to explain the high synchrotron brightness of radio relics (see [Botteon et al., 2020a](#), for a recent discussion).

Recent observations of radio relics show not only bright arc-like structures, but also more complex morphologies such as S-shapes (e.g., [de Gasperin et al., 2022](#)), flat relics with varying thickness (e.g., [van Weeren et al., 2016](#); [Rajpurohit et al., 2020a,b](#)) and filamentary structures (e.g. [Trasatti et al., 2015](#); [Rajpurohit et al., 2022b](#); [Chibueze et al., 2023](#)). There is also a small set of radio relics that show a curvature that points in the “wrong” direction. Instead of the typical outward-bent (convex) shape of the relic, away from the cluster center, they show an inward-bent (concave) morphology. Examples of these relics can be found in the *Ant Cluster* (PSZ2 G145.92-12.53) ([Botteon et al., 2021](#)), PSZ2 G186.99+38.65 ([Botteon et al., 2022](#)), *Source D1* in Abell 3266 ([Riseley et al., 2022](#)), SPT-CL J2023-5535 ([HyeongHan et al., 2020](#)), Abell 168 ([Dwarakanath et al., 2018](#)) and the southern relic in CIZA J2242.8+5301 (e.g., [van Weeren et al., 2010](#); [Stroe et al., 2013, 2016](#); [Hoang et al., 2017](#); [Di Gennaro et al., 2018](#)). They can show steep synchrotron spectra which would indicate Mach numbers of the underlying shocks that are in disagreement with the critical Mach numbers found to be required to efficiently accelerate CR electrons (e.g., [Kang et al., 2019](#)) and some of their spectra are better fit by broken power-laws rather than a single one hinting toward overlapping (re-)acceleration processes as shown in [Riseley et al. \(2022\)](#) and initially also in [Owen et al. \(2014\)](#); [Trasatti et al. \(2015\)](#); [Parekh et al. \(2022\)](#). However, follow-up observations indicate that there is no spectral break in the majority of these relics after all ([Benson et al., 2017](#); [Rajpurohit et al., 2022a](#)), making the source *D1* the only relic so far that

shows this peculiar spectral behavior. The southern relic of CIZA J2242.8+5301 shows additional strong variations of the synchrotron slope, which makes it hard to explain in the context of DSA at a single shock front (see discussion in [Di Gennaro et al., 2018](#)). Cosmological simulations of galaxy clusters show that mergers between clusters are not isolated events and that merger shocks can deform as they expand into highly complex and turbulent ICM (e.g. [Hoefl et al., 2008](#); [Skillman et al., 2013](#); [Wittor et al., 2017](#); [Nuza et al., 2017](#)). In this work, we propose that a possible formation mechanism for these ‘Wrong Way’ relics (as they are referred to in [Riseley et al., 2022](#)) is the collision of an outwards traveling shock front with an in-falling substructure. We investigate this scenario in the sibling simulation of an ultra-high resolution MHD simulation of a $M_{\text{vir}} \approx 1.3 \times 10^{15} M_{\odot}$ galaxy cluster introduced in [Steinwandel et al. \(2023b\)](#), where we attached a population of CR protons and electrons to every resolution element of our simulation. This effectively turns every particle into a tracer particle for CRs, while also accounting for feedback by the CR component on the thermal gas. We resolve these populations with a spectral resolution of 12 bins for protons and 48 bins for electrons over a range of 6 orders of magnitude in momentum. The distribution function of the CRs is updated on-the-fly at every timestep of the simulation according to the method presented in [Böss et al. \(2023c\)](#). This allows us to study CR electron injection at colliding shocks and the subsequent cooling of the relativistic electron population. To the best of our knowledge, this simulation is the first of its kind. This work is structured as follows: In Sec. 14.2 we describe the simulation code, CR model, and initial conditions used in this work. In Sec. 14.3 we study the ‘Wrong Way’ Relic (WWR) found in the simulation and its origin. Sec. 14.4 contains a discussion of our findings and a comparison to observed systems. Finally, Sec. 14.5 contains our conclusion and outlook for future work.

14.2 Methods

The simulation used in this work was carried out with the Tree-SPMHD code `OPENGADGET3`. `OPENGADGET3` is a derivative of `GADGET2` ([Springel, 2005](#)) with improvements to the hydro and gravity solvers as well as additional physics modules. The SPH solver is updated as described in [Beck et al. \(2016b\)](#) to include higher order kernels and their bias correction (see [Dehnen & Aly, 2012](#)) and artificial viscosity as well as physical conduction to improve the mixing behavior and shock capturing of SPH (e.g. [Price, 2012](#); [Hopkins, 2013](#); [Hu et al., 2014](#)). Magnetohydrodynamics (MHD) have been implemented by [Dolag et al. \(2009a\)](#) with updates to include non-ideal MHD in the form of constant (physical) diffusion and dissipation presented in [Bonafede et al. \(2011\)](#). Conduction is modeled via a conjugate gradient solver ([Petkova & Springel, 2009](#); [Arth et al., 2014](#); [Steinwandel et al., 2020b](#)), with a suppression factor of the Spitzer value for conduction of 5 percent. We adopt a Wendland C4 kernel ([Wendland, 1995, 2004](#)) with 200 neighbors and bias correction as suggested by [Dehnen & Aly \(2012\)](#).

We employ the on-the-fly spectral CR model `CRESCENDO` introduced in [Böss et al. \(2023c\)](#) to model the time evolution of CR protons and electrons in every resolution element of our simulation. The time evolution of distributions of CRs in the absence of CR transport, diffusion in

momentum space, and catastrophic losses can be described by

$$\frac{Df(p, \mathbf{x}, t)}{Dt} = \left(\frac{1}{3} \nabla \cdot \mathbf{u} \right) p \frac{\partial f(p, \mathbf{x}, t)}{\partial p} \quad (14.1)$$

$$+ \frac{1}{p^2} \frac{\partial}{\partial p} \left(p^2 \sum_l b_l f(p, \mathbf{x}, t) \right) \quad (14.2)$$

$$+ j(\mathbf{x}, p, t), \quad (14.3)$$

where we used $\frac{Df}{Dt} = \frac{\partial f}{\partial t} + \mathbf{u} \cdot \nabla f$ due to `OPENGADGET3` being a Lagrangian code. The right side of Eq. 14.1 describes changes due to adiabatic compression or expansion of the gas the CRs are confined in, Eq. 14.2 describes energy losses, and Eq. 14.3 is the source term. We represent $f(p, \mathbf{x}, t)$ as piece-wise powerlaws in momentum space with 2 bins/dex for protons and 8 bins/dex for electrons in the dimensionless momentum range $\hat{p} \equiv \frac{p_i}{m_i c} \in [0.1, 10^5]$, where p_i and m_i refer to the momentum and mass for protons and electrons, respectively. The distribution function is updated at every timestep following the two-moment approach as introduced in [Miniati \(2001\)](#) by computing CR number and energy changes per bin. Adiabatic changes are accounted for at every timestep via the density change within an SPH particle. We model energy losses of electrons due to synchrotron emission and inverse Compton scattering off CMB photons. As a source term we employ the DSA parametrization by [Kang & Ryu \(2013\)](#) for the dependency on sonic Mach number ($\eta(\mathcal{M}_s)$), which allows for DSA at shocks beyond a critical Mach number $\mathcal{M}_s > 2$ and saturates at a maximum efficiency of $\eta_{\max} \approx 0.2$. In addition to that, we use the model by [Pais et al. \(2018\)](#) for the dependency of CR acceleration efficiency on shock obliquity ($\eta(\theta_B)$). Ultimately we divert a fraction

$$\eta_{\text{tot}} = \eta(\mathcal{M}_s) \times \eta(\theta_B) \quad (14.4)$$

of the entropy change over the shock into the CR component. We detect the shock properties on-the-fly in the simulation with the shock finder introduced by [Beck et al. \(2016a\)](#) with improvements to compute the shock obliquity as the angle between the pressure gradient within the kernel (which we treat as the shock normal $\hat{\mathbf{n}}$) and the magnetic field vector upstream of the shock \mathbf{B}_u . The slope of the injected CR spectrum follows linear DSA theory and we use a fixed electron to proton injection ratio of $K_{e/p} = 0.01$. The CR component exerts feedback on the thermal gas by solving the pressure integral

$$P_{\text{CR},c} = \frac{4\pi c}{3} a^4 \int_{p_{\min}}^{p_{\text{cut}}} dp p^3 f(p) \quad (14.5)$$

between the minimum momentum p_{\min} represented by the CR population and the cutoff of the distribution function p_{cut} . We start the CR injection at $z = 4$ to avoid too strong time constraints due to very efficient high-momentum energy losses of CR electrons.

Synchrotron emission is calculated directly from the evolved electron distribution function (see Sec. 11.1 for details).

We use a zoomed-in initial condition of a massive galaxy cluster with a virial mass of $M_{\text{vir}} \approx 1.3 \times 10^{15} M_{\odot}$ from the sample presented in [Bonafede et al. \(2011\)](#). The cluster is up-sampled

to 250x base resolution, which corresponds to a mass resolution of $M_{\text{gas}} \approx 8.7 \times 10^5 M_{\odot}$ and $M_{\text{DM}} \approx 4.7 \times 10^6 M_{\odot}$ for gas and dark matter particles, respectively. We reach a maximum resolution for a gas particle of $h_{\text{sml},\text{min}} \approx 1$ kpc with a gravitational softening of $\epsilon = 0.48 h^{-1} c$ kpc. The cluster was selected from a lower-resolution dark matter-only simulation of a Gpc volume, which is large enough to provide a large sample of systems above a few $10^{15} M_{\odot}$. The parent simulation used a WMAP7 cosmology with $\Omega_0 = 0.24$, $\Omega_{\Lambda} = 0.76$, $\Omega_{\text{baryon}} = 0.04$, $h = 0.72$ and $\sigma_8 = 0.8$, which we also adopt for the present simulation. We start the simulation at redshift $z = 310$ and seed a constant magnetic field in the x-direction with $B_0 = 10^{-14}$ G (see [Steinwandel et al., 2022](#), for a study of the impact of the choice of B_0). The initial conditions of this cluster at this resolution have been used to study the interaction between internal- and accretion shocks in [Zhang et al. \(2020b,a\)](#) and its magnetic field has been studied in [Steinwandel et al. \(2023b\)](#).

14.3 Results

14.3.1 Merger Geometry

The ‘Wrong Way’ relic in our simulation originates from a triple-merger at $z \sim 0.35 - 0.2$. We show the schematic of the merger geometry in Fig. 14.1. A high-velocity merger with a 1:10 mass ratio between impactor ($M_2 \approx 10^{14} M_{\odot}$) and target ($M_1 \approx 10^{15} M_{\odot}$) with a large impact parameter of $b \approx 500$ kpc drives two shock waves. These shocks follow the canonical picture (e.g. Fig. 7 in [van Weeren et al., 2019](#)) of the lighter merging partner (M_2) driving a strong bow-shock (S_2 in our schematic), while the heavier merging partner (M_1) drives a weaker counter shock (S_1) in the in-fall direction of the lighter partner. This counter shock is subsequently impacted by a third merger partner (M_3), a group of galaxies with a total mass of $M_3 \approx 2 \times 10^{13} M_{\odot}$, which ultimately passes through the shock surface and falls into the larger merger partner (M_1) in a low-impact parameter merger with $b \approx 35$ kpc. The impact of the group deforms the weaker counter shock (S_1) first from a convex shape at $z = 0.32$ to a concave shape at $z = 0.29$ and subsequently to a v-like shape pointing toward the cluster center at $z = 0.27$, which also leads to a complex superposition of the different parts original shock surface with different mach numbers as well as differently aged cosmic ray electron population.

Due to our system being a single, isolated cluster, we cannot make any predictions for the minimum critical mass of an in-falling sub-structure that is able to deform such a shock front or the statistical frequency of such an event. We leave this question for future work with cosmological boxes, to allow for a statistical analysis.

14.3.2 The Simulated ‘Wrong Way’ Radio Relic

Fig. 14.2 from top to bottom shows the time evolution of the countershock S_1 in the xz -plane of the simulation and its phasing through morphologies matching various ‘Wrong Way’ relics. The bottom row shows the same relic as the row above in the yz -plane. From left to right we show the X-ray surface brightness, CR electron energy contained in the part of the potentially synchrotron

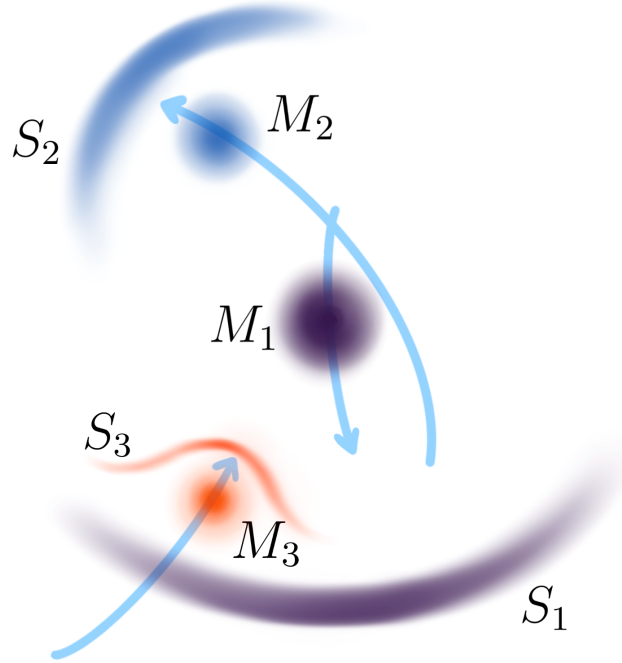


Figure 14.1: A simplified schematic of the merger geometry that produces the ‘Wrong Way’ relic. The initial merger between M_1 and M_2 drives two shocks, the weaker of which is subsequently impacted by a third substructure M_3 . This impact deforms parts of the outwards traveling shock S_1 and produces the WWR S_3 .

bright population with $E > 1$ GeV, the synchrotron surface brightness at 1.4 GHz, and the slope of the synchrotron spectrum obtained by fitting a power-law to the surface brightness at 144 MHz and 1.4 GHz. These images are obtained by mapping the SPH data to a 2D grid following the algorithm described in Dolag et al. (2005a) with a pixel-size of $\Delta_{\text{pix}} \approx 1$ kpc. This corresponds to a resolution of $\theta_{\text{pix}} \approx 0.24''$ at $z = 0.27$ and with that is significantly below current observational limits. Accompanying to that we show the distribution of sonic Mach number \mathcal{M}_s of the different panels of Fig. 14.2 in Fig. 14.3 and the synchrotron spectra in Fig. 14.4. In Fig. 14.5 we show the histograms of pixels in Fig. 14.2 as a function of synchrotron intensity and spectral slope.

At $z = 0.32$, in the top row of Fig. 14.2, we see the acceleration of CR electrons at the counter shock of the main merger event. Fig. 14.3 shows that only a fraction of the shocked particles are above the critical Mach number $\mathcal{M}_{s,\text{crit}} = 2$ and with that can accelerate CRs. We can readily identify the part of the shock surface that accelerates CRs in the center of the images, as it is the most synchrotron bright part and shows a relatively flat synchrotron spectrum. These CRs are accelerated at the contact surface between outwards traveling shock and the atmosphere of the in-falling halo. The steeper parts of the spectrum in the upper right corner of the images indicate that these electrons have been accelerated at earlier times of the shock propagation and have been freely cooling since. This is also evident in the synchrotron spectrum in Fig. 14.4, which shows

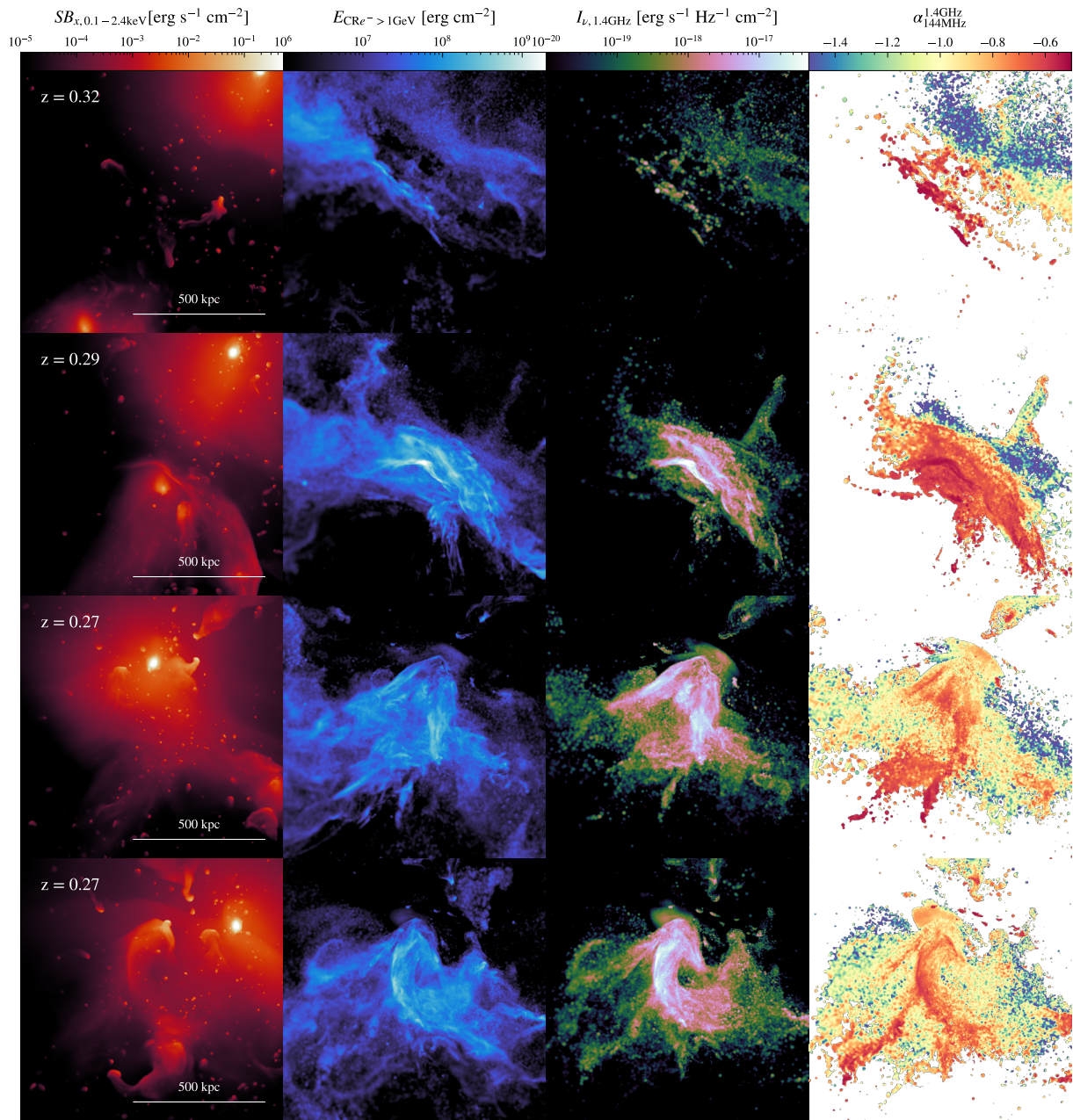


Figure 14.2: From left to right: X-ray surface brightness, CR electron energy of electrons with $E > 1$ GeV, synchrotron surface brightness at 1.4 GHz, and the slope of the synchrotron spectrum between 144 MHz and 1.4 GHz. The upper three rows show the time evolution of the in-falling group in the xz -plane of the simulation, and the lowest row shows the same relic at $z = 0.27$ in the yz -plane. To obtain the images the SPH data is mapped to a grid with a resolution of $\Delta_{\text{pix}} \approx 1$ kpc, which corresponds to a resolution of $\theta_{\text{pix}} \approx 0.24''$ at $z = 0.27$

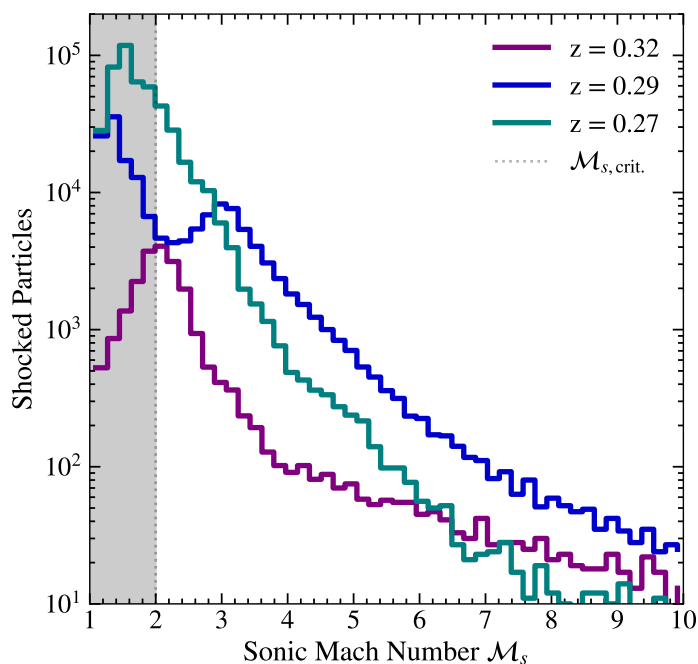


Figure 14.3: Histograms of the sonic Mach number \mathcal{M}_s for the three output times shown in Fig. 14.2. The colors correspond to the different times and the dotted line indicates the critical Mach number beyond which CR (re-)acceleration can occur in our model.

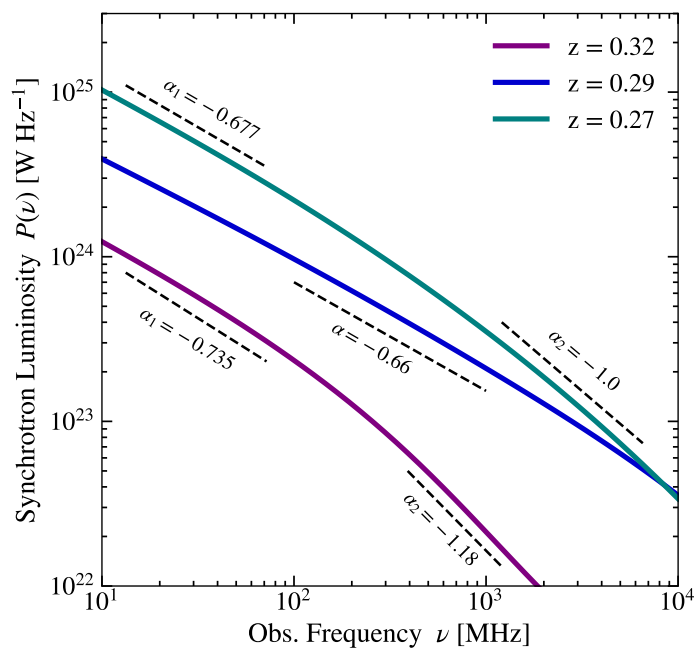


Figure 14.4: Time evolution of the synchrotron spectrum. Colors correspond to the times in Fig. 14.2 and 14.3. Dashed lines and labels show the spectral slope in the indicated frequency ranges.

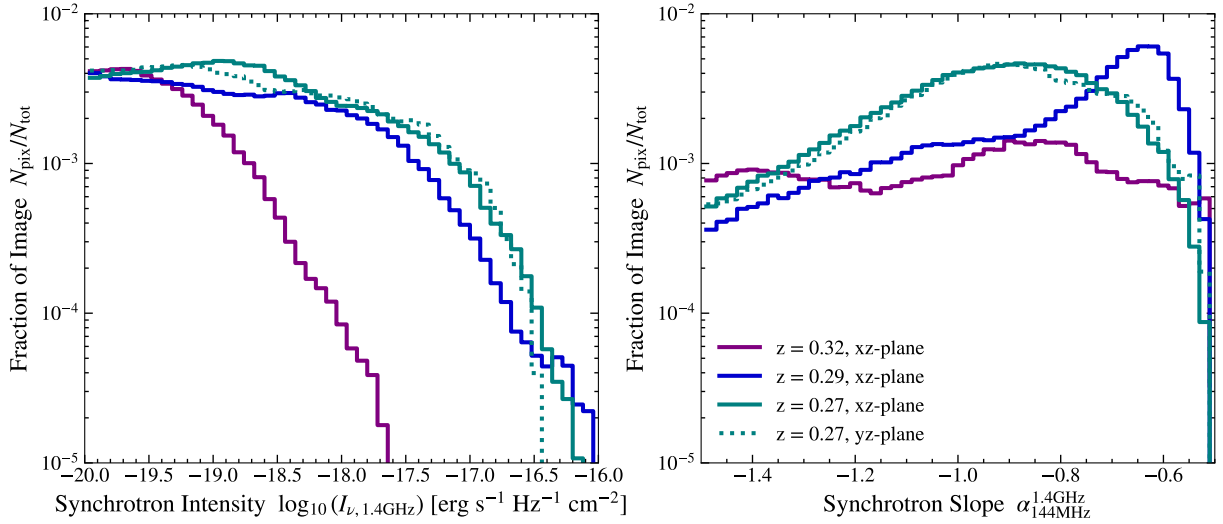


Figure 14.5: Histograms of the synchrotron surface brightness (*left*) and spectral slope (*right*) obtained from the images in Fig. 14.2. As before colors correspond to the times in Fig. 14.2 and 14.3. The dotted line indicates the same relic at $z = 0.27$ in the yz -plane of the simulation, as in the lowest row of Fig. 14.2.

a strong break above $\nu \sim 200$ MHz. The countershock is initially not very synchrotron bright, akin to the counter-shock in Abell 3667 (e.g. [de Gasperin et al., 2022](#)) or CIZA J2242.8+5301 ([Di Gennaro et al., 2018](#)).

At $z = 0.29$ the collision between outwards traveling counter shock and the bow-shock of the in-falling group (M_3) increases the sonic Mach number and with that the acceleration efficiency of the shock (see e.g. [Kang, 2021](#); [Inchingolo et al., 2022](#), for studies of multi-shock scenarios). Fig. 14.3 shows that while the majority of the shocked particles remain sub-critical, the shock develops a second Mach number peak around Mach 3. This significantly increases the synchrotron surface brightness at the contact surface of the shocks, flattens the synchrotron spectrum to almost the theoretical limit of DSA, and erases the spectral break. A spectral slope of $\alpha_{100\text{MHz}}^{1\text{GHz}} = -0.66$ indicates $M_s \approx 3.6$, in good agreement with the underlying Mach number distribution. This injection domination can also be seen in Fig. 14.5 where the images at $z = 0.29$ show a strong bump in synchrotron slopes between $|\alpha| \approx 0.7 - 0.55$ and a small bump in synchrotron intensity around $I_\nu \approx 10^{-16.5} - 10^{-16}$ erg s $^{-1}$ Hz $^{-1}$ cm $^{-2}$.

The in-falling sub-structure deforms the outwards traveling shock toward a relic pointing “the wrong way”, similar to the source *DI* observed by [Riseley et al. \(2022\)](#). In the case of our relic, the flat spectrum part is further extended, which we attribute to the shock being further bent inwards, compared to *DI*.

In Fig. 14.6 we rotate the image into the merger plane and can see how the aged, steep-spectrum population disappears behind the newly injected electrons at the inward bent relic. Comparing to the same rotation at $z = 0.32$ indicates that the best morphological fit to *DI* would lie between $z = 0.32$ and $z = 0.29$, however there is no output available at this time.

The collision between shock waves is also visible in our X-ray image (left panel, second row in Fig. 14.2), which matches the detection of a shock in X-ray by Sanders et al. (2022). The in-fall scenario proposed here also produces a radio relic-like structure within r_{500} , which is unlikely in the classical picture of radio relics (e.g., Vazza et al., 2012).

At $z = 0.27$, as the in-falling halo passes through the outwards traveling shock its own bow-shock collides with the older shock, causing the relic to deform further into a v-shaped morphology, such as in the counter shock to the *sausage relic* (e.g. Stroe et al., 2013; Di Gennaro et al., 2018), or the relic in Abell 2256 (Rajpurohit et al., 2022b). The Mach number distribution over the shock surface has become smoother at this point, with the bulk of the shock being sub-critical, however, the total number of particles with $M_s > 2$ has increased compared to the relic at $z = 0.29$. This leads to efficient acceleration at a part of the shock surface, visible in increased synchrotron surface brightness and flatter synchrotron spectra.

In general, the relic is however cooling and adiabatic compression dominated. This becomes visible in Fig. 14.5 where synchrotron intensity is increased in the $I_\nu \sim 10^{-17.5} - 10^{-16.5}$ erg s⁻¹ Hz⁻¹ cm⁻² range. However, spectra are generally steeper, indicating that the increase in intensity is partly by injection and partly by adiabatic compression of an already cooling electron population.

A morphological best match for the relic in Abell 2256 is expected to lie between $z = 0.29 - 0.27$ shown here, however, the simulation output for this time is not available. For the lower panels of Fig. 14.2 we rotate the image by 90°, as this projection more closely resembles the observations of Di Gennaro et al. (2018). The collision of two shocks as shown here leads to a superposition of multiple DSA-like events due to strong variations of the Mach number over the shock surface. This leads to strong variations of synchrotron surface brightness and spectral shape between the regions of the shock surface where efficient (re-) acceleration can take place and the regions that are dominated by cooling and adiabatic compression.

These variations can also be seen in the integrated spectrum in Fig. 14.4, where the lower frequency end of the spectrum is strongly injection dominated and the high-frequency end of the spectrum shows a significant steepening beyond $\nu \sim 1$ GHz in the cooling dominated part. This result is valid for the two lower panels of Fig. 14.2, as we are dealing with integrated quantities. We have confirmed this by comparing the integrated spectrum obtained based on the data directly from the SPH particles as well as integrated maps under three different projections. We find no qualitative difference between these approaches.

14.3.3 Relic rotations

In Fig. 14.6 we rotate the WWR in our simulation into the merger plane. The panels show a rotation by 30° around the x -axis from the xz -plane. At $z = 0.32$ we can see that the recently injected CRs stem from the first contact between outwards traveling shock and the atmosphere of the in-falling halo. This leads to a similar morphology as in Riseley et al. (2022), however, the shock is a lot less pronounced due to the early stage of the contact. At $z = 0.29$, as the relic rotates into the merger plane we can see that it is bent further into the cluster center than the Riseley et al. (2022) relic, indicating that it is further progressed than the observed counterpart. This hides the steep, aged spectrum behind the newly injected electrons, leading to the flat spectrum part

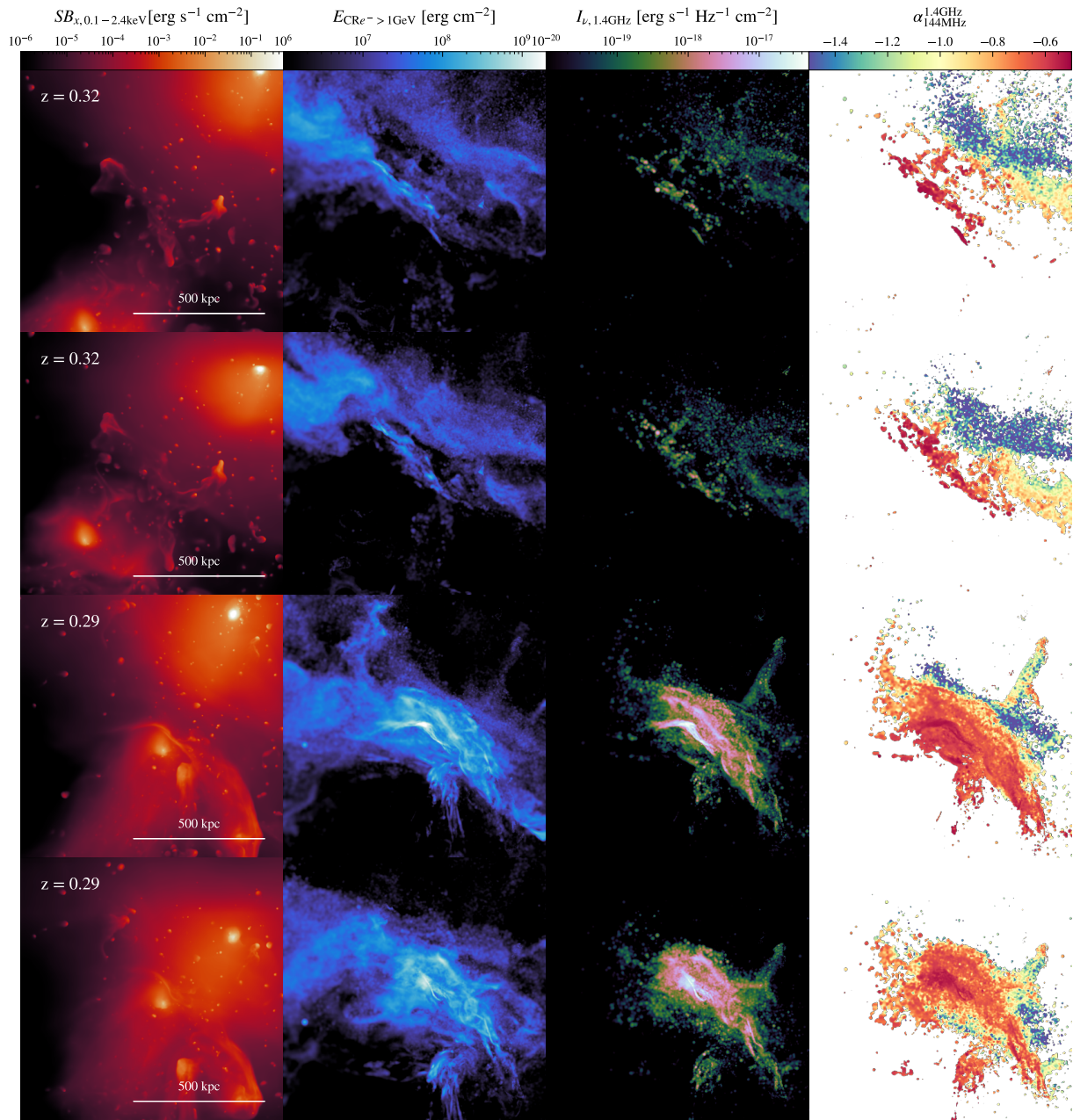


Figure 14.6: Similar to Fig. 14.2 we show our WWR at $z = 0.29$ and $z = 0.27$. The first and third rows show the default projection in the xz -plane, and the second and fourth rows show the relic rotated into the merger plane. Please note that the lower limit in the left-most column is one order of magnitude lower compared to Fig. 14.2 to improve the visibility of the contact between outwards moving shock and the atmosphere of the in-falling halo.

dominating the image. We, therefore, conclude that an ideal reproduction of source *DI* would lie between $z = 0.32 - 0.29$, most likely shortly after $z = 0.32$.

14.4 Discussion

To discuss our findings we will compare the morphologies in chronological order to similar observed systems. Albeit the number of observed WWRs is still small, the recent discoveries due to ASKAP and MeerKAT indicate that with increased sensitivity a number of new WWRs can be detected over time.

14.4.1 Abell 520

Before the onset of the WWR morphology our cluster undergoes an internal merger with an in-falling group in the cluster periphery. This group falls into the cluster at a similar trajectory as the cluster driving the current shock waves and is therefore in the path of the weaker counter-shock of the ongoing merger. A similar setup is observed in Abell 520 by [Hoang et al. \(2019\)](#). They detect a shock with Mach number $\mathcal{M}_{\text{SW}} = 2.6^{+0.3}_{-0.2}$ propagating in SW direction with a weaker counter-shock moving with $\mathcal{M}_{\text{SW}} = 2.1 \pm 0.2$ in NE direction. Along the NE diagonal Chandra observations by [Andrade-Santos et al. \(2017\)](#) indicate in-falling matter along a similar path as the ongoing merger. This shows that the geometric setup is possible, albeit rare and Abell 520 could host a WWR in the future.

14.4.2 Abell 3266

At $z = 0.32 - 0.29$ our WWR resembles the one observed by [Riseley et al. \(2022\)](#), at a distance of ~ 1 Mpc from the center of Abell 3266. Their relic is very faint and shows a very steep spectral index of $\alpha = -2.76$ in the part that is observable in frequencies above 1043 MHz. The lower frequency end of the relic spectrum is significantly flatter, with a spectral index of $\alpha \approx -0.72$. This indicates that there is a re-acceleration process which is superimposed on an older cooling spectrum, even though the very steep spectrum still poses problems under this assumption (see discussion in [Riseley et al., 2022](#)). X-ray observations with eROSITA ([Sanders et al., 2022](#)) show a number of discrete sources in close proximity to *DI*, but no extended sources that could indicate an infalling group. The extended sources *X4* and *X6* that lie in (projected) close proximity to *DI* have significantly higher photometric redshifts ($z = 0.532$ for *X4* and $z = 0.907$ for *X6*) than Abell 3266 ($z = 0.0589$, [Struble & Rood, 1999](#)), which shows that these are background sources and not in-falling groups. However, as can be seen in the left panel of Fig. 14.2 at $z = 0.27$, depending on the projection it is not necessarily easy to distinguish the in-falling structure in the X-ray emission.

14.4.3 PSZ2G145.92-12.53

Another concave radio relic detected in PSZ2G145.92-12.53 similarly shows an increase in X-ray flux with concave morphology in close proximity to the relic (see Fig. 1 in [Botteon et al., 2021](#)). We note that there is also a detected peak in X-ray surface brightness akin to the one observed in the *Rim* region in PSZ2G145.92-12.53, indicating that similar effects may be at play there, as briefly discussed by the authors.

14.4.4 Abell 2256

As previously discussed, at $z = 0.27$ in the xz plane, corresponding to the third row in Fig. 14.2, our WWR closely resembles the steep radio relic found in Abell 2256. [Rajpurohit et al. \(2022b\)](#) note an association between the relic and the source F, without an X-ray counterpart (see also [Owen et al., 2014](#); [Ge et al., 2020](#)). This could hint toward the group having passed the shock before in a similar process as discussed here. The superposition of injected and cooling parts of the shock surface can also be seen in the color-color plots in [Rajpurohit et al. \(2022b\)](#), which indicate that the relic consists of a number of overlapping substructures. The (re-) acceleration of particles in the turbulent downstream of S_1 , which becomes the upstream of S_3 , also produces filamentary structures seen in the relativistic electron component (second panels from left in Fig. 14.2) as observed in Abell 2256 (see e.g. [Dominguez-Fernandez et al., 2021](#); [Wittor et al., 2023](#), for detailed studies of surface structures in radio relics). The observed relic shows very little spectral steepening, making it difficult to discern if it was bent against its propagation direction. The little steepening that is being detected however points toward the cluster center akin to our simulated relic, which can indicate a similar process to the one we discussed here.

14.4.5 CIZA J2242.8+5301

In the case of the counter shock to the sausage relic in CIZA J2242.8+5301 the reason for the strong variations of synchrotron spectral index is still under debate (see discussion in [Di Gennaro et al., 2018](#)). In the context of our merger scenario these variations can be understood as follows: As the outwards traveling shock (S_1) collides with the bow-shock of the in-falling substructure (M_3) and is deformed, the resulting shock surface (S_3) shows strong variations in sonic Mach number. Wherever the sonic Mach number is $\mathcal{M}_s < 2$ our DSA model allows no CR (re-) acceleration and the pre-existing population is simultaneously cooling due to synchrotron and IC losses and being adiabatically compressed by the sub-critical shock. This leads to a continuously steepening synchrotron spectrum, while the adiabatic compression leads to an increase in synchrotron surface brightness. In regions of the shock surface where $\mathcal{M}_s > 2$ there is ongoing (re-) acceleration of CR electrons, which lead to a flatter spectrum than for the cooled population. This superposition of cooling- and acceleration dominated areas on the shock surface leads to a strong variation of synchrotron spectral index, as can be seen in the bottom row of Fig. 14.2.

14.5 Conclusion

In this work we showed the first results of a high-resolution simulation of a massive galaxy cluster with an on-the-fly spectral Fokker-Planck solver to study the acceleration, advection and aging of CR electrons in cosmological zoom-in simulations. We applied this simulation to study a rare form of radio relics that show inward-bent, instead of the typical outward-bent morphologies. Our results can be summarized as follows:

- In complex merging systems with multiple ongoing mergers collisions between bow-shocks of in-falling substructures and outwards traveling merger shocks can deform the outwards traveling shocks in a way that is morphologically very similar to the currently reported ‘*Wrong Way*’ relics.
- These collisions between shocks increase the Mach number at the contact surface of the shocks and with that boost the (re-)acceleration efficiency of CR electrons. This makes their detection easier than that of the cooled, outwards moving shock.
- The inclusion of an on-the-fly spectral treatment of CR electrons allows to reproduce the large variance of synchrotron spectral slope across the relic surface. This variance stems from the co-existence of an aged CR electron population in the outwards traveling shock and newly injected CRs at the high Mach number regions of the shock surface.

Future work will expand our sample size of radio relics by performing further zoom-in simulations of the cluster set presented in [Bonafede et al. \(2011\)](#) at 250x base resolution and will study surface structure and polarisation properties of these relics, as well as γ -ray emission by the accelerated protons.

15 | Simulating the LLocal Web (SLOW): Synchrotron Emission from the Local Cosmic Web

Co-Authors: Klaus Dolag, Ulrich P. Steinwandel, Elena Hernández-Martínez,
Benjamin Seidel and Jenny G. Sorce

We applied CRESCENDO to a realization of the SLOW simulation set (Dolag et al., 2023b). This work has been submitted to A&A and is currently undergoing peer review. A preprint is available as Böss et al. (2023a).

Abstract

Aims: Detecting diffuse synchrotron emission from the cosmic web is still a challenge for current radio telescopes. We aim to make predictions for the detectability of cosmic web filaments from simulations.

Methods: We present the first cosmological MHD simulation of a $500 h^{-1} c\text{Mpc}$ volume with an on-the-fly spectral cosmic ray (CR) model. This allows us to follow the evolution of populations of CR electrons and protons within every resolution element of the simulation. We model CR injection at shocks while accounting for adiabatic changes to the CR population and high energy loss processes of electrons. The synchrotron emission is then calculated from the aged electron population under the assumption of different models for the origin and amplification of magnetic fields. We compare the amplified primordial magnetic field directly obtained within the MHD simulation, to several magnetic field models motivated by the thermodynamic and kinematic properties taken from the underlying simulation. We use constrained initial conditions, which closely resemble the local Universe, in order to compare to observational counterparts. These results are compared to a higher resolution zoom-in simulation of the Coma cluster, to study the impact of resolution and turbulent re-acceleration of CRs on the results.

Results: We find a consistent injection of CRs at accretion shocks onto cosmic web filaments and galaxy clusters. This leads to diffuse emission from filaments of the order $S_\nu \approx 0.1 \mu\text{Jy beam}^{-1}$ for a potential LOFAR observation at 144 MHz, when assuming the most optimistic magnetic field model and the inclusion of an on-the-fly treatment of re-acceleration of electrons by turbulence. The flux can however be increased by up to two orders of magnitude for different choices of CR injection parameters. This can bring the flux within a factor of 10 of the current limits for

direct detection. We find a spectral index of the simulated synchrotron emission from filaments of $\alpha \approx -1.0 - -1.5$.

15.1 Introduction

From observations of galaxy clusters, we can assume an efficient acceleration of Cosmic Ray (CR) electrons (CRe) which provide powerful tracers of the intra-cluster medium's magnetic field such as radio relics and radio halos (see [van Weeren et al., 2019](#), for a review). The recent discovery of "Radio Mega Halos" ([Cuciti et al., 2022](#)) and "Radio Bridges" (e.g. [Govoni et al., 2019](#); [Botteon et al., 2020b](#); [Bonafede et al., 2021](#); [Venturi et al., 2022](#); [Radiconi et al., 2022](#)) also indicates that there must be a substantial population of relativistic electrons even further from the cluster center than previously expected. This poses a number of theoretical problems for the acceleration of electrons and their stabilization against energy losses, as well as magnetic field strength in these regimes. The canonical process of CR acceleration in galaxy clusters is diffusive shock acceleration (see [Drury, 1983](#), for a review), where particles are accelerated from the thermal pool by scattering off magneto-hydrodynamic (MHD) turbulence up- and downstream of shock fronts, gaining energy at every crossing from up- to downstream. This naturally produces a power-law distribution of CRs in momentum space, consistent with the power-law slope of the synchrotron spectrum of radio relics. Hybrid- and particle-in-cell (PIC) simulations of CR acceleration find that the acceleration efficiency at the shock depends strongly on sonic Mach number (see e.g. studies by [Kang & Ryu, 2013](#); [Caprioli & Spitkovsky, 2014](#); [Ryu et al., 2019](#)), which would indicate a highly efficient acceleration of CRs in the cluster periphery, e.g. at accretion shocks around galaxy clusters and cosmic filaments where high Mach number shocks are found in simulations (e.g. [Ryu et al., 2003](#); [Pfrommer et al., 2006](#); [Vazza et al., 2009, 2011](#); [Schaal & Springel, 2015](#); [Banfi et al., 2020](#); [Ha et al., 2023](#)). However, detailed studies on the efficiency of CRe acceleration in high- β (with $\beta = \frac{P_{\text{th}}}{P_B} \sim 10 - 50$) plasmas are typically performed for the high-temperature, low Mach number shocks (e.g. [Guo et al., 2014](#); [Kang et al., 2019](#); [Kobzar et al., 2021](#); [Ha et al., 2021](#)) to understand the discrepancy between predicted electron acceleration efficiency and radio brightness of radio relics (see [Botteon et al., 2020a](#), for a detailed discussion). [Ha et al. \(2023\)](#) recently performed PIC simulations with a high- β , low temperature ($T = 10^4$ K) and high sonic Mach number ($\mathcal{M}_s = 25 - 100$) setup to study the acceleration efficiency of CRe in accretion shocks. Applying their model to post-process outputs from a cosmological simulation, they find emission of the order $S_\nu \sim 1 - 10$ mJy beam $^{-1}$ for accretion shocks around a Coma-like cluster, which is in agreement with emission by an accretion shock reported by [Bonafede et al. \(2022\)](#).

The second ingredient to potential synchrotron emission in filaments is the magnetic field strength in these environments. These field strengths can be estimated from rotation measurements, where the intrinsic polarisation angle of a strongly polarized source, like synchrotron emission by electrons accelerated in an AGN jet, is rotated by the magnetic field along the line-of-sight to the observer. These observations indicate magnetic field strengths of 10-100 nG (e.g. [Vernstrom et al., 2019](#); [Carretti et al., 2022](#); [O'Sullivan et al., 2019, 2020, 2023](#)). Alternatively, the stacking of cluster pairs and filaments can provide upper limits on the synchrotron emission and with

that the superposition of CRe population and magnetic field strength (e.g. [Brown et al., 2017](#); [Vernstrom et al., 2017, 2021](#); [Locatelli et al., 2021](#); [Hoang et al., 2023](#)). Direct observations of radio emission from cosmic web filaments could help disentangle this superposition and therefore give insight into the CRe acceleration, as well as the magnetic field strength and structure in cosmic web filaments.

A number of numerical studies have made predictions for such observations by taking into account different models for magnetic fields and CRe components and applying them to large-scale simulations.

[Vazza et al. \(2015b\)](#) used MHD simulations of a $(50 \text{ Mpc})^3$ volume ([Vazza et al., 2014](#)) and applied shock detection and the CR acceleration model of [Hoeft & Brüggen \(2007\)](#) to study potential synchrotron emission by shock accelerated electrons in accretion shocks and internal shocks in cosmic web filaments. They varied their magnetic field strength by re-scaling their simulated magnetic field with a density model and find in the high amplification model a diffuse emission from filaments of the order $\sim \mu\text{Jy beam}^{-1}$.

[Brown et al. \(2017\)](#) use a different approach by modeling CR electrons as secondaries of shock-accelerated protons. These protons are expected to live for longer than one Hubble time in the low-density cosmic web filaments and can scatter with thermal protons into charged pions, which decay into electrons and positrons (e.g. [Blasi et al., 2007](#)). These secondary models require a substantial primary proton population to produce considerable secondary electrons which is in conflict with the current non-detection of γ -ray photons that should also originate from this process (see e.g. [Wittor et al., 2019](#), and references therein). [Brown et al. \(2017\)](#) took the model by [Dolag et al. \(2004\)](#), which constructs radio power based on secondaries from a volume-filling proton population with a proton to thermal pressure ratio of $X_{\text{cr}} = 0.01$ and applied it to a constrained simulation resembling the local cosmic web ([Dolag et al., 2004, 2005a](#)). This allowed them to use S-PASS data to constrain the diffuse flux from synchrotron emission in cosmic web filaments to $I_{1.4\text{GHz}} < 0.073 \mu\text{Jy arcsec}^{-2}$, which is just below the current detection limit of e.g. the EMU survey ([Norris et al., 2011](#)).

[Oei et al. \(2022\)](#) used a $(100 \text{ Mpc})^3$ cosmological MHD simulation by [Vazza et al. \(2019\)](#) to obtain synchrotron emission by accretion and merger shocks, again following the [Hoeft & Brüggen \(2007\)](#) model. They construct a specific intensity function of the synchrotron cosmic web, by ray-tracing through their simulation box, while taking into account the cosmological distance effects of the emitted radiation. With this they find specific intensities of the order $I_{\nu} \xi^{-1} \sim 0.1 \text{ Jy deg}^{-2}$ at $\nu = 150 \text{ MHz}$, with ξ being the poorly constrained efficiency parameter of electron acceleration.

Here we will take a different approach to a prediction of synchrotron emission from the cosmic web, by injecting and evolving a population of CRe at shocks and studying the magnetic field strengths required to obtain synchrotron emission compatible with current observational limits. In this work we will study potential emission from CRs accelerated at shocks in merger- and accretion-shocks of galaxy clusters and accretion-shocks around cosmic web filaments. For this, we employ the first realization of a cosmological MHD simulation of a $(500 h^{-1} c\text{Mpc})^3$ box with an on-the-fly Fokker-Planck solver to model CR proton and electron evolution. Here we will only focus on the electron populations, leaving the study of protons to future work. This paper is structured as follows: In Sec. 15.2 we will describe the simulation and the code

Table 15.1: List of the presented simulations. From left to right we list the name, mass of the gas particles, mass of the DM particles, gravitational softening, the maximum resolution at $z = 0$ and the maximum allowed value for D_0 .

Name	$M_{\text{gas}} [M_{\odot}]$	$M_{\text{DM}} [M_{\odot}]$	$\epsilon [h^{-1} \text{ckpc}]$	$h_{\text{sml,min}} [\text{kpc}]$	$D_{0,\text{max}} [\text{s}^{-1}]$
SLOW-CR3072 ³	8.5×10^7	4.6×10^8	2.7	6.24	0
COMA	1.0×10^7	5.7×10^7	1.0	3.6	0
COMA- D_{pp} -LOW	1.0×10^7	5.7×10^7	1.0	3.7	10^{-17}
COMA- D_{pp} -HIGH	1.0×10^7	5.7×10^7	1.0	3.5	5×10^{-17}

configuration employed for this work. In Sec. 15.3 we study full sky projections of the injected CR electrons and their synchrotron emission under different magnetic field models. In Sec. 15.4 we will focus on the analysis of non-thermal emission from our replica of the Coma cluster and its surrounding filament structure. Sec. 15.5 extends this analysis to the full simulation domain to study the emissivity of all cosmic web filaments. In Sec. 15.6 we will compare our results to the post-processing model by [Hoeft & Brüggén \(2007\)](#) and discuss the impact of free parameters in our CR model on our results and their observational prospects. Finally, Sec. 15.7 contains our conclusions and a summary of our work.

15.2 Methods

15.2.1 Initial Conditions

The initial conditions of the simulations have been described extensively in [Sorce \(2018\)](#); [Dolag et al. \(2023b\)](#), so we limit the description here to a short overview.

We set up constrained initial conditions based on velocity field reconstructions in the local Universe ([Carlesi et al., 2016](#); [Sorce, 2018](#), and references therein). In this method, a Wiener Filter algorithm ([Zaroubi et al., 1995, 1998](#)) is applied to reconstruct the 3D peculiar velocities of galaxies from the COSMICFLOWS-2 distance modulus survey ([Tully et al., 2013](#)). This survey undergoes several treatments upstream and downstream this reconstruction ([Doumler et al., 2013c,a,b](#); [Sorce et al., 2014](#); [Sorce, 2015](#); [Sorce et al., 2017](#); [Sorce & Tempel, 2017, 2018](#)). Subsequently, using the constrained realization algorithm ([Hoffman & Ribak, 1991](#)) it can be used to construct a density field of the local Universe at an initial redshift, a.k.a the constrained initial conditions. The resolution of the density field is then increased to reach our study requirement using the GINNUNGAGAP software¹.

These initial conditions have been used, for instance, to study individual clusters such as Virgo ([Sorce et al., 2016](#); [Olchanski & Sorce, 2018](#); [Sorce et al., 2019](#); [Lebeau et al., 2023](#)), as well as the large-scale environment around the Local Group ([Carlesi et al., 2016, 2017](#)), and other clusters ([Sorce et al., 2023](#)), in particular, the Coma cluster ([Malavasi et al., 2023](#)). Previous work on ultra-high energy CRs showed how these constrained initial conditions help provide

¹<https://code.google.com/p/ginnungagap/>

predictions for observations (Hackstein et al., 2018).

In this work we will study the SLOW-CR3072³ simulation, which consists of 2×3072^3 particles in a volume of $V = (500 h^{-1} c \text{ Mpc})^3$. This leads to a mass resolution of $M_{\text{gas}} \approx 8.5 \times 10^7 M_{\odot}$ and $M_{\text{DM}} \approx 4.6 \times 10^8 M_{\odot}$ for gas and DM particles, respectively. The maximum resolution of gas particles in our simulation corresponds to $h_{\text{sml},\text{min}} \approx 6.24 \text{ kpc}$ at $z = 0$.

In order to test the impact of resolution on our results we also performed zoom-in simulations of the Coma cluster at eight times the resolution of the cosmological box. To create such zoom-in initial conditions, a DM-only simulation has been extended far into the future, e.g. up to an expansion factor of $a \approx 1000$, to identify the gravitationally bound region of the supercluster the target cluster is a part of. Then, the spatial region in the simulation which contains all particles bound to the Coma supercluster has been identified. This region is then traced back to the corresponding, Lagrangian volume in the initial conditions, which is then sampled with the particles taken from much higher resolution versions of the box, e.g. in this case by the one sampled with 6144^3 particles in total. In order to smooth the resolution difference at the boundaries while minimizing the total particle number, boundary layers were added to the high-resolution region, using the lower-resolution versions of the full box in descending order of particle number (3072^3 , 1536^3 , 768^3 and 384^3 for the remainder of the box). The refinement of the initial conditions leads to a mass resolution for the high-resolution region of $M_{\text{gas}} \approx 1 \times 10^7 M_{\odot}$ and $M_{\text{DM}} \approx 5.7 \times 10^7 M_{\odot}$ for gas and DM particles, respectively. Here we reach a maximum resolution of gas particles of $h_{\text{sml},\text{min}} \approx 3.7 \text{ kpc}$. We list all simulations discussed in this work in Tab. 15.1.

All simulations were run using a *Planck* cosmology (Planck Collaboration et al., 2014) with matter densities $\Omega_{\text{m}} = 0.307$ and $\Omega_{\text{baryon}} = 0.048$, a cosmological constant of $\Omega_{\Lambda} = 0.692$ and the Hubble parameter $H_0 = 67.77 \text{ km s}^{-1} \text{ Mpc}^{-1}$.

15.2.2 Simulation Code

We employ OPENGADGET3 (Groth et al., 2023), an advanced version of the cosmological TREE-SPH code GADGET2 (Springel, 2005).

OPENGADGET3 uses a Barnes and Hut tree (Barnes & Hut, 1986) to solve the gravity at short range and a PM-grid for long-range forces. For the zoom-in simulations used in this work, the PM-grid is split to add a higher resolution grid on the central region to save computing time.

All simulations presented in this work are non-radiative CR-MHD simulations. OPENGADGET3 uses an updated SPH implementation (Beck et al., 2016b) with a spatially and time-dependent high-resolution shock capturing scheme (Dolag et al., 2005c; Cullen & Dehnen, 2010). The simulations presented here were run with a Wendland C_4 kernel with 200 neighbors and bias correction (as introduced in Dehnen & Aly, 2012), to ensure stabilization against the tensile (pairing) instability that arises for kernels that do not have a positive definite Fourier transformation. Our SPH implementation is further stabilized by a high-resolution maximum entropy scheme, which in this work is realized by physical, rather than artificial thermal conduction. This thermal conduction is solved using a bi-conjugate gradient solver (Petkova & Springel, 2009; Arth et al., 2014; Steinwandel et al., 2020b) to account for anisotropic conduction along magnetic field lines. The MHD solver was presented in Dolag et al. (2009a) and extended in Bonafede et al. (2011) to include non-ideal MHD in the form of magnetic diffusion and a sub-grid model for magnetic

dissipation in the form of magnetic reconnection, which can heat the thermal gas.

We employ an on-the-fly shock finder (Beck et al., 2016a) to compute the necessary shock quantities for CR acceleration.

Cosmic Rays are represented as populations of protons and electrons and evolved in time using an on-the-fly Fokker-Planck solver, which we will discuss in more detail in the next section.

15.2.3 Cosmic Ray Model

To model Cosmic Rays we employ the on-the-fly Fokker-Planck solver CRESCENDO introduced in Böss et al. (2023c) and will only briefly outline the solver and the parameters used here in comparison to the previous work. CRESCENDO attaches a population of CR protons and electrons to all resolution elements of the simulation. These populations are assumed to be isotropic in momentum space and are represented as piece-wise power-laws

$$f(p) = f_i \left(\frac{p}{p_i} \right)^{-q_i} \quad (15.1)$$

for a number of logarithmically spaced bins. Both protons and electrons are considered in the dimensionless momentum range $\hat{p} \equiv \frac{p}{mc} \in [0.1, 10^5]$, where m is the mass of the individual particle species. We discretize the populations with 8 bins (1.33/dex) for protons and 24 bins (4/dex) for electrons. This choice of resolution is mainly driven by memory constraints, with the focus on still being able to model accurate high-momentum losses for electrons. These populations are then evolved in time by solving the diffusion-advection equation in the two-moment approach, following Miniati (2001) (see also Girichidis et al., 2020; Ogrodnik et al., 2021; Hopkins et al., 2022a, for other recent on-the-fly spectral CR models).

We account for injection at shocks via diffusive shock acceleration (DSA), adiabatic changes due to density changes of the surrounding thermal gas, and energy losses of electrons due to synchrotron emission and inverse Compton (IC) scattering off CMB photons. This reduces the Fokker-Planck equation that describes the time evolution of our CR populations to

$$\frac{Df(p, \mathbf{x}, t)}{Dt} = \left(\frac{1}{3} \nabla \cdot \mathbf{u} \right) p \frac{\partial f(p, \mathbf{x}, t)}{\partial p} \quad (15.2)$$

$$+ \frac{1}{p^2} \frac{\partial}{\partial p} \left(p^2 \sum_l b_l f(p, \mathbf{x}, t) \right) \quad (15.3)$$

$$+ j(\mathbf{x}, p, t), \quad (15.4)$$

where Eq. 15.2 denotes changes due to adiabatic expansion/compression of surrounding gas, Eq. 15.3 denotes radiative changes due to synchrotron emission and inverse Compton scattering off CMB photons with $\sum_l b_l \equiv \left| \frac{dp}{dt} \right|_{\text{syn}} + \left| \frac{dp}{dt} \right|_{\text{IC}}$ and Eq. 15.4 denotes the source term of CRs. In this work the source term $j(\mathbf{x}, p, t)$ describes CR acceleration at shocks, modeled following the DSA parametrization by Kang & Ryu (2013). In addition to that, we use the obliquity-dependent model as introduced by Pais et al. (2018) for protons which are primarily accelerated at quasi-parallel shocks, and shift it by 90° for electrons. Please see Sec. 6.1.6 for more details. We inject

the energy into the full momentum range as a single power law following a linear DSA slope in momentum space

$$q = \frac{3r}{r-1}; \quad r = \frac{(\gamma+1)\mathcal{M}_s^2}{(\gamma-1)\mathcal{M}_s^2+2} \quad (15.5)$$

where r is the shock compression ratio, γ is the adiabatic index of the gas and \mathcal{M}_s is the sonic Mach number. The DSA parametrization by [Kang & Ryu \(2013\)](#) imposes a critical Mach number $\mathcal{M}_s = 2$, below which no efficient CR acceleration can happen. We employ a fixed electron to proton energy ratio of $K_{ep} = 0.01$.

For this run, we use closed boundary conditions at the lower end of the distribution function, as it provides more numerical stability and mimics low-momentum cooling on adiabatic compression, which is not explicitly included in this simulation. We solve Eq. 15.2 in the *two-moment approach* by accounting for CR number and energy changes per bin for both protons and electrons for reasons of numerical stability (see [Girichidis et al., 2020](#), for a discussion of the benefit for protons).

Feedback from the CR component to the thermal gas in the form of comoving pressure is calculated by solving the integral

$$P_{\text{CR},c} = \frac{4\pi}{3} a^4 \int_{p_{\text{min}}}^{p_{\text{cut}}} dp p^2 T(p) f(p) \quad (15.6)$$

under the approximation $T(p) \approx pc$. We start the injection of CRs at $z = 4$. All these effects are computed on-the-fly for *every* gas particle active in the timestep. Constraints on computing memory made it impossible to also account for transport processes, besides advection, which we account for naturally since the CR populations are attached to our lagrangian SPH particles. We will study the effect of transport processes on CRs in galaxy clusters in future zoom-in simulations instead.

15.2.4 Fermi-II Re-acceleration

We implemented an on-the-fly treatment of turbulent re-acceleration of CRs and will briefly outline the implementation here. For details please see Sec. 9. To follow the turbulent re-acceleration of CRs we adopt the model by [Cassano & Brunetti \(2005\)](#). We use the unified-cooling approach which extends the $b_l(p)$ term in Eq. 15.3 to include the systematic component of the re-acceleration

$$\sum_l b_l(p) \equiv \left(\frac{dp}{dt} \right)_{\text{cool}}^{\text{synch}} + \left(\frac{dp}{dt} \right)_{\text{cool}}^{\text{IC}} + \left(\frac{dp}{dt} \right)_{\text{acc}}^{\text{sys}}. \quad (15.7)$$

Following [Cassano & Brunetti \(2005\)](#) the change in momentum due to turbulent re-acceleration per timestep can be expressed as

$$\left(\frac{dp}{dt} \right)_{\text{acc}}^{\text{sys}} = -\chi p \approx -2 \frac{D_{\text{pp}}}{p} = -2D_0(t) p, \quad (15.8)$$

where we used $D_{\text{pp}} = D_0(t) p^2$.

The computation of $D_0(t)$ is quite expensive and the way it is coupled to Eq. 15.2 puts a significant timestep constraint on the solver. We therefore sub-cycle the solver if $D_0(t) \times \Delta t$ surpasses a critical value. Additionally, we introduce a cap for $D_0(t)$ to avoid too strong impacts of individual particles on the total runtime of the simulation.

Due to the additional computational cost, we switched this mode off in SLOW-CR3072³ and ran comparison zoom-in simulations with the mode switched on. For COMA, we switched the mode off to obtain a comparison and see the impact of resolution. In the case of the zoom-in simulations COMA- D_{pp} -LOW and COMA- D_{pp} -HIGH we run the turbulent re-acceleration on-the-fly, but cap the values of D_0 , which limits the need to sub-cycle the solver. For COMA- D_{pp} -LOW, we cap the value at $D_{0,\text{max}} = 10^{-17} \text{ s}^{-1}$, which lies at the lower end of the values reported in appendix B in Donnert (2014). For COMA- D_{pp} -HIGH, we cap at $D_{0,\text{max}} = 5 \times 10^{-17} \text{ s}^{-1}$, which is close to the maximum value reported in the same reference. However, this model will need to be revised to include recent results that indicate that preferentially the solenoidal component of turbulence can efficiently re-accelerate CRs (Brunetti, 2016; Brunetti & Vazza, 2020), or allow for other re-acceleration mechanisms (e.g. Tran et al., 2023).

15.2.5 Synchrotron Emission

As in the introductory paper for CRESCENDO we compute the synchrotron emissivity j_ν in units of $[\text{erg s}^{-1} \text{ Hz}^{-1} \text{ cm}^{-3}]$ as

$$j_\nu(t) = \frac{\sqrt{3}e^3}{m_e^2 c^3} B(t) \sum_{i=0}^{N_{\text{bins}}} \int_0^{\pi/2} d\theta \sin^2 \theta \int_{\hat{p}_i}^{\hat{p}_{i+1}} d\hat{p} 4\pi \hat{p}^2 f(\hat{p}, t) K(x) \quad (15.9)$$

where e is the elementary charge of an electron, m_e its mass, c the speed of light, \hat{p} the dimensionless momentum and $K(x)$ is the first synchrotron function

$$K(x) = x \int_x^\infty dz K_{5/3}(z) \quad (15.10)$$

using the Bessel function $K_{5/3}$ at a ratio between observation frequency ν and critical frequency ν_c

$$x \equiv \frac{\nu}{\nu_c} = \frac{\nu}{C_{\text{crit}} B(t) \sin \theta \hat{p}^2}; \quad C_{\text{crit}} = \frac{3e}{4\pi m_e c} \quad (15.11)$$

All scalings of the synchrotron emission with frequency and magnetic field strength arise directly from the evolved CR electron distribution function $f(\hat{p}, t)$ in Eq. 15.9, without further assumptions or imposed limits (see Appendix A in Böss et al., 2023b, for a more detailed description).

15.3 Full-Sky Projections

Having a full-box simulation of a constrained local Universe puts us in the unique position to study full-sky projections as observed from our Milky-Way replica. To obtain the projections we

map the SPH particles of our simulation onto a HEALPIX sphere (Górski et al., 2005) following the algorithm described in Dolag et al. (2005b). All figures in this section were obtained from the output at redshift $z = 0$.

15.3.1 Cosmic Ray Electrons

We show the full-sky projection of our CR electron component in Fig. 15.1. The labeled clusters are our best matches for the observed counterparts (Hernández-Martínez et al., in prep.) and the circles indicate their projected virial radii.

We show the two opposite ends of the CR electron energy range. The upper plot shows the mean CR electron energy density along the line-of-sight in a radius range $r = 10 - 300$ Mpc for CRs in the energy range $E \in [5 - 500]$ MeV. This traces the electrons with the longest lifetimes, with a bias towards electrons that have been accelerated and advected into high-density regions. These electrons provide potential seed populations for re-acceleration by subsequent shocks and/or turbulence.

We find a persistent population of CR electrons in galaxy clusters and the cosmic web. However, this can only be considered to be an upper limit, especially in the highest-density regions, as we do not explicitly treat low-momentum energy losses for CRs. Hence this picture should be viewed more as a tracer for shock injection and adiabatic compression and with that a tracer of potential CR electron seed populations. A distinct feature and advantage of an on-the-fly approach for CR evolution is that we find large-scale halos of electron energy density around clusters and filaments. This is consistent with recent observations of Radio Mega-Halos (Cuciti et al., 2022), indicating a significant population of CR electrons in the cluster volume. It has been shown by Beduzzi et al. (2023) that given a turbulent velocity $v_{\text{turb}} > \sim 150 \text{ km s}^{-1}$ (which is only a factor of 1.5 larger than e.g. the measurements of the atmosphere in Perseus by Hitomi Collaboration et al., 2018) these electrons have almost unlimited lifetimes and with that can remain synchrotron bright at low frequencies, providing the basis for these Radio Mega Halos. We will discuss the implications of this in future work focusing on radio halos and radio relics in our simulation.

In the lower panel of Fig. 15.1 we show the energy contained in electrons with energies above 1 GeV. These electrons are potentially synchrotron-bright at frequencies of 144 MHz. Since the cooling times of these CRs are of the order $\sim 10^2 - 10^3$ Myrs this predominantly traces recent injection. We find significant injection at the accretion shocks of most clusters, as well as the accretion shocks around cosmic web filaments. This shows that accretion shocks around filaments, together with internal shocks provide a significant, volume-filling source for high energy CRs, available to emit radio emission, given sufficiently strong magnetic fields. Please note that in order to provide a cleaner picture of the accretion shocks around cosmic web filaments and clusters we cropped out the inner 40 Mpc around the point of view to avoid pollution by nearby structures. This pollution can be seen in the upper panel of Fig. 15.1 as a slight hue in parts of the sky. Hence Virgo is not visible in the lower image, as it lies within this cutout region.

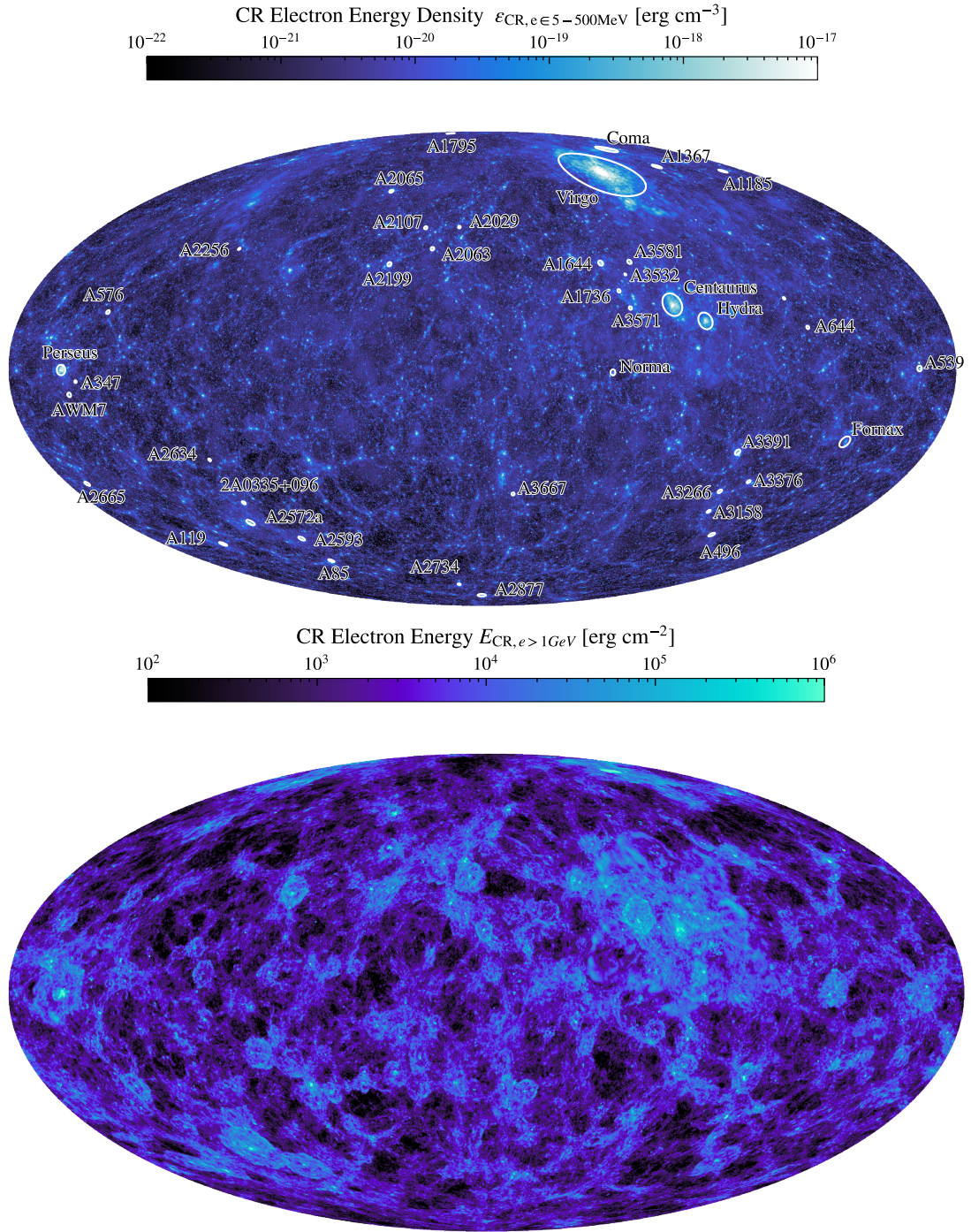


Figure 15.1: Full-Sky projections of the CR electron component. *Upper panel:* Energy density of electrons in the range $E \in [5 - 500]$ MeV as the mean along the line of sight in a radius range $r = 10 - 300$ Mpc. This traces the injected energy density of the CR electrons with the longest lifetimes. Circles indicate the projected r_{vir} of the cross-identified clusters (Hernández-Martínez et al., in prep.). *Lower panel:* CR electrons with energies $E_{CR,e} > 1$ GeV integrated along the line of sight in a radius range $r = 40 - 300$ Mpc. The short cooling times of these electrons lead to this map tracing recent injection events. Please note the larger inner cutout region of 40 Mpc that is used to clean up the image. Hence Virgo is missing from the lower map.

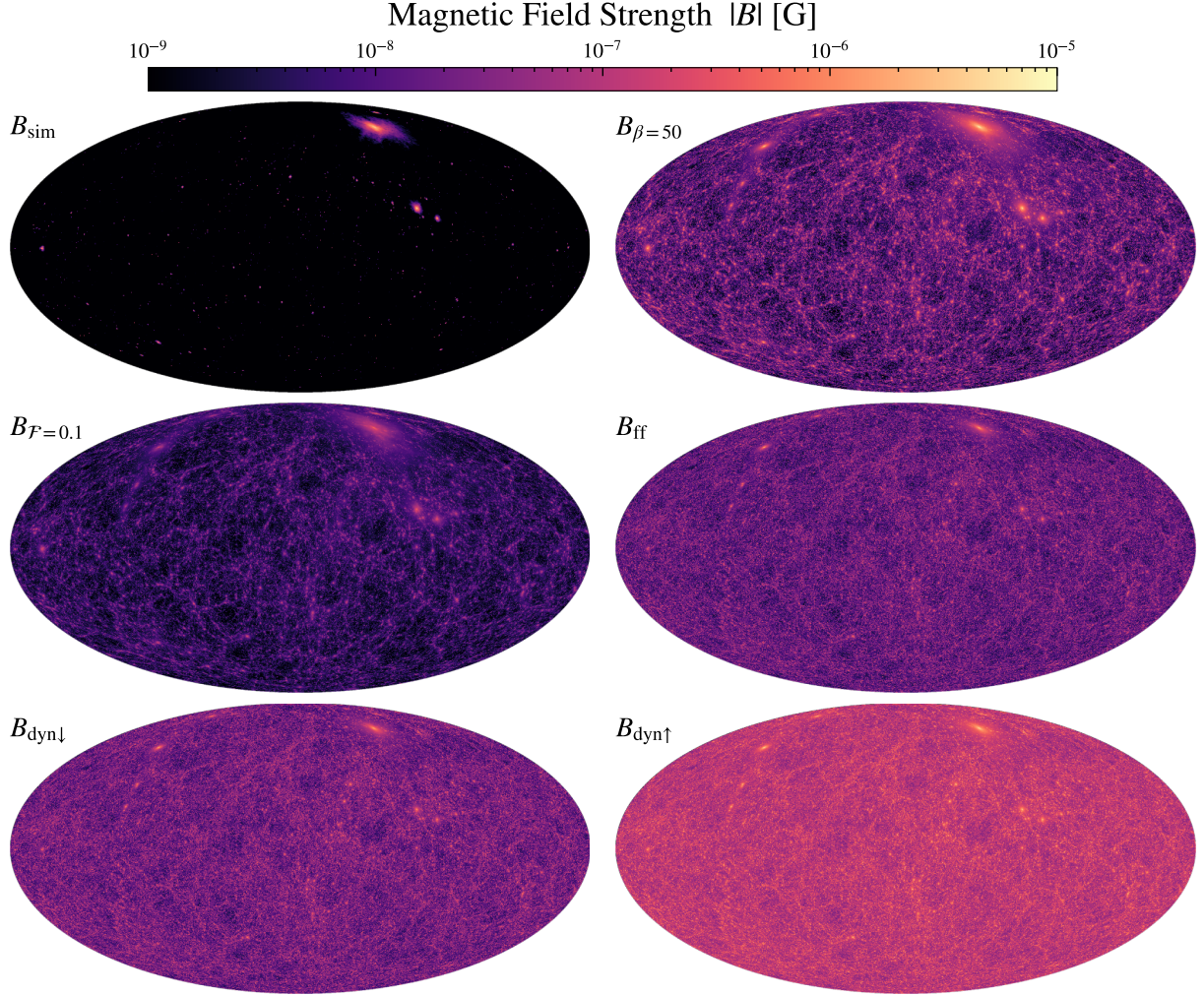


Figure 15.2: We show full sky projections of the mean magnetic field along the line of sight for the simulated magnetic field and post-processing models. *Upper left panel:* Simulated magnetic field obtained from the simulation. *Upper right panel:* Modelled magnetic field, assuming a plasma beta of $\beta \equiv \frac{P_{\text{th}}}{P_{\text{B}}} = 50$. *Center left panel:* Modelled magnetic field based on a fraction $\mathcal{F} = 0.1$ of the turbulent pressure. *Center right panel:* Modelled magnetic field based on flux freezing $B \propto \rho^{2/3}$. *Lower left panel:* Modelled magnetic field, assuming a saturated turbulent dynamo scaling $B \propto \rho^{1/2}$ down to $n_e = 10^{-4} \text{ cm}^{-3}$ and flux freezing below this density. *Lower right panel:* Modelled magnetic field, assuming a saturated turbulent dynamo scaling for all density regimes.

15.3.2 Magnetic field

Since the synchrotron emissivity scales strongly with the magnetic field strength ($L_\nu \propto B^{\alpha_0+1}$, where α_0 is the spectral index of the synchrotron spectrum) the observability of synchrotron emission of the cosmic web is tightly linked to the magnetic field strength in filaments. The magnetic field in our simulation is set up as $\mathbf{B} = (10^{-12}, 0, 0)$ G (comoving) at the starting redshift $z = 120$. This field then evolves and is amplified by adiabatic compression and dynamo processes (see e.g. [Stasyszyn et al., 2010](#); [Pakmor et al., 2014](#); [Marinacci et al., 2015](#); [Vazza et al., 2014, 2018, 2021b](#); [Steinwandel et al., 2022, 2023b](#)). As this is a non-radiative simulation without star formation or cooling we cannot account for astrophysical sources of magnetic field which can contribute to volume-filling magnetic fields in low-density regions ([Beck et al., 2013](#); [Garaldi et al., 2021](#)). While we obtain reasonable values in galaxy clusters (of the order $\sim \mu\text{G}$, see e.g. [Bonafede et al., 2010](#); [van Weeren et al., 2019](#), the latter for a review), the magnetic field strength in filaments remains negligible. We attribute this to a lack of resolution in the filaments to drive an efficient turbulent dynamo to amplify the magnetic field (see [Steinwandel et al., 2022](#), for an extensive study performed with our simulation code).

To test the implications of different magnetic field structures we adopt five magnetic field models, two based on pressure scaling and three based on density scaling. We show the mean magnetic field along the line of sight in a radius range $r = 10 - 300$ Mpc, for the simulation and the scaling models in Fig. 15.2.

First, we test a simple model where the magnetic field pressure is a constant factor of the thermal pressure P_{th} , such that

$$B_\beta = \sqrt{\frac{8\pi P_{\text{th}}}{\beta}}, \quad (15.12)$$

where we assume a constant plasma- β of $\beta = 50$. This is an optimistic model, given that such low values of beta are typically only found in the central regions of clusters, while realistic values for filaments and accretion shocks are of the order $\beta \sim 10^2 - 10^3$ (see e.g. [Ha et al., 2023](#)).

Second, we calculate the magnetic field as a fraction \mathcal{F} of the turbulent pressure

$$B_{\mathcal{F}} = \sqrt{\mathcal{F} 4\pi \rho v_{\text{turb}}^2}. \quad (15.13)$$

\mathcal{F} can be estimated from the magnetic Reynolds number following Tab. 1 in [Schober et al. \(2015\)](#) and takes typical values of $\mathcal{F} \approx 0.01 - 0.1$ in the systems we are interested in. We again adopt the upper limit of this estimation with $\mathcal{F} = 0.1$.

For the magnetic field models scaling with the density we first use a simple flux-freezing model where initial magnetic fields are amplified by adiabatic compression in collapsing halos. Following [Hoeft et al. \(2008\)](#) we adapt

$$B_{\text{ff}} = \frac{B}{0.1\mu\text{G}} \left(\frac{n_e}{10^{-4}\text{cm}^{-3}} \right)^{2/3}. \quad (15.14)$$

In ultra-high resolution simulations of massive galaxy clusters [Steinwandel et al. \(2023b\)](#) find that the turbulent dynamo is the dominant amplification process, even in low-density regions down

to $n_e \sim 10^{-4}$. From this, we extrapolate two turbulent dynamo models. The first assumes that the turbulent dynamo amplifies the magnetic field down to densities of $n_e \sim 10^{-3}$ and below that amplification happens via adiabatic compression.

$$B_{\text{dyn},\downarrow}(\rho) = \begin{cases} 30 \times 10^{-9} \left(\frac{n_e}{10^{-5} \text{cm}^{-3}} \right)^{2/3} & [\text{G}], \text{ if } n_e < 10^{-3} \text{ cm}^{-3} \\ 0.65 \times 10^{-6} \left(\frac{n_e}{10^{-3} \text{cm}^{-3}} \right)^{1/2} & [\text{G}], \text{ if } n_e > 10^{-3} \text{ cm}^{-3} \end{cases} \quad (15.15)$$

For the adiabatic compression part with $n_e \leq 10^{-3}$ we set the parameters such as to intersect with the recent observations by Carretti et al. (2022), which point to $B_0 \sim 30$ nG at filaments with densities of $n_{e,0} = 10^{-5} \text{cm}^{-3}$ and assume a turbulent dynamo scaling that results in $B \sim \mu\text{G}$ in cluster centers. This model can be considered as a lower limit.

We also consider an upper limit, as a pure saturated dynamo scaling with density as

$$B_{\text{dyn},\uparrow}(\rho) = B_0 \left(\frac{n_e}{n_{e,0}} \right)^{\frac{1}{2}}, \quad (15.16)$$

where we fit the results from Steinwandel et al. (2023b) and extend the scaling to lower densities with $B_0 \sim 100$ nG at $n_{e,0} = 10^{-5} \text{cm}^{-3}$. In contrast to the previous scaling this matches magnetic field strengths in cluster centers very well, but over-estimates the magnetic field strength in filaments by roughly one order of magnitude, compared to the Carretti et al. (2022). It is however consistent with previous works by Vernstrom et al. (2017); Brown et al. (2017); O'Sullivan et al. (2019); Locatelli et al. (2021) who allow for up to 250 nG.

15.3.3 Synchrotron Emission

By folding the lower panel of Fig. 15.1 with the different panels of Fig. 15.2 according to Eq. 15.9 we can obtain the synchrotron emissivity. From there we arrive at the intrinsic synchrotron surface brightness by integrating the emissivity of the SPH particles along the line of sight. We show the result of this for the previously introduced magnetic field models in Fig. 15.3.

In the case of the simulated magnetic field we only obtain synchrotron emission from galaxy clusters. The emission in cluster centers is of the order ~ 10 lower compared to observations, which is mainly driven by the flatter radio spectra. Our simulated spectra in the box stem purely from direct injection and advection, due to the omission of on-the-fly turbulent re-acceleration. We will discuss this in more detail for the filaments of Coma in Sec. 15.4 and for the radio emission in Coma, Virgo, and Perseus in Dolag et al. (in prep). The lack of emission in the filaments stems from the steeper dropoff of the magnetic field as a function of density. As discussed before the simulated magnetic field strength in the filaments is well below the nG level and with that would require substantial CR injection to be synchrotron bright.

Assuming a magnetic field following a constant plasma- β ($B_{\beta=50}$) yields more interesting results. We still primarily get synchrotron emission from the cluster centers, however, we also see more emission by smaller clusters that do not have a strong enough simulated magnetic field to be synchrotron bright. In addition, we also see more relics far from the cluster center, such as in

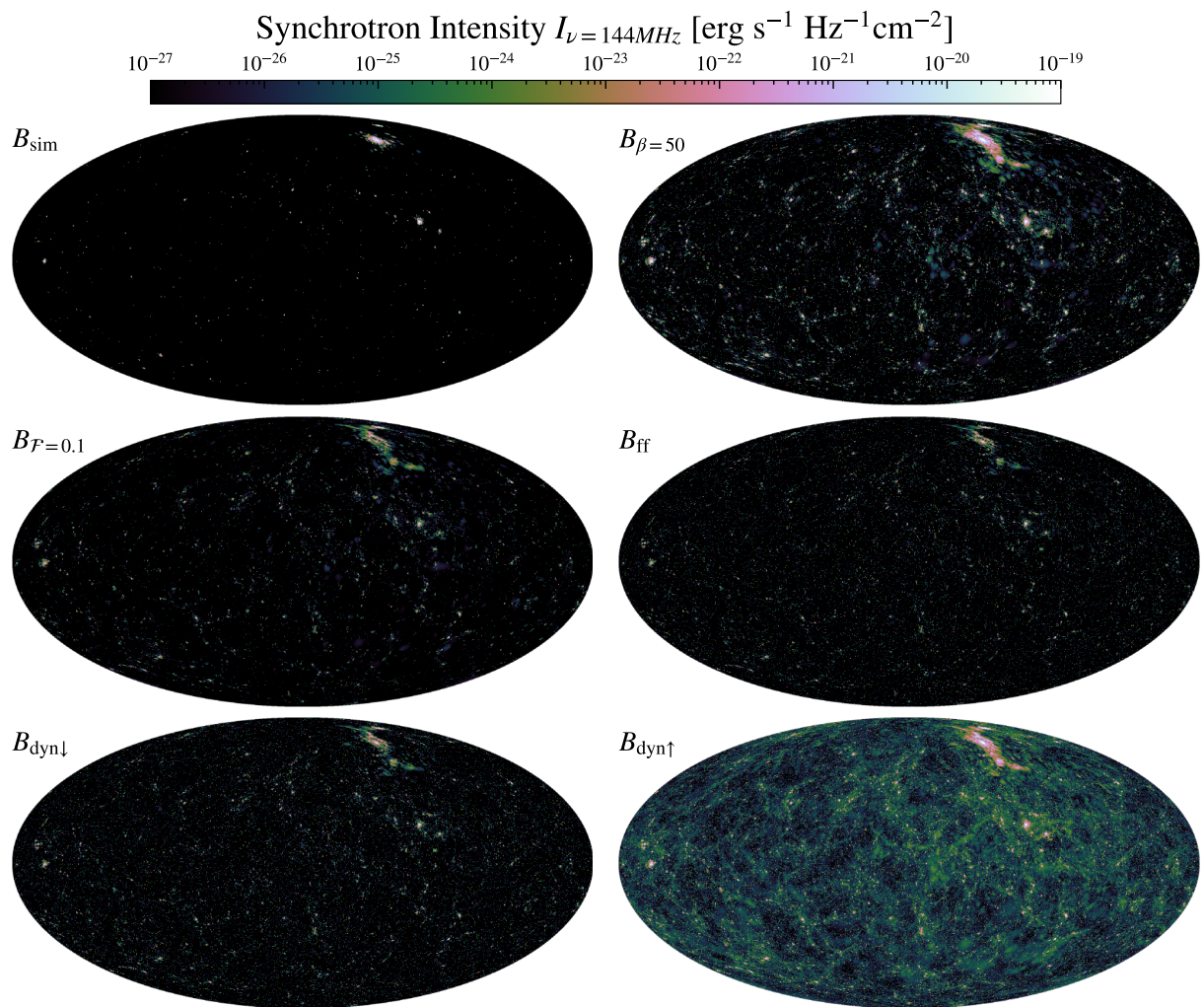


Figure 15.3: We show the (intrinsic) synchrotron intensity at 144 MHz integrated along the line of sight between $r = 10 - 300$ Mpc. The different panels show the emission calculated based on the magnetic field configurations shown in Fig. 15.2.

our Perseus replica to the very left of the map. This stems from the magnetic field scaling with the thermal pressure and with that automatically tracing regions of over-pressure, namely shocks. We can observe some filamentary structure in the synchrotron emission, however, this is mainly driven by the halos inside the filaments, rather than diffuse emission from filaments.

The magnetic field scaling with turbulent velocity ($B_{\mathcal{F}=0.1}$) produces morphologically similar features as the constant plasma- β case. This naturally originates from shocks inducing a substantial amount of turbulent energy (e.g., [Ryu et al., 2003](#); [Vazza et al., 2011](#)), so this model again amplifies magnetic field strength and with that synchrotron emission at shocks. We note however that the general magnetic field strength is roughly one order of magnitude lower than compared to the plasma- β case, which leads to a roughly two orders of magnitude lower synchrotron emission. The density-dependent magnetic field models B_{ff} and $B_{\text{dyn},\downarrow}$ both show similar behavior. Their density scaling is identical in the density regions of filaments and their absolute values also only differ slightly. This leads to the previously seen filamentary emission driven by halos in the filaments, but no diffuse emission in filaments.

$B_{\text{dyn},\uparrow}$ is the only model that produces considerable diffuse synchrotron emission from filaments. We find consistent diffuse emission within the filaments and in some regions in the northern part of the map the magnetic field is even strong enough to illuminate part of the accretion shocks into the clusters. These accretion shocks can be seen as dim circles around the clusters, akin to the recently discovered "Odd Radio Circles" (e.g., [Norris et al., 2021](#); [Koribalski et al., 2021](#); [Dolag et al., 2023a](#)). The emission by filaments and accretion shocks have intensities more than 5 orders of magnitude lower than the intensities in cluster centers, making prospects of direct detection very difficult, as expected. Further, from a numerical standpoint, it is difficult to capture the spurious shocks in the low-density environment around filaments. This mainly stems from the numerical resolution in these low-density regions. We will discuss the impact of resolution on our findings in Sec. 15.4.

15.4 The Coma Filaments

To study the potential synchrotron emission from cosmic web filaments in more detail we will now focus on the Coma cluster replica found in our simulation and its surroundings. The cosmic web filaments around our Coma replica have recently been studied in [Malavasi et al. \(2023\)](#), where they find good agreement with indications from observations, which provides a reasonable basis for our analysis.

15.4.1 Impact of Resolution

In order to test the impact of resolution on our results we add to our analysis by presenting results from zoom-in simulations of the Coma cluster (COMA, COMA- D_{pp} -LOW, COMA- D_{pp} -HIGH) at eight times the resolution of the cosmological box (SLOW-CR3072³). We show the comparison between SLOW-CR3072³ and COMA in the top and bottom panels of Fig. 15.4. From left to right we show surface density, the absolute strength of the simulated magnetic field, CR electron energy of the electrons with energies above 1 GeV, and the turbulent re-acceleration coefficient

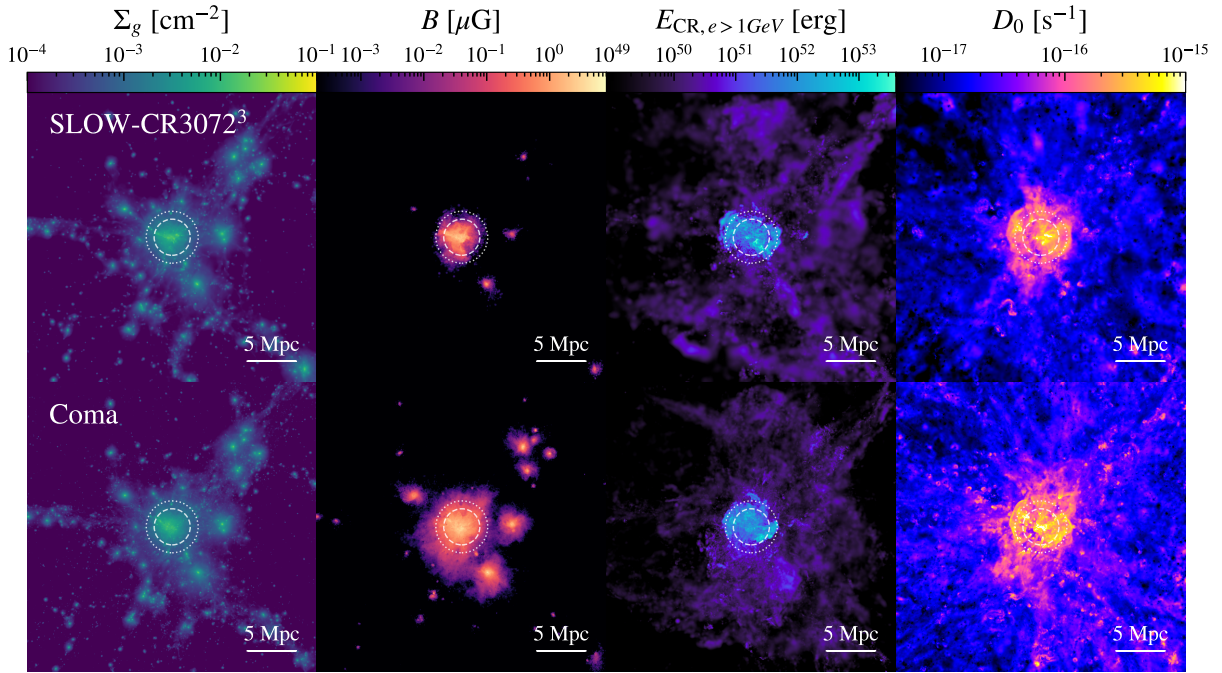


Figure 15.4: We show a cutout around our Coma replica with a side-length of $d = 20h^{-1}c\text{Mpc}$. The circles represent r_{200} and r_{500} . From left to right we show surface density, absolute value of the simulated magnetic field, CR electron energy of electrons with energies above 1 GeV and turbulent re-acceleration coefficient. The upper panels show the cluster in the full cosmological box, the lower panels show it in the zoomed-in re-simulation.

as given in Eq. 9.9.

We find excellent morphological agreement between the different setups, as can be seen in the density plot in the left panels, providing us with a good basis for comparison. In Coma itself we can also see reasonable agreement in the magnetic field strength (second panels), injected CR energy (third panels), and re-acceleration coefficient (last panels).

However, as we move away from Coma we can observe the impact of resolution. In the magnetic field strength, this is evident as the magnetic field retains higher values further from the cluster center in the case of the zoom-in simulation. As discussed previously we attribute this to the lack of resolution to drive an efficient amplification via the turbulent dynamo, as shown in [Steinwandel et al. \(2022\)](#).

Another impact of resolution can be seen in the CR electron panels, where the increased resolution in the zoom-in simulation leads to a more accurate shock capturing and with that improved CR injection. This can be seen both in the strong shock of the ongoing merger, as well as in the surrounding medium. In the zoom-in simulation, even the equatorial shock from the current merger is captured, with the cluster in the full box only showing a hint of this shock in direct comparison.

Both simulations show an envelope of a previous shock moving away from the center and

colliding with the accretion shock (see e.g. [Zhang et al., 2020a,b](#), for a high-resolution study of this process). We find prominent acceleration of CRs at a filament to the top-right of the cluster in both simulations. This is however better refined in the zoom-in simulation, where a clear filament can be seen in the CR component, while the box simulation shows more CR injection on one side of the filament than the other.

15.4.2 Fermi-II Re-Acceleration

The turbulent re-acceleration maps in the right-most panels of Fig. 15.4 again agree reasonably in morphology and absolute value. We find strong potential for re-acceleration in the post-shock regions of the merger and the center of the cluster. Here values reach up to $D_0 \sim 10^{-15} \text{ s}^{-1}$, more than one order of magnitude higher than the maximum reported in [Donnert \(2014\)](#). This shows how conservative a cap at $D_0 = 5 \times 10^{-17} \text{ s}^{-1}$ is in the case of a massive galaxy cluster. However the filaments only reach values of $D_0 \sim 3 \times 10^{-17} \text{ s}^{-1}$. Since we focus on filaments in this work we accept this limitation for the benefit of substantially lower run-time of the simulation.

15.4.3 Synchrotron Flux

In Fig. 15.5 we show the expected synchrotron flux of our simulated Coma cluster and its environment, assuming a LOFAR beam size of $\theta = 60'' \times 60''$ (as in Fig. 2 of [Bonafede et al., 2022](#)). We convert the intrinsic radio power P_ν to an observed flux by placing our Coma replica at a redshift of $z = 0.0231$ and converting it via $S_\nu = \frac{P_\nu}{4\pi D_L^2}$ where we use our intrinsic [Planck Collaboration et al. \(2014\)](#) cosmology for the computation of the luminosity distance D_L .

Top panels show the Coma replica in the cosmological box (SLOW-CR3072³), the second row shows the cluster in the zoom-in simulation without turbulent re-acceleration (COMA), in the third row we include turbulent re-acceleration and cap the value of D_0 at $D_{0,\text{max}} = 10^{-17} \text{ s}^{-1}$ (COMA- D_{pp} -LOW) and the lowest panels show the zoom-in simulation with D_0 capped at $D_{0,\text{max}} = 5 \times 10^{-17} \text{ s}^{-1}$ (COMA- D_{pp} -HIGH). From left to right we show the flux from the simulated magnetic field and the different magnetic field models introduced in Sec. 15.3.2.

We will focus on the results of our on-the-fly treatment of CRs here and will discuss the comparison to the [Hoeft & Brüggén \(2007\)](#) model shown in the lowest panels of Fig. 15.5 in Sec. 15.6.1.

In SLOW-CR3072³ and COMA we find the peak of the simulated flux of the radio halo lies roughly one to two orders of magnitude below the observed peak of $\sim 10 - 50 \text{ mJy beam}^{-1}$ ([Bonafede et al., 2022](#)). COMA- D_{pp} -LOW and COMA- D_{pp} -HIGH both reach these values, which we attribute to the on-the-fly treatment of turbulent re-acceleration. The relic replica in our simulation is only really visible in the zoom-in simulations with the simulated magnetic field and there it is 1-2 orders of magnitude less luminous than the observed one. We attribute this for one to the NAT-relic connection in the real Coma cluster, which cannot be reproduced here since we don't include galaxy formation and AGN jet physics in this simulation. A second reason is the known discrepancy between current DSA models and the up-to 10 percent efficiency required to reproduce radio relic brightness (see discussion in [Botteon et al., 2020a](#)). We will discuss the impact of CR injection parameter choices in more detail in Sec. 15.6. In general, we find that the simulated magnetic field drops off too steeply as a function of radius and with that is not strong

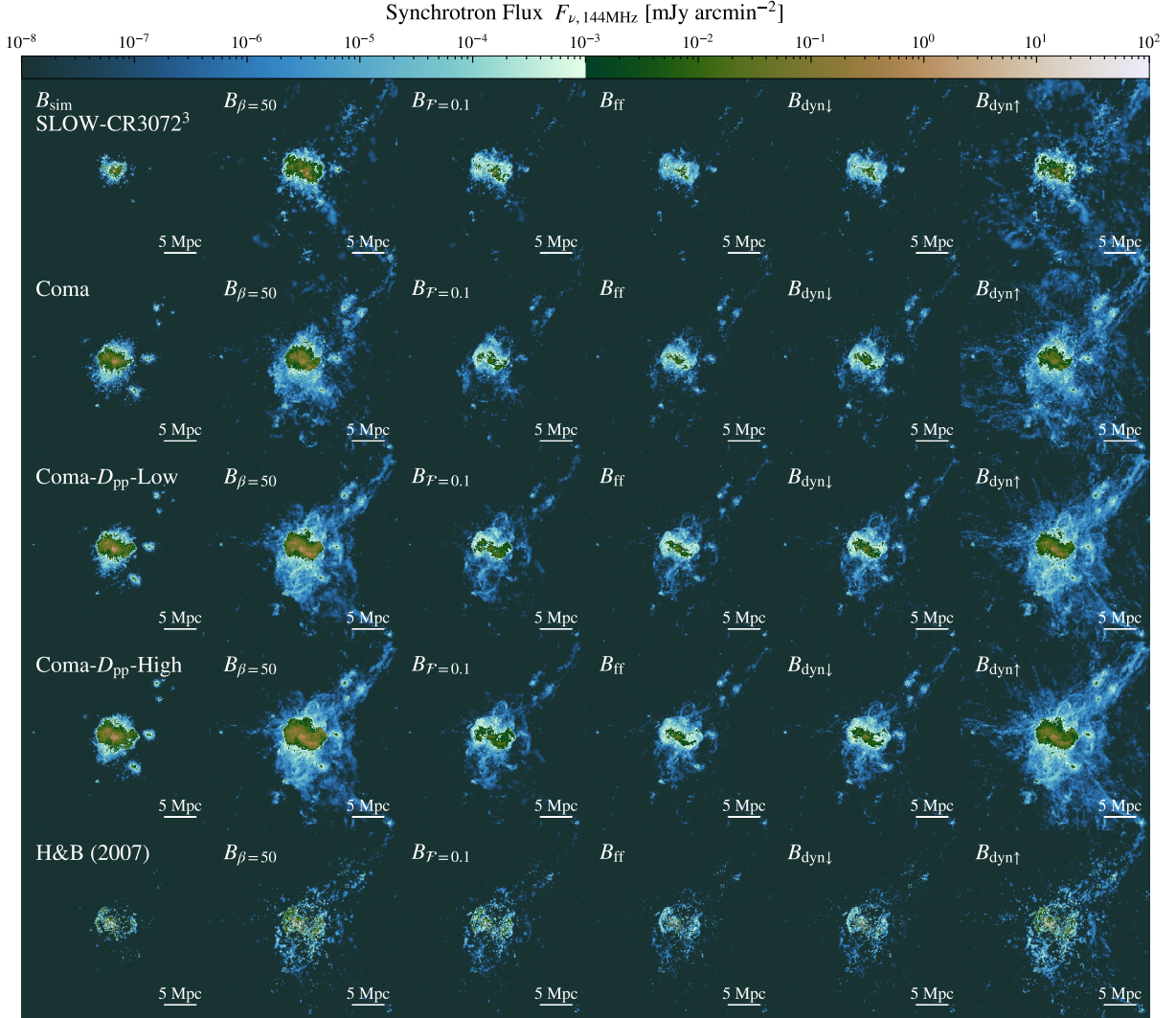


Figure 15.5: Same cutout as in Fig. 15.4. We show the synchrotron flux at 144 MHz, assuming a LOFAR beam size of $\theta = 60'' \times 60''$ as in [Bonafede et al. \(2022\)](#). The color bar is split at $1 \mu\text{Jy beam}^{-1}$, which is a factor two above the sensitivity limit in the stacking approach by [Hoang et al. \(2023\)](#). From top to bottom, we show the different simulation runs, and from left to right we vary the magnetic field models. The lowest row shows the result of painting on synchrotron emission with the [Hoefl & Brüggen \(2007\)](#) model in a post-processing approach. For this, we use the COMA- D_{pp} -Low simulation due to the better performance of the shock finder at this resolution, compared to SLOW-CR3072³.

enough in the filaments to provide diffuse synchrotron emission of any considerable value. Applying the magnetic field model based on a constant plasma- β ($B_{\beta=50}$) yields more synchrotron emission in the surrounding medium of the cluster for all simulations. In the case of SLOW-CR3072³ this gives a glimpse at the synchrotron flux of the accretion shock onto the filament in the top-right corner of the image. However, it is very dim due to our shock finder being resolution-limited. With the zoom-in simulations, this accretion shock is more pronounced and brighter by roughly one order of magnitude, due to the more accurate shock capturing and with that more consistent acceleration. The inclusion of turbulent re-acceleration in COMA- D_{pp} -Low and COMA- D_{pp} -High further boosts this emission by roughly one order of magnitude. Remnants of a shock from a previous merger, perpendicular to the ongoing merger, can be seen as diffuse emission around the cluster in the zoom-in simulations due to the stronger magnetic field. In the case of the zoom simulations with turbulent re-acceleration, this aged CRe population is stabilized against cooling losses and therefore significantly brighter than in the pure shock injection case. This is especially evident in the connecting filament to the top-right, between our Coma replica and the two in-falling structures. The simulations COMA- D_{pp} -Low and COMA- D_{pp} -High show stronger and more diffuse synchrotron emission than the simulations without turbulent re-acceleration, showing that especially in the periphery of galaxy clusters an on-the-fly treatment of turbulent re-acceleration helps to stabilize CRe against cooling so they can potentially remain synchrotron bright.

As was the case with Fig. 15.3 the models $B_{\mathcal{F}=0.1}$, B_{ff} and $B_{dyn,\downarrow}$ produce morphologically very similar results. In the case of SLOW-CR3072³ they show more diffuse synchrotron emission further from the cluster center, due to a less steep radial drop-off of the magnetic field compared to the simulated one. This gives synchrotron flux of two orders of magnitude less than in the cluster center in the connection region between the center and relic. In the case of the zoom-in simulations with turbulent re-acceleration, we find similar behavior with generally more synchrotron flux from the smaller halos around Coma. The model $B_{\mathcal{F}=0.1}$ provides the most synchrotron flux in comparison, stemming from the turbulence injected by the recent merger activity and with that stronger magnetic field in these areas.

$B_{dyn,\uparrow}$ generally provides the strongest magnetic field in the filaments, which directly translates to the most synchrotron flux in the case of this model. In SLOW-CR3072³ we again see some of the accretion shock onto the top-right filament, while in the zoom-in simulations, this is the magnetic field model that provides some tangible diffuse emission from the filaments connecting to Coma. For COMA this flux reaches $F_{\nu} \sim 0.01 - 0.1 \text{ nJy beam}^{-1}$ and with that lies significantly below current observational capabilities, by 3-4 orders of magnitude compared to the noise level achieved in Hoang et al. (2023). The addition of turbulent re-acceleration coefficient in COMA- D_{pp} -High increases the synchrotron flux by roughly 2-3 orders of magnitude, bringing it into the range of $F_{\nu} \sim 1 - 10 \text{ nJy beam}^{-1}$. This lies only 1-2 orders of magnitude below the sensitivity achieved in stacking.

15.4.4 Resolved Synchrotron Spectrum

The simulation of the CR electron spectra allows us to self-consistently model synchrotron spectra from the injected and aged electron populations. In Fig. 15.7 we show the resolved spectral index

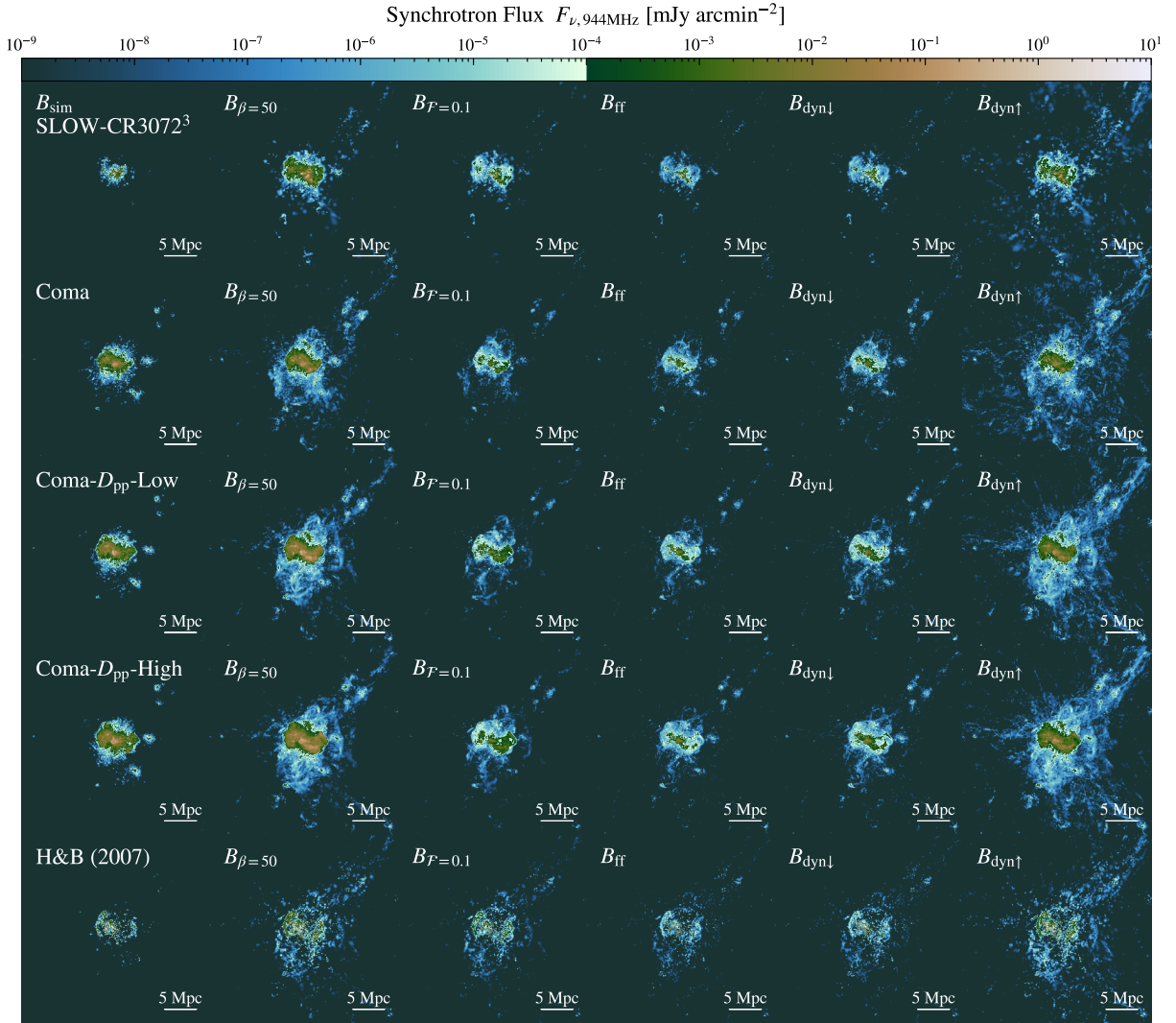


Figure 15.6: The same as Fig.15.5, but for observations at 944 MHz.

maps between 144 MHz and 944 MHz. We construct these spectra by fitting a single power-law to the surface brightness per pixel of the images in Fig. 15.5 and images with the same resolution obtained at a frequency of 944 MHz (see Fig. 15.6) as

$$\alpha_{144\text{MHz}}^{944\text{MHz}}(\text{pix}) = \frac{\log_{10}(I_{144\text{MHz}}(\text{pix})) - \log_{10}(I_{944\text{MHz}}(\text{pix}))}{\log_{10}(144 \text{ MHz}) - \log_{10}(944 \text{ MHz})}. \quad (15.17)$$

We impose a surface brightness cutoff similar to the one in Fig. 15.5, beyond which we do not consider pixels for the slope calculation. This helps to avoid polluting the image with extremely low surface brightness emission that nonetheless can show a flat spectrum due to recent injection at high Mach number accretion shocks. In addition, we exclude spectral indices smaller than $\alpha < -3$, also purely for visualisation reasons.

The spectral index maps show two main behaviors.

One, we find the typical spectral steepening in the wake of the ongoing merger shocks. This stems from the synchrotron and IC cooling the CR electrons experience after the shock passage. We find that the steepening strongly depends on the magnetic field model, which we will discuss in more detail in an upcoming companion paper to [Böss et al. \(2023b\)](#), where we will study radio relics in more detail.

Second, in the most optimistic magnetic field models which show enough diffuse synchrotron emission from the filaments to be able to model a synchrotron slope, we find a spectral index for diffuse emission in filaments of $\alpha \sim -1.0 - -1.5$. This is in excellent agreement with recent observations by [Vernstrom et al. \(2023\)](#). With our imposed limits for slope construction, however, we only find sufficient diffuse emission in the filament to perform this slope construction for the magnetic field models $B_{\beta=50}$ and $B_{\text{dyn},\uparrow}$.

15.5 Full Box

15.5.1 CR Electron Injection

In Fig. 15.8 we show the density-temperature phase-space of all particles contained in SLOW-CR3072³. The background and the inset plot show the total mass contained per phase-space element, indicated by the color bar on top. Contours show the total CR energy per phase-space element, contained in electrons with energies above 1 GeV. These contours show two main acceleration regions. One in the moderate density, high-temperature region associated with merger shocks in the cluster periphery. These CRs could be seen in the form of radio relics, given sufficient magnetic field strength. The other in the low density and moderate temperature region of the warm-hot intergalactic medium (WHIM) with temperatures $T_{\text{WHIM}} \sim 10^5 - 10^7$ K ([Cen & Ostriker, 1999](#); [Davé et al., 2001](#)) where we can expect accretion shocks onto clusters and filaments. This provides a basis for potential synchrotron emission in cosmic web filaments, provided the magnetic field is sufficiently strong.

15.5.2 Synchrotron Emissivity

Fig. 15.9 shows the density-synchrotron emissivity phase space for the simulated and modeled magnetic field. As in Fig. 15.8 the background shows the total mass contained per phase-space element, here for the emissivity as calculated from the simulation SLOW-CR3072³. We only calculate the mean of the particles with emissivities above $j_\nu > 10^{-52}$ erg s⁻¹ Hz⁻¹ cm⁻³, since the majority of the SPH particles in the simulations do not contain a CRe population, so the mean including all particles is close to zero. Lines show the mean value per density interval for SLOW-CR3072³ and the zoom-in simulations COMA, COMA- D_{pp} -Low and COMA- D_{pp} -High. The arrow indicates the upper limit found in [Hoang et al. \(2023\)](#) for $n_e = 10^{-5}$ cm⁻³. We list the values for j_ν we find in this density bin in Tab. 15.2.

In the case of SLOW-CR3072³ we fall below the upper limit of [Hoang et al. \(2023\)](#) by at least 1.5 orders of magnitude for all considered magnetic field configurations. As discussed in the

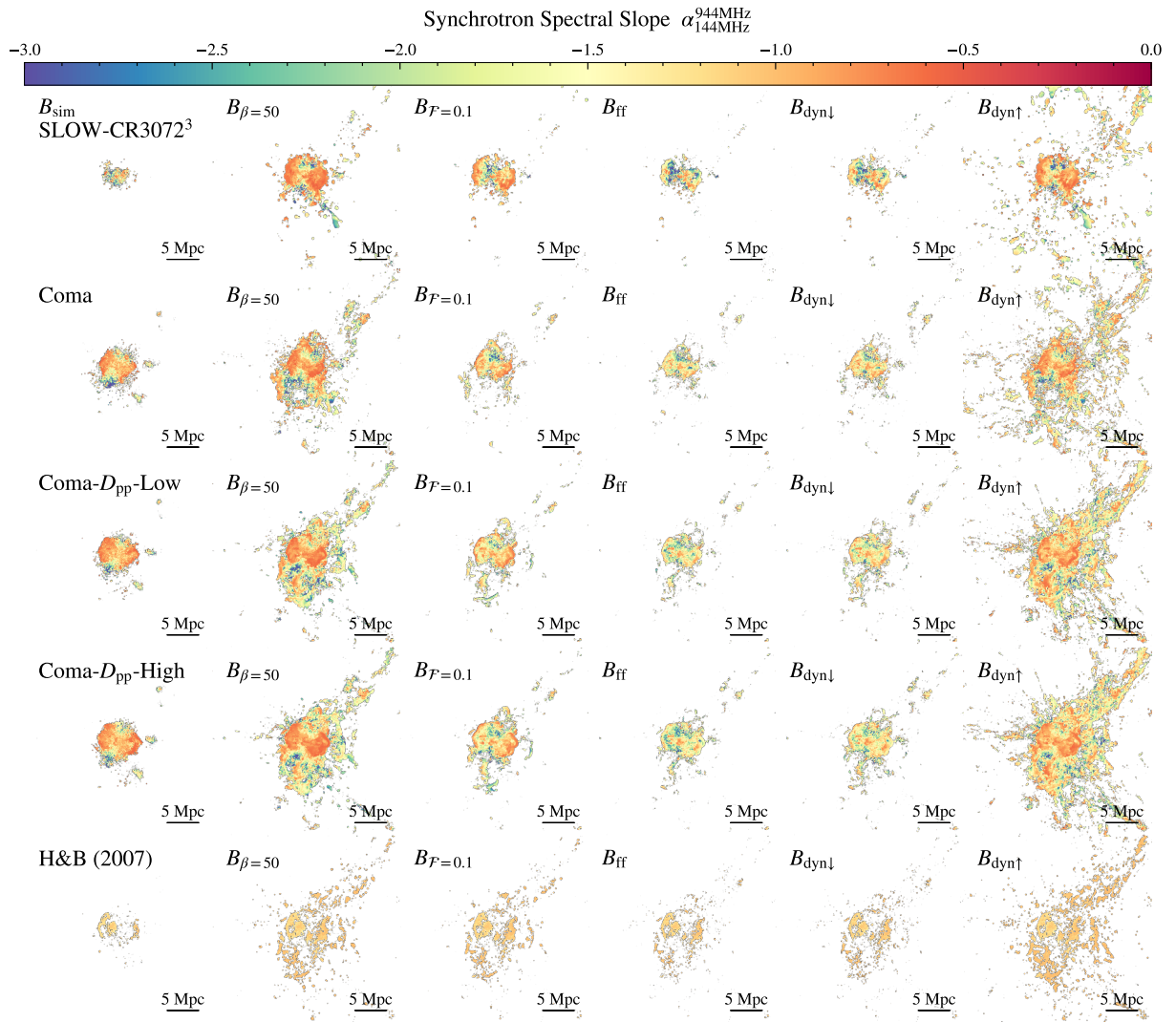


Figure 15.7: Resolved synchrotron spectrum maps accompanying to Fig. 15.5. We construct the synchrotron slope between the images of Fig. 15.5 and images with the same resolution at 944 MHz by fitting a single power-law between the respective pixel values. We impose a surface brightness cutoff for the slope construction, similar to the one in Fig. 15.5 and also cut pixels with slopes $\alpha < -3$.

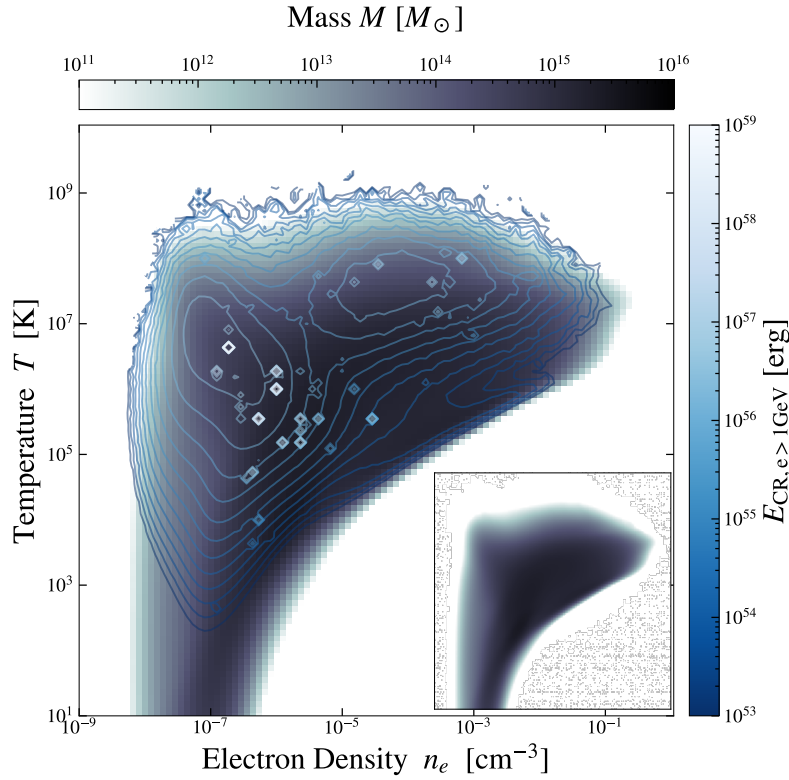


Figure 15.8: Density - temperature phase diagram of all gas particles in the simulation. The colored background shows the mass histogram in phase space. The inset plot shows the same but without contours for clarity. The contours in the main plot show the CR electron energy of CRs with energies above 1 GeV contained per phase-space element.

previous section this can be attributed to the lack of resolution to capture all of the spurious accretion shocks and to the lack of re-acceleration to stabilize the recently injected population against cooling. The highest mean emissivity at $n_e = 10^{-5} \text{ cm}^{-3}$ for SLOW-CR3072³ with $j_\nu \approx 5 \times 10^{-45} \text{ erg s}^{-1} \text{ Hz}^{-1} \text{ cm}^{-3}$ is mainly driven by small number statistics, due to the steep radial drop of the simulated magnetic field and with that only a few synchrotron bright particles contributing to the mean in this density bin. Lower limits in SLOW-CR3072³ can be found with the models B_{ff} and $B_{\text{dyn},\downarrow}$, which both show synchrotron emissivities four orders of magnitude below the observational limits. The more optimistic magnetic field models $B_{\beta=50}$, $B_{\mathcal{F}=0.1}$ and $B_{\text{dyn},\uparrow}$ still lie significantly below the observational limit by 2-3 orders of magnitude.

The zoom-in simulations again show the impact of resolution and inclusion of turbulent re-acceleration. With the shock finder performing better at this resolution the spurious accretion shocks are found more consistently, which leads to a consistent increase in synchrotron emissivity in low-density regions. This can be seen in the bump of synchrotron emissivity below $n_e \sim 5 \times 10^{-4} \text{ cm}^{-3}$ which is where we expect to see the turnover from internal merger shocks to accretion shocks (e.g. [Vazza et al., 2011](#)). The inclusion of turbulent re-acceleration increases this bump by stabilizing the injected electrons against radiative losses in the cluster periphery in the density

Table 15.2: Accompanying to Fig. 15.9 we list the values for the synchrotron emissivity j_ν at 144 MHz at the $n_e = 10^{-5} \text{ cm}^{-3}$ bin. All values are in units $[\text{erg s}^{-1} \text{ Hz}^{-1} \text{ cm}^{-3}]$. From left to right we list the different simulations and top to bottom the different magnetic field models introduced in Sec. 15.3.2.

<i>B</i> -field Model	SLOW-CR3072 ³	COMA	COMA- D_{pp} -LOW	COMA- D_{pp} -HIGH
B_{sim}	4.157×10^{-46}	2.303×10^{-45}	1.036×10^{-44}	6.889×10^{-45}
$B_{\beta=50}$	1.337×10^{-46}	1.485×10^{-45}	4.772×10^{-45}	7.611×10^{-45}
$B_{\mathcal{F}=0.1}$	1.874×10^{-47}	4.127×10^{-46}	5.523×10^{-46}	9.300×10^{-46}
B_{ff}	1.502×10^{-48}	1.822×10^{-47}	5.032×10^{-47}	9.323×10^{-47}
$B_{\text{dyn},\downarrow}$	3.248×10^{-47}	2.498×10^{-46}	8.581×10^{-47}	1.516×10^{-46}
$B_{\text{dyn},\uparrow}$	3.248×10^{-47}	2.498×10^{-46}	1.001×10^{-45}	1.427×10^{-45}

range $n_e \sim 10^{-5} - 10^{-4} \text{ cm}^{-3}$. This has interesting implications for Radio Mega Halos, which we will discuss in upcoming work. We find that the effect of turbulent re-acceleration is of special importance for the emissivity in the regime $n_e \sim 10^{-4} - 10^{-5} \text{ cm}^{-3}$, which is what we focus on in this work.

In the case of the simulated magnetic field model B_{sim} we find that the mean emissivity in COMA lies just half an order of magnitude below the emissivity limit. Compared with the other magnetic field models we find that the increase in resolution in COMA consistently increases the synchrotron emissivity by one order of magnitude compared to SLOW-CR3072³. As this increase is magnetic field model independent we can conclude that it is injection driven, meaning that we capture more of the spurious accretion shocks in the zoom-in simulation COMA, compared to the full cosmological box SLOW-CR3072³.

The inclusion of turbulent re-acceleration further increases the synchrotron emissivity by half an order of magnitude for B_{sim} . With turbulent re-acceleration included both simulations COMA- D_{pp} -LOW and COMA- D_{pp} -HIGH are in reasonable agreement with the upper limit by [Hoang et al. \(2023\)](#). However, as was the case for SLOW-CR3072³ this is again impacted by small-number statistics, as the total number of emitting particles is lower due to a steeper radial dropoff of the magnetic field.

The lower magnetic field models B_{ff} and $B_{\text{dyn},\downarrow}$ both result in emissivities two orders of magnitude below the observational limit. For $B_{\beta=50}$ we find emissivities just below the observational limit, we note however that this model is biased towards accretion shocks due to its scaling with the thermal pressure. Both $B_{\mathcal{F}=0.1}$ and $B_{\text{dyn},\uparrow}$ lie roughly one order of magnitude below the observational limit.

As we will discuss in Sec. 15.6, these one to two orders of magnitude can be covered by a variation of choice of CR injection parameters, giving the possibility of diffuse emission just below the detection limit, even with more conservative magnetic field estimates. On the other end, $B_{\beta=50}$, $B_{\mathcal{F}=0.1}$ and $B_{\text{dyn},\uparrow}$ as the more optimistic magnetic field models show mean emissivities that again lie just below the observational limit of stacking, consistent with previous results in Sec. 15.4.

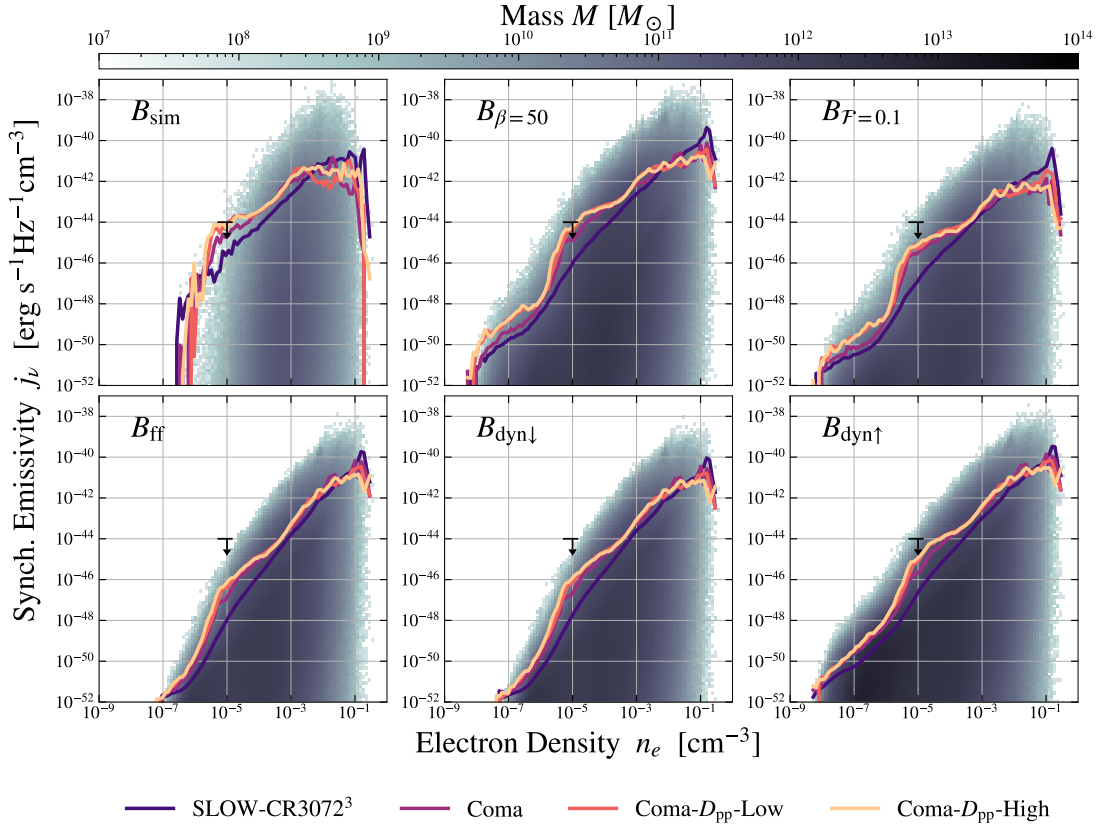


Figure 15.9: The individual panels show the phase-space diagrams in the density-synchrotron emissivity phase-space, containing all gas particles in the simulation. The background shows mass histograms per phase-space element from the original simulation output. The colored lines indicate the mean synchrotron emissivity per density interval for the cosmological box simulation and the zoom-in simulations with and without turbulent re-acceleration. All emissivities are calculated at a frequency of $\nu = 144$ MHz. The upper limit of the synchrotron emissivity is taken from [Hoang et al. \(2023\)](#).

15.6 Discussion

15.6.1 Comparison to post-processing

First, we want to compare the result from our on-the-fly solver to the post-processing model by [Hoeft & Brüggén \(2007\)](#). We use their acceleration efficiency function Ψ and $\xi_e = 10^{-5}$, similar to [Nuza et al. \(2017\)](#). We applied their model to COMA- D_{pp} -Low to make use of the improved shock finder performance compared to SLOW-CR3072³ and show the results in the lowest panels of Fig. 15.5.

For the relics in our Coma replica, we find that the [Hoeft & Brüggén \(2007\)](#) model provides reasonable results and most notably sharper relics. While in our simulations the region between

cluster center and relic is filled with electrons that have been accelerated in the shock passage and subsequently advected downstream of the shock, a post-processing model only accounts for the acceleration at the currently detected shock. This naturally leads to thinner shocks, as the downstream CRs are not accounted for.

However, when it comes to the diffuse model synchrotron emission of filaments a post-processing model faces a number of limitations. For one it is naturally coupled to the performance of the shock finder at the time of output. As can be seen in the panels for $B_{\beta=50}$ and $B_{\text{dyn},\uparrow}$, which produce volume-filling synchrotron emission with our on-the-fly treatment of CRs, this emission is comparable in absolute flux where it is present, however, it is confined only to the regions of active shock detection. This leads to very spurious emission only at the detected accretion shocks. Shock detection in simulations is numerically challenging and requires a number of filtering steps to distinguish between real shocks, cold fronts, and shearing flows (see e.g. [Vazza et al., 2009](#); [Schaal & Springel, 2015](#); [Beck et al., 2016a](#)). This leads to highly transient shock surfaces and introduces difficulties in finding consistent shock surfaces in and around galaxy clusters and filaments at a single timestep. To add to the complication this naturally scales with the numerical resolution, making it easier to detect shocks in the higher resolved ICM than in the lower resolved WHIM (see e.g. [Vazza et al., 2011](#), for a comparison between different numerical models).

While this is true for every individual timestep of the simulation, we find that due to our on-the-fly treatment of CRs and the fact that they can potentially be injected at every timestep in every particle, helps alleviate this problem. As a SPH particle moves through the region of an accretion shock it is highly likely that the shock will be detected at some point through the shock passage and we are not necessarily reliant on the detection happening at the output timestep. This leads to the smoother injection of CRs and with that a more diffuse emission in the filament volume, as can be seen in direct comparison between the lower two rows of the right-most column in Fig. 15.5.

We also find that the advection of CRs with the thermal gas plays a role in the volume-filling synchrotron emission of filaments, provided that the electrons are stabilized against cooling by turbulent re-acceleration. This can be seen in direct comparison between e.g. the right-most row for COMA, COMA- D_{pp} -Low and COMA- D_{pp} -HIGH in Fig. 15.5. Naturally, a pure post-processing model cannot account for this process and is therefore entirely driven by in-situ emission. This has been addressed by multiple groups and has led to a number of recent developments of Fokker-Planck solvers with or without tracer particles to account for CR electron injection and transport in large-scale simulations (e.g. [Wittor et al., 2017](#); [Yang & Ruszkowski, 2017](#); [Winner et al., 2019](#); [Ogrodnik et al., 2021](#); [Vazza et al., 2021b](#); [Hopkins et al., 2022a](#)).

15.6.2 Choice of CR injection parameters

In this work, we have used a fixed set of CR parameters and evolved the injected CR population in time. These parameters are namely the injection momentum \hat{p}_{inj} as the momentum where the non-thermal power-law of the CR electron population starts, the efficiency $\eta(\mathcal{M}_s, X_{\text{cr}}, \theta_B)$ as the fraction of shock energy that is available to accelerate CRs to relativistic energies and finally the ratio between proton and electron injection K_{ep} . Most of these parameters are poorly constrained

Table 15.3: We list the injection parameters used in this work and selected work in the literature on non-thermal emission by CRs in the large-scale structure of the Universe. From left to right we list the indicated work, Mach number dependent acceleration efficiency, magnetic field angle dependent efficiency, injection ratio between electrons and protons, and injection momentum.

Reference	$\eta(\mathcal{M}_s)$	$\eta(\theta_B)$	K_{ep}	\hat{p}_{inj}
This Work	Kang & Ryu (2013)	Pais et al. (2018)	0.01	0.1
Hoefl et al. (2008)	Hoefl & Brüggén (2007)	-	0.05	Eq. 15.19
Pinzke et al. (2013)	Pinzke et al. (2013)	-	Eq. 15.21	Eq. 15.20
Hong et al. (2014a)	Kang & Ryu (2013)	-	-	0.01
Vazza et al. (2015a)	Kang & Ryu (2013)	0.3	0.01	Eq. 15.18
Donnert et al. (2016)	Kang & Ryu (2013)	-	0.01	0.1
Wittor et al. (2017)	Kang & Ryu (2013)	$\Theta(\theta - \theta_{crit})$	0.05	Eq. 15.19
Ha et al. (2023)	Ha et al. (2023)	-	Eq. 15.21	Eq. 15.20

in the high Mach number, high- β plasma shocks expected in and around cosmic web filaments, with only a small number of studies available (e.g. Kang & Ryu, 2013; Guo et al., 2014; Ryu et al., 2019; Kang et al., 2019; Kobzar et al., 2021; Ha et al., 2023). We will briefly discuss the impact of these parameters on the synchrotron emission in cosmic web filaments. An overview of our parameters and the ones used in previous work in the literature can be found in Tab. 15.3.

Injection Momentum \hat{p}_{inj}

The strongest impact is caused by the choice of the connection point between thermal and non-thermal electron populations, \hat{p}_{inj} , beyond which the power-law distribution starts. Typical fixed values used in previous work of this point lie around $\hat{p}_{inj} = 0.01 - 0.1$ (e.g. Hong et al., 2014a; Donnert et al., 2016). For the electrons to be efficiently accelerated by DSA their gyro radius must be of the order of that of the protons, which means a dependence of injection momentum on the magnetic field and the temperature downstream of the shock.

Kang & Ryu (2013) for example model this as

$$p_{inj} \approx 1.17m_p v_2 \left(1 + \frac{1.07}{\epsilon_B} \right) \quad (15.18)$$

where m_p is the proton mass, v_2 is the downstream velocity of the shock, and $\epsilon_B = B_0/B_\perp$ is the ratio between the mean magnetic field along the shock normal and the amplitude of the post-shock MHD turbulence.

The Hoefl & Brüggén (2007) model omits the explicit magnetic field dependence and relates the injection momentum only to the temperature downstream of the shock (T_2). This leads to an injection momentum of

$$\hat{p}_{inj,e} \sim \frac{10k_B T_2}{m_e c^2} \quad (15.19)$$

which for typical shocks in the ICM with $T_2 \sim 10^8$ K is of the order $\hat{p}_{inj,e} \sim 0.1 - 0.2$.

A similar parametrisation is used e.g. in Kang et al. (2019); Vazza et al. (2021b); Ha et al. (2023)

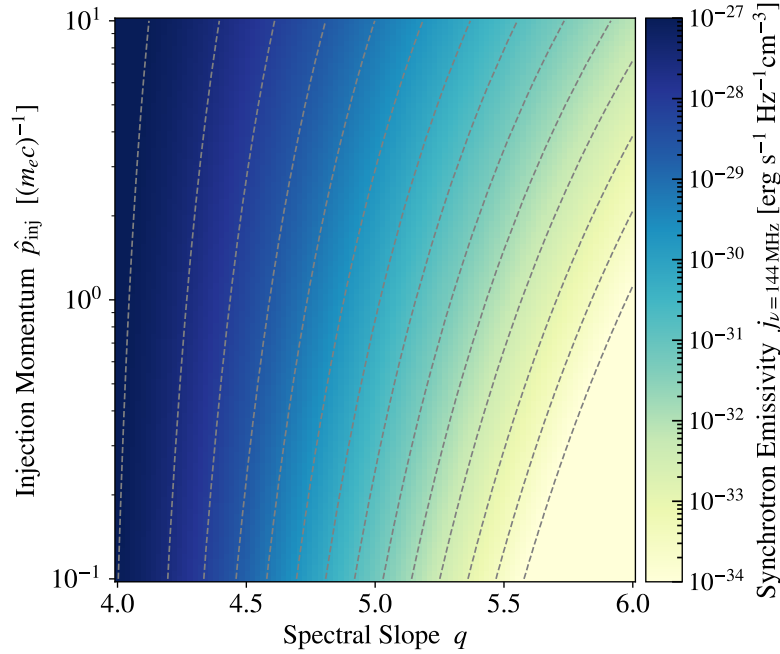


Figure 15.10: We show the synchrotron emissivity of an electron spectrum with a power-law slope q extending between an injection momentum \hat{p}_{inj} and a maximum momentum $\hat{p}_{\text{max}} = 10^6$. Each spectrum is normalized to contain a total energy density of $\epsilon = 1 \text{ erg cm}^{-3}$ and emits in a magnetic field with $B = 1 \mu\text{G}$. The color shows emissivity and contour lines indicate half an order of magnitude in difference.

with

$$\hat{p}_{\text{inj,e}} \approx \frac{3 \sqrt{\frac{m_e}{m_p}} P_{\text{th,p}}}{m_e c} = \frac{3 \sqrt{2 k_B m_e T_2}}{m_e c} \quad (15.20)$$

which for the shocks in our simulated cosmic web filaments with typical downstream temperatures of $T_2 \sim 10^7 \text{ K}$ would be of the order $\hat{p}_{\text{inj}} \approx 0.17$. This makes our choice of a fixed $\hat{p}_{\text{inj}} \approx 0.1$ a reasonable assumption, especially for cold accretion shocks. We show the impact of the choice of the injection momentum on the synchrotron emissivity in Fig. 15.10. Given the high sonic Mach number we detect in the surrounding of filaments with $\mathcal{M}_s \gg 10$, the standard RH jump conditions converge towards $q = 4$. For this value of q , even a two orders of magnitude higher injection momentum only introduces a half order of magnitude higher synchrotron emission.

Acceleration Efficiency $\eta(\mathcal{M}_s, X_{\text{cr}}, \theta_B)$

Mach number dependent efficiency models that have been used in previous simulations typically show a strong dependence on Mach number for weak shocks $\mathcal{M}_s < 5$ and saturate at a fixed value for strong shocks $\mathcal{M}_s > 7 - 10$ (e.g. [Hoefl & Brüggén, 2007](#); [Kang & Jones, 2007](#); [Kang & Ryu, 2013](#); [Caprioli & Spitkovsky, 2014](#); [Ryu et al., 2019](#)). This saturation value varies by about one order of magnitude (see the left panel of Fig. 6.1 for our parametrization of the

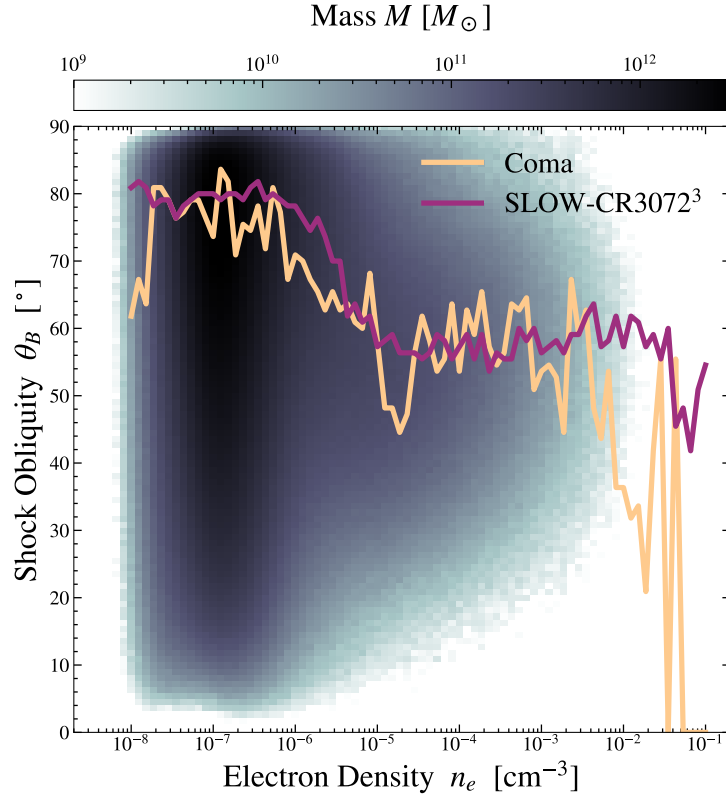


Figure 15.11: Density - shock obliquity phase map. The colors indicate the 2D mass histogram for SLOW-CR3072³, while the line indicates the maximum of the histograms for SLOW-CR3072³ and COMA as a function of density.

different DSA models). For accretion shocks, whose Mach numbers lie within the range of the efficiency models above the saturation value this means that the injected energy and with that the synchrotron emission scales linearly with this saturation value. With our choice of the Kang & Ryu (2013) efficiency model, we lie in the middle of the range for the saturation values. A different model choice would therefore change the potential synchrotron brightness by half an order of magnitude, up or down. We note, however, that DSA models for high sonic Mach number, high- β , and low-temperature shocks are scarce and further investigation in this direction is needed.

In the case of magnetic field angle dependent acceleration efficiency ($\eta(\theta_B)$) Vazza et al. (2017); Wittor et al. (2017) find that allowing CR electron acceleration only at quasi-perpendicular shocks with $\theta > 60^\circ$ does not significantly alter the expected emission from accretion shocks onto clusters and cosmic web filaments. This stems from the alignment of the shock surface and magnetic field, due to the adiabatic compression and with that amplification of the magnetic field only working on the perpendicular component. In Fig. 15.11 we show the density - shock obliquity phase space of SLOW-CR3072³ and COMA. We find a similar trend of shock obliquity increasing for low-density regions.

However, we also see a shock obliquity of $\theta_B \approx 60^\circ$ for higher densities. This result is in agreement with the findings of [Banfi et al. \(2020\)](#), see their Fig. 17. [Wittor et al. \(2017\)](#) showed that for any upstream shock obliquity θ_{pre} , the shock passage will always align the obliquity towards $\theta = 90^\circ$. This process only depends on the upstream obliquity and the shock compression ratio, which makes it more efficient for higher Mach number shocks.

Hence, if accounting for a shock obliquity dependent acceleration efficiency, we preferentially accelerate CR electrons over CR protons. This can help ease the tension between CR acceleration efficiency models and the lack of diffuse γ -ray detection in galaxy clusters (see e.g. [Wittor et al., 2019](#), for a discussion). We will address this question as well in upcoming work, analyzing the proton component of our SLOW-CR3072³ simulation.

Electron to Proton Ratio K_{ep}

The final free parameter is the electron to proton injection ratio K_{ep} . This is poorly constrained and is typically taken as a canonical value from SNe as $K_{\text{ep}} = 0.001 - 0.01$ (e.g. [Park et al., 2015](#)). [Kang \(2020\)](#) follow an alternative approach by making this parameter injection slope dependent as

$$K_{\text{ep}} = \left(\frac{m_e}{m_p} \right)^{(q_{\text{inj}}-3)/2} . \quad (15.21)$$

At strong accretion shocks with injection slope of $q_{\text{inj}} \approx 4$ this gives a value of $K_{\text{ep}} \approx 0.023$. This means we underestimate the injection of CRE by a factor of 2.3 by using our constant value. However, it is not clear what role non-linear DSA effects can play in these shock environments and if this can lead to a steepening of the injection slope (see [Caprioli et al., 2020](#); [Diesing & Caprioli, 2021](#)). Given the sensitivity of K_{ep} on the injection slope and the uncertainty of the real slope, we note that further study is required.

[Vazza et al. \(2015b\)](#) test this value for radio relics and find that to explain observed radio emission they require a $K_{\text{ep}} \geq 10 - 10^{-2}$ to avoid γ -ray emission in conflict with Fermi-LAT observations. Recent results indicate that this over-injection of CR protons can also be remedied by the shock-obliquity dependent acceleration of CRs (see [Wittor, 2021](#)). Given that the observed brightness of radio relics is still an open problem this variance in values for K_{ep} introduces a large variance in potential synchrotron emission. The emission in our model scales linearly with K_{ep} , so larger values for K_{ep} can significantly boost the synchrotron emission in filaments. We will investigate the impact of choosing an on-the-fly calculation of K_{ep} in future zoom-in simulations.

15.6.3 Impact of star formation and AGN feedback

With our simulation being non-radiative we do not account for star formation or AGN feedback. We therefore also cannot account for CR injection by these processes. In the following, we will briefly discuss the potential impact of this on our results. AGN can potentially provide a significant CR electron seed population that can advect and diffuse in the cluster volume (see e.g. [ZuHone et al., 2021](#); [Vazza et al., 2023](#)). However, this advection is expected to be confined to clusters, where the most powerful AGN are expected to be located. There the injected electron can potentially be re-energized by cluster merger shocks and can be observed as the so-called

radio phoenixes (van Weeren et al., 2019). The jets of AGN can also inject significant turbulence, as e.g. observed in Perseus (Sanders et al., 2016a). This turbulence can then re-accelerate fossil electrons and provide the basis for radio halos.

We will aim to include AGN feedback in the near future, as modeling of radio galaxies in our sample should help to estimate the background pollution by discreet sources and their impact on our results. This is however beyond the scope of this work.

CR proton injection at SNe has been found to drive and/or modify the structure of galactic winds and the CGM (e.g. Pfrommer et al., 2017; Butsky & Quinn, 2018; Fielding et al., 2020; Ji et al., 2020; Girichidis et al., 2023). CR protons generally have lifetimes exceeding the Hubble time in the low-density CGM/ICM (see e.g. Fig 7 in Brunetti & Lazarian, 2007, for an illustration of CR proton cooling times at different densities). There they can nonetheless interact with the thermal background gas and be scattered into π -ons and, depending on the charge of the π -on, decay into γ -photons or electrons/positrons. These electrons could then contribute to diffuse synchrotron emission. In the context of CR proton acceleration at merger shocks, this process has been proposed as a source of radio halos (e.g. Dolag & Enßlin, 2000). However, the non-detection of diffuse γ -ray emission from galaxy clusters puts a strong upper limit on this process (e.g. Pinzke & Pfrommer, 2010; Pinzke et al., 2011; Ackermann et al., 2014).

15.6.4 Observational Prospects

Given the potential impact of so-far poorly constrained CR injection parameters on our results we can make a best-case assumption of the observational requirements for direct observation of diffuse synchrotron emission from cosmic web filaments. We will discuss this again for the filaments we find around our Coma cluster replica, as it provides the widest range of parameters in our set due to the zoom-in re-simulation. As shown in the lower panels of Fig. 15.5, the most optimistic magnetic field model B together with the higher resolution and turbulent re-acceleration leads to a diffuse synchrotron flux from the filaments of $S_{\nu=144 \text{ MHz}} \approx 0.1 \mu\text{Jy beam}^{-1}$ for a beam size of $\theta = 60'' \times 60''$. This is three orders of magnitude below the noise of $\sigma_{\text{rms}} = 0.4 \text{ mJy beam}^{-1}$ given in Bonafede et al. (2022). However, the choice of other parameters for p_{inj} and K_{ep} could boost this emission by up to two orders of magnitude. This would indicate diffuse emission just a factor of ten below the current noise level. The stacking approach by Hoang et al. (2023) reduces the noise to $\sigma_{\text{noise}} = 0.6 \mu\text{Jy beam}^{-1}$, which lies just a factor of \sim five above the diffuse emission we find in the most optimistic scenario. This is also consistent in the emissivity calculation, where the mean emissivity lies within an order of magnitude of the upper limit found by Hoang et al. (2023). We did the same analysis for 1.4 GHz and found even lower surface brightness in the cosmic web region of our Coma analog. In the high-frequency band we find maximum surface brightness of diffuse emission from the cosmic web filaments of the order $S_{\nu=1.4 \text{ GHz}} = 0.1 \text{ nJy beam}^{-1}$ for a MeerKAT beam of $\theta = 5'' \times 5''$ (as in e.g. de Gasperin et al., 2022). Direct observations as in de Gasperin et al. (2022) with a $5'' \times 5''$ beam have a noise level of $\sigma_{\text{noise}} = 5.3 \mu\text{Jy beam}^{-1}$ and the EMU survey (Norris et al., 2011) with a $10'' \times 10''$ beam provides a sensitivity of $\sigma_{\text{noise}} = 10 \mu\text{Jy beam}^{-1}$, which would be five orders of magnitude above our most optimistic scenario, making detection at high frequencies even less likely, as expected (e.g. Vazza et al., 2015b).

15.7 Conclusions

We presented results from the first constrained cosmological simulation with an on-the-fly Fokker-Planck solver to study the time evolution of CR electron populations on a cosmological scale. We used this simulation to study potential diffuse synchrotron emission from cosmic web filaments. Our results can be summarized as follows:

- We find the acceleration of CR electrons in clusters and on accretion shocks onto clusters and cosmic web filaments. The electrons with the longest lifetimes settle into large halos around clusters and in cosmic web filaments. Given enough magnetic field strength and stabilization against cooling losses, by e.g. Fermi-II re-acceleration, these electrons can provide the basis for synchrotron emission in these regions.
- We tested six different magnetic field configurations to study the threshold for obtaining considerable diffuse emission from cosmic web filaments and found that with our choice of CR injection parameters we require fields of the order $B \sim 100$ nG to obtain considerable emission.
- To test the impact of resolution in our simulation and the inclusion of on-the-fly turbulent re-acceleration we performed zoom-in simulations of our Coma cluster replica. We find that higher resolution and with that a more accurate capture of accretion shocks increases the synchrotron emission by an order of magnitude in low-density regions and the inclusion of turbulent re-acceleration by another order of magnitude. This would in turn decrease the required magnetic field strength to obtain the same level of synchrotron emission as in the low-resolution full box by one order of magnitude. Bringing it into agreement with current observations with $B \approx 30$ nG.
- With our chosen parameters for CR injection the surface brightness of diffuse emission from cosmic web filaments lies three orders of magnitude below the current noise limit for direct detection with LOFAR and 5 orders of magnitude below the noise limit for direct detections with M_{EER}KAT.
- In the most optimistic model for magnetic field strength and CR injection parameters we can estimate synchrotron emission only a factor ~ 5 below the noise level currently achievable by stacking of radio images.
- In the models that provide significant synchrotron emission from the filaments, we find that the spectral index of diffuse emission is of the order $\alpha \approx -1.0 - -1.5$, in agreement with recent observations by [Vernstrom et al. \(2023\)](#).

In future work, we will present the results of SLOW-CR3072³ for the radio halos of our Coma, Perseus, and Virgo replicas, radio halo relations, and γ -ray emission from the CR proton population. We will further increase our sample size of zoom-in simulations and vary the parameters for CR injection and turbulent re-acceleration to study their impact on the time evolution of radio halos.

16 | Simulating the LOcal Web (SLOW): γ -ray Emission from the Local Universe

Co-Authors: Ildar Khabibullin, Klaus Dolag, Ulrich P. Steinwandel, Elena Hernández-Martínez and Jenny G. Sorce

At the time of writing this paper is undergoing internal review and is in preparation to be published in A&A.

Abstract

Context: Diffuse γ -ray emission from the cosmic web remains out of reach for current observations. Detecting this emission would provide constraints on intergalactic magnetic fields as well as dark matter interaction models.

Aims: We aim to provide estimates for diffuse γ -ray emission from galaxy clusters and the cosmic web.

Methods: In this work we show results from the first cosmological MHD simulation with an on-the-fly spectral cosmic ray model. We model CR injection at shocks, account for adiabatic changes and advection of CR protons, and obtain their γ -ray emissivity directly from the simulated CR spectra. For this, we use constrained initial conditions, which closely resemble the local Universe, in order to compare to Fermi-LAT data.

Results: We find CR proton acceleration at all structure formation and accretion shocks in galaxy clusters and cosmic web filaments. These protons provide the basis for diffuse γ -ray emission in these regimes. The absolute value of the diffuse γ -ray emission in our simulation lies four orders of magnitude below the current upper limits found by Fermi-LAT. Future work with higher resolution zoom-in simulation is required to study the impact of resolution on our shock finder, as well as CR injection parameters in more detail.

16.1 Introduction

γ -ray astronomy holds the potential to give insight into a number of non-thermal processes in the intra-cluster medium (ICM) and the intergalactic medium (IGM). On the one hand γ photons emitted by quasars help constrain the intergalactic magnetic field strength and correlation lengths

from a lower limit (e.g. [Alves Batista & Saveliev, 2020](#); [MAGIC Collaboration et al., 2022](#)). These photons hold enough energy to produce spontaneous electron-positron pairs along their path from a quasar through a cosmic void, to Earth. These electron-positron pairs can then couple to the background magnetic field and be deflected from their original path. Subsequently, these electrons/positrons can potentially Compton upscatter a CMB photon into the X-ray to γ -ray energy range, and given the right scattering geometry this photon could be observed at Earth with a time-delay relative to the main γ -emission of the source (e.g. [Plaga, 1995](#); [Neronov & Semikoz, 2007, 2009](#); [Chen et al., 2015](#)). Depending on the magnetic field geometry and potential helicity this could lead to a halo around the point-source, which could be skewed to one side of the source (e.g. [Neronov & Semikoz, 2009](#); [Alves Batista et al., 2016](#); [Alves Batista & Saveliev, 2021b](#)). The non-detection of such a signal currently poses a lower limit on magnetic fields in voids of $B_{\min} \approx 10^{-14}$ G (e.g. [MAGIC Collaboration et al., 2022](#)).

Direct observation of diffuse γ -ray emission in galaxy clusters on the other hand could provide insight into the relativistic proton component in the ICM. In galaxy clusters, the main mechanism of CR proton production is Diffusive Shock Acceleration (DSA) at shocks driven by mergers during the hierarchical structure formation process (e.g. [Brüggen et al., 2012](#), for reviews of GC shocks). These shocks have been studied in detail in the X-ray band due to the shock-induced temperature increase (e.g. [Böhringer & Werner, 2010](#), for a review) as well as via the radio emission attributed to efficient CR electron acceleration in the so-called radio relics (see [van Weeren et al., 2019](#), for a review). Due to the inefficient energy-loss mechanisms of relativistic protons (see e.g. Fig. 7 in [Brunetti & Lazarian, 2007](#)) they should be long-lived and with that be able to be transported all through the cluster volume.

These relativistic protons can then interact with the thermal background gas and scatter into $\pi^{0,\pm}$ -ons. The neutral π^0 further decays into two γ photons. However, the current lack of a detection of such diffuse emission (see e.g. [Ackermann et al., 2014, 2015, 2016](#)) with Fermi-LAT puts a limit of roughly 1% of the thermal energy density on the relativistic proton energy density (however there are indications for diffuse γ -ray emission towards the Coma cluster by [Xi et al., 2018](#); [Adam et al., 2021](#); [Baghmanyant et al., 2022](#)).

This puts strain on most of the theories on the efficiency of proton acceleration at merger shocks in the ICM (see e.g. [Kang & Jones, 2007](#); [Kang & Ryu, 2013](#)) which model CR acceleration efficiencies to match radio observations. Under the assumption that CR proton acceleration is more efficient than CR electron acceleration, this would produce CR proton to thermal pressure ratios of up to 20% (see [Wittor, 2021](#), for a recent review).

More recent models include the shock obliquity, the angle between shock propagation and background magnetic field, as it has been shown that different obliquities drive different kinds of plasma instabilities which favor either proton or electron acceleration (e.g. [Caprioli & Spitkovsky, 2014](#); [Ha et al., 2018b](#); [Ryu et al., 2019](#)). Given that protons are found to be most efficiently accelerated at quasi-parallel shocks and observations of radio relic polarisation (e.g. [Stroe et al., 2013, 2016](#); [Di Gennaro et al., 2018](#)) as well as simulations (e.g. [Wittor et al., 2017](#); [Banfi et al., 2020](#)) indicate that a large fraction of merger shocks are quasi-perpendicular, this would make merger shocks inefficient at accelerating CR protons, helping to alleviate this problem.

Previous studies have found that with an acceleration efficiency of up to 50%, significantly above the currently favored efficiencies, detection of diffuse γ -ray emission is just out of reach of

Fermi-LAT (Pinzke & Pfrommer, 2010; Pinzke et al., 2011). More recent simulations by Vazza et al. (2016) showed that the acceleration efficiency (η) should be of the order $\eta \approx 10^{-3}$ to avoid disagreement with the non-detection by Fermi-LAT. This was followed up recently by Ha et al. (2020) with the most recent Mach number dependent DSA parametrization by Ryu et al. (2019) which gives a range of $\eta \approx 10^{-3} - 10^{-2}$ for weak intra-cluster shocks with $\mathcal{M}_s \sim 2.25 - 5$. They equally find that this level of efficiency is in agreement with the current upper limits by Fermi-LAT.

However, none of these simulations explicitly follow the CR proton distribution functions within the simulation but follow either a total energy budget of CRs without information on the spectral slope or model a CR spectrum in post-processing. It is therefore worth revisiting this problem in current state-of-the-art simulations.

For this work we employ the first simulation of a CR-MHD simulation of a $500 h^{-1} c\text{Mpc}$ constrained cosmological volume with an on-the-fly Fokker-Planck solver to model CR proton and electron acceleration at shocks, adiabatic changes and energy losses due to synchrotron emission and inverse Compton scattering off CMB photons.

We presented the results of this simulation related to synchrotron emission from the Cosmic Web in Böss et al. (2023a), or Chapter 15. In this work we will focus on the CR proton component of the same simulation, to study the expected γ -ray emission from galaxy clusters while accounting for the interplay of CR proton acceleration at accretion shocks, their advection within the ICM and re-acceleration by merger shocks.

The paper is structured as follows: In Section 16.2 we will describe the simulation and the code modules employed for this work, as well as our modeling of γ -ray emission by π -on decay from CR proton scattering. Section 16.3 contains our predictions of γ -ray emission for the full sky via this process. In Section 16.4 we show the γ luminosity in comparison to the Fermi-LAT limits and compare the spectra of some prominent clusters to observations in Section 16.5.2. Section 16.6 contains a discussion of numerical constraints and choice of CR injection parameters. Finally Section 16.7 contains our conclusions and a summary of our work.

16.2 Methods

16.2.1 Initial Conditions

We use the same simulations as in Chapter 15, hence we will only present a brief summary of the initial conditions and refer the interested reader again to Sorce (2018); Dolag et al. (2023b). These initial conditions are constrained based on galaxy distance modulus and observational redshift, thus peculiar velocity (Carlesi et al., 2016; Sorce, 2018). The 3D peculiar velocities of galaxies are obtained from the COSMICFLOWS-2 distance modulus survey (Tully et al., 2013) using a Wiener Filter algorithm (Zaroubi et al., 1995, 1998) and applying a number of reconstruction steps (Doumler et al., 2013c,a,b; Sorce et al., 2014; Sorce, 2015; Sorce et al., 2017; Sorce & Tempel, 2017, 2018). Ultimately a density field of the local Universe is constructed at the initial redshift, using the constrained realization algorithm by Hoffman & Ribak (1991), and its

resolution is increased to the desired value, using the GINNUNGAGAP software¹. The simulation used in this work is a cosmological box with a side length of $L = 500h^{-1} \text{ cMpc}$, centered on the Milky Way. Throughout this work we use a *Planck* cosmology (Planck Collaboration et al., 2014) with matter densities $\Omega_m = 0.307$ and $\Omega_{\text{baryon}} = 0.048$, a cosmological constant of $\Omega_\Lambda = 0.692$ and the Hubble parameter $H_0 = 67.77 \text{ km s}^{-1} \text{ Mpc}^{-1}$.

16.2.2 Simulation Code

The simulation was run using OPENGADGET3 (Groth et al., 2023), a cosmological TREE-SPH code based on GADGET2 (Springel, 2005).

Gravity in OPENGADGET3 is solved using a BH-tree at short range and a PM-grid for long-range forces. We employ an updated SPH implementation (Beck et al., 2016b) with a spatially and time-dependent high-resolution shock-capturing scheme (Dolag et al., 2005c; Cullen & Dehnen, 2010), a Wendland C_4 kernel with 200 neighbors and bias correction (as introduced in Dehnen & Aly, 2012), to ensure stabilization against the tensile (pairing) instability and a high-resolution maximum entropy scheme in the form of (anisotropic) thermal conduction. To account for the anisotropic thermal conduction along magnetic field lines we use a bi-conjugate gradient solver (Petkova & Springel, 2009; Arth et al., 2014; Steinwandel et al., 2020b).

The MHD solver was presented in Dolag et al. (2009a). We also include non-ideal MHD in the form of magnetic diffusion and dissipation as introduced in Bonafede et al. (2011).

Shock properties needed for CR acceleration are captured on the fly with the algorithm described in (Beck et al., 2016a).

16.2.3 Cosmic Ray Model

As in Chapter 15 we use the on-the-fly Fokker-Planck solver CRESCENDO introduced in Böss et al. (2023c) to include Cosmic Rays in our simulation. CRESCENDO represents the population of CR protons and electrons as piece-wise powerlaws in momentum space and evolves their distribution function in time by solving the diffusion-advection equation in the two-moment approach, following Miniati (2001). We account for injection at shocks following diffusive shock acceleration (DSA), adiabatic changes due to density changes of the surrounding thermal gas, and energy losses of electrons due to synchrotron emission and inverse Compton (IC) scattering off CMB photons. This reduces the Fokker-Planck equation that describes the time evolution of CR populations to

$$\frac{Df(p, \mathbf{x}, t)}{Dt} = \left(\frac{1}{3} \nabla \cdot \mathbf{u} \right) p \frac{\partial f(p, \mathbf{x}, t)}{\partial p} \quad (16.1)$$

$$+ \frac{1}{p^2} \frac{\partial}{\partial p} \left(p^2 \sum_l b_l f(p, \mathbf{x}, t) \right) \quad (16.2)$$

$$+ j(\mathbf{x}, p, t). \quad (16.3)$$

¹<https://code.google.com/p/ginnungagap/>

Both protons and electrons are considered in the dimensionless momentum range $\hat{p} \equiv \frac{p}{mc} \in [0.1, 10^5]$, where m is the mass of the individual particle species. We discretized the populations with 8 bins (1.3/dex) for protons and 24 bins (4/dex) for electrons. CR acceleration is modeled following the DSA model by [Kang & Ryu \(2013\)](#) and the shock obliquity-dependent efficiency model by [Pais et al. \(2018\)](#). We inject the fraction of shock energy which is available for CR acceleration into the full momentum range of the CR population as a single power law following a linear DSA slope at a fixed electron to proton ratio of $K_{ep} = 0.01$. The fixed injection momentum of $\hat{p}_{inj} = 0.1$ is a compromise between typical injection momenta of $\hat{p}_{inj} \sim 0.01$ for accretion shocks and $\hat{p}_{inj} = 1$ for merger shocks in the ICM (see bottom panel of Fig. 8 in [Ha et al., 2023](#)). For this run, we use closed boundary conditions at the lower end of the distribution function, as it provides more numerical stability and mimics low-momentum cooling on adiabatic compression, which is not explicitly included in this simulation.

16.2.4 Gamma-Ray Emission

Gamma-Ray Emission from a proton spectrum

We compute the γ -ray emission directly from the distribution functions of CR protons obtained from the on-the-fly Fokker-Planck solver, without any further assumptions for gas particles that do not contain a CR population.

For γ -ray emission in the range of 100 MeV to 100 GeV, the decay of π^0 mesons is the dominating channel, with Bremsstrahlung and inverse Compton up-scattering of background photons being sub-dominant by roughly an order of magnitude (see Fig. 13 in [Yang et al., 2018](#)). To model the γ -ray emission by π^0 -decay we closely follow the approach by [Werhahn et al. \(2021\)](#) and compute the source function for a given γ -photon energy E_γ in units [$\gamma \text{ erg}^{-1} \text{ s}^{-1} \text{ cm}^{-3}$] as

$$q_\gamma(E_\gamma) = \frac{4\pi}{m_p} n_H \int_{\hat{p}_{thr}}^{\hat{p}_{max}} d\hat{p} \hat{p}^2 f(\hat{p}) \frac{d\sigma_\gamma(E_\gamma, \hat{p})}{dE_\gamma} \quad (16.4)$$

where n_H is the number density of hydrogen, \hat{p}_{thr} is the threshold momentum for π^0 production, \hat{p}_{max} is the maximum momentum of the distribution function $f(\hat{p})$ in dimensionless momentum space and

$$\frac{d\sigma_\gamma(E_\gamma, \hat{p})}{dE} = A_{max}(T_p(\hat{p})) F(T_p(\hat{p}), E_\gamma) \quad (16.5)$$

is the differential γ -ray cross-section as parametrized in [Kafexhiu et al. \(2014\)](#). Here E_γ is the photon energy and $T_p(\hat{p})$ is the kinetic energy of the protons. $A_{max}(T_p(\hat{p}))$ describes the peak of the differential cross section and $F(T_p(\hat{p}), E_\gamma)$ parametrizes the fit to the simulated spectrum.

We use their fit to the GEANT4 data and integrate Eq. 16.4 by solving the contribution of each momentum bin individually, accounting for partially filled bins between \hat{p}_{thr} and \hat{p}_i .

From Eq. 16.4 we can obtain an emissivity per photon energy E_γ in units [$\gamma \text{ s}^{-1} \text{ cm}^{-3}$] from

$$j_\gamma(E_\gamma) = E_\gamma q_\gamma \quad . \quad (16.6)$$

Eq. 16.4 relates to the total photon flux in units [$\gamma \text{ s}^{-1} \text{ cm}^{-2}$] for a given energy band $E \in [E_1, E_2]$ via

$$F_\gamma = \frac{1}{4\pi d^2} \int_{\Omega} dV \int_{E_1}^{E_2} dE q_\gamma \quad (16.7)$$

and its luminosity in units [erg s^{-1}] via

$$L_\gamma = \int_{\Omega} dV \int_{E_1}^{E_2} dE E j_\gamma \quad (16.8)$$

where Ω is the volume of the emitting region, in our case the volume of an SPH particle with a CR proton population. The emissivity per particle across the whole observational band is found by omitting the volume integral in Eq. 16.8.

We compare our results to the implementation in the MINOT package (Adam et al., 2020) in Sec. 11.3.4.

Analytic model for Gamma-Ray Emission

To compare to previous work in the literature we compute the γ -ray emission following the analytic model by Pfrommer & Enßlin (2004). They give the source function of γ -rays from a power-law energy spectrum of protons with slope α_p as

$$q_\gamma(E_\gamma) dE_\gamma dV \approx c \sigma_{pp} n_H \tilde{n}_{\text{CR}} \frac{2^{4-\alpha_\gamma}}{3\alpha_\gamma} \quad (16.9)$$

$$\times \left(\frac{m_{\pi^0} c^2}{\text{GeV}} \right)^{-\alpha_\gamma} \left[\left(\frac{2E_\gamma}{m_{\pi^0} c^2} \right)^{\delta_\gamma} + \left(\frac{2E_\gamma}{m_{\pi^0} c^2} \right)^{-\delta_\gamma} \right]^{\frac{-\alpha_\gamma}{\delta_\gamma}} \quad (16.10)$$

$$\times \frac{dE_\gamma}{\text{GeV}} dV \quad (16.11)$$

where $\sigma_{pp} = 32 \times (0.96 + e^{4.4-2.4\alpha_\gamma})$ mbarn is the effective cross section for the pp-process, $\alpha_\gamma = 4.3(\alpha_p - 1/2)$ is the slope of the γ -ray spectrum and $\delta_\gamma = 0.14\alpha_\gamma^{-1.6} + 0.44$ is the shape parameter. The CR proton number density \tilde{n}_{CR} relates to the thermal energy density ϵ_{th} via Eq. 8 in Pfrommer & Enßlin (2004) as

$$\tilde{n}_{\text{CR}} = X_{\text{cr}} \epsilon_{\text{th}} \frac{2(\alpha_p - 1)}{m_p c^2} \left(\frac{m_p c^2}{\text{GeV}} \right)^{\alpha_p - 1} \left[\mathcal{B} \left(\frac{\alpha_p - 2}{2}, \frac{3 - \alpha_p}{2} \right) \right]^{-1} \quad (16.12)$$

where $\mathcal{B}(x, y)$ is the beta-function.

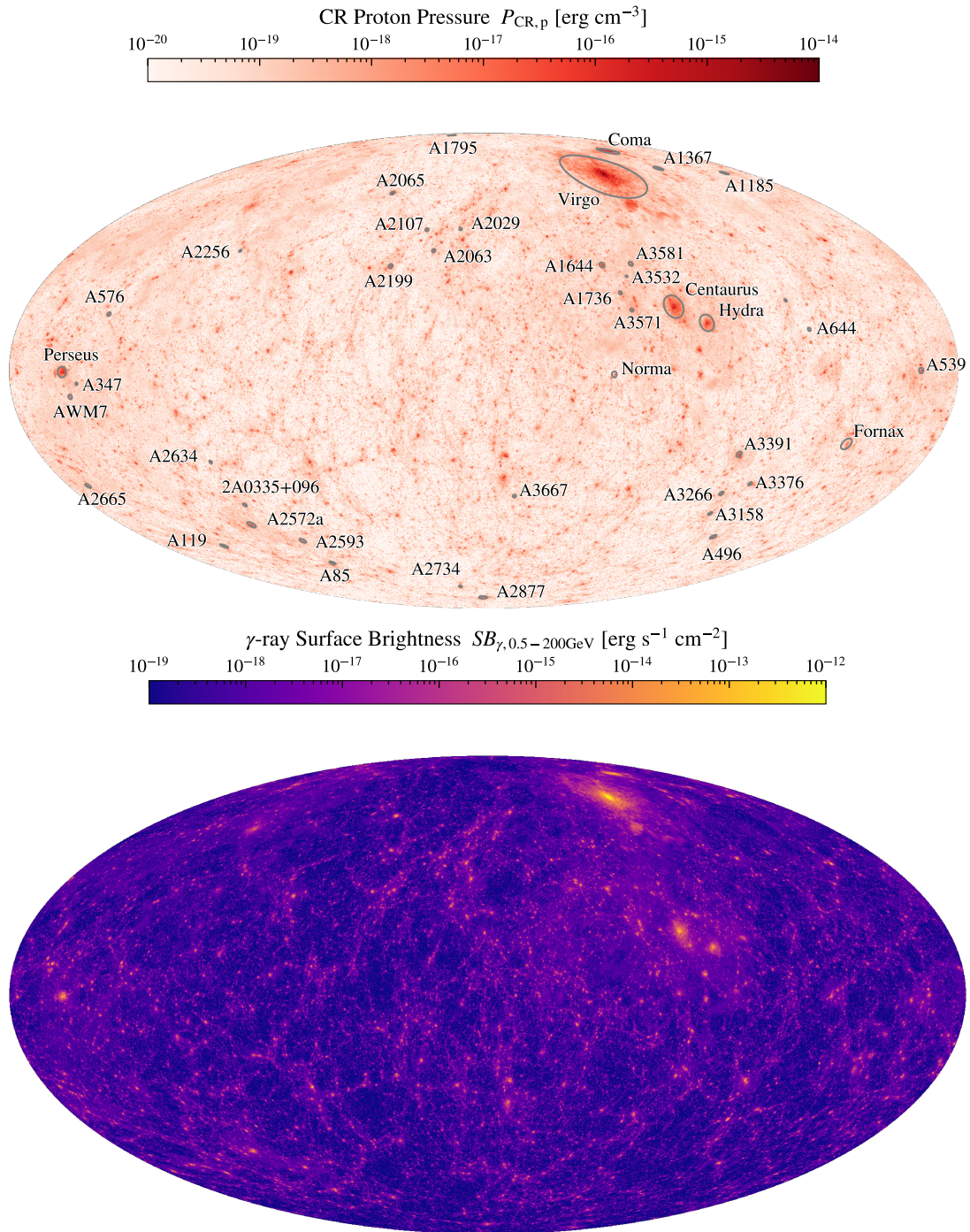


Figure 16.1: *Top*: Full-sky projection of the CR proton pressure component as the mean value along the line of sight between $r = 10 - 300$ Mpc. This shows predominantly the total injected proton component with adiabatic compression as it settles into the higher-density regions of clusters and filaments. Circles indicate the projected r_{vir} of each of the labeled cluster matches. *Bottom*: γ -ray surface brightness obtained by integrating over the CR proton spectra according to Eq. 16.8 in the Fermi-LAT band $E_{\gamma} \in [0.5 - 200]$ GeV.

16.3 Full-Sky Projections

As in Chapter 15 we will first focus on the morphological analysis of the results. For this, we again mapped the simulation output on a HEALPIX sphere (Górski et al., 2005) following the algorithm described in Dolag et al. (2005a). We chose the same observer view as in Dolag et al. (2023b) to match the position of the simulated and observed clusters in our full sky projection as closely as possible. Full-sky projections are performed for the output at $z = 0$.

16.3.1 Cosmic Ray Protons

Cosmic Ray protons experience hardly any energy losses in the environments of galaxy clusters and cosmic web filaments. The main energy loss mechanism for the overall energy density of CR protons are Coulomb losses due to interaction with the background thermal gas. This naturally scales with density and is therefore of little importance in the extremely low-density environment of cosmic web filaments. Even in GCs the cooling time of low-momentum protons is of the order of the Hubble time (e.g. Blasi et al., 2007) and therefore of little importance to the overall evolution of the proton spectra.

In Fig. 16.1 we show the mean CR proton pressure along the line-of-sight for the inner 300 Mpc of the simulation. We cut at this radius to avoid projection effects by the box corners. Labels indicate the cross-identified clusters from Hernandez et al. (in prep) and the circles indicate the projected virial radius of each cluster.

We find a population of CR protons injected by merger and accretion shocks in all cosmic structures. These protons then advect through the cluster and filament volume, setting into large halos and tracing the cosmic web filaments. In the galaxy cluster, we find populations of CR protons that extend up to the virial radius. Beyond that most, if not all, clusters show a faint halo of CRp even far beyond the virial radius, filling the volume between the virial radius and the virial shock, which has been pushed further from the virial radius by internal merger shocks (see Zhang et al., 2020a,b). The same holds for cosmic web filaments, where we find CR proton populations closely following the cosmological structure. As in the case of clusters we find extended regions of CR proton component around cosmic web filaments. A pronounced example of this can be found e.g. to the bottom-left of A2199 in the center of the image. We even find cases of visible shock acceleration, such as a shock to the left of Perseus, or a double shock to the top-left of A576 at the edge of the map.

16.3.2 Gamma-Ray Emission

As CR protons settle into high-density regions in the cluster center and filaments they can scatter with the thermal background protons and produce π^0 -ons. We model their surface brightness in the energy band observable by Fermi-LAT $E_\gamma \in [0.5 - 200]$ GeV in the lower panel of Fig. 16.1. Please note that this is the intrinsic surface brightness, not corrected for cosmological distance. This allows us to make estimates of relative brightness between peak emission in clusters and filaments in general and disregard the actual distance to the individual clusters.

In general, we find consistent central surface brightness for most of the visible galaxy clusters.

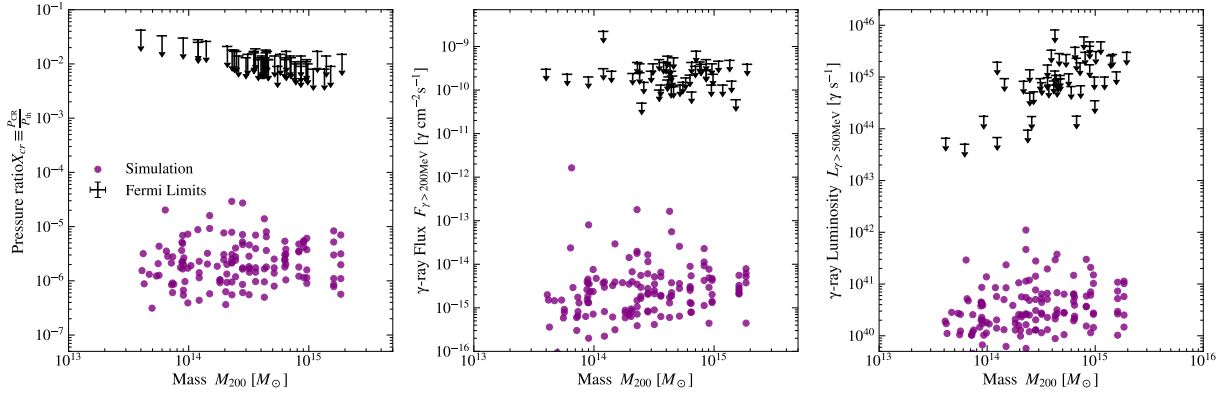


Figure 16.2: We show the results for the 150 most massive clusters in the simulation box with a virial mass $M_{\text{vir}} > 5 \times 10^{14} M_{\odot}$. *Left panel:* CR proton to thermal pressure ratio obtained in the momentum range $\hat{p} \in [0.1, 10^5]$. *Middle panel:* γ -ray flux obtained at the position of our point of view in Fig. 16.1 in the energy band $\gamma \in [0.5 - 200]$ GeV. *Right panel:* γ -ray luminosity in the same energy band.

They reach central values of $I_{\gamma} = 10^{-13} - 10^{-12} \text{ erg s}^{-1} \text{ cm}^{-2}$, which decreases by 2-3 orders of magnitude towards r_{vir} . Diffuse emission in filaments and around galaxy clusters lies 4-5 orders of magnitude below the central peak, making detection in this regime highly unlikely in the near future.

Also in γ -rays, we can see the effects of shock acceleration. This is especially evident in the shock in Perseus, to the left of the map. We will study the γ -ray emission from merger shocks in upcoming work, using higher resolution zoom-in initial conditions.

16.4 Fermi-LAT limits

In Fig. 16.2 we show the comparison of our simulation to the upper limits by [Ackermann et al. \(2014\)](#). The top panel shows the ratio between thermal pressure and CR proton pressure $X_{\text{cr}} = \frac{P_{\text{th}}}{P_{\text{CR,p}}}$. Please note that $P_{\text{CR,p}}$ can only be considered a lower limit, due to our approach of solving the distribution function in the ultra-relativistic limit. In the range of $\hat{p} \in [0.1, 1.0]$ this is not an exact approximation, leading to an under-estimate of the pressure (see discussion in [Girichidis et al., 2020](#)).

The lower panel shows the γ -ray flux as calculated at the same viewpoint used for the full-sky projections in [Dolag et al. \(2023b\)](#). We find that the flux is for most clusters 4.5-5 orders of magnitude below the upper limits found in [Pinzke et al. \(2011\)](#); [Ackermann et al. \(2014\)](#). The pressure ratio however is generally 3.5-4 orders of magnitude below the derived upper limits.

We find that the reason for this discrepancy is two-fold:

One reason is the numerical behavior of our shock finder. As discussed in Chapter 15, our shock finder is resolution limited at this resolution level. This means that we do not capture all shocks, especially in the low Mach number regime inside galaxy clusters. These shocks should contribute

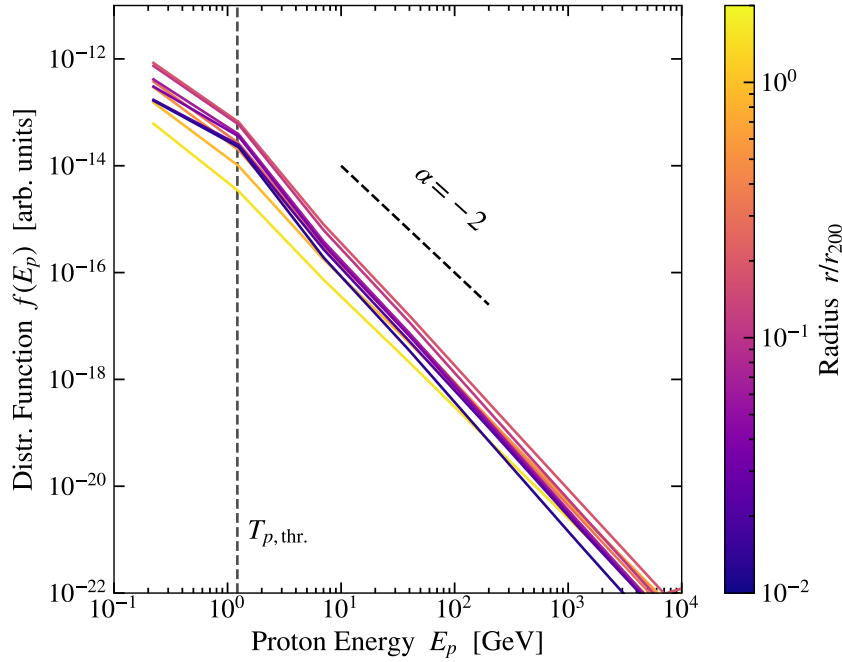


Figure 16.3: Mean distribution function in energy space, within our Coma cluster replica. We bin the spectra in 20 radial bins indicated by the different colors. The vertical dashed line indicates the threshold energy beyond which protons can be scattered into π^0 -ons.

significantly to the γ -ray emission in galaxy clusters, as the protons accelerated at these shocks can advect and diffuse/stream through the cluster volume. Since γ -ray emission scales linearly with density, observability is biased towards the denser ICM, rather than the WHIM where our shock finder performs better. In addition, due to our shock obliquity-dependent acceleration model and the bias towards high obliquity shocks due to the alignment of the magnetic field with the shock surface over the shock passage, we artificially suppress proton acceleration (see Fig. 15.11 in Chapter 15). We will discuss the impact of the shock finder performance on our findings in more detail in Sec. 16.6.1.

The second reason can be seen in Fig. 16.3. Here we show the distribution function of the protons in energy space, color-coded by their distance from the center. In this case for the example of our simulated Coma cluster replica.

We find flat spectra in the outskirts of the cluster seen in the bright yellow line, approaching a power law with index $\alpha = -2$. This stems from strong shocks in the cluster periphery, caused by accretion and outward-moving merger shocks. As we move further inside the cluster, shown with increasingly darker lines we observe two behaviors.

One, the spectra get steeper, since these protons have been accelerated by weaker shocks, typically $\mathcal{M}_s \sim 2-4$ in cluster centers (e.g. [Ryu et al., 2003](#); [Vazza et al., 2011](#); [Kang & Ryu, 2013](#); [Skillman et al., 2013](#); [Schaal & Springel, 2015](#); [Banfi et al., 2020](#)).

Second, the lowest energy bin flattens due to adiabatic compression and our closed lower boundary of the spectrum. This shifts protons to higher momentum bins, without allowing for an influx

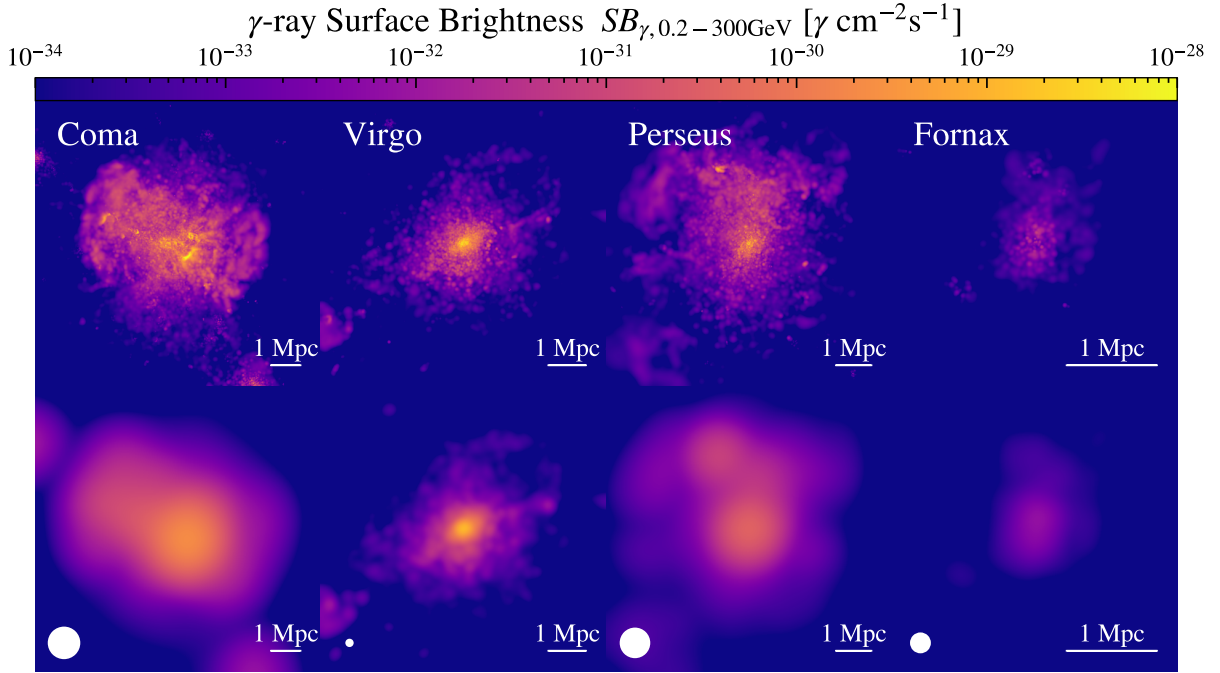


Figure 16.4: We show the γ -ray surface brightness for four prominent clusters. Each image has a width of $3r_{\text{vir}}$ of the respective cluster. The top panels show the simulation output. The bottom panels show the same images as above but smoothed with a Gaussian beam with the single photon angular resolution at 1 GeV of $\theta = 0.6^\circ$ of the Fermi-LAT instrument (Atwood et al., 2009). The white circle in the lower-left corner indicates the size of $\theta = 0.6^\circ$ at the observed redshift of the cluster.

of protons from the supra-thermal pool. With these steeper spectra, a larger fraction of the total energy density resides in the lower momentum bins. So less energy in these bins leads to significantly less total pressure. This is however independent of the γ -ray emission since the threshold energy for π^0 -on production as indicated by the horizontal dashed line lies at 1.22 GeV and with that beyond the flattened bin.

16.5 Coma, Virgo, Perseus and Fornax

Next, we want to focus on the γ -ray emission from the reproductions of Coma, Virgo, Perseus, and Fornax in our simulation.

16.5.1 Surface Brightness

In Fig. 16.4 we show the γ -ray surface brightness of our cluster replicas. We compute the surface brightness by integrating over Eq. 16.4 in the energy range $E_\gamma \in [0.2 - 300]$ GeV. Each panel has a width equivalent to $3r_{\text{vir}}$ of the respective cluster. The top panels show the clusters at the

resolution of the simulation. Bottom panels are smoothed with a Gaussian beam corresponding to the single photon angular resolution at 1 GeV of $\theta = 0.6^\circ$ of the Fermi-LAT instrument (Atwood et al., 2009). We show the size of this angle in the lower left corner of the images for the redshifts of the observed cluster counterparts.

Our Coma cluster is the dynamically most active of the four clusters shown. It is in the process of undergoing a 1:10 merger, driving two shocks in the horizontal direction. These shocks accelerate CR protons and exhibit γ -ray surface brightnesses roughly 3 orders of magnitude below the central peak. We also find evidence for CR acceleration at the center, due to small internal shocks, which show the highest surface brightness in Coma. Due to the angular resolution of Fermi-LAT, these structures would not be distinguishable however, as can be seen in the bottom panel.

Virgo on the other hand is a very relaxed cluster in our simulation, with no ongoing merger activity (see Lebeau et al., 2023, for a detailed study of our Virgo replica). This leads to a more peaked central emission, with a steeper decline in surface brightness towards the outskirts of the cluster.

Our Perseus replica is in the process of a minor merger with a large impact parameter, where a small sub-halo on a highly eccentric orbit drives a shock wave in Perseus' periphery (akin to the main merger geometry in Böss et al., 2023b). The shock can be seen to the top-left of the image, with the substructure driving the shock visible as the brightest peak to the top of the image. This ongoing merger activity leads to an overall more perturbed cluster and more extended γ -ray emission.

Fornax is the cluster of the four that shows the least γ -ray emission. This stems predominantly from the lower mass, which leads to weaker structure formation shocks, since in-falling substructure falls onto shallower potential wells, compared to the previous clusters. The Fornax replica in our simulation is also quite relaxed, without ongoing merger activity. This is another reason for the relative lack of γ -ray emission.

Nonetheless, we find that all clusters in our set exhibit at least some diffuse γ -ray emission in their ICM, which is tightly linked with their mass and dynamical state.

16.5.2 Spectra

In Fig. 16.5 we show the integrated flux spectra of our Coma, Virgo, Perseus, and Fornax cluster replica. The top panels show the flux spectrum, obtained by the particles and using the distance between cluster and viewpoint for the full-sky images. Solid lines show our results and error bars show observational upper limits, where available. For Coma, we compare to the results by Xi et al. (2018); Adam et al. (2021); Baghmany et al. (2022). Upper limits for Virgo are provided by Ackermann et al. (2015); H. E. S. S. Collaboration et al. (2023) and for Perseus by Aleksić et al. (2010, 2012); Cherenkov Telescope Array Consortium et al. (2023). Finally, for Fornax, we compare to observations by Ando & Nagai (2012) and the simulations by Pinzke et al. (2011). Dashed and dotted lines show the model by Pfrommer & Enßlin (2004) with a fixed $X_{\text{cr}} = 0.01$. Here dashed lines show the result for a proton energy spectrum with slope $\alpha_p = 2.5$, dotted lines with $\alpha_p = 2.4$, and dashed-dotted lines with $\alpha_p = 2.2$. The lower panels show the spectral slope of the γ -ray spectrum obtained between neighboring photon energy bins.

In general, we find a consistent picture to Fig. 16.2. Our spectra show fluxes four orders of

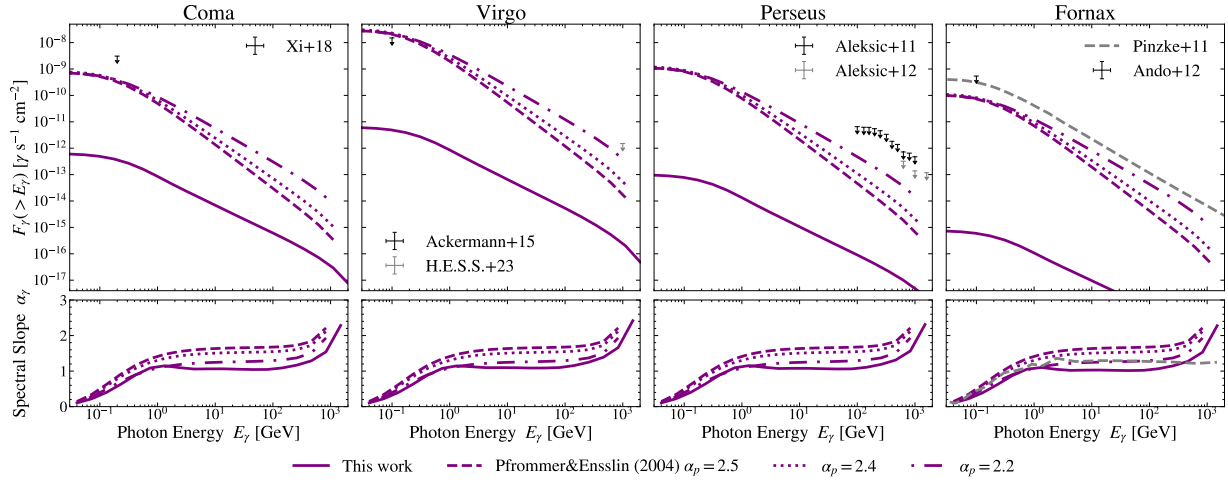


Figure 16.5: Integrated γ -ray spectra for our four selected clusters: Coma, Virgo, Perseus, and Fornax. Solid lines show our results, while arrows indicate the upper limits from observations, where available. Different dashed lines show the results from applying the model by [Pfrommer & Enßlin \(2004\)](#) for a fixed $X_{\text{CR}} = 0.01$ under varying proton energy slopes.

magnitude below the observational limits. Comparing to the [Pfrommer & Enßlin \(2004\)](#) model shows that this is partly driven by the distances of the cluster. With their model, we still lie one order of magnitude below the observational limit for Coma, while Virgo lies above the observational limit. We attribute this to the variance of the position of the replicated clusters, relative to the real clusters (see [Dolag et al., 2023b](#)), which naturally has a strong impact on the flux as it scales with the inverse distance squared.

Like [Pinzke et al. \(2011\)](#) we find a universal γ -ray slope, for energies above 1 GeV. We show their spectrum for the Fornax cluster as a gray dashed line in the right-most panel of Fig. 16.5. They find a spectral slope of the γ -ray flux which scales as $\alpha_\gamma \approx -1.2$, corresponding to a mean energy slope of $\alpha_p \approx 2.2$. This can also be seen in the corresponding [Pfrommer & Enßlin \(2004\)](#) line. In our simulation, we however find a spectral slope of the γ -ray flux of $\alpha_\gamma \approx -1$, which indicates a mean energy slope for the proton population of $\alpha_p \approx 2.0$. This is the limit for spectra accelerated by DSA. We attribute this again to the resolution limitations of our shock finder. As we showed in Chapter 15 and will discuss in Sec. 16.6.1 the resolution of the cosmological box is not sufficient to reliably capture low Mach number shocks in the ICM. We are instead biased to stronger shocks, which lead to flatter CR spectra.

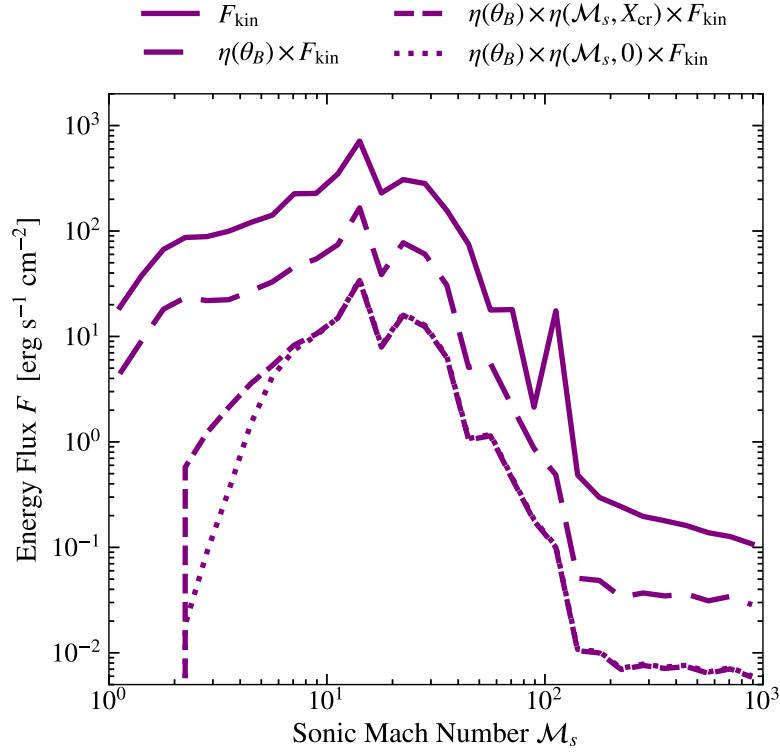


Figure 16.6: Histograms of the dissipated energy. The solid line shows the total kinetic energy flux as identified in the shock finder. The long dashed line shows the energy flux available for CR proton acceleration when accounting for the shock obliquity-dependent acceleration model $\eta(\theta_B)$. The short dashed line shows the energy flux available for CR acceleration when accounting for $\eta(\theta_B)$ and re-acceleration of protons as a function of the sonic Mach number. The dotted line shows the same as the dashed line when only accounting for the acceleration of protons from the thermal pool.

16.6 Discussion

16.6.1 Impact of shock finder accuracy

To illustrate the impact of the performance by our shock finder, we compute the dissipated energy available for CR proton acceleration as in [Ryu et al. \(2003\)](#)

$$F_{\text{CR}} = \eta(\mathcal{M}_s, X_{\text{cr}}, \theta_B) \times F_{\text{kin}} = \frac{1}{2} \eta(\mathcal{M}_s, X_{\text{cr}}, \theta_B) \rho_u v_s^3, \quad (16.13)$$

where v_s is the shock velocity, ρ_u the upstream density and $\eta(\mathcal{M}_s, X_{\text{cr}}, \theta_B)$ the acceleration efficiency. In Fig. 16.6 we show the histogram of dissipated energy as a function of sonic Mach number for the whole simulation domain. The solid line shows the total dissipated energy.

We find that due to resolution constraints, the shock finder does not capture all low Mach number

shocks in the clusters, as can be seen by the lower end of the histogram. Compared to work by [Ryu et al. \(2003\)](#); [Schaal & Springel \(2015\)](#); [Banfi et al. \(2020\)](#) we find that the dissipated energy decreases below $\mathcal{M}_s \sim 20$, while in the previous works the majority of the energy dissipated at shock lies in the range $\mathcal{M}_s \leq 5$. From their histograms, we estimate a factor of ~ 2 orders of magnitude under-prediction of the dissipated energy in this low Mach number range. This energy is dissipated in the code and heats the gas, it is just not necessarily captured by the shock finder, which leads to an under-injection of CR protons.

Another impact of the shock finder on our results is due to our inclusion of a shock obliquity-dependent efficiency model. As already discussed in Chapter 15, we find shock obliquities that are biased towards high obliquity shocks (see Fig. 15.11). This stems from the shock finder capturing a numerically broadened shock. As the shock propagates through the medium only the perpendicular component of the magnetic field is compressed, leading to an alignment of the shock surface and magnetic field vector. In our numerically broadened shock, we capture also the decaying flank of the Mach number distribution, in which the magnetic field is already preferentially aligned with the shock surface. This, together with our description for $\eta(\theta_B)$, leads to an artificial suppression of CR proton accelerations. As can be seen in the dashed line of Fig. 16.6, the mean value of $\eta(\theta_B) \sim 0.1 - 0.2$ reduces the available energy for CR proton acceleration by a factor 5-10.

16.6.2 Impact of CR injection parameters

As in Chapter 15 we want to briefly discuss the choice of CR injection parameters has on our results. For protons the relevant parameters are the injection momentum p_{inj} , the injection slope q_{inj} and the overall acceleration efficiency $\eta(\mathcal{M}_s, X_{\text{cr}}, \theta_B)$.

Injection Momentum \hat{p}_{inj}

For this work, we used a fixed injection momentum of $\hat{p}_{\text{inj}} = 0.1$. In other recent work (e.g. [Ha et al., 2020](#)) the injection momentum is computed on-the-fly as

$$\hat{p}_{\text{inj,p}} = \chi \frac{p_{\text{th,p}}}{m_p c} = 3.0 - 3.5 \frac{\sqrt{2k_B m_p T_2}}{m_p c} \quad (16.14)$$

where we used $\chi \approx 3.0-3.5$ from [Ryu et al. \(2019\)](#). Compared to the impact of p_{inj} on synchrotron emission the impact in γ -ray production is quite significant, as can be seen in Fig. 16.7. For strong shocks where $q \sim 4$ the difference between $p_{\text{inj}} = 0.01$ and $p_{\text{inj}} = 1$ only leads to a difference of half an order of magnitude in emissivity. This changes drastically, however, when considering shocks of $\mathcal{M}_s \approx 3$ and with that $q = 4.5$. These weak shocks are expected in the cluster periphery where they are visible as radio relics (see [van Weeren et al., 2019](#), for a recent review). At a slope of $q = 4.5$, we find a reduction of two orders of magnitude in emissivity for an equal reduction in p_{inj} . For $\mathcal{M}_s \approx 2$ shocks with $q = 5$ this discrepancy even increases to three orders of magnitude. As these CR protons are accelerated even further in the cluster center and can therefore advect in the cluster volume this has strong implications for the total γ -ray emission. We note however

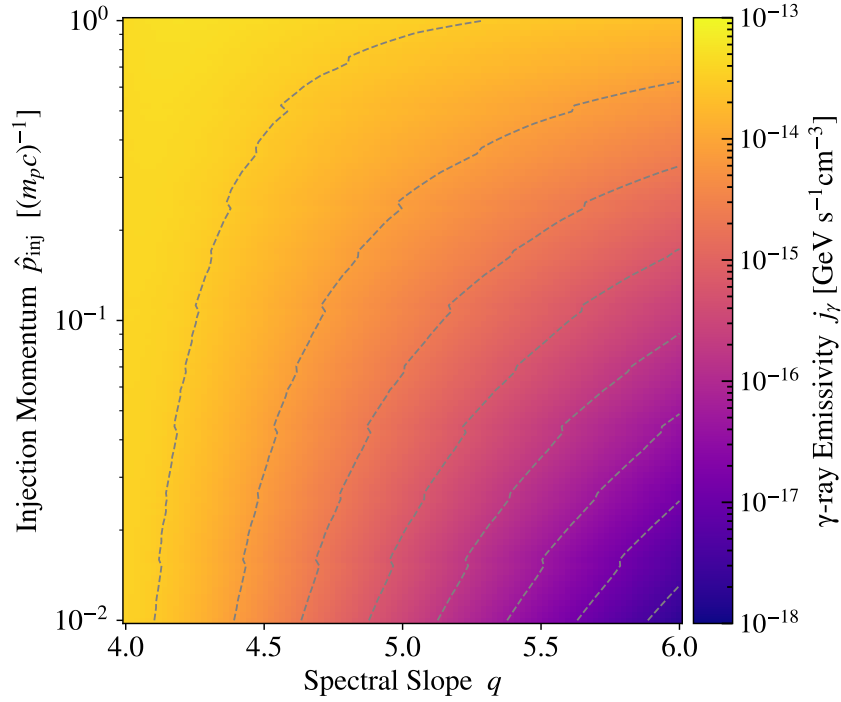


Figure 16.7: γ -ray emissivity as a function of spectral slope q and injection momentum \hat{p}_{inj} for a fixed total energy density in CR protons. The dashed lines show contours spaced by half an order of magnitude.

that our conservative approach to using a fixed injection momentum of $\hat{p}_{\text{inj}} = 0.1$ leads to an increased emission compared to typical values of \hat{p}_{inj} when computed directly from Eq. 16.14.

Injection Slope q_{inj}

The strong dependence of γ -ray emissivity on q also has implications for the parametrization of q_{inj} . As discussed in Chapter 15, in recent work by [Caprioli et al. \(2020\)](#) the authors find a magnetosonic post-cursor wave that can efficiently scatter particles from the shock acceleration region. The development of this wave depends on the ratio between downstream Alfvén velocity $v_{A,2}$ and downstream velocity u_2 and modifies q_{inj} to

$$q_{\text{inj}} = \frac{3r}{r - 1 - \alpha}; \quad \alpha \equiv \frac{v_{A,2}}{u_2} \quad (16.15)$$

where r is the shock compression ratio.

For the low Mach number shocks in the ICM, even small values for α with $\alpha \leq 0.2$ can have a significant impact on the injection slope. As can be seen in Fig. 16.7 for our fixed value of $\hat{p}_{\text{inj}} = 0.1$ a steepening of the spectrum by 0.5 or 1 leads to a decrease of half and order or one order of magnitude in emissivity, respectively.

However, this parametrization was found for low- β supernova shocks, which expand into a

medium that is vastly different than the high- β ICM considered here. There is currently no work in the literature that explores the dependence $q_{\text{inj}}(\alpha)$, however, preliminary studies show that for high- β shocks it may not be relevant (Damiano Caprioli, priv. communication).

Acceleration Efficiency $\eta(\mathcal{M}_s, X_{\text{cr}}, \theta_B)$

For this work, we employ the DSA parametrization of Kang & Ryu (2013), which shows a strong dependence on sonic Mach number \mathcal{M}_s for CR proton acceleration from the thermal pool. The re-acceleration efficiency is significantly larger, as can be seen, e.g. in Fig. 16.6, however, our injection model interpolates between acceleration and re-acceleration based on the value of X_{cr} currently in present in the SPH particle and the reference value for X_{cr} in the model, which in the case of Kang & Ryu (2013) is $X_{\text{cr}} = 0.05$. Since the initial acceleration from the thermal pool is so inefficient for low Mach number shocks, we rarely reach these values, as can be seen in the top panel of Fig. 16.2. This leads to our model being driven by initial acceleration, rather than re-acceleration. Especially for low Mach number shocks with $\mathcal{M}_s \sim 2-3$ this leads to a difference of one order of magnitude in acceleration efficiency, compared to the full re-acceleration case.

A more recent model by Ryu et al. (2019) for proton acceleration at quasi-parallel, low Mach number ($\mathcal{M}_s = 2.25 - 5$) and high- β shocks shows that the acceleration of protons from the thermal pool can be more efficient than assumed in the Kang & Ryu (2013) model. They also find a less significant difference between acceleration and re-acceleration.

However, the Ryu et al. (2019) model only allows for acceleration of particles beyond $\mathcal{M}_s = 2.25$, narrowing the range of available shocks to accelerate CRs slightly.

Previous work by Aleksić et al. (2010); Pinzke & Pfrommer (2010) use efficiency models that reach 50% at strong shocks and decreases to 4% at $\mathcal{M}_s \approx 1.7$ (Enßlin et al., 2007). Compared to our parametrization of the Kang & Ryu (2013) model this is a factor of 2.5 higher for strong shocks and one order of magnitude higher for weak shocks. Together with the shock obliquity-dependent acceleration model, which is absent in these works, this can account for a discrepancy of two orders of magnitude in γ -ray emission from CR protons accelerated at weak shocks in galaxy clusters.

16.6.3 Impact of Cosmic Ray Transport

The nature and velocity of CR transport in the ICM is still strongly under debate. The two most common flavors of CR transport are CR diffusion, where CRs propagate along magnetic field lines with a constant, or energy-dependent diffusion coefficient, or CR streaming where CRs stream down a CR pressure gradient with a streaming velocity v_{st} which generally depends on the magnetic field strength and density in the medium and is of the order of the Alfvén, or sound speed (see e.g. Enßlin et al., 2011, for a detailed discussion). With the long cooling times of CR protons, it can be expected that independent of the exact nature of these transport processes, CR protons will fill the entire cluster volume over the Hubble time.

Including CR transport in simulations adds a significant numerical challenge and cost (see Hanasz et al., 2021, for a recent review), which made it unfeasible for this large cosmological simulation. Due to the lagrangian nature of our simulation code, however, we automatically account for the

advection of CRs, which is expected to be the dominant transport process for low energy CR protons (Enßlin et al., 2011; Wiener et al., 2013, 2018; Reichherzer et al., 2023).

We expect the potential inclusion of streaming to reduce the γ -ray flux from the center of the cluster, as CR protons stream down the CR pressure gradient towards the cluster periphery.

The inclusion of diffusion could potentially impact the expected γ -ray emission, given that the diffusion coefficient is energy-dependent. Assuming that higher energy protons diffuse faster/easier would lead to a flattening of the CR proton spectrum away from acceleration zones (see e.g. Girichidis et al., 2020, for a study of the evolution of CR proton spectra under anisotropic, energy-dependent diffusion). This would naturally flatten the γ -ray spectrum as well.

However, full cosmological simulations of galaxy clusters, including anisotropic and energy-dependent diffusion are not computationally feasible as of yet. It could nonetheless hold interesting prospects for future work.

16.7 Conclusions

In this work, we showed results from the first constrained cosmological simulation with an on-the-fly spectral Cosmic Ray model to study the time evolution of CR protons in the local Cosmic Web. Our results can be summarized as follows:

- We find CR proton acceleration at structure formation and accretion shocks in galaxy clusters and cosmic web filaments.
- The CR protons advect through the cluster and filament volume and settle into halos extending to the virial radius of clusters.
- These protons produce volume-filling, diffuse γ -ray emission on cluster scales.
- Strong shocks produce γ -ray emission with surface brightnesses roughly two orders of magnitude below the central surface brightness.
- In general we find values for the CR to thermal pressure ratio (X_{cr}) four orders of magnitude below current estimates. This is however partly driven by a lack of resolution for the on-the-fly shock finder, which can account for a missing two orders of magnitude in detected dissipated energy at low Mach number shocks.
- This discrepancy in X_{cr} translates to our predictions for diffuse γ -ray flux and luminosity lying four orders of magnitude below the current Fermi-LAT limits.

Future work will have to address the resolution limitation of our shock finder by performing higher-resolution zoom-in simulations of individual clusters. This will also allow us to vary CR acceleration parameters to provide a more conclusive prediction for diffuse γ -ray emission from galaxy clusters.

Part IV

Outlook & Conclusion

17 | Outlook

In this chapter, we want to give a brief outlook on which parts of CRESCENDO need to be improved and extended to allow its application to more physical systems.

17.1 Ultra-Relativistic Limits

We currently solve the entire spectral evolution in the ultra-relativistic limit

$$T(p) = \sqrt{p^2 c^2 + m_i^2 c^4} - m_i c^2 \approx pc . \quad (17.1)$$

For CRs just beyond the injection momentum $\hat{p}_{\text{inj}} \approx 0.01 - 0.1$ this approximation does not hold, as mentioned multiple times throughout this work. As we have been primarily interested in synchrotron emission from CRes, most of the emission stems from electrons with $\hat{p} \approx 10^4$, where the relativistic limit holds. However, it introduces an error for the injection, as we inject power-laws in momentum space with a fixed total energy, typically starting in a momentum range where the relativistic limit does not hold.

For future work that also includes simulating CRs in an ISM environment where the kinematic impact of supra-thermal particles may be important, this simplification must be overcome.

We briefly outline upcoming work that needs to be done in Appendix A.2.

17.2 AGN jets

With the increased sensitivity of instruments like LOFAR it is possible to gain further observational insights into the interaction between the tails of radio galaxies and the turbulent ICM (see e.g. the study by [Edler et al., 2022](#)). These *gently reenergized tails (GReETs)* could be studied with our model, due to the already implemented turbulence model. With the upcoming state-of-the-art AGN spin-evolution model by Sala et al. (in prep) we have the potential to study not only time-, but also spatially variable AGN jets. By attaching a CR population to the SPH particles injected or kicked by the upcoming jet model we will be able to study observations like the stabilization of CRes in radio tails against cooling via turbulence in the ICM.

The Lagrangian nature of OPENGADGET3 will further allow us to study the interaction between seed-electrons injected by AGN feedback with subsequent merger shocks (see work by [Vazza et al., 2023](#)).

17.3 Odd Radio Circles

In [Dolag et al. \(2023a\)](#) we studied the origin of Odd Radio Circles (ORCs) from merger shocks in galaxy formation. For this, we used CRESCENDO in a post-processing mode on a high-resolution simulation with a very high snapshot output rate. While this high output rate helped alleviate some of the problems with the lack of information usually accompanying post-processing models it did not allow for capturing all shocks detected over the time-evolution of the simulation. This simulation was also purely hydrodynamic and did not include a magnetic field.

We aim to perform a simulation of ORC formation while using CRESCENDO on-the-fly to obtain more information on the underlying shock structure and allow for re-acceleration at subsequent shocks.

17.4 Radio Mega Halos

Possibly the most relevant work for cosmological simulations including CRs will be to explore the formation process of Radio Mega Halos ([Cuciti et al., 2022](#), see also Sec. 3.1.3). To the best of our knowledge, there is currently no simulation reported in the literature that models these Mega Halos self-consistently in a fully cosmological context (but see [Beduzzi et al., 2023](#), for an exploration of such modeling with a population of tracer-particles in a subset of the cluster volume).

To model these Mega Halos we will need to improve our treatment of CR re-acceleration by turbulence, or other processes (see e.g. [Tran et al., 2023](#)). We will further have to revisit acceleration efficiency models for CRs in high- β plasmas to increase the total CR seed population within the cluster volume.

Finally, we will need to improve our treatment of magnetic field amplification, via either implementing a Biermann battery or a subgrid model for magnetic field amplification at shocks (e.g. [Caprioli et al., 2009](#)), to counter the too steep radial decline of magnetic field strength we typically find in our simulations (see e.g. [Steinwandel et al., 2022](#)).

18 | Conclusion

In this work, we summarized the implementation of a new spectral Cosmic Ray model to study the impact of Cosmic Rays (CRs) on cosmological structure formation and non-thermal emission originating from the Large-Scale Structure (LSS) of the Universe.

We showed that we can model the injection of CR populations at shocks with state-of-the-art Diffusive Shock Acceleration (DSA) models that account for a dependence of the acceleration efficiency on sonic Mach number and magnetic field geometry. Their subsequent energy changes due to adiabatic changes of the surrounding gas, radiative energy losses, and turbulent re-acceleration are captured with high accuracy. From the aged CR populations we can recover observables such as the synchrotron emission of Cosmic Ray electrons (CRe) and γ -ray emission from π -on decay by Cosmic Ray protons (CRp) scattering off thermal background protons. Further, we have taken initial steps to include SNe as a source for CRs and have prepared a framework for anisotropic, momentum-dependent diffusion. This will allow us to apply our model to simulations of galaxy formation, once these parts of the model are finished and tested.

To validate our model in more realistic, but still idealized, simulations we performed a series of simulations of idealized Galaxy Cluster (GC) mergers (Böss et al., 2023c). This allowed us to reproduce key observables of radio relics, like the synchrotron spectrum and the steepening of the spectrum downstream of the shock due to the aging CRe populations. We were further able to obtain Cosmic Ray proton (CRp) populations in agreement with current γ -ray limits when employing the latest models for DSA and accounting for shock obliquity-dependent acceleration.

In Chapter 14 (and Böss et al., 2023b) we applied our CR model to a zoom-in simulation of a massive GC with unprecedented resolution, to study the complex interaction of CRs and merger shocks in a realistic GC. We found that Radio Relics (RRs) which are driven by merger shocks traveling outwards from the cluster center can be deformed by infalling substructure. These deformations can produce RR morphologies that are consistent with those of the recently discovered “Wrong Way Radio Relics”, allowing us to postulate a formation mechanism for these relics via colliding shock waves in clusters undergoing complex mergers.

We extended our application of CRESCENDO to a full cosmological volume by performing a simulation with a constrained initial condition, closely resembling the Local Universe in Chapter 15&16.

We analyzed the CRe component in Chapter 15 (also in Böss et al., 2023a) and found a considerable seed population of CRes within galaxy clusters and cosmic web filaments. Looking at the high-energy part of our CRe population we found the consistent acceleration of CRes at the accretion shocks of GCs and cosmic web filaments, providing the basis for diffuse synchrotron emission in these regimes. We then tested this under the assumption of different models for cosmic magnetic fields and obtained full-sky images of synchrotron emission from the local cosmic structure. To study the impact of resolution and turbulent re-acceleration we performed a number of zoom-in simulations of the Coma cluster and were able to make predictions of the diffuse synchrotron flux from cosmic web filaments connected to the Coma cluster. These limits lie 1-2 orders of magnitude below the current upper limits obtained from a non-detection by LOFAR. Due to the spectral nature of our CR model, we were also able to produce resolved spectral index maps of the diffuse emission around Coma, indicating synchrotron spectra with a slope $|\alpha| \approx 1 - 2$. This can motivate further observations at different radio frequencies. Finally, we discussed the impact of our choices of CR injection parameters. We found that in the case of the most optimistic parameter choices we obtain diffuse synchrotron emission just below the detection limit of current radio telescopes.

In Chapter 16 we then analyzed the CRp component to make predictions for the non-thermal pressure support in GCs from CRps and the diffuse γ -ray emission caused by the scattering of CRps off the thermal background plasma. As in the case of CRes we found populations of CRps in clusters and cosmic web filaments. We then modeled the γ -ray surface brightness and concluded that while we find γ -ray emission from both GCs and cosmic web filaments, the emission in filaments is four orders of magnitude below that of the cluster center, making direct detection highly unlikely for the foreseeable future. Subsequently, we analyzed the GCs found in our simulation and compared the CRp to thermal pressure ratio, γ -ray flux, and γ -ray luminosity to the current upper limits found with Fermi-LAT. Generally, our values lie 3-4 orders of magnitude below the current Fermi-LAT limits, which we attribute in part to the obliquity-dependent acceleration model and in part to the sub-optimal performance of our shock finder in the cluster center, where most of the γ -ray emission is expected. We then focused our analysis on our replicas of the Coma, Virgo, Perseus, and Fornax clusters, as they are the most likely candidates where diffuse γ -ray could be detected. As for the whole cluster sample, we find that the flux lies significantly below the observed values. We could again obtain spectra, this time of the γ -ray flux, and found a general spectral index of $\alpha_\gamma \approx -1$ in the photon energy range $E \in [1, 100]$ GeV. Finally, we again discussed the impact of our choice of CR injection parameters and found a potentially significant impact of the injection momentum p_{inj} and the injection slope q_{inj} on our results.

In general, we can conclude that we implemented a versatile and highly efficient CR model into the cosmological code `OPENGADGET3`. We have applied it to a broad range of systems in the LSS of the Universe to model non-thermal emission in GCs and cosmic web filaments with unprecedented fidelity. Future work with `CRESCENDO` will allow us to study the complex interaction between AGN jets and shocks in GCs, as well as gain insight into the origin of Radio Mega Halos and ORCs.

Bibliography

- Abdo, A. A., Ackermann, M., Ajello, M., et al. (2009), *Fermi Discovery of Gamma-ray Emission from NGC 1275*, *Astrophysical Journal*, 699(1), 31
- Ackermann, M., Ajello, M., Albert, A., et al. (2014), *Search for Cosmic-Ray-induced Gamma-Ray Emission in Galaxy Clusters*, *Astrophysical Journal*, 787(1), 18
- Ackermann, M., Ajello, M., Albert, A., et al. (2016), *Search for Gamma-Ray Emission from the Coma Cluster with Six Years of Fermi-LAT Data*, *Astrophysical Journal*, 819(2), 149
- Ackermann, M., Ajello, M., Albert, A., et al. (2015), *Search for Extended Gamma-Ray Emission from the Virgo Galaxy Cluster with FERMI-LAT*, *Astrophysical Journal*, 812(2), 159
- Ackermann, M., Ajello, M., Allafort, A., et al. (2013), *Detection of the Characteristic Pion-Decay Signature in Supernova Remnants*, *Science*, 339(6121), 807
- Adam, R., Goksu, H., Brown, S., et al. (2021), *γ -ray detection toward the Coma cluster with Fermi-LAT: Implications for the cosmic ray content in the hadronic scenario*, *Astronomy and Astrophysics*, 648, A60
- Adam, R., Goksu, H., Leingärtner-Goth, A., et al. (2020), *MINOT: Modeling the intracluster medium (non-)thermal content and observable prediction tools*, *Astronomy and Astrophysics*, 644, A70
- Agostinelli, S., Allison, J., Amako, K., et al. (2003), *G EANT4—a simulation toolkit*, *Nuclear Instruments and Methods in Physics Research A*, 506(3), 250
- Aguilar, M., Alberti, G., Alpat, B., et al. (2013), *First Result from the Alpha Magnetic Spectrometer on the International Space Station: Precision Measurement of the Positron Fraction in Primary Cosmic Rays of 0.5-350 GeV*, *Physical Review Letters*, 110(14), 141102
- Akamatsu, H., Fujita, Y., Akahori, T., et al. (2017), *Properties of the cosmological filament between two clusters: A possible detection of a large-scale accretion shock by Suzaku*, *Astronomy and Astrophysics*, 606, A1
- Akamatsu, H., van Weeren, R. J., Ogorean, G. A., et al. (2015), *Suzaku X-ray study of the double radio relic galaxy cluster CIZA J2242.8+5301*, *Astronomy and Astrophysics*, 582, A87

- Aleksić, J., Alvarez, E. A., Antonelli, L. A., et al. (2012), *Detection of very-high energy γ -ray emission from <ASTROBJ>NGC 1275</ASTROBJ> by the MAGIC telescopes*, *Astronomy and Astrophysics*, 539, L2
- Aleksić, J., Antonelli, L. A., Antoranz, P., et al. (2010), *MAGIC Gamma-ray Telescope Observation of the Perseus Cluster of Galaxies: Implications for Cosmic Rays, Dark Matter, and NGC 1275*, *Astrophysical Journal*, 710(1), 634
- Allen, G. E., Houck, J. C., and Sturmer, S. J. (2008), *Evidence of a Curved Synchrotron Spectrum in the Supernova Remnant SN 1006*, *Astrophysical Journal*, 683(2), 773
- Allison, J., Amako, K., Apostolakis, J., et al. (2006), *Geant4 developments and applications*, *IEEE Transactions on Nuclear Science*, 53(1), 270
- Alves Batista, R. and Saveliev, A. (2020), *Multimessenger Constraints on Intergalactic Magnetic Fields from the Flare of TXS 0506+056*, *Astrophysical Journal, Letters*, 902(1), L11
- Alves Batista, R. and Saveliev, A. (2021a), *The Gamma-Ray Window to Intergalactic Magnetism*, *Universe*, 7(7), 223
- Alves Batista, R. and Saveliev, A. (2021b), *The Gamma-Ray Window to Intergalactic Magnetism*, *Universe*, 7(7), 223
- Alves Batista, R., Saveliev, A., Sigl, G., and Vachaspati, T. (2016), *Probing intergalactic magnetic fields with simulations of electromagnetic cascades*, *Physical Review D*, 94(8), 083005
- Amano, T. and Hoshino, M. (2022), *Theory of Electron Injection at Oblique Shock of Finite Thickness*, *Astrophysical Journal*, 927(1), 132
- Ando, S. and Nagai, D. (2012), *Fermi-LAT constraints on dark matter annihilation cross section from observations of the Fornax cluster*, *Journal of Cosmology and Astroparticle Physics*, 2012(7), 017
- Andrade-Santos, F., Jones, C., Forman, W. R., et al. (2017), *The Fraction of Cool-core Clusters in X-Ray versus SZ Samples Using Chandra Observations*, *Astrophysical Journal*, 843(1), 76
- Angulo, R. E. and Hahn, O. (2022), *Large-scale dark matter simulations*, *Living Reviews in Computational Astrophysics*, 8(1), 1
- Arbey, A. and Mahmoudi, F. (2021), *Dark matter and the early Universe: A review*, *Progress in Particle and Nuclear Physics*, 119, 103865
- Arth, A., Dolag, K., Beck, A. M., et al. (2014), *Anisotropic thermal conduction in galaxy clusters with MHD in Gadget*, arXiv e-prints, arXiv:1412.6533
- Arth, A., Donnert, J., Steinwandel, U., et al. (2019), *WVTICs – SPH initial conditions for everyone*, arXiv e-prints, arXiv:1907.11250

- Atwood, W. B., Abdo, A. A., Ackermann, M., et al. (2009), *The Large Area Telescope on the Fermi Gamma-Ray Space Telescope Mission*, *Astrophysical Journal*, 697(2), 1071
- Bacchi, M., Feretti, L., Giovannini, G., and Govoni, F. (2003), *Deep images of cluster radio halos*, *Astronomy and Astrophysics*, 400, 465
- Baghmanyan, V., Zargaryan, D., Aharonian, F., et al. (2022), *Detailed study of extended γ -ray morphology in the vicinity of the Coma cluster with Fermi Large Area Telescope*, *Monthly Notices of the RAS*, 516(1), 562
- Balbus, S. A. and Potter, W. J. (2016), *Surprises in astrophysical gasdynamics*, *Reports on Progress in Physics*, 79(6), 066901
- Banfi, S., Vazza, F., and Wittor, D. (2020), *Shock waves in the magnetized cosmic web: the role of obliquity and cosmic ray acceleration*, *Monthly Notices of the RAS*, 496(3), 3648
- Barnes, J. and Hut, P. (1986), *A hierarchical $O(N \log N)$ force-calculation algorithm*, *Nature*, 324(6096), 446
- Beck, A. M., Dolag, K., and Donnert, J. M. F. (2016a), *Geometrical on-the-fly shock detection in smoothed particle hydrodynamics*, *Monthly Notices of the RAS*, 458(2), 2080
- Beck, A. M., Dolag, K., Lesch, H., and Kronberg, P. P. (2013), *Strong magnetic fields and large rotation measures in protogalaxies from supernova seeding*, *Monthly Notices of the RAS*, 435(4), 3575
- Beck, A. M., Murante, G., Arth, A., et al. (2016b), *An improved SPH scheme for cosmological simulations*, *Monthly Notices of the RAS*, 455(2), 2110
- Beck, R. (2015), *Magnetic fields in spiral galaxies*, *Astronomy and Astrophysics Reviews*, 24, 4
- Beduzzi, L., Vazza, F., Brunetti, G., et al. (2023), *On the origin of Mega Radiohalos*, arXiv e-prints, arXiv:2306.03764
- Bell, A. R. (1978a), *The acceleration of cosmic rays in shock fronts - I.*, *Monthly Notices of the RAS*, 182, 147
- Bell, A. R. (1978b), *The acceleration of cosmic rays in shock fronts - II.*, *Monthly Notices of the RAS*, 182, 443
- Bell, A. R. (2013), *Cosmic ray acceleration*, *Astroparticle Physics*, 43, 56
- Benson, B., Wittman, D. M., Golovich, N., et al. (2017), *MC²: A Deeper Look at ZwCl 2341.1+0000 with Bayesian Galaxy Clustering and Weak Lensing Analyses*, *Astrophysical Journal*, 841(1), 7
- Berlok, T., Pakmor, R., and Pfrommer, C. (2020), *Braginskii viscosity on an unstructured, moving mesh accelerated with super-time-stepping*, *Monthly Notices of the RAS*, 491(2), 2919

- Berlok, T., Quataert, E., Pessah, M. E., and Pfrommer, C. (2021), *Suppressed heat conductivity in the intracluster medium: implications for the magneto-thermal instability*, Monthly Notices of the RAS, 504(3), 3435
- Biermann, L. (1950), *Über den Ursprung der Magnetfelder auf Sternen und im interstellaren Raum (miteinem Anhang von A. Schlüter)*, Zeitschrift Naturforschung Teil A, 5, 65
- Biffi, V., ZuHone, J. A., Mroczkowski, T., et al. (2022), *The velocity structure of the intracluster medium during a major merger: simulated microcalorimeter observations*, arXiv e-prints, arXiv:2201.12370
- Blandford, R. D. and Ostriker, J. P. (1978), *Particle acceleration by astrophysical shocks.*, Astrophysical Journal, Letters, 221, L29
- Blasi, P. (2013), *The origin of galactic cosmic rays*, Astronomy and Astrophysics Reviews, 21, 70
- Blasi, P., Gabici, S., and Brunetti, G. (2007), *Gamma Rays from Clusters of Galaxies*, International Journal of Modern Physics A, 22(4), 681
- Bocquet, S., Saro, A., Mohr, J. J., et al. (2015), *Mass Calibration and Cosmological Analysis of the SPT-SZ Galaxy Cluster Sample Using Velocity Dispersion σ_v and X-Ray Y_X Measurements*, Astrophysical Journal, 799(2), 214
- Böhringer, H. and Werner, N. (2010), *X-ray spectroscopy of galaxy clusters: studying astrophysical processes in the largest celestial laboratories*, Astronomy and Astrophysics Reviews, 18(1-2), 127
- Bonafede, A., Brunetti, G., Rudnick, L., et al. (2022), *The Coma Cluster at LOFAR Frequencies. II. The Halo, Relic, and a New Accretion Relic*, Astrophysical Journal, 933(2), 218
- Bonafede, A., Brunetti, G., Vazza, F., et al. (2021), *The Coma Cluster at LOw Frequency ARray Frequencies. I. Insights into Particle Acceleration Mechanisms in the Radio Bridge*, Astrophysical Journal, 907(1), 32
- Bonafede, A., Cassano, R., Brüggem, M., et al. (2017), *On the absence of radio haloes in clusters with double relics*, Monthly Notices of the RAS, 470(3), 3465
- Bonafede, A., Dolag, K., Staszczyn, F., et al. (2011), *A non-ideal magnetohydrodynamic GADGET: simulating massive galaxy clusters*, Monthly Notices of the RAS, 418(4), 2234
- Bonafede, A., Feretti, L., Giovannini, G., et al. (2009a), *Revealing the magnetic field in a distant galaxy cluster: discovery of the complex radio emission from MACS J0717.5 +3745*, Astronomy and Astrophysics, 503(3), 707
- Bonafede, A., Feretti, L., Murgia, M., et al. (2010), *The Coma cluster magnetic field from Faraday rotation measures*, Astronomy and Astrophysics, 513, A30

- Bonafede, A., Giovannini, G., Feretti, L., et al. (2009b), *Double relics in Abell 2345 and Abell 1240. Spectral index and polarization analysis*, *Astronomy and Astrophysics*, 494(2), 429
- Bonafede, A., Vazza, F., Brüggén, M., et al. (2013), *Measurements and simulation of Faraday rotation across the Coma radio relic*, *Monthly Notices of the RAS*, 433(4), 3208
- Bonamente, M., Mirakhor, M., Lieu, R., and Walker, S. (2022), *A WHIM origin for the soft excess emission in the Coma cluster*, *Monthly Notices of the RAS*, 514(1), 416
- Bond, J. R., Kofman, L., and Pogosyan, D. (1996), *How filaments of galaxies are woven into the cosmic web*, *Nature*, 380(6575), 603
- Böss, L. M., Dolag, K., Steinwandel, U. P., et al. (2023a), *Simulating the Local Web (SLOW) – III: Synchrotron Emission from the Local Cosmic Web*, arXiv e-prints, arXiv:2310.13734
- Böss, L. M., Steinwandel, U. P., and Dolag, K. (2023b), *A Formation Mechanism for “Wrong Way” Radio Relics*, *Astrophysical Journal, Letters*, 957(2), L16
- Böss, L. M., Steinwandel, U. P., Dolag, K., and Lesch, H. (2023c), *CRESCENDO: an on-the-fly Fokker-Planck solver for spectral cosmic rays in cosmological simulations*, *Monthly Notices of the RAS*, 519(1), 548
- Botteon, A., Brunetti, G., Ryu, D., and Roh, S. (2020a), *Shock acceleration efficiency in radio relics*, *Astronomy and Astrophysics*, 634, A64
- Botteon, A., Brunetti, G., van Weeren, R. J., et al. (2020b), *The Beautiful Mess in Abell 2255*, *Astrophysical Journal*, 897(1), 93
- Botteon, A., Cassano, R., van Weeren, R. J., et al. (2021), *Discovery of a Radio Halo (and Relic) in a $M_{500} < 2 \times 10^{14} M_{\odot}$ Cluster*, *Astrophysical Journal, Letters*, 914(2), L29
- Botteon, A., Shimwell, T. W., Cassano, R., et al. (2022), *The Planck clusters in the LOFAR sky. I. LoTSS-DR2: New detections and sample overview*, *Astronomy and Astrophysics*, 660, A78
- Braginskii, S. I. (1965), *Transport Processes in a Plasma*, *Reviews of Plasma Physics*, 1, 205
- Brandenburg, A. and Subramanian, K. (2005), *Astrophysical magnetic fields and nonlinear dynamo theory*, *Physics Reports*, 417(1-4), 1
- Brentjens, M. A. and de Bruyn, A. G. (2005), *Faraday rotation measure synthesis*, *Astronomy and Astrophysics*, 441(3), 1217
- Brown, S. and Rudnick, L. (2011), *Diffuse radio emission in/around the Coma cluster: beyond simple accretion*, *Monthly Notices of the RAS*, 412(1), 2
- Brown, S., Vernstrom, T., Carretti, E., et al. (2017), *Limiting magnetic fields in the cosmic web with diffuse radio emission*, *Monthly Notices of the RAS*, 468(4), 4246

- Brüggen, M., Bykov, A., Ryu, D., and Röttgering, H. (2012), *Magnetic Fields, Relativistic Particles, and Shock Waves in Cluster Outskirts*, *Space Science Reviews*, 166(1-4), 187
- Brunetti, G. (2016), *The challenge of turbulent acceleration of relativistic particles in the intra-cluster medium*, *Plasma Physics and Controlled Fusion*, 58(1), 014011
- Brunetti, G., Cassano, R., Dolag, K., and Setti, G. (2009), *On the evolution of giant radio halos and their connection with cluster mergers*, *Astronomy and Astrophysics*, 507(2), 661
- Brunetti, G. and Jones, T. W. (2014), *Cosmic Rays in Galaxy Clusters and Their Nonthermal Emission*, *International Journal of Modern Physics D*, 23(4), 1430007
- Brunetti, G. and Lazarian, A. (2007), *Compressible turbulence in galaxy clusters: physics and stochastic particle re-acceleration*, *Monthly Notices of the RAS*, 378(1), 245
- Brunetti, G. and Lazarian, A. (2016), *Stochastic reacceleration of relativistic electrons by turbulent reconnection: a mechanism for cluster-scale radio emission?*, *Monthly Notices of the RAS*, 458(3), 2584
- Brunetti, G. and Vazza, F. (2020), *Second-order Fermi Reacceleration Mechanisms and Large-Scale Synchrotron Radio Emission in Intracluster Bridges*, *Physical Review Letters*, 124(5), 051101
- Bulbul, E., Chiu, I. N., Mohr, J. J., et al. (2019), *X-Ray Properties of SPT-selected Galaxy Clusters at $0.2 < z < 1.5$ Observed with XMM-Newton*, *Astrophysical Journal*, 871(1), 50
- Bulbul, E., Randall, S. W., Bayliss, M., et al. (2016), *Probing the Outskirts of the Early-Stage Galaxy Cluster Merger A1750*, *Astrophysical Journal*, 818(2), 131
- Burn, B. J. (1966), *On the depolarization of discrete radio sources by Faraday dispersion*, *Monthly Notices of the RAS*, 133, 67
- Butsky, I. S., Fielding, D. B., Hayward, C. C., et al. (2020), *The Impact of Cosmic Rays on Thermal Instability in the Circumgalactic Medium*, *Astrophysical Journal*, 903(2), 77
- Butsky, I. S. and Quinn, T. R. (2018), *The Role of Cosmic-ray Transport in Shaping the Simulated Circumgalactic Medium*, *Astrophysical Journal*, 868(2), 108
- Bykov, A. M., Vazza, F., Kropotina, J. A., et al. (2019), *Shocks and Non-thermal Particles in Clusters of Galaxies*, *Space Science Reviews*, 215(1), 14
- Caprioli, D., Blasi, P., Amato, E., and Vietri, M. (2009), *Dynamical feedback of self-generated magnetic fields in cosmic ray modified shocks*, *Monthly Notices of the RAS*, 395(2), 895
- Caprioli, D., Haggerty, C. C., and Blasi, P. (2020), *Kinetic Simulations of Cosmic-Ray-modified Shocks. II. Particle Spectra*, *Astrophysical Journal*, 905(1), 2

- Caprioli, D. and Spitkovsky, A. (2014), *Simulations of Ion Acceleration at Non-relativistic Shocks. I. Acceleration Efficiency*, *Astrophysical Journal*, 783(2), 91
- Caprioli, D., Zhang, H., and Spitkovsky, A. (2018), *Diffusive shock re-acceleration*, *Journal of Plasma Physics*, 84(3)
- Carilli, C. L. and Taylor, G. B. (2002), *Cluster Magnetic Fields*, *Annual Review of Astron and Astrophys*, 40, 319
- Carlesi, E., Hoffman, Y., Sorce, J. G., and Gottlöber, S. (2017), *Constraining the mass of the Local Group*, *Monthly Notices of the RAS*, 465(4), 4886
- Carlesi, E., Sorce, J. G., Hoffman, Y., et al. (2016), *Constrained Local UniversE Simulations: a Local Group factory*, *Monthly Notices of the RAS*, 458(1), 900
- Carretti, E., O'Sullivan, S., Vacca, V., et al. (2022), *Magnetic field evolution in cosmic filaments with LOFAR data*, *arXiv e-prints*, arXiv:2210.06220
- Cassano, R. and Brunetti, G. (2005), *Cluster mergers and non-thermal phenomena: a statistical magneto-turbulent model*, *Monthly Notices of the RAS*, 357(4), 1313
- Cassano, R., Ettori, S., Brunetti, G., et al. (2013), *Revisiting Scaling Relations for Giant Radio Halos in Galaxy Clusters*, *Astrophysical Journal*, 777(2), 141
- Cassano, R., Ettori, S., Giacintucci, S., et al. (2010), *On the Connection Between Giant Radio Halos and Cluster Mergers*, *Astrophysical Journal, Letters*, 721(2), L82
- Cavaliere, A. and Fusco-Femiano, R. (1976), *Reprint of 1976A&A...49..137C. X-rays from hot plasma in clusters of galaxies.*, *Astronomy and Astrophysics*, 500, 95
- Cen, R. and Ostriker, J. P. (1999), *Where Are the Baryons?*, *Astrophysical Journal*, 514(1), 1
- Chabrier, G. (2003), *Galactic Stellar and Substellar Initial Mass Function*, *Publications of the Astronomical Society of the Pacific*, 115(809), 763
- Chan, T. K., Keres, D., Gurvich, A. B., et al. (2021), *The impact of cosmic rays on dynamical balance and disk-halo interaction in Lstar disk galaxies*, *arXiv e-prints*, arXiv:2110.06231
- Chan, T. K., Kereš, D., Hopkins, P. F., et al. (2019), *Cosmic ray feedback in the FIRE simulations: constraining cosmic ray propagation with GeV γ -ray emission*, *Monthly Notices of the RAS*, 488(3), 3716
- Chen, W., Chowdhury, B. D., Ferrer, F., et al. (2015), *Intergalactic magnetic field spectra from diffuse gamma-rays*, *Monthly Notices of the RAS*, 450(4), 3371
- Cherenkov Telescope Array Consortium, T., :, Abe, K., et al. (2023), *Prospects for γ -ray observations of the Perseus galaxy cluster with the Cherenkov Telescope Array*, *arXiv e-prints*, arXiv:2309.03712

- Chibueze, J. O., Akamatsu, H., Parekh, V., et al. (2023), *MeerKAT's view of double radio relic galaxy cluster Abell 3376*, Publications of the ASJ, 75, S97
- Churazov, E., Brüggen, M., Kaiser, C. R., et al. (2001), *Evolution of Buoyant Bubbles in M87*, Astrophysical Journal, 554(1), 261
- Clarke, T. E., Kronberg, P. P., and Böhringer, H. (2001), *A New Radio-X-Ray Probe of Galaxy Cluster Magnetic Fields*, Astrophysical Journal, Letters, 547(2), L111
- Colless, M., Peterson, B. A., Jackson, C., et al. (2003), *The 2dF Galaxy Redshift Survey: Final Data Release*, arXiv e-prints, astro-ph/0306581
- Cristofari, P., Blasi, P., and Caprioli, D. (2021), *Cosmic ray protons and electrons from supernova remnants*, Astronomy and Astrophysics, 650, A62
- Cuciti, V., Cassano, R., Brunetti, G., et al. (2021a), *Radio halos in a mass-selected sample of 75 galaxy clusters. II. Statistical analysis*, Astronomy and Astrophysics, 647, A51
- Cuciti, V., Cassano, R., Brunetti, G., et al. (2021b), *Radio halos in a mass-selected sample of 75 galaxy clusters. I. Sample selection and data analysis*, Astronomy and Astrophysics, 647, A50
- Cuciti, V., Cassano, R., Sereno, M., et al. (2023), *The Planck clusters in the LOFAR sky V. LoTSS-DR2: Mass - radio halo power correlation at low frequency*, arXiv e-prints, arXiv:2305.04564
- Cuciti, V., de Gasperin, F., Brüggen, M., et al. (2022), *Galaxy clusters enveloped by vast volumes of relativistic electrons*, Nature, 609(7929), 911
- Cullen, L. and Dehnen, W. (2010), *Inviscid smoothed particle hydrodynamics*, Monthly Notices of the RAS, 408(2), 669
- Davé, R., Cen, R., Ostriker, J. P., et al. (2001), *Baryons in the Warm-Hot Intergalactic Medium*, Astrophysical Journal, 552(2), 473
- Davies, G. and Widrow, L. M. (2000), *A Possible Mechanism for Generating Galactic Magnetic Fields*, Astrophysical Journal, 540(2), 755
- Davis, M., Efstathiou, G., Frenk, C. S., and White, S. D. M. (1985), *The evolution of large-scale structure in a universe dominated by cold dark matter*, Astrophysical Journal, 292, 371
- de Gasperin, F., Rudnick, L., Finoguenov, A., et al. (2022), *MeerKAT view of the diffuse radio sources in Abell 3667 and their interactions with the thermal plasma*, Astronomy and Astrophysics, 659, A146
- de Gasperin, F., van Weeren, R. J., Brüggen, M., et al. (2014), *A new double radio relic in PSZ1 G096.89+24.17 and a radio relic mass-luminosity relation*, Monthly Notices of the RAS, 444(4), 3130

- de Hoffmann, F. and Teller, E. (1950), *Magneto-Hydrodynamic Shocks*, *Physical Review*, 80(4), 692
- Dehnen, W. and Aly, H. (2012), *Improving convergence in smoothed particle hydrodynamics simulations without pairing instability*, *Monthly Notices of the RAS*, 425(2), 1068
- Dermer, C. D. (1986), *Secondary production of neutral pi-mesons and the diffuse galactic gamma radiation*, *Astronomy and Astrophysics*, 157(2), 223
- Di Gennaro, G., van Weeren, R. J., Hoeft, M., et al. (2018), *Deep Very Large Array Observations of the Merging Cluster CIZA J2242.8+5301: Continuum and Spectral Imaging*, *Astrophysical Journal*, 865(1), 24
- Di Gennaro, G., van Weeren, R. J., Rudnick, L., et al. (2021), *Downstream Depolarization in the Sausage Relic: A 1-4 GHz Very Large Array Study*, *Astrophysical Journal*, 911(1), 3
- Diehl, S., Rockefeller, G., Fryer, C. L., et al. (2012), *Generating Optimal Initial Conditions for Smoothed Particle Hydrodynamics Simulations*, arXiv e-prints, arXiv:1211.0525
- Diesing, R. and Caprioli, D. (2021), *Steep Cosmic-Ray Spectra with Revised Diffusive Shock Acceleration*, *Astrophysical Journal*, 922(1), 1
- Dolag, K., Bartelmann, M., and Lesch, H. (1999), *SPH simulations of magnetic fields in galaxy clusters*, *Astronomy and Astrophysics*, 348, 351
- Dolag, K., Borgani, S., Murante, G., and Springel, V. (2009a), *Substructures in hydrodynamical cluster simulations*, *Monthly Notices of the RAS*, 399(2), 497
- Dolag, K., Borgani, S., Schindler, S., et al. (2008a), *Simulation Techniques for Cosmological Simulations*, *Space Science Reviews*, 134(1-4), 229
- Dolag, K., Böss, L. M., Koribalski, B. S., et al. (2023a), *Insights on the Origin of Odd Radio Circles from Cosmological Simulations*, *Astrophysical Journal*, 945(1), 74
- Dolag, K. and Enßlin, T. A. (2000), *Radio halos of galaxy clusters from hadronic secondary electron injection in realistic magnetic field configurations*, *Astronomy and Astrophysics*, 362, 151
- Dolag, K., Gaensler, B. M., Beck, A. M., and Beck, M. C. (2015), *Constraints on the distribution and energetics of fast radio bursts using cosmological hydrodynamic simulations*, *Monthly Notices of the RAS*, 451(4), 4277
- Dolag, K., Grasso, D., Springel, V., and Tkachev, I. (2004), *Mapping Deflections of Ultrahigh Energy Cosmic Rays in Constrained Simulations of Extragalactic Magnetic Fields*, *Soviet Journal of Experimental and Theoretical Physics Letters*, 79, 583

- Dolag, K., Grasso, D., Springel, V., and Tkachev, I. (2005a), *Constrained simulations of the magnetic field in the local Universe and the propagation of ultrahigh energy cosmic rays*, *Journal of Cosmology and Astroparticle Physics*, 2005(1), 009
- Dolag, K., Hansen, F. K., Roncarelli, M., and Moscardini, L. (2005b), *The imprints of local superclusters on the Sunyaev-Zel'dovich signals and their detectability with Planck*, *Monthly Notices of the RAS*, 363(1), 29
- Dolag, K., Kachelriess, M., Ostapchenko, S., and Tomàs, R. (2011), *Lower Limit on the Strength and Filling Factor of Extragalactic Magnetic Fields*, *Astrophysical Journal, Letters*, 727(1), L4
- Dolag, K., Komatsu, E., and Sunyaev, R. (2016), *SZ effects in the Magneticum Pathfinder simulation: comparison with the Planck, SPT, and ACT results*, *Monthly Notices of the RAS*, 463(2), 1797
- Dolag, K., Reinecke, M., Gheller, C., and Imboden, S. (2008b), *Splotch: visualizing cosmological simulations*, *New Journal of Physics*, 10(12), 125006
- Dolag, K., Schindler, S., Govoni, F., and Feretti, L. (2001), *Correlation of the magnetic field and the intra-cluster gas density in galaxy clusters*, *Astronomy and Astrophysics*, 378, 777
- Dolag, K., Sorce, J. G., Pilipenko, S., et al. (2023b), *Simulating the Local Web (SLOW): I. Anomalies in the local density field*, arXiv e-prints, arXiv:2302.10960
- Dolag, K. and Stasyszyn, F. (2009), *An MHD GADGET for cosmological simulations*, *Monthly Notices of the RAS*, 398(4), 1678
- Dolag, K., Stasyszyn, F., Donnert, J., and Pakmor, R. (2009b), *Magnetic fields and cosmic rays in galaxy clusters and large scale structures*, in *Cosmic Magnetic Fields: From Planets, to Stars and Galaxies*, edited by K. G. Strassmeier, A. G. Kosovichev, J. E. Beckman, volume 259, 519–528
- Dolag, K., Vazza, F., Brunetti, G., and Tormen, G. (2005c), *Turbulent gas motions in galaxy cluster simulations: the role of smoothed particle hydrodynamics viscosity*, *Monthly Notices of the RAS*, 364(3), 753
- Dominguez-Fernandez, P., Brüggen, M., Vazza, F., et al. (2021), *Morphology of radio relics - I. What causes the substructure of synchrotron emission?*, *Monthly Notices of the RAS*, 500, 795
- Domínguez-Fernández, P., Brüggen, M., Vazza, F., et al. (2021), *Morphology of radio relics - II. Properties of polarized emission*, *Monthly Notices of the RAS*, 507(2), 2714
- Domínguez-Fernández, P., Vazza, F., Brüggen, M., and Brunetti, G. (2019), *Dynamical evolution of magnetic fields in the intracluster medium*, *Monthly Notices of the RAS*, 486(1), 623

- Donnert, J. and Brunetti, G. (2014), *An efficient Fokker-Planck solver and its application to stochastic particle acceleration in galaxy clusters*, Monthly Notices of the RAS, 443(4), 3564
- Donnert, J., Dolag, K., Brunetti, G., et al. (2010a), *Radio haloes from simulations and hadronic models - I. The Coma cluster*, Monthly Notices of the RAS, 401(1), 47
- Donnert, J., Dolag, K., Cassano, R., and Brunetti, G. (2010b), *Radio haloes from simulations and hadronic models - II. The scaling relations of radio haloes*, Monthly Notices of the RAS, 407(3), 1565
- Donnert, J., Dolag, K., Lesch, H., and Müller, E. (2009), *Cluster magnetic fields from galactic outflows*, Monthly Notices of the Royal Astronomical Society, 392(3), 1008
- Donnert, J., Vazza, F., Brüggem, M., and ZuHone, J. (2018), *Magnetic Field Amplification in Galaxy Clusters and Its Simulation*, Space Science Reviews, 214(8), 122
- Donnert, J. M. F. (2014), *Initial conditions for idealized clusters mergers, simulating 'El Gordo'*, Monthly Notices of the RAS, 438(3), 1971
- Donnert, J. M. F., Beck, A. M., Dolag, K., and Röttgering, H. J. A. (2017), *Simulations of the galaxy cluster CIZA J2242.8+5301 - I. Thermal model and shock properties*, Monthly Notices of the RAS, 471(4), 4587
- Donnert, J. M. F., Stroe, A., Brunetti, G., et al. (2016), *Magnetic field evolution in giant radio relics using the example of CIZA J2242.8+5301*, Monthly Notices of the RAS, 462(2), 2014
- Doumler, T., Courtois, H., Gottlöber, S., and Hoffman, Y. (2013a), *Reconstructing cosmological initial conditions from galaxy peculiar velocities - II. The effect of observational errors*, Monthly Notices of the RAS, 430(2), 902
- Doumler, T., Gottlöber, S., Hoffman, Y., and Courtois, H. (2013b), *Reconstructing cosmological initial conditions from galaxy peculiar velocities - III. Constrained simulations*, Monthly Notices of the RAS, 430(2), 912
- Doumler, T., Hoffman, Y., Courtois, H., and Gottlöber, S. (2013c), *Reconstructing cosmological initial conditions from galaxy peculiar velocities - I. Reverse Zeldovich Approximation*, Monthly Notices of the RAS, 430(2), 888
- Drury, L. O. (1983), *An introduction to the theory of diffusive shock acceleration of energetic particles in tenuous plasmas*, Reports on Progress in Physics, 46(8), 973
- Dubois, Y., Commerçon, B., Marcowith, A., and Brahim, L. (2019), *Shock-accelerated cosmic rays and streaming instability in the adaptive mesh refinement code Ramses*, Astronomy and Astrophysics, 631, A121
- Durrer, R. and Neronov, A. (2013), *Cosmological magnetic fields: their generation, evolution and observation*, Astronomy and Astrophysics Reviews, 21, 62

- Dursi, L. J. and Pfrommer, C. (2008), *Draping of Cluster Magnetic Fields over Bullets and Bubbles—Morphology and Dynamic Effects*, *Astrophysical Journal*, 677(2), 993
- Dwarakanath, K. S., Parekh, V., Kale, R., and George, L. T. (2018), *Twin radio relics in the nearby low-mass galaxy cluster Abell 168*, *Monthly Notices of the RAS*, 477(1), 957
- Eckert, D., Gaspari, M., Vazza, F., et al. (2017), *On the Connection between Turbulent Motions and Particle Acceleration in Galaxy Clusters*, *Astrophysical Journal, Letters*, 843(2), L29
- Eckert, D., Jauzac, M., Shan, H., et al. (2015), *Warm-hot baryons comprise 5-10 per cent of filaments in the cosmic web*, *Nature*, 528(7580), 105
- Eddington, A. S. (1916), *The distribution of stars in globular clusters*, *Monthly Notices of the RAS*, 76, 572
- Eidler, H. W., de Gasperin, F., Brunetti, G., et al. (2022), *Abell 1033: Radio halo and gently reenergized tail at 54 MHz*, *Astronomy and Astrophysics*, 666, A3
- Eilek, J. A. (1979), *Particle reacceleration in radio galaxies*, *The Astrophysical Journal*, 230, 373
- Einstein, A. (1916), *Die Grundlage der allgemeinen Relativitätstheorie*, *Annalen der Physik*, 354(7), 769
- Enßlin, T., Pfrommer, C., Miniati, F., and Subramanian, K. (2011), *Cosmic ray transport in galaxy clusters: implications for radio halos, gamma-ray signatures, and cool core heating*, *Astronomy and Astrophysics*, 527, A99
- Ensslin, T. A., Biermann, P. L., Klein, U., and Kohle, S. (1998), *Cluster radio relics as a tracer of shock waves of the large-scale structure formation*, *Astronomy and Astrophysics*, 332, 395
- Enßlin, T. A. and Brüggen, M. (2002), *On the formation of cluster radio relics*, *Monthly Notices of the RAS*, 331(4), 1011
- Enßlin, T. A., Pfrommer, C., Springel, V., and Jubelgas, M. (2007), *Cosmic ray physics in calculations of cosmological structure formation*, *Astronomy and Astrophysics*, 473(1), 41
- Ettori, S. and Fabian, A. C. (2000), *Chandra constraints on the thermal conduction in the intracluster plasma of A2142*, *Monthly Notices of the RAS*, 317(3), L57
- Evrard, A. E., Metzler, C. A., and Navarro, J. F. (1996), *Mass Estimates of X-Ray Clusters*, *Astrophysical Journal*, 469, 494
- Fabian, A. C., Walker, S. A., Russell, H. R., et al. (2016), *HST imaging of the dusty filaments and nucleus swirl in NGC4696 at the centre of the Centaurus Cluster*, *Monthly Notices of the RAS*, 461(1), 922

- Feretti, L., Fusco-Femiano, R., Giovannini, G., and Govoni, F. (2001), *The giant radio halo in Abell 2163*, *Astronomy and Astrophysics*, 373, 106
- Feretti, L. and Giovannini, G. (1998), *Diffuse radio emission in the Coma cluster*, in *Untangling Coma Berenices: A New Vision of an Old Cluster*, edited by A. Mazure, F. Casoli, F. Durret, D. Gerbal, 123
- Feretti, L., Giovannini, G., Govoni, F., and Murgia, M. (2012), *Clusters of galaxies: observational properties of the diffuse radio emission*, *Astronomy and Astrophysics Reviews*, 20, 54
- Fermi, E. (1949), *On the Origin of the Cosmic Radiation*, *Physical Review*, 75(8), 1169
- Fermi, E. (1950), *High Energy Nuclear Events*, *Progress of Theoretical Physics*, 5(4), 570
- Fielding, D. B., Tonnesen, S., DeFelippis, D., et al. (2020), *First Results from SMAUG: Uncovering the Origin of the Multiphase Circumgalactic Medium with a Comparative Analysis of Idealized and Cosmological Simulations*, *Astrophysical Journal*, 903(1), 32
- Forman, W., Jones, C., Churazov, E., et al. (2007), *Filaments, Bubbles, and Weak Shocks in the Gaseous Atmosphere of M87*, *Astrophysical Journal*, 665(2), 1057
- Gamow, G. (1946), *Expanding Universe and the Origin of Elements*, *Physical Review*, 70(7-8), 572
- Garaldi, E., Pakmor, R., and Springel, V. (2021), *Magnetogenesis around the first galaxies: the impact of different field seeding processes on galaxy formation*, *Monthly Notices of the Royal Astronomical Society*, 502(4), 5726
- Ge, C., Liu, R.-Y., Sun, M., et al. (2020), *Chandra and XMM-Newton observations of A2256: cold fronts, merger shocks, and constraint on the IC emission*, *Monthly Notices of the RAS*, 497(4), 4704
- Gendron-Marsolais, M., Hlavacek-Larrondo, J., van Weeren, R. J., et al. (2017), *Deep 230-470 MHz VLA observations of the mini-halo in the Perseus cluster*, *Monthly Notices of the RAS*, 469(4), 3872
- Ghizzardi, S., Rossetti, M., and Molendi, S. (2010), *Cold fronts in galaxy clusters*, *Astronomy and Astrophysics*, 516, A32
- Giacconi, R., Murray, S., Gursky, H., et al. (1972), *The Uhuru catalog of X-ray sources.*, *Astrophysical Journal*, 178, 281
- Giacintucci, S., Markevitch, M., Cassano, R., et al. (2017), *Occurrence of Radio Minihalos in a Mass-limited Sample of Galaxy Clusters*, *Astrophysical Journal*, 841(2), 71
- Ginzburg, V. L. and Syrovatskii, S. I. (1965), *Cosmic Magnetobremstrahlung (synchrotron Radiation)*, *Annual Review of Astron and Astrophys*, 3, 297

- Giovannini, G., Bonafede, A., Feretti, L., et al. (2009), *Radio halos in nearby ($z < 0.4$) clusters of galaxies*, *Astronomy and Astrophysics*, 507(3), 1257
- Giovannini, G., Feretti, L., Venturi, T., et al. (1993), *The Halo Radio Source Coma C and the Origin of Halo Sources*, *Astrophysical Journal*, 406, 399
- Girardi, M., Boschin, W., Gastaldello, F., et al. (2016), *A multiwavelength view of the galaxy cluster Abell 523 and its peculiar diffuse radio source*, *Monthly Notices of the RAS*, 456(3), 2829
- Girichidis, P., Naab, T., Walch, S., et al. (2016), *Launching Cosmic-Ray-driven Outflows from the Magnetized Interstellar Medium*, *Astrophysical Journal, Letters*, 816(2), L19
- Girichidis, P., Pfrommer, C., Hanasz, M., and Naab, T. (2020), *Spectrally resolved cosmic ray hydrodynamics - I. Spectral scheme*, *Monthly Notices of the RAS*, 491(1), 993
- Girichidis, P., Pfrommer, C., Pakmor, R., and Springel, V. (2022), *Spectrally resolved cosmic rays - II. Momentum-dependent cosmic ray diffusion drives powerful galactic winds*, *Monthly Notices of the RAS*, 510(3), 3917
- Girichidis, P., Werhahn, M., Pfrommer, C., et al. (2023), *Spectrally resolved cosmic rays – III. Dynamical impact and properties of the circumgalactic medium*, arXiv e-prints, arXiv:2303.03417
- Górski, K. M., Hivon, E., Banday, A. J., et al. (2005), *HEALPix: A Framework for High-Resolution Discretization and Fast Analysis of Data Distributed on the Sphere*, *Astrophysical Journal*, 622(2), 759
- Gould, R. J. (1972), *Energy loss of fast electrons and positrons in a plasma*, *Physica*, 60(1), 145
- Govoni, F., Dolag, K., Murgia, M., et al. (2010), *Rotation measures of radio sources in hot galaxy clusters*, *Astronomy and Astrophysics*, 522, A105
- Govoni, F., Murgia, M., Feretti, L., et al. (2005), *A2255: The first detection of filamentary polarized emission in a radio halo*, *Astronomy and Astrophysics*, 430, L5
- Govoni, F., Orrù, E., Bonafede, A., et al. (2019), *A radio ridge connecting two galaxy clusters in a filament of the cosmic web*, *Science*, 364(6444), 981
- Groth, F., Steinwandel, U. P., Valentini, M., and Dolag, K. (2023), *The cosmological simulation code OPENGADGET3 - implementation of meshless finite mass*, *Monthly Notices of the RAS*, 526(1), 616
- Guo, F. and Mathews, W. G. (2011), *Cosmic-ray-dominated AGN Jets and the Formation of X-ray Cavities in Galaxy Clusters*, *Astrophysical Journal*, 728(2), 121
- Guo, X., Sironi, L., and Narayan, R. (2014), *Non-thermal Electron Acceleration in Low Mach Number Collisionless Shocks. I. Particle Energy Spectra and Acceleration Mechanism*, *Astrophysical Journal*, 794(2), 153

- H. E. S. S. Collaboration, :, Aharonian, F., et al. (2023), *Constraining the cosmic-ray pressure in the inner Virgo Cluster using H.E.S.S. observations of M 87*, arXiv e-prints, arXiv:2305.09607
- Ha, J.-H., Kim, S., Ryu, D., and Kang, H. (2021), *Effects of Multiscale Plasma Waves on Electron Preacceleration at Weak Quasi-perpendicular Intracluster Shocks*, *Astrophysical Journal*, 915(1), 18
- Ha, J.-H., Ryu, D., and Kang, H. (2018a), *Properties of Merger Shocks in Merging Galaxy Clusters*, *Astrophysical Journal*, 857(1), 26
- Ha, J.-H., Ryu, D., and Kang, H. (2020), *Gamma-Ray and Neutrino Emissions due to Cosmic-Ray Protons Accelerated at Intracluster Shocks in Galaxy Clusters*, *Astrophysical Journal*, 892(2), 86
- Ha, J.-H., Ryu, D., and Kang, H. (2023), *Cosmic-Ray Acceleration and Nonthermal Radiation at Accretion Shocks in the Outer Regions of Galaxy Clusters*, *Astrophysical Journal*, 943(2), 119
- Ha, J.-H., Ryu, D., Kang, H., and van Marle, A. J. (2018b), *Proton Acceleration in Weak Quasi-parallel Intracluster Shocks: Injection and Early Acceleration*, *Astrophysical Journal*, 864(2), 105
- Hackstein, S., Vazza, F., Brüggén, M., et al. (2018), *Simulations of ultra-high energy cosmic rays in the local Universe and the origin of cosmic magnetic fields*, *Monthly Notices of the RAS*, 475(2), 2519
- Hanasz, M. and Lesch, H. (2003), *Incorporation of cosmic ray transport into the ZEUS MHD code. Application for studies of Parker instability in the ISM*, *Astronomy and Astrophysics*, 412, 331
- Hanasz, M., Strong, A. W., and Girichidis, P. (2021), *Simulations of cosmic ray propagation*, *Living Reviews in Computational Astrophysics*, 7(1), 2
- Helder, E. A., Vink, J., Bykov, A. M., et al. (2012), *Observational Signatures of Particle Acceleration in Supernova Remnants*, *Space Science Reviews*, 173(1-4), 369
- Hitomi Collaboration, Aharonian, F., Akamatsu, H., et al. (2016), *The quiescent intracluster medium in the core of the Perseus cluster*, *Nature*, 535(7610), 117
- Hitomi Collaboration, Aharonian, F., Akamatsu, H., et al. (2018), *Atmospheric gas dynamics in the Perseus cluster observed with Hitomi*, *Publications of the ASJ*, 70(2), 9
- Hoang, D. N., Brüggén, M., Botteon, A., et al. (2022), *Diffuse radio emission from non-Planck galaxy clusters in the LoTSS-DR2 fields*, *Astronomy and Astrophysics*, 665, A60
- Hoang, D. N., Brüggén, M., Zhang, X., et al. (2023), *A search for intercluster filaments with LOFAR and eROSITA*, *Monthly Notices of the RAS*, 523(4), 6320

- Hoang, D. N., Shimwell, T. W., Stroe, A., et al. (2017), *Deep LOFAR observations of the merging galaxy cluster CIZA J2242.8+5301*, Monthly Notices of the RAS, 471(1), 1107
- Hoang, D. N., Shimwell, T. W., van Weeren, R. J., et al. (2019), *Radio observations of the merging galaxy cluster Abell 520*, Astronomy and Astrophysics, 622, A20
- Hoefl, M. and Brüggén, M. (2007), *Radio signature of cosmological structure formation shocks*, Monthly Notices of the RAS, 375(1), 77
- Hoefl, M., Brüggén, M., Yepes, G., et al. (2008), *Diffuse radio emission from clusters in the MareNostrum Universe simulation*, Monthly Notices of the RAS, 391(4), 1511
- Hoekstra, H., Bartelmann, M., Dahle, H., et al. (2013), *Masses of Galaxy Clusters from Gravitational Lensing*, Space Science Reviews, 177(1-4), 75
- Hoffman, Y. and Ribak, E. (1991), *Constrained Realizations of Gaussian Fields: A Simple Algorithm*, Astrophysical Journal, Letters, 380, L5
- Hong, S. E., Kang, H., and Ryu, D. (2015a), *Radio and X-Ray Shocks in Clusters of Galaxies*, Astrophysical Journal, 812(1), 49
- Hong, S. E., Kang, H., and Ryu, D. (2015b), *Radio and X-Ray Shocks in Clusters of Galaxies*, Astrophysical Journal, 812(1), 49
- Hong, S. E., Ryu, D., Kang, H., and Cen, R. (2014a), *Shock Waves and Cosmic Ray Acceleration in the Outskirts of Galaxy Clusters*, Astrophysical Journal, 785(2), 133
- Hong, S. E., Ryu, D., Kang, H., and Cen, R. (2014b), *Shock Waves and Cosmic Ray Acceleration in the Outskirts of Galaxy Clusters*, Astrophysical Journal, 785(2), 133
- Hopkins, P. F. (2013), *A general class of Lagrangian smoothed particle hydrodynamics methods and implications for fluid mixing problems*, Monthly Notices of the RAS, 428(4), 2840
- Hopkins, P. F., Butsky, I. S., Panopoulou, G. V., et al. (2022a), *First predicted cosmic ray spectra, primary-to-secondary ratios, and ionization rates from MHD galaxy formation simulations*, Monthly Notices of the RAS, 516(3), 3470
- Hopkins, P. F., Chan, T. K., Squire, J., et al. (2021), *Effects of different cosmic ray transport models on galaxy formation*, Monthly Notices of the Royal Astronomical Society, 501(3), 3663
- Hopkins, P. F., Squire, J., and Butsky, I. S. (2022b), *A consistent reduced-speed-of-light formulation of cosmic ray transport valid in weak- and strong-scattering regimes*, Monthly Notices of the RAS, 509(3), 3779
- Hu, C.-Y., Naab, T., Walch, S., et al. (2014), *SPHGal: smoothed particle hydrodynamics with improved accuracy for galaxy simulations*, Monthly Notices of the RAS, 443(2), 1173

- Hubble, E. (1929), *A Relation between Distance and Radial Velocity among Extra-Galactic Nebulae*, Proceedings of the National Academy of Science, 15(3), 168
- HyeonHan, K., Jee, M. J., Rudnick, L., et al. (2020), *Discovery of a Radio Relic in the Massive Merging Cluster SPT-CL J2023-5535 from the ASKAP-EMU Pilot Survey*, Astrophysical Journal, 900(2), 127
- Inchingolo, G., Wittor, D., Rajpurohit, K., and Vazza, F. (2022), *Radio relics radio emission from multishock scenario*, Monthly Notices of the RAS, 509(1), 1160
- Inogamov, N. A. and Sunyaev, R. A. (2003), *Turbulence in Clusters of Galaxies and X-ray Line Profiles*, Astronomy Letters, 29, 791
- Jarrett, T. H., Chester, T., Cutri, R., et al. (2003), *The 2MASS Large Galaxy Atlas*, Astronomical Journal, 125(2), 525
- Ji, S., Chan, T. K., Hummels, C. B., et al. (2020), *Properties of the circumgalactic medium in cosmic ray-dominated galaxy haloes*, Monthly Notices of the RAS, 496(4), 4221
- Johnston-Hollitt, M., Govoni, F., Beck, R., et al. (2015), *Using SKA Rotation Measures to Reveal the Mysteries of the Magnetised Universe*, in *Advancing Astrophysics with the Square Kilometre Array (AASKA14)*, 92
- Jones, F. C. and Ellison, D. C. (1991), *The plasma physics of shock acceleration*, Space Science Reviews, 58(1), 259
- Jones, T. and Kang, H. (2005), *An efficient numerical scheme for simulating particle acceleration in evolving cosmic-ray modified shocks*, Astroparticle Physics, 24(1), 75
- Jones, T. W., Ryu, D., and Engel, A. (1999), *Simulating Electron Transport and Synchrotron Emission in Radio Galaxies: Shock Acceleration and Synchrotron Aging in Axisymmetric Flows*, Astrophysical Journal, 512(1), 105
- Jubelgas, M., Springel, V., and Dolag, K. (2004), *Thermal conduction in cosmological SPH simulations*, Monthly Notices of the RAS, 351(2), 423
- Jubelgas, M., Springel, V., Enßlin, T., and Pfrommer, C. (2008), *Cosmic ray feedback in hydrodynamical simulations of galaxy formation*, Astronomy and Astrophysics, 481(1), 33
- Kafexhiu, E., Aharonian, F., Taylor, A. M., and Vila, G. S. (2014), *Parametrization of gamma-ray production cross sections for pp interactions in a broad proton energy range from the kinematic threshold to PeV energies*, Phys. Rev. D, 90, 123014
- Kang, H. (2020), *Semi-Analytic Models for Electron Acceleration in Weak ICM Shocks*, Journal of Korean Astronomical Society, 53, 59
- Kang, H. (2021), *Re-acceleration of Cosmic Ray Electrons by Multiple ICM Shocks*, arXiv e-prints, arXiv:2108.01876

- Kang, H. and Jones, T. W. (2007), *Self-similar evolution of cosmic-ray-modified quasi-parallel plane shocks*, *Astroparticle Physics*, 28(2), 232
- Kang, H. and Ryu, D. (2013), *Diffusive Shock Acceleration at Cosmological Shock Waves*, *Astrophysical Journal*, 764(1), 95
- Kang, H., Ryu, D., and Ha, J.-H. (2019), *Electron Preacceleration in Weak Quasi-perpendicular Shocks in High-beta Intracluster Medium*, *Astrophysical Journal*, 876(1), 79
- Kardashev, N. S. (1962), *Nonstationarity of Spectra of Young Sources of Nonthermal Radio Emission*, *Soviet Astronomy*, 6, 317
- Kim, C.-G., Ostriker, E. C., Somerville, R. S., et al. (2020), *First Results from SMAUG: Characterization of Multiphase Galactic Outflows from a Suite of Local Star-forming Galactic Disk Simulations*, *ApJ*, 900(1), 61
- Kobzar, O., Niemiec, J., Amano, T., et al. (2021), *Electron Acceleration at Rippled Low-mach-number Shocks in High-beta Collisionless Cosmic Plasmas*, *Astrophysical Journal*, 919(2), 97
- Kolmogorov, A. (1941), *The Local Structure of Turbulence in Incompressible Viscous Fluid for Very Large Reynolds' Numbers*, *Akademiia Nauk SSSR Doklady*, 30, 301
- Kolmogorov, A. N. (1991), *The Local Structure of Turbulence in Incompressible Viscous Fluid for Very Large Reynolds Numbers*, *Proceedings of the Royal Society of London Series A*, 434(1890), 9
- Koribalski, B. S., Norris, R. P., Andernach, H., et al. (2021), *Discovery of a new extragalactic circular radio source with ASKAP: ORC J0102-2450*, *Monthly Notices of the RAS*, 505(1), L11
- Krasnoselskikh, V., Balikhin, M., Walker, S. N., et al. (2013), *The Dynamic Quasiperpendicular Shock: Cluster Discoveries*, *Space Science Reviews*, 178(2-4), 535
- Kravtsov, A. V. and Borgani, S. (2012), *Formation of Galaxy Clusters*, *Annual Review of Astron and Astrophys*, 50, 353
- Krymskii, G. F. (1977), *A regular mechanism for the acceleration of charged particles on the front of a shock wave*, *Akademiia Nauk SSSR Doklady*, 234, 1306
- Kuchar, P. and Enßlin, T. A. (2011), *Magnetic power spectra from Faraday rotation maps. REALMAF and its use on Hydra A*, *Astronomy and Astrophysics*, 529, A13
- Kulsrud, R. and Pearce, W. P. (1969), *The Effect of Wave-Particle Interactions on the Propagation of Cosmic Rays*, *Astrophysical Journal*, 156, 445
- Kulsrud, R. M. (1999), *A Critical Review of Galactic Dynamos*, *Annual Review of Astron and Astrophys*, 37, 37

- Kulsrud, R. M. and Zweibel, E. G. (2008), *On the origin of cosmic magnetic fields*, Reports on Progress in Physics, 71(4), 046901
- Kunz, M. W., Jones, T. W., and Zhuravleva, I. (2022), *Plasma Physics of the Intracluster Medium*, in *Handbook of X-ray and Gamma-ray Astrophysics*, 56
- Lacki, B. C., Thompson, T. A., and Quataert, E. (2010), *The Physics of the Far-infrared-Radio Correlation. I. Calorimetry, Conspiracy, and Implications*, Astrophysical Journal, 717(1), 1
- Laing, R. A., Bridle, A. H., Parma, P., and Murgia, M. (2008), *Structures of the magnetoionic media around the Fanaroff-Riley Class I radio galaxies 3C31 and Hydra A*, Monthly Notices of the RAS, 391(2), 521
- Large, M. I., Mathewson, D. S., and Haslam, C. G. T. (1959), *A High-Resolution Survey of the Coma Cluster of Galaxies at 408 Mc/s.*, Nature, 183(4676), 1663
- Lazarian, A. (2009), *Obtaining Spectra of Turbulent Velocity from Observations*, Space Science Reviews, 143(1-4), 357
- Lebeau, T., Sorce, J. G., Aghanim, N., et al. (2023), *Mass bias in clusters of galaxies: Projection effects on the case study of Virgo replica*, arXiv e-prints, arXiv:2310.02326
- Lee, W., James Jee, M., Finner, K., et al. (2022), *Discovery of a Double Radio Relic in ZwCl1447.2+2619: A Rare Testbed for Shock-acceleration Models with a Peculiar Surface-brightness Ratio*, Astrophysical Journal, 924(1), 18
- Lee, W., Jee, M. J., Kang, H., et al. (2020), *Reconstruction of Radio Relics and X-Ray Tails in an Off-axis Cluster Merger: Hydrodynamical Simulations of A115*, Astrophysical Journal, 894(1), 60
- Lee, W., Pillepich, A., ZuHone, J., et al. (2023), *Radio relics in massive galaxy cluster mergers in the TNG-Cluster simulation*, arXiv e-prints, arXiv:2311.06340
- Lesch, H. and Birk, G. T. (1998), *Can large-scale magnetic fields survive during the pre-recombination era of the universe?*, Physics of Plasmas, 5(7), 2773
- Liang, H., Hunstead, R. W., Birkinshaw, M., and Andreani, P. (2000), *A Powerful Radio Halo in the Hottest Known Cluster of Galaxies 1E 0657-56*, Astrophysical Journal, 544(2), 686
- Locatelli, N., Vazza, F., Bonafede, A., et al. (2021), *New constraints on the magnetic field in cosmic web filaments*, Astronomy and Astrophysics, 652, A80
- Longair, M. S. (2011), *High Energy Astrophysics*
- MacDonald, J. and Mullan, D. J. (2004), *Magnetic fields in massive stars: dynamics and origin*, Monthly Notices of the RAS, 348(2), 702

- MAGIC Collaboration, Acciari, V. A., Agudo, I., et al. (2022), *A lower bound on intergalactic magnetic fields from time variability of 1ES 0229+200 from MAGIC and Fermi/LAT observations*, arXiv e-prints, arXiv:2210.03321
- Malavasi, N., Sorce, J. G., Dolag, K., and Aghanim, N. (2023), *The cosmic web around the Coma cluster from constrained cosmological simulations. I. Filaments connected to Coma at $z = 0$* , *Astronomy and Astrophysics*, 675, A76
- Mannheim, K. and Schlickeiser, R. (1994), *Interactions of cosmic ray nuclei*, *Astronomy and Astrophysics*, 286, 983
- Marcowith, A., van Marle, A. J., and Plotnikov, I. (2021), *The cosmic ray-driven streaming instability in astrophysical and space plasmas*, *Physics of Plasmas*, 28(8), 080601
- Marin-Gilabert, T., Valentini, M., Steinwandel, U. P., and Dolag, K. (2022), *The role of physical and numerical viscosity in hydrodynamical instabilities*, *Monthly Notices of the RAS*, 517(4), 5971
- Marinacci, F., Vogelsberger, M., Mocz, P., and Pakmor, R. (2015), *The large-scale properties of simulated cosmological magnetic fields*, *Monthly Notices of the RAS*, 453(4), 3999
- Marinacci, F., Vogelsberger, M., Pakmor, R., et al. (2018), *First results from the IllustrisTNG simulations: radio haloes and magnetic fields*, *Monthly Notices of the RAS*, 480(4), 5113
- Markevitch, M., Mazzotta, P., Vikhlinin, A., et al. (2003), *Chandra Temperature Map of A754 and Constraints on Thermal Conduction*, *Astrophysical Journal, Letters*, 586(1), L19
- Medvedev, M. V. and Loeb, A. (1999), *Generation of Magnetic Fields in the Relativistic Shock of Gamma-Ray Burst Sources*, *Astrophysical Journal*, 526(2), 697
- Mehlert, D., Seitz, S., Saglia, R. P., et al. (2001), *Gravitationally lensed high redshift galaxies in the field of 1E0657-56*, *Astronomy and Astrophysics*, 379, 96
- Menanteau, F., Hughes, J. P., Sifón, C., et al. (2012), *The Atacama Cosmology Telescope: ACT-CL J0102-4915 “El Gordo,” a Massive Merging Cluster at Redshift 0.87*, *Astrophysical Journal*, 748(1), 7
- Mimica, P., Aloy, M. A., Agudo, I., et al. (2009), *Spectral Evolution of Superluminal Components in Parsec-Scale Jets*, *Astrophysical Journal*, 696(2), 1142
- Miniati, F. (2001), *COSMOCR: A numerical code for cosmic ray studies in computational cosmology*, *Computer Physics Communications*, 141(1), 17
- Miniati, F. (2014), *The Matryoshka Run: A Eulerian Refinement Strategy to Study the Statistics of Turbulence in Virialized Cosmic Structures*, *Astrophysical Journal*, 782(1), 21

- Miniati, F., Jones, T. W., Kang, H., and Ryu, D. (2001), *Cosmic-Ray Electrons in Groups and Clusters of Galaxies: Primary and Secondary Populations from a Numerical Cosmological Simulation*, *Astrophysical Journal*, 562(1), 233
- Molnar, S. M. and Broadhurst, T. (2017), *Shocks and Tides Quantified in the “Sausage” Cluster, CIZA J2242.8+5301 Using N-body/Hydrodynamical Simulations*, *Astrophysical Journal*, 841(1), 46
- Molnar, S. M. and Broadhurst, T. (2018), *Multi-phenomena Modeling of the New Bullet-like Cluster ZwCl 008.8+52 Using N-body/Hydrodynamical Simulations*, *Astrophysical Journal*, 862(2), 112
- Morlino, G. and Caprioli, D. (2012), *Strong evidence for hadron acceleration in Tycho’s supernova remnant*, *Astronomy & Astrophysics*, 538, A81
- Morlino, G. and Celli, S. (2021), *Cosmic ray electrons released by supernova remnants*, *Monthly Notices of the RAS*, 508(4), 6142
- Mulcahy, D. D., Horneffer, A., Beck, R., et al. (2014), *The nature of the low-frequency emission of M 51. First observations of a nearby galaxy with LOFAR*, *Astronomy and Astrophysics*, 568, A74
- Naab, T. and Ostriker, J. P. (2017), *Theoretical Challenges in Galaxy Formation*, *Annual Review of Astron and Astrophys*, 55(1), 59
- Navarro, J. F., Frenk, C. S., and White, S. D. M. (1996), *The Structure of Cold Dark Matter Halos*, *Astrophysical Journal*, 462, 563
- Navarro, J. F., Frenk, C. S., and White, S. D. M. (1997), *A Universal Density Profile from Hierarchical Clustering*, *Astrophysical Journal*, 490(2), 493
- Nelson, D., Pillepich, A., Ayromlou, M., et al. (2023), *Introducing the TNG-Cluster Simulation: overview and physical properties of the gaseous intracluster medium*, arXiv e-prints, arXiv:2311.06338
- Neronov, A., Pol, A. R., Caprini, C., and Semikoz, D. (2021), *NANOGrav signal from magnetohydrodynamic turbulence at the QCD phase transition in the early Universe*, *Physical Review D*, 103(4), L041302
- Neronov, A. and Semikoz, D. V. (2007), *A method of measurement of extragalactic magnetic fields by TeV gamma ray telescopes*, *Soviet Journal of Experimental and Theoretical Physics Letters*, 85(10), 473
- Neronov, A. and Semikoz, D. V. (2009), *Sensitivity of γ -ray telescopes for detection of magnetic fields in the intergalactic medium*, *Physical Review D*, 80(12), 123012

- Nicastro, F., Krongold, Y., Mathur, S., and Elvis, M. (2017), *A decade of warm hot intergalactic medium searches: Where do we stand and where do we go?*, *Astronomische Nachrichten*, 338(281), 281
- Norris, R. P., Hopkins, A. M., Afonso, J., et al. (2011), *EMU: Evolutionary Map of the Universe*, *Publications of the Astron. Soc. of Australia*, 28(3), 215
- Norris, R. P., Intema, H. T., Kapińska, A. D., et al. (2021), *Unexpected circular radio objects at high Galactic latitude*, *Publications of the Astron. Soc. of Australia*, 38, e003
- Nuza, S. E., Gelszinnis, J., Hoeft, M., and Yepes, G. (2017), *Can cluster merger shocks reproduce the luminosity and shape distribution of radio relics?*, *Monthly Notices of the RAS*, 470(1), 240
- Oei, M. S. S. L., van Weeren, R. J., Vazza, F., et al. (2022), *Filamentary baryons and where to find them. A forecast of synchrotron radiation from merger and accretion shocks in the local Cosmic Web*, *Astronomy and Astrophysics*, 662, A87
- Ogrean, G. A., Brügger, M., van Weeren, R., et al. (2014), *Multiple density discontinuities in the merging galaxy cluster CIZA J2242.8+5301*, *Monthly Notices of the RAS*, 440(4), 3416
- Ogrodnik, M. A., Hanasz, M., and Wóltański, D. (2021), *Implementation of Cosmic Ray Energy Spectrum (CRESP) Algorithm in PIERNIK MHD Code. I. Spectrally Resolved Propagation of Cosmic Ray Electrons on Eulerian Grids*, *Astrophysical Journal, Supplement*, 253(1), 18
- Olchanski, M. and Sorce, J. G. (2018), *Merger types forming the Virgo cluster in recent gigayears*, *Astronomy and Astrophysics*, 614, A102
- O'Sullivan, S. P., Brügger, M., Vazza, F., et al. (2020), *New constraints on the magnetization of the cosmic web using LOFAR Faraday rotation observations*, *Monthly Notices of the RAS*, 495(3), 2607
- O'Sullivan, S. P., Machalski, J., Van Eck, C. L., et al. (2019), *The intergalactic magnetic field probed by a giant radio galaxy*, *Astronomy and Astrophysics*, 622, A16
- O'Sullivan, S. P., Shimwell, T. W., Hardcastle, M. J., et al. (2023), *The Faraday Rotation Measure Grid of the LOFAR Two-metre Sky Survey: Data Release 2*, *Monthly Notices of the RAS*, 519(4), 5723
- Owen, F. N., Rudnick, L., Eilek, J., et al. (2014), *Wideband Very Large Array Observations of A2256. I. Continuum, Rotation Measure, and Spectral Imaging*, *Astrophysical Journal*, 794(1), 24
- Pais, M., Pfrommer, C., Ehlert, K., and Pakmor, R. (2018), *The effect of cosmic ray acceleration on supernova blast wave dynamics*, *Monthly Notices of the RAS*, 478(4), 5278

- Pakmor, R., Marinacci, F., and Springel, V. (2014), *Magnetic Fields in Cosmological Simulations of Disk Galaxies*, *Astrophysical Journal, Letters*, 783(1), L20
- Parekh, V., Kincaid, R., Thorat, K., et al. (2022), *MOSS I: Double radio relics in the Saraswati supercluster*, *Monthly Notices of the RAS*, 509(2), 3086
- Pariev, V. I., Colgate, S. A., and Finn, J. M. (2007), *A Magnetic α - ω Dynamo in AGN Disks. II. Magnetic Field Generation, Theories, and Simulations*, *Astrophysical Journal*, 658(1), 129
- Park, J., Caprioli, D., and Spitkovsky, A. (2015), *Simultaneous Acceleration of Protons and Electrons at Nonrelativistic Quasiparallel Collisionless Shocks*, *Phys. Rev. Lett.*, 114(8), 085003
- Parker, E. N. (1955), *Hydromagnetic Dynamo Models.*, *Astrophysical Journal*, 122, 293
- Parrish, I. J., McCourt, M., Quataert, E., and Sharma, P. (2012), *The effects of anisotropic viscosity on turbulence and heat transport in the intracluster medium*, *Monthly Notices of the RAS*, 422(1), 704
- Pearce, C. J. J., van Weeren, R. J., Andrade-Santos, F., et al. (2017), *VLA Radio Observations of the HST Frontier Fields Cluster Abell 2744: The Discovery of New Radio Relics*, *Astrophysical Journal*, 845(1), 81
- Perrone, L. M., Berlok, T., and Pfrommer, C. (2023), *Does the magneto-thermal instability survive whistler-suppression of thermal conductivity in galaxy clusters?*, arXiv e-prints, arXiv:2311.02163
- Perrott, Y. C., Carvalho, P., Elwood, P. J., et al. (2021), *A 15.5 GHz detection of the galaxy cluster minihalo in RXJ1720.1+2638*, *Monthly Notices of the RAS*, 508(2), 2862
- Petkova, M. and Springel, V. (2009), *An implementation of radiative transfer in the cosmological simulation code GADGET*, *Monthly Notices of the RAS*, 396(3), 1383
- Pfrommer, C. (2008), *Simulating cosmic rays in clusters of galaxies - III. Non-thermal scaling relations and comparison to observations*, *Monthly Notices of the RAS*, 385(3), 1242
- Pfrommer, C. and Enßlin, T. A. (2004), *Constraining the population of cosmic ray protons in cooling flow clusters with γ -ray and radio observations: Are radio mini-halos of hadronic origin?*, *Astronomy and Astrophysics*, 413, 17
- Pfrommer, C., Enßlin, T. A., and Springel, V. (2008), *Simulating cosmic rays in clusters of galaxies - II. A unified scheme for radio haloes and relics with predictions of the γ -ray emission*, *Monthly Notices of the RAS*, 385(3), 1211
- Pfrommer, C., Enßlin, T. A., Springel, V., et al. (2007), *Simulating cosmic rays in clusters of galaxies - I. Effects on the Sunyaev-Zel'dovich effect and the X-ray emission*, *Monthly Notices of the RAS*, 378(2), 385

- Pfrommer, C., Pakmor, R., Schaal, K., et al. (2017), *Simulating cosmic ray physics on a moving mesh*, Monthly Notices of the RAS, 465(4), 4500
- Pfrommer, C., Springel, V., Enßlin, T. A., and Jubelgas, M. (2006), *Detecting shock waves in cosmological smoothed particle hydrodynamics simulations*, Monthly Notices of the RAS, 367(1), 113
- Pillepich, A., Springel, V., Nelson, D., et al. (2018), *Simulating galaxy formation with the IllustrisTNG model*, Monthly Notices of the RAS, 473(3), 4077
- Pinzke, A., Oh, S. P., and Pfrommer, C. (2013), *Giant radio relics in galaxy clusters: reacceleration of fossil relativistic electrons?*, Monthly Notices of the RAS, 435(2), 1061
- Pinzke, A., Oh, S. P., and Pfrommer, C. (2017), *Turbulence and particle acceleration in giant radio haloes: the origin of seed electrons*, Monthly Notices of the RAS, 465(4), 4800
- Pinzke, A. and Pfrommer, C. (2010), *Simulating the γ -ray emission from galaxy clusters: a universal cosmic ray spectrum and spatial distribution*, Monthly Notices of the RAS, 409(2), 449
- Pinzke, A., Pfrommer, C., and Bergström, L. (2011), *Prospects of detecting gamma-ray emission from galaxy clusters: Cosmic rays and dark matter annihilations*, Physical Review D, 84(12), 123509
- Plaga, R. (1995), *Detecting intergalactic magnetic fields using time delays in pulses of γ -rays*, Nature, 374(6521), 430
- Planck Collaboration, Ade, P. A. R., Aghanim, N., et al. (2014), *Planck 2013 results. XVI. Cosmological parameters*, Astronomy and Astrophysics, 571, A16
- Planck Collaboration, Aghanim, N., Akrami, Y., et al. (2020a), *Planck 2018 results. I. Overview and the cosmological legacy of Planck*, Astronomy and Astrophysics, 641, A1
- Planck Collaboration, Aghanim, N., Akrami, Y., et al. (2020b), *Planck 2018 results. VI. Cosmological parameters*, Astronomy and Astrophysics, 641, A6
- Pohl, M., Hoshino, M., and Niemiec, J. (2020), *PIC simulation methods for cosmic radiation and plasma instabilities*, Progress in Particle and Nuclear Physics, 111, 103751
- Ponnada, S. B., Panopoulou, G. V., Butsky, I. S., et al. (2023), *Synchrotron Emission on FIRE: Equipartition Estimators of Magnetic Fields in Simulated Galaxies with Spectrally-Resolved Cosmic Rays*, arXiv e-prints, arXiv:2309.04526
- Press, W. H. and Schechter, P. (1974), *Formation of Galaxies and Clusters of Galaxies by Self-Similar Gravitational Condensation*, Astrophysical Journal, 187, 425
- Price, D. J. (2012), *Smoothed particle hydrodynamics and magnetohydrodynamics*, Journal of Computational Physics, 231(3), 759

- Radiconi, F., Vacca, V., Battistelli, E., et al. (2022), *The thermal and non-thermal components within and between galaxy clusters Abell 399 and Abell 401*, Monthly Notices of the RAS, 517(4), 5232
- Ragagnin, A., Dolag, K., Wagner, M., et al. (2020), *Gadget3 on GPUs with OpenACC*, arXiv e-prints, arXiv:2003.10850
- Rajpurohit, K., Hoeft, M., Vazza, F., et al. (2020a), *New mysteries and challenges from the Toothbrush relic: wideband observations from 550 MHz to 8 GHz*, Astronomy and Astrophysics, 636, A30
- Rajpurohit, K., Hoeft, M., Wittor, D., et al. (2022a), *Turbulent magnetic fields in the merging galaxy cluster MACS J0717.5+3745*, Astronomy and Astrophysics, 657, A2
- Rajpurohit, K., van Weeren, R. J., Hoeft, M., et al. (2022b), *Deep Low-frequency Radio Observations of A2256. I. The Filamentary Radio Relic*, Astrophysical Journal, 927(1), 80
- Rajpurohit, K., Vazza, F., Hoeft, M., et al. (2020b), *A perfect power-law spectrum even at the highest frequencies: The Toothbrush relic*, Astronomy and Astrophysics, 642, L13
- Randall, S. W., Nulsen, P. E. J., Jones, C., et al. (2015), *A Very Deep Chandra Observation of the Galaxy Group NGC 5813: AGN Shocks, Feedback, and Outburst History*, Astrophysical Journal, 805(2), 112
- Reichherzer, P., Bott, A. F. A., Ewart, R. J., et al. (2023), *Efficient micromirror confinement of sub-TeV cosmic rays in galaxy clusters*, arXiv e-prints, arXiv:2311.01497
- Reimer, O., Pohl, M., Sreekumar, P., and Mattox, J. R. (2003), *EGRET Upper Limits on the High-Energy Gamma-Ray Emission of Galaxy Clusters*, Astrophysical Journal, 588(1), 155
- Richard-Laferrrière, A., Russell, H. R., Fabian, A. C., et al. (2023), *Constraints on thermal conductivity in the merging cluster Abell 2146*, Monthly Notices of the RAS, 526(4), 6205
- Riess, A. G., Nugent, P. E., Gilliland, R. L., et al. (2001), *The Farthest Known Supernova: Support for an Accelerating Universe and a Glimpse of the Epoch of Deceleration*, Astrophysical Journal, 560(1), 49
- Riseley, C. J., Bonnassieux, E., Vernstrom, T., et al. (2022), *Radio fossils, relics, and haloes in Abell 3266: cluster archaeology with ASKAP-EMU and the ATCA*, Monthly Notices of the RAS, 515(2), 1871
- Roettiger, K., Burns, J. O., and Stone, J. M. (1999), *A Cluster Merger and the Origin of the Extended Radio Emission in Abell 3667*, Astrophysical Journal, 518(2), 603
- Roncarelli, M., Gaspari, M., Etti, S., et al. (2018), *Measuring turbulence and gas motions in galaxy clusters via synthetic Athena X-IFU observations*, Astronomy and Astrophysics, 618, A39

- Rubin, V. C., Ford, W. K., J., and Thonnard, N. (1980), *Rotational properties of 21 SC galaxies with a large range of luminosities and radii, from NGC 4605 ($R=4\text{kpc}$) to UGC 2885 ($R=122\text{kpc}$)*, *Astrophysical Journal*, 238, 471
- Ruszkowski, M., Enßlin, T. A., Brüggén, M., et al. (2007), *Impact of tangled magnetic fields on fossil radio bubbles*, *Monthly Notices of the RAS*, 378(2), 662
- Ruszkowski, M. and Pfrommer, C. (2023), *Cosmic ray feedback in galaxies and galaxy clusters – A pedagogical introduction and a topical review of the acceleration, transport, observables, and dynamical impact of cosmic rays*, arXiv e-prints, arXiv:2306.03141
- Ruszkowski, M., Yang, H. Y. K., and Reynolds, C. S. (2017a), *Cosmic-Ray Feedback Heating of the Intracluster Medium*, *Astrophysical Journal*, 844(1), 13
- Ruszkowski, M., Yang, H. Y. K., and Zweibel, E. (2017b), *Global Simulations of Galactic Winds Including Cosmic-ray Streaming*, *Astrophysical Journal*, 834(2), 208
- Ruzmaikin, A. A., Sokolov, D. D., and Shukurov, A. M. (1988), *Magnetic Fields of Galaxies*, volume 133
- Rybicki, G. B. and Lightman, A. P. (1979), *Radiative processes in astrophysics*
- Ryu, D., Kang, H., and Ha, J.-H. (2019), *A Diffusive Shock Acceleration Model for Protons in Weak Quasi-parallel Intracluster Shocks*, *Astrophysical Journal*, 883(1), 60
- Ryu, D., Kang, H., Hallman, E., and Jones, T. W. (2003), *Cosmological Shock Waves and Their Role in the Large-Scale Structure of the Universe*, *Astrophysical Journal*, 593(2), 599
- Sanders, J. S., Biffi, V., Brüggén, M., et al. (2022), *Studying the merging cluster Abell 3266 with eROSITA*, *Astronomy and Astrophysics*, 661, A36
- Sanders, J. S., Fabian, A. C., Russell, H. R., et al. (2016a), *Detecting edges in the X-ray surface brightness of galaxy clusters*, *Monthly Notices of the RAS*, 460(2), 1898
- Sanders, J. S., Fabian, A. C., Taylor, G. B., et al. (2016b), *A very deep Chandra view of metals, sloshing and feedback in the Centaurus cluster of galaxies*, *Monthly Notices of the RAS*, 457(1), 82
- Sarazin, C. L. (1986), *X-ray emission from clusters of galaxies*, *Reviews of Modern Physics*, 58(1), 1
- Sarazin, C. L. (2002), *The Physics of Cluster Mergers*, in *Merging Processes in Galaxy Clusters*, edited by L. Feretti, I. M. Gioia, G. Giovannini, volume 272 of *Astrophysics and Space Science Library*, 1–38
- Sarkar, A., Randall, S., Su, Y., et al. (2022), *Discovery of a Premerger Shock in an Intercluster Filament in Abell 98*, *Astrophysical Journal, Letters*, 935(2), L23

- Sayers, J., Sereno, M., Etori, S., et al. (2021), *CLUMP-3D: the lack of non-thermal motions in galaxy cluster cores*, Monthly Notices of the RAS, 505(3), 4338
- Schaal, K. and Springel, V. (2015), *Shock finding on a moving mesh - I. Shock statistics in non-radiative cosmological simulations*, Monthly Notices of the RAS, 446(4), 3992
- Schaye, J., Kugel, R., Schaller, M., et al. (2023), *The FLAMINGO project: cosmological hydrodynamical simulations for large-scale structure and galaxy cluster surveys*, Monthly Notices of the RAS, 526(4), 4978
- Schekochihin, A. A. (2022), *MHD turbulence: a biased review*, Journal of Plasma Physics, 88(5), 155880501
- Schekochihin, A. A. and Cowley, S. C. (2006), *Turbulence, magnetic fields, and plasma physics in clusters of galaxies*, Physics of Plasmas, 13(5), 056501
- Schlickeiser, R. (2002), *Cosmic Ray Astrophysics*
- Schober, J., Schleicher, D. R. G., Federrath, C., et al. (2015), *Saturation of the turbulent dynamo*, Physical Review E, 92(2), 023010
- Schuecker, P., Finoguenov, A., Miniati, F., et al. (2004), *Probing turbulence in the Coma galaxy cluster*, Astronomy and Astrophysics, 426, 387
- Semenov, V. A., Kravtsov, A. V., and Diemer, B. (2021), *Entropy-Conserving Scheme for Modeling Nonthermal Energies in Fluid Dynamics Simulations*, arXiv e-prints, arXiv:2107.14240
- Shalaby, M., Lemmerz, R., Thomas, T., and Pfrommer, C. (2022), *The Mechanism of Efficient Electron Acceleration at Parallel Nonrelativistic Shocks*, Astrophysical Journal, 932(2), 86
- Shalaby, M., Thomas, T., and Pfrommer, C. (2021), *A New Cosmic-Ray-driven Instability*, Astrophysical Journal, 908(2), 206
- Shull, J. M., Smith, B. D., and Danforth, C. W. (2012), *The Baryon Census in a Multiphase Intergalactic Medium: 30% of the Baryons May Still be Missing*, Astrophysical Journal, 759(1), 23
- Sijacki, D., Pfrommer, C., Springel, V., and Enßlin, T. A. (2008), *Simulations of cosmic-ray feedback by active galactic nuclei in galaxy clusters*, Monthly Notices of the RAS, 387(4), 1403
- Sijacki, D. and Springel, V. (2006), *Physical viscosity in smoothed particle hydrodynamics simulations of galaxy clusters*, Monthly Notices of the RAS, 371(3), 1025
- Simionescu, A., ZuHone, J., Zhuravleva, I., et al. (2019), *Constraining Gas Motions in the Intra-Cluster Medium*, Space Science Reviews, 215(2), 24

- Skilling, J. (1975a), *Cosmic ray streaming - I. Effect of Alfvén waves on particles.*, Monthly Notices of the RAS, 172, 557
- Skilling, J. (1975b), *Cosmic ray streaming - II. Effect of particles on Alfvén waves.*, Monthly Notices of the RAS, 173, 245
- Skilling, J. (1975c), *Cosmic ray streaming - III. Self-consistent solutions.*, Monthly Notices of the RAS, 173, 255
- Skillman, S. W., Xu, H., Hallman, E. J., et al. (2013), *Cosmological Magnetohydrodynamic Simulations of Galaxy Cluster Radio Relics: Insights and Warnings for Observations*, Astrophysical Journal, 765(1), 21
- Smolinski, D. C., Wittor, D., Vazza, F., and Brüggén, M. (2023), *A multishock scenario for the formation of radio relics*, Monthly Notices of the RAS, 526(3), 4234
- Sod, G. A. (1978), *A survey of several finite difference methods for systems of nonlinear hyperbolic conservation laws*, Journal of Computational Physics, 27(1), 1
- Somerville, R. S. and Davé, R. (2015), *Physical Models of Galaxy Formation in a Cosmological Framework*, Annual Review of Astron and Astrophys, 53, 51
- Sorce, J. G. (2015), *Minimization of biases in galaxy peculiar velocity catalogues*, Monthly Notices of the RAS, 450(3), 2644
- Sorce, J. G. (2018), *Galaxy clusters in local Universe simulations without density constraints: a long uphill struggle*, Monthly Notices of the RAS, 478(4), 5199
- Sorce, J. G., Blaizot, J., and Dubois, Y. (2019), *Virgo: an unlikely cluster of galaxies because of its environment*, Monthly Notices of the RAS, 486(3), 3951
- Sorce, J. G., Courtois, H. M., Gottlöber, S., et al. (2014), *Simulations of the Local Universe constrained by observational peculiar velocities*, Monthly Notices of the RAS, 437(4), 3586
- Sorce, J. G., Gottlöber, S., Hoffman, Y., and Yepes, G. (2016), *How did the Virgo cluster form?*, Monthly Notices of the RAS, 460(2), 2015
- Sorce, J. G., Hoffman, Y., and Gottlöber, S. (2017), *Towards an optimal sampling of peculiar velocity surveys for Wiener Filter reconstructions*, Monthly Notices of the RAS, 468(2), 1812
- Sorce, J. G., Mohayaee, R., Aghanim, N., et al. (2023), *Velocity waves in the Hubble diagram: signature of local galaxy clusters*, arXiv e-prints, arXiv:2301.01305
- Sorce, J. G. and Tempel, E. (2017), *How does the grouping scheme affect the Wiener Filter reconstruction of the local Universe?*, Monthly Notices of the RAS, 469(3), 2859
- Sorce, J. G. and Tempel, E. (2018), *Galaxy clusters in simulations of the local Universe: a matter of constraints*, Monthly Notices of the RAS, 476(4), 4362

- Spitzer, Lyman, J. (1956a), *On a Possible Interstellar Galactic Corona.*, *Astrophysical Journal*, 124, 20
- Spitzer, L. (1956b), *Physics of Fully Ionized Gases*
- Spitzer, L. (1962), *Physics of Fully Ionized Gases*
- Springel, V. (2005), *The cosmological simulation code GADGET-2*, *Monthly Notices of the RAS*, 364(4), 1105
- Springel, V. and Farrar, G. R. (2007), *The speed of the ‘bullet’ in the merging galaxy cluster IE0657-56*, *Monthly Notices of the RAS*, 380(3), 911
- Springel, V., Frenk, C. S., and White, S. D. M. (2006), *The large-scale structure of the Universe*, *Nature*, 440(7088), 1137
- Springel, V. and Hernquist, L. (2002), *Cosmological smoothed particle hydrodynamics simulations: the entropy equation*, *Monthly Notices of the RAS*, 333(3), 649
- Springel, V. and Hernquist, L. (2003), *Cosmological smoothed particle hydrodynamics simulations: a hybrid multiphase model for star formation*, *Monthly Notices of the RAS*, 339(2), 289
- Springel, V., Pakmor, R., Pillepich, A., et al. (2018), *First results from the IllustrisTNG simulations: matter and galaxy clustering*, *Monthly Notices of the RAS*, 475(1), 676
- Springel, V., White, S. D. M., Jenkins, A., et al. (2005), *Simulations of the formation, evolution and clustering of galaxies and quasars*, *Nature*, 435(7042), 629
- Stasyszyn, F., Nuza, S. E., Dolag, K., et al. (2010), *Measuring cosmic magnetic fields by rotation measure-galaxy cross-correlations in cosmological simulations*, *Monthly Notices of the RAS*, 408(2), 684
- Stecker, F. W. (1970), *The Cosmic γ -Ray Spectrum from Secondary Particle Production in Cosmic-Ray Interactions*, *Astrophysics and Space Science*, 6(3), 377
- Stecker, F. W. (1971), *Cosmic gamma rays*, volume 249 of 1
- Steinwandel, U. P., Böss, L. M., Dolag, K., and Lesch, H. (2022), *On the Small-scale Turbulent Dynamo in the Intracluster Medium: A Comparison to Dynamo Theory*, *Astrophysical Journal*, 933(2), 131
- Steinwandel, U. P., Dolag, K., Böss, L., and Marin-Gilabert, T. (2023a), *Towards cosmological simulations of the magnetized intracluster medium with resolved Coulomb collision scale*, arXiv e-prints, arXiv:2306.04692

- Steinwandel, U. P., Dolag, K., Böss, L., and Marin-Gilabert, T. (2023b), *Towards cosmological simulations of the magnetized intracluster medium with resolved Coulomb collision scale*, arXiv e-prints, arXiv:2306.04692
- Steinwandel, U. P., Dolag, K., Lesch, H., et al. (2020a), *On the origin of magnetic driven winds and the structure of the galactic dynamo in isolated galaxies*, Monthly Notices of the RAS, 494(3), 4393
- Steinwandel, U. P. and Goldberg, J. A. (2023), *Some stars fade quietly: Varied Supernova explosion outcomes and their effects on the multi-phase interstellar medium*, arXiv e-prints, arXiv:2310.11495
- Steinwandel, U. P., Moster, B. P., Naab, T., et al. (2020b), *Hot phase generation by supernovae in ISM simulations: resolution, chemistry, and thermal conduction*, Monthly Notices of the RAS, 495(1), 1035
- Stephens, S. A. and Badhwar, G. D. (1981), *Production Spectrum of Gamma-Rays in Interstellar Space Through Neutral Pion Decay*, Astrophysics and Space Science, 76(1), 213
- Stroe, A., Harwood, J. J., Hardcastle, M. J., and Röttgering, H. J. A. (2014), *Spectral age modelling of the ‘Sausage’ cluster radio relic*, Monthly Notices of the RAS, 445(2), 1213
- Stroe, A., Shimwell, T., Rumsey, C., et al. (2016), *The widest frequency radio relic spectra: observations from 150 MHz to 30 GHz*, Monthly Notices of the RAS, 455(3), 2402
- Stroe, A., van Weeren, R. J., Intema, H. T., et al. (2013), *Discovery of spectral curvature in the shock downstream region: CIZA J2242.8+5301*, Astronomy and Astrophysics, 555, A110
- Struble, M. F. and Rood, H. J. (1999), *A Compilation of Redshifts and Velocity Dispersions for ACO Clusters*, Astrophysical Journal, Supplement, 125(1), 35
- Stuardi, C., Bonafede, A., Lovisari, L., et al. (2021), *The intracluster magnetic field in the double relic galaxy cluster Abell 2345*, Monthly Notices of the RAS, 502(2), 2518
- Stuardi, C., Bonafede, A., Rajpurohit, K., et al. (2022), *Using the polarization properties of double radio relics to probe the turbulent compression scenario*, Astronomy and Astrophysics, 666, A8
- Stuardi, C., Bonafede, A., Wittor, D., et al. (2019), *Particle re-acceleration and Faraday-complex structures in the RXC J1314.4-2515 galaxy cluster*, Monthly Notices of the RAS, 489(3), 3905
- Subramanian, K., Shukurov, A., and Haugen, N. E. L. (2006), *Evolving turbulence and magnetic fields in galaxy clusters*, Monthly Notices of the RAS, 366(4), 1437
- Sunyaev, R. A. and Zeldovich, Y. B. (1972), *The Observations of Relic Radiation as a Test of the Nature of X-Ray Radiation from the Clusters of Galaxies*, Comments on Astrophysics and Space Physics, 4, 173

- Tegmark, M., Strauss, M. A., Blanton, M. R., et al. (2004), *Cosmological parameters from SDSS and WMAP*, Physical Review D, 69(10), 103501
- Thierbach, M., Klein, U., and Wielebinski, R. (2003), *The diffuse radio emission from the Coma cluster at 2.675 GHz and 4.85 GHz*, Astronomy and Astrophysics, 397, 53
- Tornatore, L., Borgani, S., Dolag, K., and Matteucci, F. (2007), *Chemical enrichment of galaxy clusters from hydrodynamical simulations*, Monthly Notices of the RAS, 382(3), 1050
- Tran, A. and Sironi, L. (2020), *Electron Heating in Perpendicular Low-beta Shocks*, Astrophysical Journal, Letters, 900(2), L36
- Tran, A., Sironi, L., Ley, F., et al. (2023), *Electron Reacceleration via Ion Cyclotron Waves in the Intracluster Medium*, Astrophysical Journal, 948(2), 130
- Trasatti, M., Akamatsu, H., Lovisari, L., et al. (2015), *The radio relic in Abell 2256: overall spectrum and implications for electron acceleration*, Astronomy and Astrophysics, 575, A45
- Tully, R. B., Courtois, H. M., Dolphin, A. E., et al. (2013), *Cosmicflows-2: The Data*, Astronomical Journal, 146(4), 86
- Tully, R. B., Pomarède, D., Graziani, R., et al. (2019), *Cosmicflows-3: Cosmography of the Local Void*, Astrophysical Journal, 880(1), 24
- Vacca, V., Govoni, F., Murgia, M., et al. (2022a), *Puzzling large-scale polarization in the galaxy cluster Abell 523*, Monthly Notices of the RAS, 514(4), 4969
- Vacca, V., Murgia, M., Govoni, F., et al. (2012), *The intracluster magnetic field power spectrum in A2199*, Astronomy and Astrophysics, 540, A38
- Vacca, V., Shimwell, T., Perley, R. A., et al. (2022b), *Spectral study of the diffuse synchrotron source in the galaxy cluster Abell 523*, Monthly Notices of the RAS, 511(3), 3389
- Vaidya, B., Mignone, A., Bodo, G., et al. (2018), *A Particle Module for the PLUTO Code. II. Hybrid Framework for Modeling Nonthermal Emission from Relativistic Magnetized Flows*, Astrophysical Journal, 865(2), 144
- Vallee, J. P. (1975), *Magnetic field in the intergalactic region*, Nature, 254(5495), 23
- van de Weygaert, R. and Platen, E. (2011), *Cosmic Voids: Structure, Dynamics and Galaxies*, in *International Journal of Modern Physics Conference Series*, volume 1 of *International Journal of Modern Physics Conference Series*, 41–66
- van Weeren, R. J., Brüggén, M., Röttgering, H. J. A., and Hoeft, M. (2011a), *Using double radio relics to constrain galaxy cluster mergers: a model of double radio relics in CIZA J2242.8+5301*, Monthly Notices of the RAS, 418(1), 230

- van Weeren, R. J., Brüggen, M., Röttgering, H. J. A., and Hoeft, M. (2011b), *Using double radio relics to constrain galaxy cluster mergers: a model of double radio relics in CIZA J2242.8+5301*, Monthly Notices of the RAS, 418(1), 230
- van Weeren, R. J., Brunetti, G., Brüggen, M., et al. (2016), *LOFAR, VLA, and Chandra Observations of the Toothbrush Galaxy Cluster*, Astrophysical Journal, 818(2), 204
- van Weeren, R. J., de Gasperin, F., Akamatsu, H., et al. (2019), *Diffuse Radio Emission from Galaxy Clusters*, Space Science Reviews, 215(1)
- van Weeren, R. J., Röttgering, H. J. A., Brüggen, M., and Hoeft, M. (2010), *Particle Acceleration on Megaparsec Scales in a Merging Galaxy Cluster*, Science, 330(6002), 347
- Vazza, F., Brüggen, M., Gheller, C., et al. (2017), *Simulations of extragalactic magnetic fields and of their observables*, Classical and Quantum Gravity, 34(23), 234001
- Vazza, F., Brüggen, M., Gheller, C., and Wang, P. (2014), *On the amplification of magnetic fields in cosmic filaments and galaxy clusters*, Monthly Notices of the RAS, 445(4), 3706
- Vazza, F., Brüggen, M., van Weeren, R., et al. (2012), *Why are central radio relics so rare?*, Monthly Notices of the RAS, 421(3), 1868
- Vazza, F., Brüggen, M., Wittor, D., et al. (2016), *Constraining the efficiency of cosmic ray acceleration by cluster shocks*, Monthly Notices of the RAS, 459(1), 70
- Vazza, F., Brunetti, G., Brüggen, M., and Bonafede, A. (2018), *Resolved magnetic dynamo action in the simulated intracluster medium*, Monthly Notices of the RAS, 474(2), 1672
- Vazza, F., Brunetti, G., and Gheller, C. (2009), *Shock waves in Eulerian cosmological simulations: main properties and acceleration of cosmic rays*, Monthly Notices of the RAS, 395(3), 1333
- Vazza, F., Dolag, K., Ryu, D., et al. (2011), *A comparison of cosmological codes: properties of thermal gas and shock waves in large-scale structures*, Monthly Notices of the RAS, 418(2), 960
- Vazza, F., Eckert, D., Brüggen, M., and Huber, B. (2015a), *Electron and proton acceleration efficiency by merger shocks in galaxy clusters*, Monthly Notices of the RAS, 451(2), 2198
- Vazza, F., Etori, S., Roncarelli, M., et al. (2019), *Detecting shocked intergalactic gas with X-ray and radio observations*, Astronomy and Astrophysics, 627, A5
- Vazza, F., Ferrari, C., Brüggen, M., et al. (2015b), *Forecasts for the detection of the magnetised cosmic web from cosmological simulations*, Astronomy and Astrophysics, 580, A119
- Vazza, F., Locatelli, N., Rajpurohit, K., et al. (2021a), *Magnetogenesis and the Cosmic Web: A Joint Challenge for Radio Observations and Numerical Simulations*, Galaxies, 9(4), 109

- Vazza, F., Wittor, D., Brüggén, M., and Brunetti, G. (2023), *Simulating the Enrichment of Fossil Radio Electrons by Multiple Radio Galaxies*, *Galaxies*, 11(2), 45
- Vazza, F., Wittor, D., Brunetti, G., and Brüggén, M. (2021b), *Simulating the transport of relativistic electrons and magnetic fields injected by radio galaxies in the intracluster medium*, *Astronomy and Astrophysics*, 653, A23
- Venturi, T., Giacintucci, S., Merluzzi, P., et al. (2022), *Radio footprints of a minor merger in the Shapley Supercluster: From supercluster down to galactic scales*, *Astronomy and Astrophysics*, 660, A81
- Vernstrom, T., Gaensler, B. M., Brown, S., et al. (2017), *Low-frequency radio constraints on the synchrotron cosmic web*, *Monthly Notices of the RAS*, 467(4), 4914
- Vernstrom, T., Gaensler, B. M., Rudnick, L., and Andernach, H. (2019), *Differences in Faraday Rotation between Adjacent Extragalactic Radio Sources as a Probe of Cosmic Magnetic Fields*, *Astrophysical Journal*, 878(2), 92
- Vernstrom, T., Heald, G., Vazza, F., et al. (2021), *Discovery of magnetic fields along stacked cosmic filaments as revealed by radio and X-ray emission*, *Monthly Notices of the RAS*, 505(3), 4178
- Vernstrom, T., West, J., Vazza, F., et al. (2023), *Polarized accretion shocks from the cosmic web*, arXiv e-prints, arXiv:2302.08072
- Veronica, A., Reiprich, T. H., Pacaud, F., et al. (2023), *The eROSITA view of the Abell 3391/95 field: Cluster Outskirts and Filaments*
- Vogelsberger, M., Genel, S., Springel, V., et al. (2014), *Introducing the Illustris Project: simulating the coevolution of dark and visible matter in the Universe*, *Monthly Notices of the RAS*, 444(2), 1518
- Vogelsberger, M., Marinacci, F., Torrey, P., and Puchwein, E. (2020), *Cosmological simulations of galaxy formation*, *Nature Reviews Physics*, 2(1), 42
- Walker, S. A., Hlavacek-Larrondo, J., Gendron-Marsolais, M., et al. (2017), *Is there a giant Kelvin-Helmholtz instability in the sloshing cold front of the Perseus cluster?*, *Monthly Notices of the RAS*, 468(2), 2506
- Weber, M., Thomas, T., and Pfrommer, C. (2022), *Comparing energy and entropy formulations for cosmic ray hydrodynamics*, arXiv e-prints, arXiv:2205.12288
- Weibel, E. S. (1959), *Spontaneously Growing Transverse Waves in a Plasma Due to an Anisotropic Velocity Distribution*, *Physical Review Letters*, 2(3), 83
- Wendland, H. (1995), *Piecewise polynomial, positive definite and compactly supported radial functions of minimal degree*, *Advances in computational Mathematics*, 4(1), 389

- Wendland, H. (2004), *Scattered data approximation*, volume 17 of 1, Cambridge university press
- Wentzel, D. G. (1974), *Cosmic-ray propagation in the Galaxy: collective effects.*, Annual Review of Astron and Astrophys, 12, 71
- Werhahn, M., Pfrommer, C., Girichidis, P., et al. (2021), *Cosmic rays and non-thermal emission in simulated galaxies. I. Electron and proton spectra compared to Voyager-1 data*, Monthly Notices of the RAS
- Werner, N., Finoguenov, A., Kaastra, J. S., et al. (2008), *Detection of hot gas in the filament connecting the clusters of galaxies Abell 222 and Abell 223*, Astronomy and Astrophysics, 482(3), L29
- Westfold, K. C. (1959), *The Polarization of Synchrotron Radiation.*, Astrophysical Journal, 130, 241
- Widrow, L. M. (2002), *Origin of galactic and extragalactic magnetic fields*, Reviews of Modern Physics, 74(3), 775
- Wiener, J., Oh, S. P., and Guo, F. (2013), *Cosmic ray streaming in clusters of galaxies*, Monthly Notices of the RAS, 434(3), 2209
- Wiener, J., Zweibel, E. G., and Oh, S. P. (2018), *High β effects on cosmic ray streaming in galaxy clusters*, Monthly Notices of the RAS, 473(3), 3095
- Willson, M. A. G. (1970), *Radio observations of the cluster of galaxies in Coma Berenices - the 5C4 survey.*, Monthly Notices of the RAS, 151, 1
- Winner, G., Pfrommer, C., Girichidis, P., and Pakmor, R. (2019), *Evolution of cosmic ray electron spectra in magnetohydrodynamical simulations*, Monthly Notices of the RAS, 488(2), 2235
- Winner, G., Pfrommer, C., Girichidis, P., et al. (2020), *Evolution and observational signatures of the cosmic ray electron spectrum in SN 1006*, Monthly Notices of the RAS, 499(2), 2785
- Wittor, D. (2021), *On the Challenges of Cosmic-Ray Proton Shock Acceleration in the Intracluster Medium*, New Astronomy, 85, 101550
- Wittor, D., Brügggen, M., Grete, P., and Rajpurohit, K. (2023), *A morphological analysis of the substructures in radio relics*, Monthly Notices of the RAS, 523(1), 701
- Wittor, D., Etori, S., Vazza, F., et al. (2021), *Exploring the spectral properties of radio relics - I: integrated spectral index and Mach number*, Monthly Notices of the RAS, 506(1), 396
- Wittor, D., Hoeft, M., Vazza, F., et al. (2019), *Polarization of radio relics in galaxy clusters*, Monthly Notices of the RAS, 490(3), 3987
- Wittor, D., Vazza, F., and Brügggen, M. (2017), *Testing cosmic ray acceleration with radio relics: a high-resolution study using MHD and tracers*, Monthly Notices of the RAS, 464(4), 4448

- Wittor, D., Vazza, F., Ryu, D., and Kang, H. (2020), *Limiting the shock acceleration of cosmic ray protons in the ICM*, Monthly Notices of the RAS, 495(1), L112
- Wong, K., Zhdankin, V., Uzdensky, D. A., et al. (2020), *First-principles Demonstration of Diffusive-advective Particle Acceleration in Kinetic Simulations of Relativistic Plasma Turbulence*, Astrophysical Journal, Letters, 893(1), L7
- Xi, S.-Q., Wang, X.-Y., Liang, Y.-F., et al. (2018), *Detection of gamma-ray emission from the Coma cluster with Fermi Large Area Telescope and tentative evidence for an extended spatial structure*, Physical Review D, 98(6), 063006
- Xu, H., Li, H., Collins, D. C., et al. (2011), *Evolution and Distribution of Magnetic Fields from Active Galactic Nuclei in Galaxy Clusters. II. The Effects of Cluster Size and Dynamical State*, Astrophysical Journal, 739(2), 77
- Xu, H., O'Shea, B. W., Collins, D. C., et al. (2008), *The Biermann Battery in Cosmological MHD Simulations of Population III Star Formation*, Astrophysical Journal, Letters, 688(2), L57
- Yang, H. Y., Ruszkowski, M., and Zweibel, E. (2018), *Unveiling the Origin of the Fermi Bubbles, Galaxies*, 6(1), 29
- Yang, H. Y. K. and Ruszkowski, M. (2017), *The Spatially Uniform Spectrum of the Fermi Bubbles: The Leptonic Active Galactic Nucleus Jet Scenario*, Astrophysical Journal, 850(1), 2
- Yang, H. Y. K., Ruszkowski, M., and Zweibel, E. G. (2022), *Fermi and eROSITA bubbles as relics of the past activity of the Galaxy's central black hole*, Nature Astronomy, 6, 584
- Zaroubi, S., Hoffman, Y., Fisher, K. B., and Lahav, O. (1995), *Wiener Reconstruction of the Large-Scale Structure*, Astrophysical Journal, 449, 446
- Zaroubi, S., Squires, G., Hoffman, Y., and Silk, J. (1998), *Deprojection of Rich Cluster Images*, Astrophysical Journal, Letters, 500(2), L87
- Zel'dovich, Y. B. (1970), *The Hypothesis of Cosmological Magnetic Inhomogeneity.*, Soviet Astronomy, 13, 608
- Zhang, C., Churazov, E., Dolag, K., et al. (2020a), *Collision of merger and accretion shocks: formation of Mpc-scale contact discontinuity in the Perseus cluster*, Monthly Notices of the RAS, 498(1), L130
- Zhang, C., Churazov, E., Dolag, K., et al. (2020b), *Encounters of merger and accretion shocks in galaxy clusters and their effects on intracluster medium*, Monthly Notices of the RAS, 494(3), 4539
- Zhuravleva, I., Churazov, E., Schekochihin, A. A., et al. (2019), *Suppressed effective viscosity in the bulk intergalactic plasma*, Nature Astronomy, 3, 832

- ZuHone, J. and Su, Y. (2022), *The Merger Dynamics of the X-ray Emitting Plasma in Clusters of Galaxies*, arXiv e-prints, arXiv:2202.06712
- ZuHone, J. A., Kunz, M. W., Markevitch, M., et al. (2015), *The Effect of Anisotropic Viscosity on Cold Fronts in Galaxy Clusters*, *Astrophysical Journal*, 798(2), 90
- ZuHone, J. A., Markevitch, M., and Johnson, R. E. (2010), *Stirring Up the Pot: Can Cooling Flows in Galaxy Clusters be Quenched by Gas Sloshing?*, *Astrophysical Journal*, 717(2), 908
- ZuHone, J. A., Markevitch, M., Ruszkowski, M., and Lee, D. (2013), *Cold Fronts and Gas Sloshing in Galaxy Clusters with Anisotropic Thermal Conduction*, *Astrophysical Journal*, 762(2), 69
- ZuHone, J. A., Markevitch, M., Weinberger, R., et al. (2021), *How Merger-driven Gas Motions in Galaxy Clusters Can Turn AGN Bubbles into Radio Relics*, *Astrophysical Journal*, 914(1), 73
- Zwicky, F. (1933), *Die Rotverschiebung von extragalaktischen Nebeln*, *Helvetica Physica Acta*, 6, 110

Acknowledgements

First, I want to thank Nadia Böss. Your unwavering support, patience, and encouragement throughout the years made all this possible.

I would like to express my deepest gratitude to my supervisors Harald Lesch and Klaus Dolag. Your support, scientific mentorship, and encouragement made this endeavor a great journey. Thank you for giving me a great playground to explore science and pursue ideas, while also bringing me back on track when I got lost in minor details.

I'm extremely grateful to Ulrich Steinwandel for co-supervision, guidance, visits to New York, and generally lots of fun.

Many thanks to Joseph O'Leary for his support, coding discussions, lots of laughs, and for spoiling me with amazing food.

I would like to thank my COMPLEX colleagues and friends Luca Sala, Elena Hernández-Martínez, Tirso Marin-Gilabert, Frederick Groth, Stephan Vladutescu-Zopp and Laura di Federico for many good memories in the office and at conferences.

I would like to extend my sincere thanks to my co-authors and the many other great scientists I had the pleasure of meeting over the last few years for helpful comments and interesting discussions.

I further would like to thank Daniel Karner and Sebastian Nuza, with whom I had the pleasure of working, and look forward to extending CRESCENDO with them in the future.

Finally, I would like to thank the rest of the CAST group at USM for the interesting discussions, JULIA nerd sessions, and great coffee breaks.

Appendix

A.1 Shocktube Tests

Table A.1: We report the parameters for the different shock tube tests used in this work. The subscripts L and R denote the quantities left and right of the initial contact discontinuity, respectively. From left to right we report model name, densities, temperatures, sonic Mach number in the case without CR acceleration and magnetic field vectors. We convert all units to physical units purely for consistency.

Model Name	ρ_L [cm $^{-3}$]	ρ_R [cm $^{-3}$]	T_L [K]	T_R [K]	$\mathcal{M}_{s,\text{analytic}}$	B_L [nG]	B_R [nG]
Sod $_{\mathcal{M}_s=3}$	356.18	44.52	$4.75 \cdot 10^3$	745.6	3.00	(0.0, 0.0, 0.0)	(0.0, 0.0, 0.0)
Sod $_{\mathcal{M}_s=4}$	356.18	44.52	$4.75 \cdot 10^3$	396.6	4.00	(0.0, 0.0, 0.0)	(0.0, 0.0, 0.0)
Sod $_{\mathcal{M}_s=5}$	356.18	44.52	$4.75 \cdot 10^3$	247.5	5.00	(0.0, 0.0, 0.0)	(0.0, 0.0, 0.0)
Sod $_{\mathcal{M}_s=6}$	356.18	44.52	$4.75 \cdot 10^3$	169.5	6.00	(0.0, 0.0, 0.0)	(0.0, 0.0, 0.0)
Sod $_{\mathcal{M}_s=7}$	356.18	44.52	$4.75 \cdot 10^3$	123.6	7.00	(0.0, 0.0, 0.0)	(0.0, 0.0, 0.0)
Sod $_{\mathcal{M}_s=8}$	356.18	44.52	$4.75 \cdot 10^3$	94.1	8.00	(0.0, 0.0, 0.0)	(0.0, 0.0, 0.0)
Sod $_{\mathcal{M}_s=9}$	356.18	44.52	$4.75 \cdot 10^3$	74.1	9.00	(0.0, 0.0, 0.0)	(0.0, 0.0, 0.0)
Sod $_{\mathcal{M}_s=10}$	356.18	44.52	$4.75 \cdot 10^3$	59.9	10.00	(0.0, 0.0, 0.0)	(0.0, 0.0, 0.0)
Sod $_{\mathcal{M}_s=15}$	356.18	44.52	$4.75 \cdot 10^3$	26.4	15.00	(0.0, 0.0, 0.0)	(0.0, 0.0, 0.0)
Sod $_{\mathcal{M}_s=20}$	356.18	44.52	$4.75 \cdot 10^3$	14.8	20.00	(0.0, 0.0, 0.0)	(0.0, 0.0, 0.0)
Sod $_{\mathcal{M}_s=30}$	356.18	44.52	$4.75 \cdot 10^3$	6.59	30.00	(0.0, 0.0, 0.0)	(0.0, 0.0, 0.0)
Sod $_{\mathcal{M}_s=40}$	356.18	44.52	$4.75 \cdot 10^3$	3.70	40.00	(0.0, 0.0, 0.0)	(0.0, 0.0, 0.0)
Sod $_{\mathcal{M}_s=50}$	356.18	44.52	$4.75 \cdot 10^3$	2.37	50.00	(0.0, 0.0, 0.0)	(0.0, 0.0, 0.0)
Sod $_{\mathcal{M}_s=60}$	356.18	44.52	$4.75 \cdot 10^3$	1.65	60.00	(0.0, 0.0, 0.0)	(0.0, 0.0, 0.0)
Sod $_{\mathcal{M}_s=70}$	356.18	44.52	$4.75 \cdot 10^3$	1.21	70.00	(0.0, 0.0, 0.0)	(0.0, 0.0, 0.0)
Sod $_{\mathcal{M}_s=80}$	356.18	44.52	$4.75 \cdot 10^3$	$9.25 \cdot 10^{-1}$	80.00	(0.0, 0.0, 0.0)	(0.0, 0.0, 0.0)
Sod $_{\mathcal{M}_s=90}$	356.18	44.52	$4.75 \cdot 10^3$	$7.31 \cdot 10^{-1}$	90.00	(0.0, 0.0, 0.0)	(0.0, 0.0, 0.0)
Sod $_{\mathcal{M}_s=100}$	356.18	44.52	$4.75 \cdot 10^3$	$5.92 \cdot 10^{-1}$	100.00	(0.0, 0.0, 0.0)	(0.0, 0.0, 0.0)
Dubios $_{\theta=0}$	356.18	44.52	$4.53 \cdot 10^3$	57.0	10.00	(0.1, 0.0, 0.0)	(0.1, 0.0, 0.0)
Dubios $_{\theta=15}$	356.18	44.52	$4.53 \cdot 10^3$	57.0	10.00	(0.097, 0.026, 0.0)	(0.097, 0.026, 0.0)
Dubios $_{\theta=30}$	356.18	44.52	$4.53 \cdot 10^3$	57.0	10.00	(0.087, 0.05, 0.0)	(0.087, 0.05, 0.0)
Dubios $_{\theta=45}$	356.18	44.52	$4.53 \cdot 10^3$	57.0	10.00	(0.07, 0.07, 0.0)	(0.07, 0.07, 0.0)
Dubios $_{\theta=60}$	356.18	44.52	$4.53 \cdot 10^3$	57.0	10.00	(0.05, 0.087, 0.0)	(0.05, 0.087, 0.0)
Dubios $_{\theta=75}$	356.18	44.52	$4.53 \cdot 10^3$	57.0	10.00	(0.026, 0.097, 0.0)	(0.026, 0.097, 0.0)
Dubios $_{\theta=90}$	356.18	44.52	$4.53 \cdot 10^3$	57.0	10.00	(0.0, 0.1, 0.0)	(0.0, 0.1, 0.0)
Cluster	$1.81 \cdot 10^{-4}$	$5.14 \cdot 10^{-5}$	$5.74 \cdot 10^8$	$1.54 \cdot 10^7$	5.54	$(3.5 \cdot 10^3, 0.0, 0.0)$	$(1.0 \cdot 10^3, 0.0, 0.0)$
CIZA	$1.13 \cdot 10^{-2}$	$1.41 \cdot 10^{-3}$	$5.58 \cdot 10^8$	$3.46 \cdot 10^7$	4.60	(0.0, 0.0, 0.0)	(0.0, 0.0, 0.0)

A.2 Non-Relativistic Limits

In this section we want to briefly outline a possibility to include the mildly-relativistic component of the distribution function in a more accurate way. This is based on [Girichidis et al. \(2022\)](#), Appendix A and can only be considered an approximation. An alternative would be to Taylor-expand the individual terms and solve them to an arbitrary order, however we will not discuss this possibility here.

Pressure Integral

First and foremost we will need to update the pressure integral to account for the changing adiabatic index between supra-thermal and relativistic CRs. As discussed in [Girichidis et al. \(2020\)](#) the transition between $\gamma = 5/3$ and $\gamma = 4/3$ takes place in the momentum range $\hat{p} \sim 0.1 - 1.0$, which is within our canonical lower boundaries.

To account for this [Girichidis et al. \(2022\)](#) rewrite the pressure integral as

$$P_{\text{cr},i} = \frac{4\pi}{3} f_i \int_{p_i}^{p_{i+1}} dp \left(\frac{p}{p_i}\right)^{-q_i} \frac{p^4 c^2}{\sqrt{m_p^2 c^4 + p^2 c^2}} \quad (\text{A.1})$$

$$\equiv \frac{4\pi}{3} f_i \mathcal{I}_{p_i}^{p_{i+1}} \quad (\text{A.2})$$

where they introduce

$$\mathcal{I}_{p_i}^{p_{i+1}} = \frac{(m_p c)^4 c}{2} \left(\frac{p_i}{m_p c}\right)^{q_i} \left[\mathcal{B}_{x(p)} \left(\frac{5 - q_i}{2}, \frac{q_i - 4}{2} \right) \right]_{p_i}^{p_{i+1}} \quad (\text{A.3})$$

with $\mathcal{B}_x(a, b)$ being the incomplete beta function and

$$x(p) = \frac{p^2}{p^2 + m_p^2 c^2}. \quad (\text{A.4})$$

Effective Adiabatic Index

As the CR model is coupled to our hydro solver via the CR pressure term we need to account for the effective adiabatic index of the thermal+CR gas composite.

From the general ansatz

$$\gamma_{\text{cr}}(p_0) = \frac{d \ln P_{\text{cr}}}{d \ln \rho} \Big|_S \quad (\text{A.5})$$

$$= \frac{\rho}{P_{\text{cr}}} \left[\frac{\partial P_{\text{cr}}}{\partial p_0} \frac{\partial p_0}{\partial \rho} + \frac{\partial P_{\text{cr}}}{\partial f_0} \frac{\partial f_0}{\partial \rho} \right] \quad (\text{A.6})$$

Girichidis et al. (2022) arrive at an expression for the adiabatic index per bin i as

$$\gamma_{\text{cr},i} = \frac{\rho}{P_{\text{cr},i}} \left(\frac{\partial P_{\text{cr},i}}{\partial f_i} \frac{\partial f_i}{\partial \rho} + \frac{\partial P_{\text{cr},i}}{\partial p_i} \frac{\partial p_i}{\partial \rho} + \frac{\partial P_{\text{cr},i}}{\partial p_{i+1}} \frac{\partial p_{i+1}}{\partial \rho} \right) \quad (\text{A.7})$$

$$= \frac{q_i}{3} - \frac{1}{3} \frac{p_i^5 c}{\sqrt{m_p^2 c^2 + p_i^2}} (\mathcal{I}_{p_i}^{p_{i+1}})^{-1} + \frac{1}{3} \frac{p_{i+1}^5 c}{\sqrt{m_p^2 c^2 + p_{i+1}^2}} \left(\frac{p_{i+1}}{p_i} \right)^{-q_i} (\mathcal{I}_{p_i}^{p_{i+1}})^{-1} \quad (\text{A.8})$$

where they used Eq. A.2. In Appendix A1 they also provide an analytic approximation for the adiabatic index of this composite as a function of momentum

$$\gamma(p_0) = \frac{5}{3} - \frac{p_0^2}{3(p_0^2 + m_p^2 c^2)} \quad (\text{A.9})$$

which can be used to test the implementation.

Energy Integral

We can also use Eq. A.2 to find a general solution for the energy integral as

$$E_{\text{cr},i} = \frac{4\pi}{\rho} f_i \mathcal{I}_{p_i}^{p_{i+1}} \quad (\text{A.10})$$

which is essential for the further steps of updating the injection and the slope finding.

Injection

We currently inject CRs by solving the energy integral in Eq. 5.12 for $f(\hat{p}_{\text{inj}})$ as given in Eq. 6.1 and subsequently interpolating the powerlaw up to \hat{p}_{max} using the injection slope q_{inj} . However, Eq. 6.1 is also solved in the relativistic limit.

We will need to update the injection by solving Eq. A.10 for f_{inj} as

$$f(p_{\text{inj}}) = \frac{\rho}{4\pi} E_{\text{inj}} \left(\mathcal{I}_{p_{\text{inj}}}^{p_{\text{max}}} \right)^{-1} \quad (\text{A.11})$$

The interpolation in momentum space can be performed in the same fashion as before, since DSA produces powerlaws in momentum space.

Slope Update

With the updated energy integral we also need to update our slope solver. As was the case in Eq. 5.28 we need to solve Eq. 5.9 and Eq. A.10 for f_i . In the general form this takes the form

$$\frac{E_i}{N_i} = \frac{3 - q_i}{p_i^3 \left(\left(\frac{p_{i+1}}{p_i} \right)^{3 - q_i} - 1 \right)} \mathcal{I}_{p_i}^{p_{i+1}} \quad (\text{A.12})$$

which as was the case for Eq. 5.28 can be solved for q_i with any suitable root finding algorithm. We note however that the incomplete beta function $\mathcal{B}_x(a, b)$ will likely add substantial computational cost, so it needs to be considered if the slope solving should be split into a non-relativistic and relativistic part.

Energy Changes

The new definition of E_i also adds complications when solving energy changes within bins. We will need to update the description for the fluxes between momentum bins, given by Eq. 5.22.

Adiabatic Changes

For adiabatic changes we can consider to by-pass this complication and solve the direct norm update by considering the conservation of phase-space density as in [Girichidis et al. \(2022\)](#), Appendix A2:

$$f_i = f_0 \left(\frac{\rho}{\rho_0} \right)^{q_i/3}. \quad (\text{A.13})$$

As adiabatic changes are expected to be self-similar and to not change the slope within the bin we would only need to re-compute N_i and E_i after the density change.

Future tests will need to quantify the numerical stability of this approach. It would however likely change the stability problem in cosmological simulations, which require us to use the no-influx boundary conditions in the current implementation.

Energy Losses and Fermi-II Re-Acceleration

Equally we will have to reformulate the energy fluxes due to radiative energy losses and Fermi-II re-acceleration. Depending on the computational cost of $\mathcal{B}_x(a, b)$ we will need to consider splitting the energy losses into a non-relativistic and relativistic parts.